

# IRE Transactions



on ANTENNAS and PROPAGATION

Volume AP-8

JULY, 1960

Number 4

*Published Bimonthly*

## In This Issue

Coupled Leaky Waveguides II: Two Parallel Slits in a Cylinder

Mutual Coupling Effects in Large Arrays II

Paraboloidal Reflector Patterns for Off-Axis Feed

Unequally-Spaced, Broad-Band Antenna Arrays

Resonant Slots with Independent Control of Amplitude and Phase

Mutual Coupling of Shunt Slots

A Wide-Band Transverse-Slot Flush-Mounted Array

Relation Between Two- and Three-Dimensional Diffraction Problems

Forward Scatter From Rain

Solution of a Reflection Problem

Experimental Swept-Frequency Tropospheric Scatter Link

Energy Density in Continuous Electromagnetic Media

PUBLISHED BY THE

Professional Group on Antennas and Propagation



## Administrative Committee

E. C. Jordan, *Chairman*

Harry Fine, *Vice-Chairman*

K. S. Kelleher, *Secretary*

R. J. Adams

H. V. Cottony

E. K. Smith

S. A. Bowhill

N. J. Gamara

K. M. Siegel

R. N. Bracewell

R. C. Hansen

L. G. Trolese

S. M. King

### Ex-Officio Members

J. I. Bohnert

J. W. Findlay

D. G. Ports

Arthur Dorne

R. L. Mattingly

P. H. Smith

### Honorary Member

L. C. Van Atta

### Chapter Chairmen

*Akron*

*Dayton*

*San Diego*

J. R. Shoemaker

C. G. Conrad

H. Dickstein

*Albuquerque-Los Alamos*

*Denver-Boulder*

*San Francisco*

D. Thorn

W. C. Coombs

R. C. Honey

*Boston*

*Los Angeles*

*Syracuse*

J. Ruze

L. A. Kurtz

E. B. Mullen

*Chicago*

*Orange Belt*

*Washington, D. C.*

H. L. Woodbury

W. S. Ward

R. J. Adams

*Columbus*

*Philadelphia*

H. B. Querido

J. T. Beardwood

S. A. Bowhill, *Editor*

H. V. Cottony, *Associate Editor (Antennas)*     A. T. Waterman, Jr., *Associate Editor (Propagation)*

K. M. Siegel, *Associate Editor (Electromagnetic Theory)*

J. W. Findlay, *Associate Editor (Radio Astronomy)*

D. C. Ports, *Advertising Editor*

---

**IRE TRANSACTIONS® PGAP** IS A PUBLICATION DEVOTED TO  
EXPERIMENTAL AND THEORETICAL PAPERS ON RADIO ANTENNAS,  
ON GUIDED OR UNGUIDED PROPAGATION OF RADIO WAVES, AND  
ON ALLIED FIELDS OF RADIO PHYSICS SUCH AS RADIO ASTRONOMY

---

**MANUSCRIPTS** should be submitted to Sidney A. Bowhill, Editor, 222 Electrical Engineering, Pennsylvania State University, University Park, Pa. Manuscripts should be original typewritten copy, double spaced, plus one carbon copy and two sets of copies of illustrations. Original illustrations will be called for if the paper is accepted. References should appear as footnotes and include author's name, title, journal, volume, initial and final page numbers, and date. Each paper must have a summary of not more than 200 words. News items concerning PGAP members and group activities should be sent to the News Editor, R. C. Hansen, Space Technology Laboratories, P.O. Box 95001, Los Angeles 45, Calif.

**ORIGINAL ILLUSTRATIONS** should be submitted as follows: All line drawings (graphs, charts, block diagrams, cutaways, etc.) should be inked uniformly and ready for reproduction. If commercially printed grids are used in graph drawings, author should be sure printer's ink is of a color that will reproduce. All halftone illustrations (photographs, wash, airbrush, or pencil renderings, etc.) should be clean and ready to reproduce. Photographs should be glossy prints. Call-outs or labels should be marked on a registered tissue overlay, not on the illustration itself. No illustration should be larger than 8 x 10 inches.

---

**Copies can be purchased from THE INSTITUTE OF RADIO ENGINEERS, 1 East 79 St., New York 21, N.Y. PRICE PER COPY:** members of the Professional Group on Antennas and Propagation, \$1.90; members of the IRE \$2.85; nonmembers, \$5.70. **ANNUAL SUBSCRIPTION PRICE:** PGAP members, included in PGAP fee of \$4.00; IRE members, \$8.50; Colleges and public libraries, \$10.00; nonmembers, \$17.00. IRE TRANSACTIONS ON ANTENNAS AND PROPAGATION. Copyright © 1960, by The Institute of Radio Engineers, Inc. Printed in U.S.A. Printed by George Banta Co., Inc., Curtis Plaza, Menasha, Wisconsin.

Second-class postage paid at MENASHA, WISCONSIN, and additional mailing offices under the act of August 24, 1912. Acceptance for mailing at a special rate of postage is provided for in the act of February 28, 1925, embodied in Paragraph 4, Section 412, P. L. & R., authorized October 26, 1927.



Andreason, M.  
Bolljahn, J. T.  
Brown, R. M., Jr.  
Carter, P. S., Jr.  
Crawford, A. B.  
Deschamps, G. A.  
DuHamel, R. H.  
Felsen, L. B.  
Goodrich, R.  
Hansen, R. C.  
Hayden, E. C.  
Hiatt, R. E.  
Honey, R. C.  
Jones, E. M. T.  
Jordan, E. C.  
Kales, M. L.  
Kelleher, K. S.  
Lo, Y. T.  
Marston, A. E.  
Mattingly, R. L.  
Morgan, S. P.  
Morita, T.  
Mortimore, T. N.  
Rumsey, V. H.  
Ruse, J.  
Sinclair, G.  
Swenson, G. W., Jr.  
Tanner, R. L.  
Twersky, V.  
Wait, J. R.  
Yen, J. L.  
Zucker, F. J.

PGAP TRANSACTIONS  
PROPAGATION REVIEWERS

Abel, W. G.  
Booker, H. G.  
Bracewell, R. N.  
Brown, S. C.  
Bullington, K.  
Carroll, T. J.  
Chisholm, J. H.  
de Bettencourt, J. T.  
Dyce, R. B.  
Eshleman, V. R.  
Findlay, J. W.  
Gautier, T. N.  
Gordon, W. E.  
Lowenthal, M.  
Manning, L. A.  
Morita, T.  
Norton, K. A.  
Pfister, W.  
Rogers, T. F.  
Rumsey, V. H.  
Straiton, A. W.  
Twersky, V.  
Trolese, L. G.  
Wheelon, A. D.

# IRE Transactions

## on

# Antennas and Propagation

Volume AP-8

JULY, 1960

Number 4

### TABLE OF CONTENTS

#### CONTRIBUTIONS

Coupled Leaky Waveguides II: Two Parallel Slits in a Cylinder.....	<i>S. Nishida</i>	354
Mutual Coupling Effects in Large Antenna Arrays II: Compensation Effects.....	<i>S. Edelberg and A. A. Oliner</i>	360
Paraboloidal Reflector Patterns for Off-Axis Feed.....	<i>S. S. Sandler</i>	368
Unequally-Spaced, Broad-Band Antenna Arrays.....	<i>D. D. King, R. F. Packard, and R. K. Thomas</i>	380
Resonant Slots with Independent Control of Amplitude and Phase.....	<i>B. J. Maxum</i>	384
Mutual Coupling of Shunt Slots.....	<i>A. F. Kay and A. J. Simmons</i>	389
A Wide-Band Transverse-Slot Flush-Mounted Array....	<i>E. M. T. Jones and J. K. Shimizu</i>	401
Relation Between a Class of Two-Dimensional and Three-Dimensional Diffraction Problems.....	<i>L. B. Felsen and S. N. Karp</i>	407
Forward Scatter From Rain.....	<i>L. H. Doherty and S. A. Stone</i>	414
Solution of a Reflection Problem by Means of a Transmission Line Analogy.....	<i>B. L. Jones and P. C. Patton</i>	418
Experimental Swept-Frequency Tropospheric Scatter Link.....	<i>W. E. Landauer</i>	423
Energy Density in Continuous Electromagnetic Media.....	<i>A. Tonning</i>	428

#### COMMUNICATIONS

Resonant Antenna Array with Tilted Beam.....	<i>E. M. Rutz</i>	435
Van Atta Reflector Array.....	<i>E. D. Sharp and M. A. Diab</i>	436
A Circular Loop Antenna with Nonuniform Current Distribution.....	<i>J. E. Lindsay, Jr.</i>	439
Pattern Synthesis Using Weighted Functions.....	<i>P. A. Bricout</i>	441
On the Excitation of Electromagnetic Surface Waves on a Curved Surface.....	<i>J. R. Wait</i>	445
Note on "The Excitation of Electromagnetic Surface Waves on a Curved Surface".....	<i>H. M. Barlow</i>	449
The Structure of HF Signals Revealed by an Oblique Incidence Sweep Frequency Sounder.....	<i>D. J. Doyle, E. D. DuCharme, and G. W. Jull</i>	449
Contributors.....		452



# contributions

## Coupled Leaky Waveguides II: Two Parallel Slits in a Cylinder\*

S. NISHIDA†

**Summary**—Theoretical expressions are derived for the effects of mutual coupling between two parallel leaky wave antennas which consists of slitted rectangular waveguides located in a cylinder. The expressions derived are presented in terms of the results for the mutual coupling of the same antennas but located in an infinite plane, with additional terms due to the curvature of the cylinder. The graphical presentation of the numerical attenuation constants for the cylindrical case are compared with those for the infinite plane.

### I. INTRODUCTION

IN this paper, two parallel slits in a cylinder with a large radius, which are excited by two slitted rectangular waveguides of the same dimensions carrying the  $H_{10}$  leaky wave, will be investigated by employing the same analytical techniques as in the companion paper.<sup>1</sup> The physical structure involved in this problem, as shown in Fig. 1, has a symmetry plane which bisects the distance between the two slits. This problem, therefore, may be reduced to two problems for the in-phase excitation and the out-of-phase excitation in the same manner as in the companion paper. Both of these orthogonal cases will be described here, but problems with arbitrarily excited slits may be solved by superposing these two cases.

\* Manuscript received by the PGAP, August 4, 1959; revised manuscript received, January 18, 1960. The research reported was conducted under Contract AF-19(604)-2031 sponsored by the AF Cambridge Res. Ctr., Air Res. and Dev. Command.

† Microwave Res. Inst., Polytechnic Institute of Brooklyn, Brooklyn, N. Y.; on leave of absence from Tohoku University, Sendai, Japan.

<sup>1</sup> S. Nishida, "Coupled leaky waveguides I: Two parallel slits in a plane," IRE TRANS. ON ANTENNAS AND PROPAGATION, vol. AP-8, pp. 323-330; May, 1960.

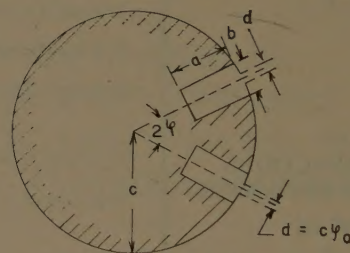


Fig. 1—The cross section of a cylinder with two parallel slits by waveguides (original problem).

In cylindrical problems with large radius, in general, the Green's function on the cylinder may be expressed by the so-called harmonic series which is very slowly convergent. It may, therefore, be necessary to obtain an alternative expression for the Green's function for computational purposes. The problem in this paper requires that the Green's function be defined in the shadow region in order to obtain the external admittance at the slit for use in a transverse network representation. For closely coupled slits, which are of the greatest interest here, it becomes necessary to employ an approximation for the Green's function which is valid in the portion of the shadow region adjacent to the illuminated region. The well-known residue series expression for the Green's function, which is a transformation of the harmonic series, is not a convenient representation because of its slow convergence in this case.

In this paper a more convenient representation for computational purposes is presented, which is ex-



pressed in terms of the infinite plane result derived in the companion paper, with additional terms due to the curvature of the cylinder. This representation is checked numerically and compared with the real part of the harmonic series. It will be shown in Fig. 3, as an example, that the comparison gives very good agreement in the case of close coupling.

By using the above representation, the external admittance to be employed in the transverse network representation will be derived in Sections IV and VI for in-phase and out-of-phase excitation, respectively. The attenuation constant of the leaky wave associated with the in-phase excitation then will be computed numerically as a typical example. The results are compared with the attenuation constant of the identical antenna located in an infinite plane.

Numerical results calculated for two different radii are presented in graphical form in Figs. 5 and 6. The calculations show that the values of attenuation constant for the wave guided along the cylinder oscillate with separation between the slits in a manner similar to that of the infinite plane case. The decay of the oscillations, however, is more rapid with a decrease in the radius of the cylinder, although the attenuation constants all have the same value for small separations. Figs. 5 and 6 also show that the period of the oscillations becomes longer with a decrease in the radius of the cylinder.

## II. IN-PHASE EXCITATION

In this case the problem is reduced to that of a single leaky waveguide with an electric wall which bisects the distance between the two waveguides, as shown in Fig. 2.

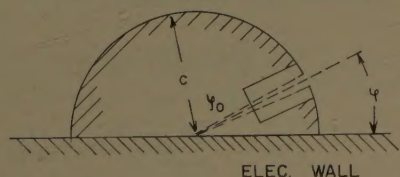


Fig. 2—The cross section of the reduced problem for in-phase excitation.

If the radius of the cylinder  $c$  is large enough compared with the dimensions of the waveguide, the influence of the curvature of a slitted side wall on the internal admittance employed in the transverse network representation may be ignored. Then, the problem can be treated in the same way as for that in the companion paper,<sup>2</sup> *i.e.*,

$$Y' = Y_{\text{int}}' + Y_{\text{ext}}',$$

where  $Y'$  represents the normalized admittance of the slit terminated in free space and where

$$Y_{\text{int}}' \simeq j \frac{\kappa b}{\pi} \ln \left( \csc \frac{\pi d}{2b} \right), \quad \kappa = \sqrt{k^2 - k_z^2}.$$

The Green's function in the open region is given by

$$G(\vartheta, \vartheta') = \sum_{n=0}^{\infty} \left( -\frac{\epsilon_n}{2} \right) \cos(n\vartheta) \cos(n\vartheta') \frac{\{J_n(\kappa\rho_<)N_n'(\kappa c) - N_n(\kappa\rho_<)J_n'(\kappa c)\}H_n^{(2)}(\kappa\rho_<)}{H_n^{(2)'}(\kappa c)} \quad (1)$$

for a circular cylinder co-ordinates,  $(f, \theta, z)$ ,  $z$ -direction of which coincides with the cylinder axis, where

$$\epsilon_n = 2 \text{ for } n \neq 0 \text{ or } 1 \text{ for } n = 0;$$

and

$$H_n^{(2)'}(\kappa c) = \left. \frac{\partial H_n^{(2)}(x)}{\partial x} \right]_{x=\kappa c}, \text{ etc.}$$

The associated dyadic admittance  $\mathbf{z}_0 \cdot \mathbf{y}(\theta, \theta') \cdot \mathbf{z}_0$ , therefore, is written as

$$\mathbf{z}_0 \cdot \mathbf{y}(\theta, \theta') \cdot \mathbf{z}_0 = \sum_{n=0}^{\infty} \frac{\epsilon_n \kappa}{j\omega\mu\pi c} \cos(n\theta) \cos(n\theta') \frac{H_n^{(2)}(\kappa c)}{H_n^{(2)'}(\kappa c)}, \quad (2)$$

where

$$\mathbf{y}(\theta, \theta') = [\mathbf{y}(\vartheta, \vartheta')]_{\rho=c}.$$

Thus, the external admittance desired here is obtained as follows:

$$Y_{\text{ext}} = \frac{1}{d} \int_{t_1}^{t_2} c d\theta \int_{t_1}^{t_2} c d\theta' \mathbf{z}_0 \cdot \mathbf{y}(\theta, \theta') \cdot \mathbf{z}_0 \quad (3)$$

where

$$t_1 = \phi - \frac{\phi_0}{2}, \quad t_2 = \phi + \frac{\phi_0}{2} \quad \text{and} \quad d = c\phi_0.$$

Or, carrying out integration, we have

$$Y_{\text{ext}} = \sum_{n=0}^{\infty} \frac{4\epsilon_n \kappa c \sin^2\left(\frac{n\phi_0}{2}\right)}{j\omega\mu\pi d n^2} \cdot \frac{H_n^{(2)}(\kappa c)}{H_n^{(2)'}(\kappa c)} \cdot \cos^2(n\phi). \quad (4)$$

The normalized external admittance, therefore, is

$$Y_{\text{ext}}' = \frac{b}{d} \sum_{n=0}^{\infty} \frac{4\epsilon_n c \sin^2\left(\frac{n\phi_0}{2}\right)}{j\pi d n^2} \cdot \frac{H_n^{(2)}(\kappa c)}{H_n^{(2)'}(\kappa c)} \cdot \cos^2(n\phi). \quad (5)$$

Eq. (5) is the result desired here, but it is not a convenient expression for numerical computation because of the slow convergence of its imaginary part. An alternative and more rapidly convergent expression is obtained from (5) in Sections III and IV below.

<sup>2</sup> *Ibid.*, Eqs. (1) to (5).



Let (5) first be recast into a more useful form. Since

$$\frac{4c^2 \sin^2\left(\frac{n\phi_0}{2}\right)}{n^2} = \int_0^d du \int_0^d du' \cos\left\{n\left(\frac{u-u'}{c}\right)\right\},$$

(5) becomes as follows:

$$\left. \begin{aligned} Y_{\text{ext}}' &= \frac{b}{d} \int_0^d du \int_0^d du' Y_0 \\ \text{where} \\ Y_c &= \sum_{n=0}^{\infty} \sum_{m=0,1} \frac{\epsilon_n}{j2\pi cd} \cdot \frac{H_n^{(2)}(\kappa c)}{H_n^{(2)'}(\kappa c)} \\ &\quad \cdot \cos\left\{n\left(2m\phi + \frac{u-u'}{c}\right)\right\} \end{aligned} \right\} \quad (6)$$

### III. APPROXIMATE REPRESENTATION OF $Y_c$

Eq. (6) can be rewritten as follows:

$$\begin{aligned} Y_c &= \sum_{m=0,1} P_m, \\ P_m &= K \sum_{n=-\infty}^{\infty} \frac{H_n^{(2)}(\kappa c)}{c H_n^{(2)'}(\kappa c)} e^{-jn\phi_m}, \end{aligned} \quad (7)$$

where

$$K = \frac{1}{j2\pi d} \quad \text{and} \quad \phi_m = 2m\phi + \frac{u-u'}{c}.$$

Eq. (7) may be transformed into an integral representation in the complex  $\nu$ -plane by employing Watson's transformation.<sup>3</sup> We, therefore, write

$$P_m = K \int_{C_1^+ + C_1^-} \frac{H_\nu^{(2)}(\kappa c) e^{-j\nu\phi_m}}{c H_\nu^{(2)'}(\kappa c)} \cdot \frac{e^{j\nu\pi}}{2j \sin \nu\pi} d\nu, \quad (8)$$

where the contours  $C_1^+$  and  $C_1^-$  are from  $-\infty + j\epsilon$  to  $\infty + j\epsilon$  and from  $-\infty - j\epsilon$  to  $\infty - j\epsilon$ , respectively. Putting  $\nu = ct$  and defining

$$\begin{aligned} f_t(c) &= \frac{H_{ct}^{(2)}(\kappa c)}{H_{ct}^{(2)'}(\kappa c)} \cdot \frac{e^{jct\pi}}{2j \sin(ct\pi)}, \\ &= \frac{H_{ct}^{(2)}(\kappa c)}{H_{ct}^{(2)'}(\kappa c)} \cdot \frac{1}{1 - e^{-j2ct\pi}}, \end{aligned}$$

we have

$$P_m = K \int_{C_1^+ + C_1^-} f_t(c) e^{-jc\phi_m t} dt. \quad (9)$$

Now, let us consider the following function:

$$f_t(\xi) = \frac{H_{\xi t}^{(2)}(\kappa \xi)}{H_{\xi t}^{(2)'}(\kappa \xi) (1 - e^{-j2t\pi \xi})}.$$

The function  $f_t(\xi)$  is finite on the positive real axis in the complex  $\xi$ -plane. We, therefore, have the formula

$$\frac{1}{j2\pi} \int_L \frac{c - \eta}{(\xi - c)(\xi - \eta)} f_t(\xi) d\xi = f_t(c) - f_t(\eta), \quad (10)$$

where  $\eta$  is a positive real number,  $\eta \gg c$  and the contour  $L$  encloses only two poles,  $\xi = c$  and  $\xi = \eta$ . Thus, (9) becomes

$$\begin{aligned} P_m &= K \int_{C_1^+ + C_1^-} f_t(\eta) e^{-jc\phi_m t} dt \\ &\quad + K \int_L \frac{c - \eta}{j2\pi(\xi - c)(\xi - \eta)} d\xi \int_{C_1^+ + C_1^-} f_t(\xi) e^{-jc\phi_m t} dt, \end{aligned} \quad (11)$$

$$P_m = Q_1 + Q_2.$$

In the first integral of the above equation,  $Q_1$ , we see that since

$$\begin{aligned} \frac{1}{1 - e^{-j2\pi t n}} &\rightarrow 0 \text{ on } C_1^+ \text{ as } \eta \rightarrow \infty, \\ &\rightarrow 1 \text{ on } C_1^- \text{ as } \eta \rightarrow \infty, \end{aligned}$$

$Q_1$  may be written as follows:

$$Q_1 = \lim_{\eta \rightarrow \infty} K \int_{C_1^+ + C_1^-} f_t(\eta) e^{-jc\phi_m t} dt,$$

$$Q_1 = \lim_{\eta \rightarrow \infty} K \int_{C_1^-} \frac{H_{\eta t}^{(2)}(\kappa \eta)}{H_{\eta t}^{(2)'}(\kappa \eta)} e^{-jc\phi_m t} dt,$$

or<sup>4</sup>

$$Q_1 = j\pi \kappa K H_0^{(2)}(\kappa c \phi_m). \quad (12)$$

The second integral of (11),  $Q_2$ , will be evaluated by the saddle point method. It may be decomposed into two terms by introducing the relations

$$\begin{aligned} \frac{1}{1 - e^{-j2\pi t \xi}} &= \sum_{n=0}^{\infty} e^{-j2n\pi t \xi} \text{ on } C_1^-, \\ &= - \sum_{n=0}^{\infty} e^{j2(n+1)\pi t \xi} \text{ on } C_1^+ \end{aligned}$$

that is

$$Q_2 = \sum_{n=0}^{\infty} K \int_L \frac{c - \eta}{j2\pi(\xi - c)(\xi - \eta)} \{q_n^{(+)} + q_n^{(-)}\} d\xi,$$

where

$$\left. \begin{aligned} q_n^{(+)} &= \int_{C_1^+} \frac{H_{\xi t}^{(2)}(\kappa \xi)}{H_{\xi t}^{(2)'}(\kappa \xi)} e^{-j\{c\phi_m - (2n+1)\pi t \xi\}} dt, \\ q_n^{(-)} &= \int_{C_1^+} \frac{H_{\xi t}^{(2)}(\kappa \xi)}{H_{\xi t}^{(2)'}(\kappa \xi)} e^{-j\{c\phi_m + 2n\pi t \xi\}} dt. \end{aligned} \right\} \quad (13)$$

The leading term of  $Q_2$ , however, is given by the term  $q_0^{(-)}$ . Since we can approximate  $Q_2$  by  $q_0^{(-)}$ , we will evaluate only this term.

<sup>3</sup> H. Bremmer, "Terrestrial Radio Waves," Elsevier Publishing Co., Inc., New York, N. Y., p. 31; 1949.

<sup>4</sup> S. Sensiper, "Cylindrical radio wave," IRE TRANS. ON ANTENNAS AND PROPAGATION, vol. AP-5, pp. 56-70; January, 1957. See especially pp. 68, 69.



Introducing the integral expression of the Hankel functions<sup>5</sup>

$$H_\nu^{(1)}(z) = -\frac{1}{\pi} \int_{\beta-j\infty}^{-\beta+j\infty} e^{jz \cos \tau_1 + j\nu(\tau_1-\pi/2)} d\tau_1,$$

$$H_\nu^{(2)}(z) = \frac{1}{\pi} \int_{-\pi+\beta-j\infty}^{\pi-\beta+j\infty} e^{-jz \cos \tau_2 - j\nu(\tau_2-\pi/2)} d\tau_2,$$

where

$$-\arg z < \beta < \pi < \arg z,$$

into  $q_0^{(-)}$  in (13), we have the following integral expression for  $q_0^{(-)}$ :

$$q_0^{(-)} = \int_{c_1^-} \frac{H_{\xi t}^{(2)}(\kappa \xi)}{H_{\xi t}^{(2)'}(\kappa \xi)} e^{-j c \phi_m t} dt,$$

$$= \int_{c_1^-} dt \int_{\beta-j\infty}^{-\beta+j\infty} d\tau_1 \int_{-\pi+\beta-j\infty}^{\pi-\beta+j\infty} d\tau_2 A e^{jh}, \quad (14)$$

where

$$A = \frac{-j \cos \tau_1}{\pi^2 H_{\xi t}^{(2)'}(\kappa \xi) H_{\xi t}^{(1)'}(\kappa \xi)},$$

$$h = \kappa \xi (\cos \tau_1 - \cos \tau_2) + \xi \left( \tau_1 - \tau_2 - \frac{c \phi_m}{\xi} \right).$$

Let the saddle point be  $(t_0, \tau_{10}, \tau_{20})$  and the values of  $A$  and  $h$  at this point  $A_0$  and  $h_0$ ; then we have approximately<sup>6</sup>

$$q_0^{(-)} \simeq \frac{(j\sqrt{2\pi})^3}{\sqrt{\Delta_0}} A_0 e^{jh_0} \quad (15)$$

where  $\Delta_0$  is Hesse's determinant evaluated at the saddle point.

The saddle point is obtained from

$$\frac{\partial h}{\partial \tau_1} = \frac{\partial h}{\partial \tau_2} = \frac{\partial h}{\partial t} = 0,$$

that is,

$$\left. \begin{aligned} t_0 &= \kappa \sin \tau_{10} = \kappa \sin \tau_{20} \\ \tau_{10} - \tau_{20} &= \frac{c \phi_m}{\xi} \end{aligned} \right\} \quad (16)$$

At this point, we have

$$\left. \begin{aligned} h_0 &= -\kappa \xi (\cos \tau_{20} - \cos \tau_{10}) = -2\kappa \xi \cos \tau_{20}, \\ \Delta_0 &= j^3 \begin{vmatrix} -\kappa \xi \cos \tau_{10} & 0 & \xi \\ 0 & \kappa \xi \cos \tau_{20} & -\xi \\ \xi & -\xi & 0 \end{vmatrix} \\ &= j\kappa \xi^3 (\cos \tau_{20} - \cos \tau_{10}) \\ &= 2j\kappa \xi^3 \cos \tau_{20}. \end{aligned} \right\} \quad (17)$$

Since the wave number  $\kappa$  has a small imaginary part with negative sign,  $h_0$  in (17) should be negative in value because the integral may exist as  $\xi \rightarrow \infty$ . The saddle point, therefore, is

$$\left. \begin{aligned} \tau_{10} &= \frac{\pi}{2} + \frac{c \phi_m}{2\xi}, \\ \tau_{20} &= \frac{\pi}{2} - \frac{c \phi_m}{2\xi}, \\ t_0 &= \kappa \sin \tau_{10} = \kappa \cos \frac{c \phi_m}{2\xi}, \end{aligned} \right\} \quad (18)$$

from (16) and (17) becomes

$$\left. \begin{aligned} h_0 &= -2\kappa \xi \sin \frac{c \phi_m}{2\xi}, \\ \Delta_0 &= 2j\kappa \xi^3 \sin \frac{c \phi_m}{2\xi} \end{aligned} \right\} \quad (19)$$

Furthermore, the product of the derivatives of the Hankel functions may be given approximately<sup>7</sup> as

$$H_{\xi t_0}^{(2)'}(\kappa \xi) H_{\xi t_0}^{(1)'}(\kappa \xi) \simeq 5 \left[ \frac{\sin\left(\frac{2\pi}{3}\right) \Gamma\left(\frac{2}{3}\right) 6^{2/3}}{3\pi} \right]^2 (\kappa \xi)^{-4/3}, \quad (20)$$

$$\simeq 0.844(\kappa \xi)^{-4/3}, \quad (21)$$

for  $\cos c \phi_m / 2\xi$  near unity.

Substituting (19) and (21) into (14), we have

$$q_0^{(-)} \simeq -j \frac{\kappa 2\sqrt{2} \sqrt[3]{\kappa \xi} \sin \frac{c \phi_m}{2\xi} e^{-j(2\kappa \xi \sin \frac{c \phi_m}{2\xi} - \pi/4)}}{0.844\sqrt{\pi} \sqrt[3]{2\kappa \xi \sin \frac{c \phi_m}{2\xi}}}, \quad (22)$$

$$\simeq -j \frac{\kappa \sqrt{\kappa c \phi_m} e^{-j(\kappa c \phi_m - \pi/4)}}{0.597 \sqrt{\pi} \sqrt[3]{(\kappa \xi)^2}}, \quad (23)$$

for  $\cos c \phi_m / 2\xi$  near unity.

The above results are valid for large positive values of  $\xi$ . For  $\xi$  in the vicinity of  $\eta$ , (23) becomes more exact because  $\eta$  is sufficiently large. We can readily show that

$$\lim_{\eta \rightarrow \infty} [\text{Eq. (23)}]_{\xi=\eta} = 0. \quad (24)$$

Thus, the first equation of (13) becomes

$$\left. \begin{aligned} Q_2 &\simeq j\pi \kappa K f(c) \\ \text{where} \\ f(c) &\simeq -\frac{\sqrt{\kappa c \phi_m} e^{-j(\kappa c \phi_m - \pi/4)}}{0.597 \sqrt{\pi} \sqrt[3]{(\kappa c)^2}} \end{aligned} \right\} \quad (25)$$

for  $\cos \phi_m / 2$  near unity.

<sup>5</sup> *Ibid.*, p. 61.

<sup>6</sup> H. Bremmer, *op. cit.*, p. 24.

<sup>7</sup> This expression has been derived from relations given in P. M. Morse and H. Feshbach, "Methods of Theoretical Physics, Part I," McGraw-Hill Book Co., Inc., New York, N. Y., p. 631; 1953.



Using the results of (12) and (25), (11) becomes

$$P_m = j\pi\kappa K [H_0^{(2)}(\kappa c\phi_m) + f(c)]. \quad (26)$$

Hence, we have

$$Y_c = \sum_{m=0,1} \frac{\kappa}{2d} [H_0^{(2)}(\kappa c\phi_m) + f(c)]. \quad (27)$$

#### IV. EXTERNAL ADMITTANCE FOR IN-PHASE EXCITATION

The normalized external admittance,  $Y_{ext}'$ , can be derived by substituting (27) into (6), that is,

$$Y_{ext}' = \frac{b}{d} \int_0^d du \int_0^d du' \sum_{m=0,1} \frac{\kappa}{2d} [H_0^{(2)}(\kappa c\phi_m) + f(c)], \quad (28)$$

where

$$\phi_m = 2m\phi + \frac{u - u'}{c},$$

$$f(c) \simeq - \frac{\sqrt{\kappa c\phi_m} e^{-j(\kappa c\phi_m - \pi/4)}}{0.597\sqrt{\pi^3}\sqrt{(\kappa c)^2}} \quad \text{for } \cos \frac{\phi_m}{2} \text{ near unity.}$$

The first term of (28) is exactly the same as that described in (9) of the companion paper, *i.e.*, as that for the external admittance of two parallel slits of spacing  $2m\phi$  in an infinite plane. The second term, therefore, must be an additional term due to the curvature of the cylinder. In (28), if  $\kappa d \ll 1$  and  $d = c\phi_0 \ll 2c\phi$ , the integral of the second term for  $m=0$  may be neglected in this problem because of its small value compared with the integral for  $m=1$ . Furthermore, the integral of  $f(c)$  may be obtained approximately by integrating the exponential contained in  $f(c)$ . Since

$$\int_0^d du \int_0^d du' e^{j\kappa(u-u')} = \frac{2}{\kappa^2} (1 - \cos \kappa d) \simeq d^2 \quad \text{for } |\kappa d| \ll 1, \quad (29)$$

we can readily lead (28) to

$$\begin{aligned} Y_{ext}' &\simeq \frac{\kappa b}{2} [1 + J_0(2\kappa c\phi)] \\ &+ j \frac{\kappa b}{2} \left[ \frac{2}{\pi} \ln \frac{\pi e}{\phi \kappa d} - N_0(2\kappa c\phi) \right] \\ &- \frac{\kappa b}{2} \frac{\sqrt{2\kappa c\phi} e^{-j(2\kappa c\phi - \pi/4)}}{0.597\sqrt{\pi^3}\sqrt{(\kappa c)^2}} \end{aligned} \quad (30)$$

by using the results in the companion paper. Thus, letting

$$Y_{ext}' = G' + jB_{ext}'$$

for real  $\kappa$ , we have

$$G' \simeq \frac{\kappa b}{2} \left[ 1 + J_0(2\kappa c\phi) - \frac{\sqrt{2\kappa c\phi} \cos\left(2\kappa c\phi - \frac{\pi}{4}\right)}{0.597\sqrt{\pi^3}\sqrt{(\kappa c)^2}} \right], \quad (31)$$

$$\begin{aligned} B_{ext}' &\simeq \frac{\kappa b}{2} \left[ \frac{2}{\pi} \ln \frac{\pi e}{\gamma \kappa d} - N_0(2\kappa c\phi) \right. \\ &\quad \left. + \frac{\sqrt{2\kappa c\phi} \sin\left(2\kappa c\phi - \frac{\pi}{4}\right)}{0.597\sqrt{\pi^3}\sqrt{(\kappa c)^2}} \right] \end{aligned} \quad (32)$$

for  $\kappa d \ll 1$  and  $\cos \phi$  near unity.

In order to check the above results, (31) is plotted in Fig. 3 with  $\kappa c = 10$  and compared with the real part (corresponding to  $G'$ ) of the harmonic series of (5). It is found that they are in very good agreement for small values of  $2\phi$ .

#### V. OUT-OF-PHASE EXCITATION

The same analysis can be employed in this case as in Sections II and III for the reduced problem shown in Fig. 4.

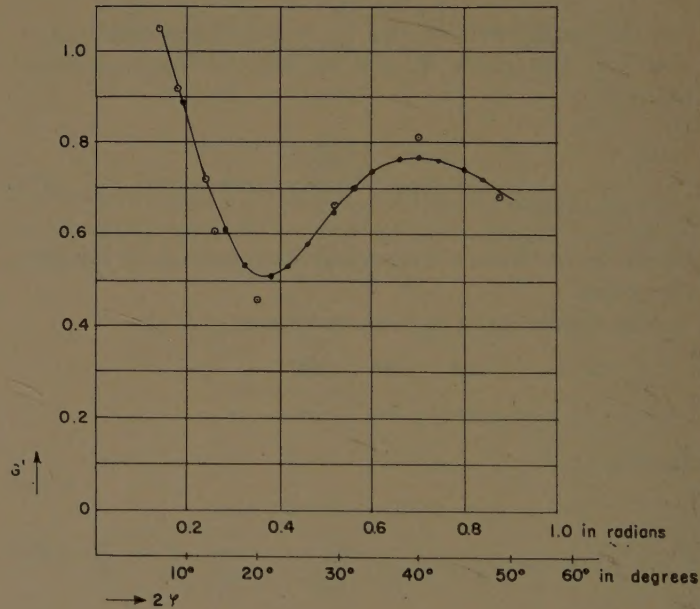


Fig. 3—The normalized conductance for  $\kappa c = 10$  plotted against the spacing between slits calculated by (5) and (31).  $\kappa c = 10$ . —●— represents approximate expression (31), ○ represents harmonic series (5).

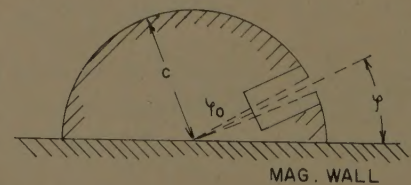


Fig. 4—The cross section of the reduced problem for out-of-phase excitation.



The Green's function in the open region in this case is given by

$$G(\vartheta, \vartheta') = \sum_{n=1}^{\infty} (-1) \sin(n\theta) \sin(n\theta') \frac{\{J_n(\kappa\rho_{<})N_n'(\kappa c) - N_n(\kappa\rho_{<})J_n'(\kappa c)\} H_n^{(2)}(\kappa\rho_{>})}{H_n^{(2)'}(\kappa c)}. \quad (33)$$

The associated dyadic admittance  $\mathbf{z}_0 \cdot \mathbf{y}(\theta, \theta') \cdot \mathbf{z}_0$ , therefore, is written as

$$\mathbf{z}_0 \cdot \mathbf{y}(\theta, \theta') \cdot \mathbf{z}_0 = \sum_{n=1}^{\infty} \frac{2\kappa}{j\omega\mu\pi c} \sin(n\theta) \sin(n\theta') \frac{H_n^{(2)}(\kappa c)}{H_n^{(2)'}(\kappa c)},$$

where

$$\mathbf{y}(\theta, \theta') = [\mathbf{y}(\vartheta, \vartheta')]_{\rho=\rho'=c}. \quad (34)$$

Thus, we have the following normalized external admittance:

$$\begin{aligned} Y_{\text{ext}}' &= \frac{\omega\mu}{\kappa d^2} \int_{t_1}^{t_2} cd\theta \int_{t_1}^{t_2} cd\theta' \mathbf{z}_0 \cdot \mathbf{y}(\theta, \theta') \cdot \mathbf{z}_0, \\ &= \frac{b}{d} \int_0^d du \int_0^d du' Y_c, \end{aligned} \quad (35)$$

$$\begin{aligned} Y_c &= \sum_{n=1}^{\infty} \sum_{m=0,1} \frac{(-1)^m}{j\pi cd} \frac{H_n^{(2)}(\kappa c)}{H_n^{(2)'}(\kappa c)} \\ &\quad \cdot \cos \left\{ n \left( 2m\phi + \frac{u-u'}{c} \right) \right\} \end{aligned} \quad (36)$$

in the same way as in Section II.

Eq. (36) is the same form as (6). We, therefore, can readily write down the approximate representation of (36) by using the results of Section III. As a result, we find

$$Y_c = \sum_{m=0,1} (-1)^m \frac{\kappa}{2d} [H_0^{(2)}(\kappa c\phi_m) + f(c)], \quad (37)$$

where  $f(c)$  is given by (25) and

$$\phi_m = 2m\phi + \frac{u-u'}{c}.$$

## VI. EXTERNAL ADMITTANCE FOR OUT-OF-PHASE EXCITATION

Substituting (37) into (35), we have

$$\begin{aligned} Y_{\text{ext}}' &= \frac{b}{d} \int_0^d du \int_0^d du' \sum_{m=0,1} (-1)^m \frac{\kappa}{2d} \\ &\quad \cdot [H_0^{(2)}(\kappa c\phi_m) + f(c)], \end{aligned} \quad (38)$$

and, in the same way as in Section IV,

$$\begin{aligned} Y_{\text{ext}}' &= G' + jB_{\text{ext}}' \\ G' &\simeq \frac{\kappa b}{2} \left[ 1 - J_0(2\kappa c\phi) \right. \\ &\quad \left. + \frac{\sqrt{2\kappa c\phi} \cos\left(2\kappa c\phi - \frac{\pi}{4}\right)}{0.597\sqrt{\pi^3}\sqrt{(\kappa c)^2}} \right], \end{aligned} \quad (39)$$

$$\begin{aligned} B_{\text{ext}}' &\simeq \frac{\kappa b}{2} \left[ \frac{2}{\pi} \ln \frac{\pi e}{\gamma \kappa d} + N_0(2\kappa c\phi) \right. \\ &\quad \left. + \frac{\sqrt{2\kappa c\phi} \sin\left(2\kappa c\phi - \frac{\pi}{4}\right)}{0.597\sqrt{\pi^3}\sqrt{(\kappa c)^2}} \right] \end{aligned} \quad (40)$$

for  $\kappa d \ll 1$  and  $\cos \phi$  near unity.

## VII. NUMERICAL EXAMPLES

The characteristics of the coupled leaky waves in the present problem may be obtained by solving for the resonances of the transverse network which includes the external admittance derived in Section IV or VI. The analytical techniques employed to solve for these resonances have been described in the companion paper. For the attenuation constant of the leaky wave, the following formula may be used:

$$\alpha a \simeq \frac{\lambda_{\theta 0}}{2a} \cdot \frac{G'(\kappa_0)}{[G'(\kappa_0)]^2 + [B'(\kappa_0)]^2}, \quad (41)$$

where

$$\lambda_{\theta 0} = \frac{\lambda}{\sqrt{1 - \left(\frac{\lambda}{2a}\right)^2}},$$

and

$$\kappa_0 = \frac{\pi}{a} \text{ (unperturbed wave number).}$$

The attenuation constants,  $\alpha a$ , calculated by (41) with  $\kappa_0 c = 10$  ( $c \pm 3.19a$ ) and  $\kappa_0 c = 20$  ( $c \simeq 6.37a$ ) are plotted in Figs. 5 and 6, respectively, as a function of the spacing between the two slits. In order to compare the attenuation constant of the coupled leaky wave in the cylinder case with that in the related infinite plane case, the dimensions and the spacing of the excitation waveguides and the operating frequency were taken to be the same as those used in the companion paper.

The phase constant of the leaky wave has not been included in the figure because its change vs the spacing



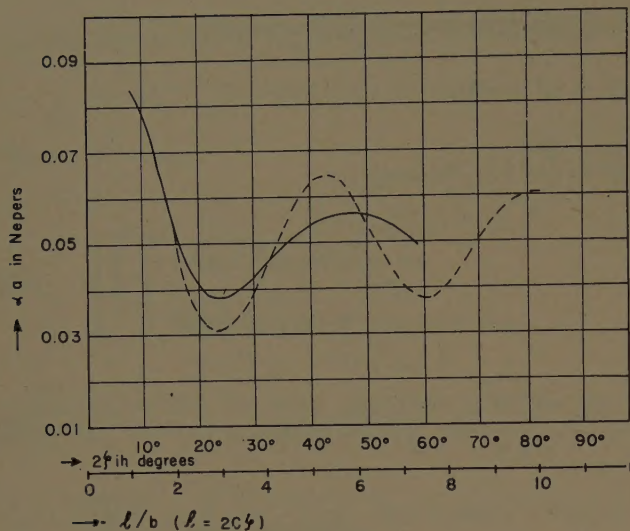


Fig. 5—Comparison between the attenuation constants of the in-phase coupled leaky wave along the slits in a cylinder with  $\kappa_0 c = 10$  and along an infinite plane with the same spacing between slits.  $a = 0.9$  inch,  $b = 0.4$  inch,  $\lambda/2a = 0.7$  inch,  $d = c\epsilon_0 = 0.1$  inch. Solid lines represents cylinder with  $\kappa_0 c = 10$  ( $c \cong 3.19a$ ). Dotted line represents plane.

is not usually significant. The phase constant can be readily calculated from the formula

$$\frac{\beta}{k} \cong \frac{\lambda}{\lambda_{g0}} \left( 1 - \frac{\lambda_{g0}^2}{4a^2\pi} \frac{B'}{G'^2 + B'^2} \right), \quad (42)$$

which has already appeared in the companion paper. Furthermore, the graphical presentation of the characteristics of out-of-phase excitation has also been omitted. Since the relationships between the in-phase

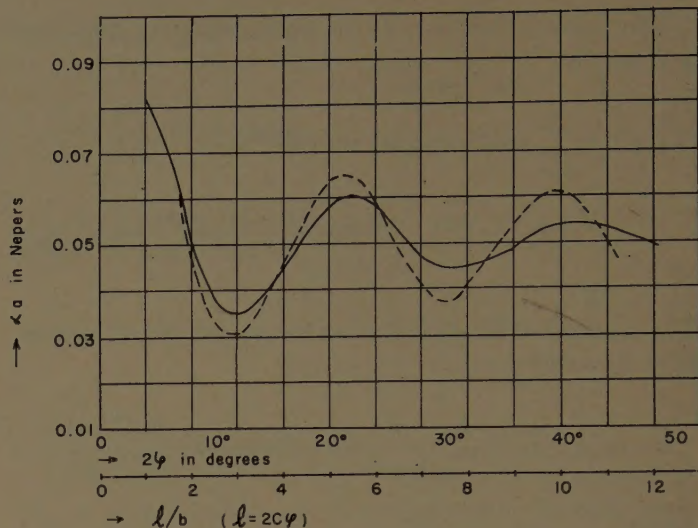


Fig. 6—Comparison between the attenuation constants of the in-phase coupled leaky wave along the slits in a cylinder with  $\kappa_0 c = 20$  and along an infinite plane with the same spacing between slits.  $a = 0.9$  inch,  $b = 0.4$  inch,  $\lambda/2a = 0.7$  inch,  $d = c\epsilon_0 = 0.01$  inch. Solid line represents cylinder with  $\kappa_0 c = 20$  ( $c \cong 6.37a$ ). Dotted line represents plane.

and out-of-phase characteristics are approximately the same in the cylinder case and the plane case, the associated curves display a very similar behavior.

#### ACKNOWLEDGMENT

The author wishes to express his gratitude to Professor A. A. Oliner for his kind direction, and to thank staff members of the Electrophysics Group of MRI for their encouragement.

## Mutual Coupling Effects in Large Antenna Arrays II: Compensation Effects\*

S. EDELBERG† AND A. A. OLINER‡

**Summary**—Mutual coupling effects in a large array cause a variation in the input impedance as a function of scan angle. This variation can be reduced considerably by the use of a compensating structure which appropriately modifies the environment of the array. A two-dimensional dipole array is treated as a typical example, and its input impedance is calculated by means of a unit cell equivalent network as a function of scan angle for different environmental situations. Reasonably constant performance up to scan angles of  $\pm 60^\circ$  is obtained on use of a periodic baffle compensation structure.

\* Manuscript received by the PGAP, August 26, 1959. The work reported in this document was performed by Lincoln Lab., a center for research operated by M.I.T., Lexington, Mass.; this work was supported by the U. S. Air Force under Air Force Contract AF 19(604)-5200.

† M.I.T., Lincoln Lab., Lexington, Mass.

‡ Microwave Res. Inst., Polytechnic Inst. of Brooklyn, Brooklyn, N. Y.

#### I. INTRODUCTION

It is pointed out in a companion paper<sup>1</sup> that the effects of mutual coupling on the central portion of a large two-dimensional array may be taken into account automatically in a direct and simple fashion by the use of a *periodic structure* approach. The point of view and its application to an array of slots is discussed there in detail. The array of slots radiates into a half-space region and the analysis indicates that the conductance of the array elements varies considerably with

<sup>1</sup> S. Edelberg and A. A. Oliner, "Mutual coupling effects in large antenna arrays I: Slot arrays," IRE TRANS. ON ANTENNAS AND PROPAGATION, vol. AP-8, May, 1960.



scan angle. It would be desirable, however, to be able to minimize or eliminate this variation, and the purpose of the present paper is to indicate that these effects of mutual coupling can be *compensated* for to a large extent if the environment of the radiating elements is suitably chosen.

Since the periodic structure approach is applicable to any type of radiating element, and since dipole arrays lend themselves much more readily than slot arrays to various environmental situations, the study in this paper is restricted to *dipole arrays*. The results, however, should be of interest in themselves in addition to being illustrative of certain general considerations.

By a *Babinet duality* argument, and by appropriate normalization considerations, the results derived in Edelberg and Oliner<sup>1</sup> for the array of slots can be carried over to the case of a corresponding array of dipoles radiating into a full space. Since the expressions for the slot array are quite accurate, those for the dipole case should likewise be reliable. The details of the duality discussion are presented in Section II.

These duality considerations also result in an *equivalent network* representation for a *unit cell* of the dipole array. The form of this equivalent network is such that the effect of many types of environment can be taken into account by simple modifications in the terminations of the network or in the inclusion of additional lengths of appropriate transmission line. For example, most dipole arrays do not radiate into free space but are backed by a ground plane. To account for this change in environment, the modification in the equivalent network is simply that the dipole element no longer sees an infinite transmission line on both sides, but on one side sees instead a length of short-circuited line.<sup>2</sup> The method can evidently be readily generalized to include a lossy or dielectric-coated ground plane, if desired.

Calculations for a perfectly reflecting ground plane indicate that the presence of the ground plane reduces the variation of impedance with scan angle. The dipole resistance, however, still drops considerably more rapidly with scan angle for scanning in the *E* plane (along the dipoles) than for scanning in the *H* plane (in the plane perpendicular to the dipoles). In an attempt to reduce this variation further with scan angle, conducting baffles are introduced in a periodic fashion. These baffles do not affect the *H* plane scanning but can exert a considerable influence on the *E* plane scan. The effect of these baffles can be accounted for by appropriate simple modifications in the unit cell equivalent network. It is found that the influence of these baffles is significant, and that the variation of dipole resistance with *E* plane scan angle can actually be inverted or can be made almost zero over a large range of scan angles, depending on the geometry of the baffles. Section III presents the

unit cell equivalent networks and expressions for the dipole input impedance both for the ground plane case and for that which includes the baffles. Numerical data are also presented which indicate the effect of scan angle.

The stress in this paper is placed on the unit cell network method of approach and on demonstrating that appropriate changes in the environment of the array can indeed compensate for the mutual coupling effects by reducing considerably the variation of impedance with scan angle. The optimum environmental configuration was not determined, however.

## II. EQUIVALENCE BETWEEN SLOT AND DIPOLE ARRAYS

The equivalent network for a unit cell of an array of planar dipoles is deduced below by Babinet duality considerations from the corresponding result for an array of slots in a ground plane.

A unit cell of the slot array when viewed in connection with the periodic guide in space is shown in Fig. 1, in which the shaded area represents magnetic walls while the unshaded area represents metallic or electric walls. The representation of the half space in terms of periodic unit cells has been discussed in detail in Edelberg and Oliner.<sup>1</sup> It is further recognized from the discussion there that the unit cell of Fig. 1 corresponds to



Fig. 1—Unit cell of slot or dipole array. If slot unit cell, shading represents magnetic walls. If dipole unit cell, shading represents electric walls.

the case of broadside radiation (or normally incident radiation). If the Babinet equivalent of the structure of Fig. 1 is taken, all magnetic and electric walls are interchanged so that the shaded areas now represent electric walls. The electric and magnetic fields are also appropriately interchanged in accordance with the interchange of the character of the walls, and the dual unit cell is seen to be characteristic of a planar dipole array. Furthermore, the almost sinusoidal slot magnetic current now becomes the almost sinusoidal dipole electric current. The electric walls occurring in the bottom walls of these dual unit cells are in both cases caused by actual metal structures, *i.e.*, the metal into which the slot is cut and the metal dipole, respectively. The magnetic

<sup>2</sup> P. S. Carter, Jr., "Mutual impedance effects in large electronic beam scanning arrays," in "Proc. Electronic Scanning Symp.," A.F. Cambridge Res. Cen.; April 29–May 1, 1958. Carter employs a similar (though not identical) network form for this case, and obtains it by a different method.



wall portions of these bottom walls, however, are caused by symmetry only; in the dipole case they clearly imply that the dipole array radiates into a full space. In the slot array case, however, radiation occurs only into a half space and the region below the slot is actually that of the rectangular feed guide. However, since the slot field in this situation differs only very slightly from that which would occur if the slot radiated into a full space, this approximation is a very good one.

The equivalent networks corresponding to these two (bisected) dual unit cells are shown in Fig. 2. The slot is characterized in susceptance terms because the susceptance is directly proportional to the slot stored power. Since only one-half of the stored power resides in the bisected unit cell, the susceptance element, which is in shunt with the periodic, or unit cell, waveguide, is given as  $B/2$ . The dipole is also in shunt with the unit cell waveguide, so that its reactance element in the bisected network is  $2X$ . Application of the Babinet equivalence procedure thus produces

$$\left(\frac{X}{Z_p}\right)_{\text{dipole}} = \frac{1}{4} \left(\frac{B}{Y_p}\right)_{\text{slot}}, \quad (1)$$

where the quantities are normalized to the *periodic waveguide*.

The susceptance value for the slot obtained in Edelberg and Oliner<sup>1</sup> was normalized to the rectangular feed guide. The necessary renormalization to the periodic guide is made in the Appendix, where the value normalized to the periodic guide is expressed in terms of the slot and array dimensions. The  $X/Z_p$  result, which corresponds to a dipole which sees the periodic waveguide on *both* sides, may thus be assumed to be known to a high degree of accuracy.

A consideration of the feed arrangement is necessary in order to obtain a complete network for a unit cell in the dipole array. As shown in Edelberg and Oliner,<sup>1</sup> the slot susceptance element is in parallel with both the periodic waveguide and the feed waveguide. The dipole reactance element, however, while being in parallel with the periodic waveguide, is in *series* with the feed line. These two arrangements are illustrated in Fig. 3; the dipole is generally split to permit a series type of feed at its midpoint, but for convenience both halves of the reactance element are lumped together in Fig. 3(b). The necessity for the distinction between the slot and dipole feed arrangements may be made clear by placing a load across the feed terminals and considering an incoming plane wave. When the slot size is shrunk to zero,  $B \rightarrow \infty$ , and all of the incident power is reflected; *i.e.*, none reaches the load. When the dipole size is shrunk to zero,  $X \rightarrow \infty$ , and all of the incident power continues past the dipole, with none of it reaching the load. As another special case, when the slot is resonant,  $B = 0$ , and substantial power goes to the load, the amount depending on the load mismatch. When the dipole is resonant,  $X = 0$ , and, again, the input load absorbs

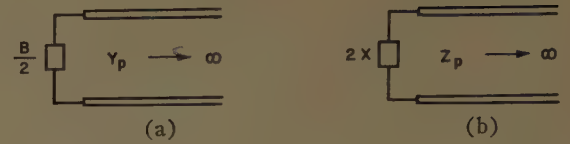


Fig. 2—Equivalent networks for the bisected unit cell of Fig. 1. (a) Slot unit cell. (b) Dipole unit cell.

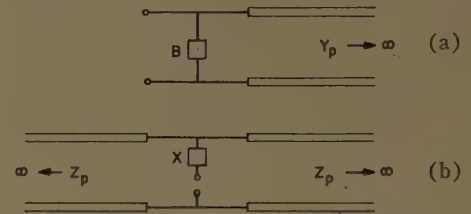


Fig. 3—Complete unit cell equivalent networks. (a) Slot array in half space. (b) Dipole array in full space.

much power. These results are in accord with the networks of Fig. 3.

The input impedance at the input load terminals of Fig. 3(b) is given by

$$\frac{Z_{in}}{Z_p} = \frac{1}{2} + j \frac{X}{Z_p}, \quad (2)$$

when the dipole radiates into a full space. But this input impedance is normalized to the periodic waveguide, *not* the feed line. We also recognize that the evaluation of  $X/Z_p$  by the Babinet equivalence procedure was effected for broadside conditions only. It was shown in Section VI of Edelberg and Oliner<sup>1</sup> that the stored power in the neighborhood of the slot does not change significantly during the scan process. Consequently, it is safe to assume that the equivalence between the slot susceptance  $B$  and the dipole reactance  $X$ , as given by (1), is also valid while the arrays are scanned. The effects caused by scanning are accounted for by the remainder of the networks of Fig. 3. In the phrasing of (2), the normalized reactance  $X/Z_p$  varies with scan angle. It can be expressed as

$$\frac{X}{Z_p} = \frac{(\text{stored power near dipole})}{Z_p |I_p|^2}; \quad (3)$$

the current  $I_p$  is

$$I_p = \iint_{\text{dipole}} \mathbf{J} \cdot \mathbf{e}_p^* dS, \quad (4)$$

where  $\mathbf{J}$  is the current density along the dipole and  $\mathbf{e}_p^*$  is the complex conjugate of  $\mathbf{e}_p$ , the mode function of the dominant mode in the periodic waveguide. This mode function changes for different directions of scan, and is fully discussed in Edelberg and Oliner.<sup>1</sup> As shown there, the factor  $|I_p|^2$  does not vary strongly with scan angle, although a small variation is introduced when the scanning is performed along the dipoles. The primary variation of  $X/Z_p$  with scan angle is caused by the na-



ture of the periodic waveguide characteristic impedance  $Z_p$ . Although expressions for  $Z_p$  are presented in Edelberg and Oliner<sup>1</sup> for all scanning conditions, we will repeat here the results for two special cases of interest. When scanning is performed along the dipoles,

$$Z_p = \sqrt{\frac{\mu}{\epsilon}} \cos \theta, \quad (5)$$

while for scanning in the plane across the dipoles,

$$Z_p = \sqrt{\frac{\mu}{\epsilon}} \frac{1}{\cos \theta}. \quad (6)$$

We see, therefore, that even if the stored power remains constant with scan and the small variation in  $|I_p|^2$  is neglected,  $X/Z_p$  will still vary considerably with scan angle  $\theta$ , and the variation will be different with different directions of scan.

It is more useful, however, to normalize the input impedance  $Z_{in}$  to the characteristic impedance  $Z_0$  of the feed line, rather than in the form of (2).

In order to obtain the input impedance *as seen from the feed line*, the value  $Z_{in}/Z_p$  must be transformed through the junction network which exists between the dipole itself and the feed line. But this junction network is intimately associated with the dipole reactance. The normalized dipole reactance as seen from the feed line may be expressed as

$$\frac{X_{in}}{Z_0} = \frac{(\text{stored power near dipole})}{Z_0 |I_0|^2}. \quad (7)$$

$$I_0 = \iint_{\text{dipole}} \mathbf{J} \cdot \mathbf{e}_0^* dS, \quad (8)$$

where  $\mathbf{e}_0$  is the mode function of the dominant mode in the feed line, and does not vary with scan angle. On comparing (7) with (3), one can write

$$\frac{X_{in}}{Z_0} = \frac{X}{Z_p} \frac{Z_p}{Z_0} \frac{|I_p|^2}{|I_0|^2}, \quad (9)$$

if the stored powers in (3) and (7) are assumed to be the same. These stored powers are not identical, actually, since that in (7) includes a contribution caused by the presence of the feed line, and this contribution, while small, is not considered in the Babinet equivalence treatment above. Eq. (9), nevertheless, can be employed with reasonable accuracy to determine the normalized reactance as would be measured in the feed line. As pointed out in Edelberg and Oliner,<sup>1</sup> the definitions of  $\mathbf{e}_0$  and  $Z_0$  are related, and their precise forms depend on the feed line involved. The ratio of currents in (9) is akin to a transformer turns ratio which incorporates the various geometrical factors that may not have been included in the definition of the characteristic impedances. To illustrate this point, let us write

$$\frac{|I_p|^2}{|I_0|^2} = n^2, \quad (10)$$

for convenience.

The input *resistance*, normalized to the feed line, may be expressed in a form identical to (7) when "stored power" is replaced by "radiated power." Comparison with an expression analogous to (3) for  $R/Z_p$  permits one to write, using (10),

$$\frac{R_{in}}{Z_0} = \frac{1}{2} \frac{Z_p}{Z_0} n^2, \quad (11)$$

since one sees from (2) that  $R/Z_p = 1/2$  for the case of radiation into a full space.

One sees from (9), (10) and (11) that the junction network between the dipole and the feed line may be approximated simply by inserting an additional transformer into the network of Fig. 3(b); the reactive content of this junction is small compared to that associated with the dipole itself, so that  $X$  is assumed unchanged in value. The new and final unit cell equivalent network for the dipole array is shown in Fig. 4. In view of the network of Fig. 4, (2) is replaced by

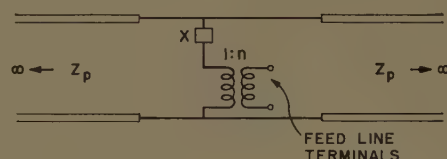


Fig. 4—Complete unit cell equivalent network for dipole array in full space, as seen from the feed line.

$$\frac{Z_{in}}{Z_0} = \frac{1}{2} \frac{Z_p}{Z_0} n^2 + j \frac{X}{Z_0} n^2, \quad (12)$$

where  $Z_{in}/Z_0$  represents the quantity which would result from an actual measurement of the input impedance performed in the feed line. The reactive portion  $n^2(X/Z_0)$  is now *essentially independent* of scan angle [as seen from (7)], but the resistive part varies with scan. As mentioned above, the turns ratio  $n$  does vary slightly with scan, particularly if scanning is performed along the dipoles, but since we are concerned now with first-order variations we shall assume  $n$  to consist of geometrical factors only and to remain constant with scan angle.

The duality considerations discussed above yield relations for an array of *flat* dipoles, with the dipole dimensions being identical to those of the slots. If application is made to an array of *round* dipoles, the customary geometrical correspondence is to choose round dipoles of the same length as the slot, but with a dipole radius equal to one-fourth of the slot width. This geometrical correlation is valid on a static basis when the dipole length is much greater than its radius. The geometrical optics correlation sets the dipole radius equal to one-



half of the slot width. The correct value no doubt lies somewhere in between, most likely closer to the static value.

### III. THE INFLUENCE OF DIFFERENT ENVIRONMENTS

The periodic structure, or unit cell, treatment of the central portion of a large array permits the influence of different environments on array performance to be determined in a direct and rapid manner. In terms of the unit cell equivalent network, a different environment is accounted for by changing the terminations on the transmission lines connected to the central reactive element. If the perturbing elements are located very close to the dipole itself, so that higher mode interaction is present, we must consider that a change has occurred in the radiating element itself rather than in the environment. Under these conditions, the change may manifest itself simply in an altered value for the central reactive element, or the effect may be severe enough to change the form of equivalent network. In the discussion below it is assumed that the changes do not alter the radiating element itself.

#### A. Dipole Array Over a Ground Plane

Most planar dipole arrays are placed over a ground plane. A side view of the geometry of such an array is shown in Fig. 5(a) while the equivalent network corresponding to a unit cell of this array is shown in Fig. 5(b). It is seen that the network of Fig. 5(b) is obtained from that of Fig. 4 by simply terminating one of the transmission lines by a short circuit, assuming the ground plane to be perfectly conducting. The input impedance to the feed line is then seen to follow directly from the equivalent network as

$$\frac{Z_{in}}{Z_0} = n^2 \frac{Z_p}{Z_0} \sin^2(kh \cos \theta) + j \left[ n^2 \frac{X}{Z_0} + \frac{1}{2} n^2 \frac{Z_p}{Z_0} \sin(2kh \cos \theta) \right], \quad (13)$$

since  $\kappa_p = k \cos \theta$ . Both the normalized resistance and reactance vary now with scan angle  $\theta$ .

It is common practice to set the height  $h$  of the array above the ground plane equal to a quarter wavelength; i.e.,

$$h = \lambda/4 = \pi/2k;$$

under these conditions the array is effectively backed by an open circuit at broadside (or normal incidence), and (13) becomes

$$\frac{Z_{in}}{Z_0} = n^2 \frac{Z_p}{Z_0} \sin^2\left(\frac{\pi}{2} \cos \theta\right) + j \left[ n^2 \frac{X}{Z_0} + \frac{1}{2} n^2 \frac{Z_p}{Z_0} \sin(\pi \cos \theta) \right]. \quad (14)$$

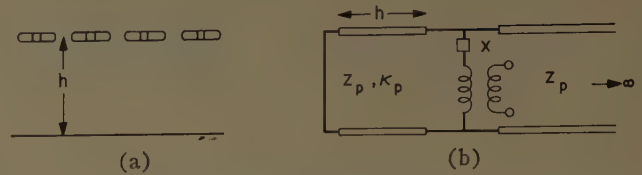


Fig. 5—Dipole array over ground plane. (a) Side view of geometry. (b) Equivalent network.

At broadside ( $\theta=0$ ), (14) reduces to the input impedance that would be found for a dipole array radiating into a half space. At other angles of scan, the value of  $Z_{in}/Z_0$  will depend on the direction of scan because of the characteristics of  $Z_p$ . If we assume that the dominant mode in the feed line is a TEM mode and that the normalization chosen is such that  $Z_0$  is equal to the wave impedance and all the geometrical factors are incorporated into  $n^2$ , which is also assumed independent of scan angle, we may then write, using (5),

$$\frac{Z_{in}}{Z_0} = n^2 \cos \theta \sin^2\left(\frac{\pi}{2} \cos \theta\right) + j \left[ n^2 \frac{X}{Z_0} + \frac{1}{2} n^2 \cos \theta \sin(\pi \cos \theta) \right], \quad (15)$$

when scanning is performed along the dipoles, and, using (6),

$$\frac{Z_{in}}{Z_0} = n^2 \frac{\sin^2\left(\frac{\pi}{2} \cos \theta\right)}{\cos \theta} + j \left[ n^2 \frac{X}{Z_0} + \frac{1}{2} n^2 \frac{\sin(\pi \cos \theta)}{\cos \theta} \right], \quad (16)$$

when the array is scanned in the plane across the dipoles. These scans may be called, respectively, *E* plane and *H* plane scans.

If the resistive portions of (15) and (16) are compared to the corresponding quantities for the dipole array in the absence of the ground plane, using (12), it is found that the variation with scan angle is reduced by the presence of the ground plane for *H* plane scanning but is increased in the case of *E* plane scanning. These observations are presented quantitatively in Fig. 6, in which data are given for both *E* and *H* plane scans, with and without ground plane, as a function of scan angle. The ordinate scale is normalized in such a manner that all curves begin at unity at broadside ( $\theta=0$ ); this is done in order to stress the variation with scan angle. It must be recalled that the actual value of input resistance at  $\theta=0$  for the ground plane case is exactly twice that for radiation into a full space.

The curves of Fig. 6 indicate that while the presence of the ground plane exerts a significant effect on the variation with scan angle, a large discrepancy is still present between the *E* and *H* plane scan cases. It is suggestive, however, of the thought that a further appropriate modification of the environment of the array



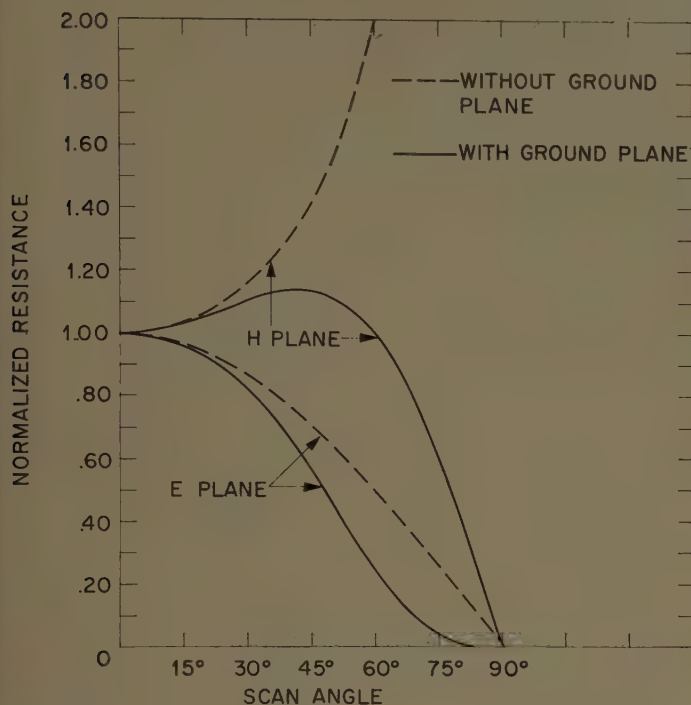


Fig. 6—Normalized input resistance of array of dipoles with and without ground plane.

may possibly reduce the variation with scan angle and make the *E* and *H* plane scan curves more nearly alike. One method for accomplishing this is described in the next section.

Before exploring this compensation method, the variation of the input reactance with scan angle should be examined. We see from (15) and (16) that an additional contribution to the reactance is present and that this additional term varies because of the change occurring in the electrical height of the array over the ground plane during the scan process. This variation is also quite different for *E* and *H* plane scans. While the variation is greater for the *H* plane scan case, the values for both cases are not excessive. A further discussion of these reactance variations is included in the next section, and a method is indicated for reducing their overall effect.

### B. Use of Baffles as a Compensation Structure

As has been pointed out above, the effect of mutual coupling in producing a variation in the input impedance value during scan can be compensated for by suitable alterations in the environment of the array. The presence of a ground plane under a dipole array has been shown to improve the *H* plane scan performance considerably, but to deteriorate that for *E* plane scan. A substantial improvement in performance would be obtained, therefore, if a compensation scheme were used which would not affect the *H* plane scan behavior but would reduce the *E* plane scan variation. An environmental structure conforming to these requirements is a periodic array of conducting baffles interlacing the dipoles, as shown in Fig. 7(a). Since the planes

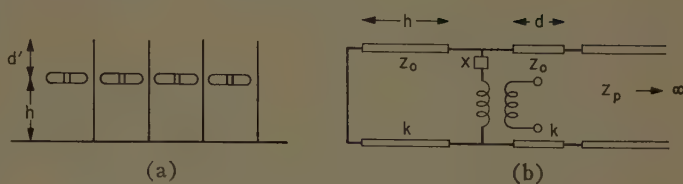


Fig. 7—Dipole array with baffles and ground plane. (a) Side view of geometry. (b) Equivalent network.

midway between the ends of the dipoles remain electric walls during *H* plane scan, the array of baffles will not affect the *H* plane scan behavior if the baffles are thin. The influence of the baffles on *E* plane scan will depend on the size of the baffles and remains to be determined.

The spacing between successive baffle planes is, of course, the same as that between dipole centers, so that as long as the array does not produce any higher order radiated beams, only the TEM mode will propagate in the parallel plate waveguides formed by successive pairs of baffles and the higher order modes will be below cutoff. The equivalent network of a unit cell of this array, taking the presence of the baffles into account, is shown in Fig. 7(b). The electrical height  $d$  of the baffle edges above the dipoles is somewhat different from the physical height  $d'$  because of the fringing field produced at these edges. To a good approximation, the difference between these heights is given by<sup>3</sup>

$$d' - d = \frac{B}{\pi} \ln 2, \quad (17)$$

where  $B$  is the spacing between successive baffles. For spacings near to a half wavelength, the physical length is seen to be almost a tenth of a wavelength longer than the electrical length. If  $d'$  is small, some higher mode interaction may occur between the dipole and the baffle edges; this interaction will modify the actual electrical length  $d$  and may slightly change the dipole reactance value  $X$ . In the discussion below, such interaction effects will be ignored because they will not alter the basic conclusions although they may influence the numerical results slightly.

If the height  $h$  of the array above the ground plane is made equal to a quarter wavelength, in conformity with the previous section, the expression for the input impedance simplifies considerably since the ground plane then backs the array by an open circuit for all scan angles. If the dominant mode in the feed guide is a TEM mode and the normalization is such that  $Z_0$  is equal to the wave impedance and  $n^2$  is a constant, as was the case in the previous section, then  $Z_0$  for the baffle region is also equal to the wave impedance. Under these conditions, the input impedance for *E* plane scan is derived directly from the equivalent network of Fig. 7(b) to be

<sup>3</sup> N. Marcuvitz, "Waveguide Handbook," M.I.T. Rad. Lab. Ser., McGraw-Hill Book Co., Inc., New York, N. Y., vol. 10, sec. 5.22, eq. (3b); 1951.

$$\frac{Z_{in}}{Z_0} = n^2 \frac{\cos \theta}{\cos^2 kd + \sin^2 kd \cos^2 \theta} + j \left[ n^2 \frac{X}{Z_0} + \frac{1}{2} n^2 \frac{\sin^2 \theta \sin 2kd}{\cos^2 kd + \sin^2 kd \cos^2 \theta} \right]. \quad (18)$$

The value of the electrical height  $kd$  of the baffle edges above the dipole array may be chosen as an adjustable parameter in order to reduce the variation of the input resistance with  $E$  plane scan, with the result that the  $E$  and  $H$  plane scan curves become more nearly alike. Rather good compensation is obtained when  $kd$  is chosen such that  $\cos kd = 1/\sqrt{3}$ ; i.e.,  $kd \approx 55^\circ$ . Eq. (18) reduces, for this value of  $kd$ , to

$$\frac{Z_{in}}{Z_0} = n^2 \frac{3 \cos \theta}{1 + 2 \cos^2 \theta} + j \left[ n^2 \frac{X}{Z_0} + n^2 \frac{\sqrt{2} \sin^2 \theta}{1 + 2\sqrt{2} \cos^2 \theta} \right]. \quad (19)$$

The input resistance values, normalized to unity at  $\theta = 0$ , are plotted in Fig. 8 as a function of scan angle  $\theta$ . It is seen that for scan angles up to  $60^\circ$  the resistance value does not vary by more than  $\pm 3$  per cent. Also shown for comparison in Fig. 8 are the  $E$  plane scan response before the insertion of the baffles, and the  $H$  plane scan behavior, which is unaffected by the presence of the baffles. As seen, there is a very significant improvement in the  $E$  plane scan performance, and the resulting  $E$  and  $H$  plane scan curves are quite similar. It might also be noted that the length  $d$  occurring in the network of Fig. 7(b) is almost a sixth of a wavelength, so that the physical height  $d'$  of the baffle edges above

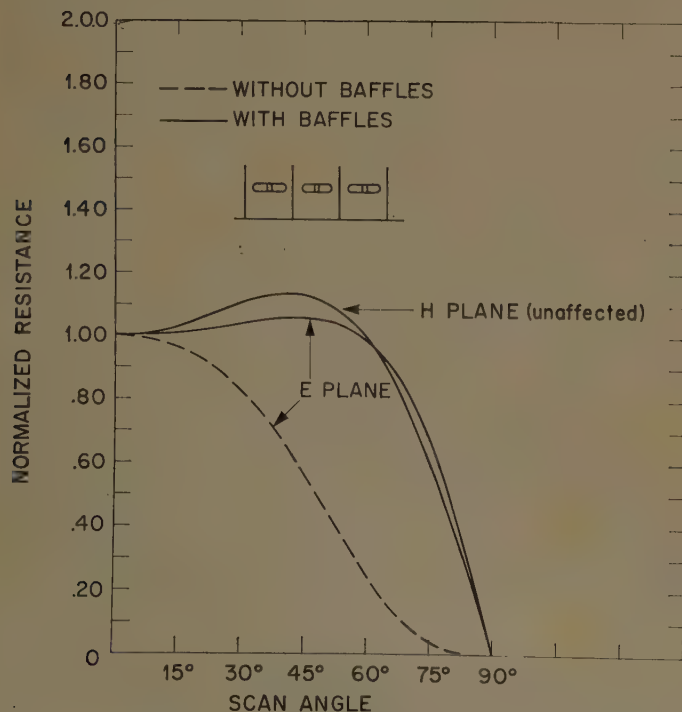


Fig. 8—Effect of compensating baffles on normalized input resistance of dipole array over a ground plane.

the dipoles is approximately a quarter of a wavelength, and any higher mode interaction should be negligible.

Since the constancy of performance of an array depends also on the input reactance values, the reactance variation must also be kept small. The reactance expressions for  $H$  and  $E$  plane scans when the baffles are present are given as part of (16) and (19), respectively. Let us temporarily ignore the  $X/Z_0$  term in each expression; the remainder of the reactance expressions (with  $n^2 = 1$  in order to normalize them in the same manner as the resistance curves of Fig. 8) are plotted in Fig. 9. It is seen that both curves are similar in shape, and that the values become fairly large for scan angles in excess of  $45^\circ$ . Since the resistance curves of Fig. 8 are rather flat up to  $\theta = 60^\circ$ , but deteriorate beyond that value, it is desirable to keep the reactance values low up to  $60^\circ$  also. This can be accomplished by suitably choosing the value of  $X/Z_0$ . If  $X/Z_0$  is made equal to  $-0.30$ , as indicated in Fig. 9 by the horizontal dashed line, the maximum reactance value for the  $E$  plane scan case is roughly halved, and that for  $H$  plane scan is considerably reduced. A larger value for  $X/Z_0$  is undesirable since the reactance at broadside would then be too large. With the choice indicated above, the effect of the reactance variation will be small except possibly near  $60^\circ$  for the  $H$  plane scan case. It should be recognized that the value of  $X/Z_0$  can be adjusted by properly choosing the length and width (or radius) of the dipole.

As a measure of the performance of the array, the input VSWR in the feed guide was computed as a function of scan angle. The VSWR values involve both the

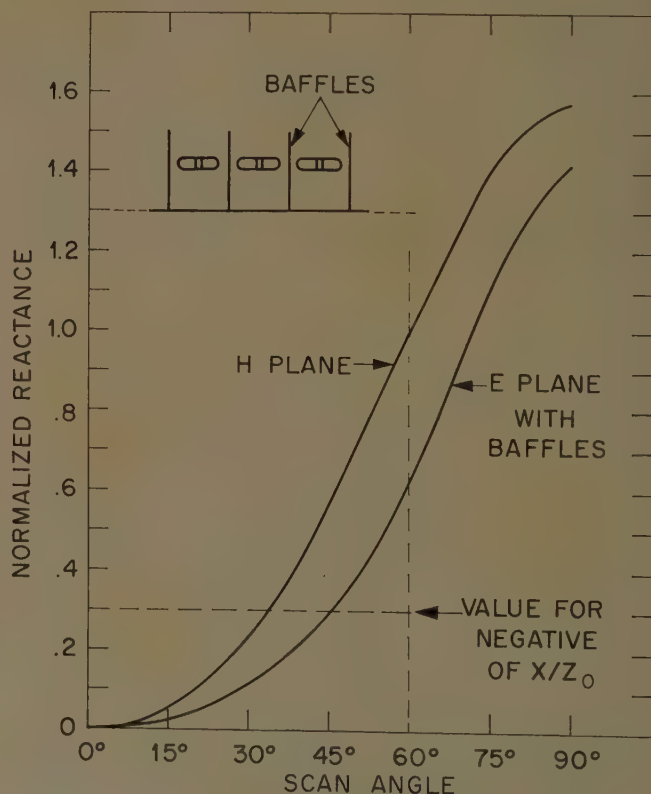


Fig. 9—Variation of normalized input reactance with scan angle in the presence of baffles.



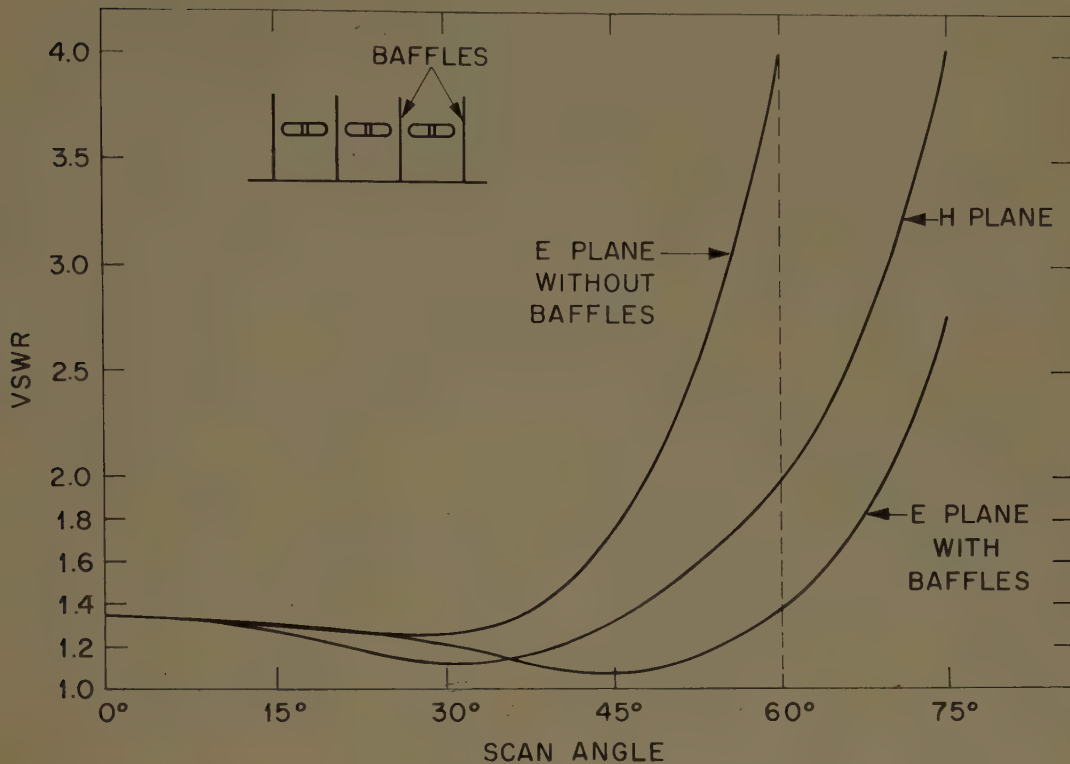


Fig. 10—Effect of compensating baffles on input VSWR.

input resistance and reactance, and were determined for the case  $n^2=1$ , which imposes a condition on the feed guide. These VSWR values are compared in Fig. 10 for the cases of  $H$  plane scan,  $E$  plane scan without baffles, and  $E$  plane scan with the baffles present. For all three cases, the value of  $X/Z_0$  was made equal to  $-0.30$ . It is seen that for scan angles below  $\pm 60^\circ$ , the VSWR for both  $H$  and  $E$  plane scan in the presence of baffles is quite good, being below 1.4 and 2.0 in this whole range for the  $E$  and  $H$  plane cases, respectively. The VSWR is below 1.4 for the  $H$  plane case for scan angles up to  $\pm 45^\circ$ . For  $E$  plane scan when the baffles are absent, the VSWR is much higher, rising to 4.0 for  $\theta=60^\circ$ . The deterioration in performance for scan angles greater than  $60^\circ$  is caused almost entirely by the drop in the resistance value in that range.

It is clear from the curves of Fig. 10 that the insertion of the baffles has considerably improved the performance of the array for scanning in the  $E$  plane. (As pointed out earlier, the  $H$  plane scan behavior is unaffected by the baffles.) The baffles were optimized in only one parameter, the height of their edge above the dipole array. Possibly a variation in the height of the dipoles above the ground plane, or the thickness of the baffles (so that the  $H$  plane scan behavior would also be affected), may result in further improvements. Also, the baffles constitute but one of many possible compensation structures. The objective in this study was not to determine an optimum compensating structure for a specific situation but rather to demonstrate that these effects of mutual coupling can be compensated for in this manner.

## APPENDIX

The susceptance value  $B/Y_p$  appearing in (1) is normalized to the periodic unit cell waveguide, while the value  $B_{t2}/Y_{pe}$  for which a theoretical expression is available from Edelberg and Oliner<sup>1</sup> is normalized to a rectangular waveguide of the same dimensions  $A$  and  $B$  as the periodic unit cell but with all metal walls. These susceptances are related by

$$\frac{B}{Y_p} = \frac{B_{t2}}{Y_{pe}} \frac{Y_{pe}}{Y_p} \frac{|V_{pe}|^2}{|V_p|^2}, \quad (20)$$

on the assumption, which is a very good one, that the replacement of metal side walls by magnetic side walls will not disturb the slot stored power. The voltage terms  $V_{pe}$  and  $V_p$  occurring in (20) are defined in (10) and (17) of Edelberg and Oliner,<sup>1</sup> and evaluated there in (19) and (20). The characteristic admittances are given by

$$\frac{Y_{pe}}{Y_p} = \frac{\kappa_{pe}}{k} = \sqrt{1 - (\lambda/2A)^2}, \quad (21)$$

consistent with the normalizations implicit in the expressions for the voltage terms. Upon use of (21) and the expressions for the voltage terms, (20) becomes

$$\frac{B}{Y_p} = \frac{B_{t2}}{Y_{pe}} 2\sqrt{1 - (\lambda/2A)^2} \left[ \frac{\cos(\pi a'/2a)}{1 - (a'/A)^2} \right]^2, \quad (22)$$

where  $a'$ ,  $a$  and  $A$  are, respectively, the widths of the slot, the rectangular feed waveguide, and the periodic unit cell waveguide, and where  $B_{t2}/Y_{pe}$  is given by (69) of Edelberg and Oliner.<sup>1</sup>

# Paraboloidal Reflector Patterns for Off-Axis Feed\*

S. S. SANDLER†

**Summary**—The problem of predicting the radiation pattern for an asymmetrically illuminated paraboloid is covered in some detail. The current distribution method is given in a final form suitable for machine computation. An approximate analytical solution using scalar diffraction methods is compared with the experimental results and the machine solution.

## I. INTRODUCTION

THE RADIATION problem of determining the pattern due to a parabolic reflector illuminated by a source placed at the focal point has been covered in some detail.<sup>1</sup> However, the related problem of an off-axis source illuminating a parabolic reflector has received little theoretical attention.<sup>2</sup>

The results given by Hildebrand<sup>2</sup> and Mauchley,<sup>3</sup> *et al.*, for an offset dipole feed are presented in integral form. The analysis was based on a current distribution method, neglecting higher-order perturbations in the radial variable. Kelleher and Coleman<sup>4</sup> attacked the problem in 1952. The separability of the two-dimensional aperture distribution was assumed. The problem was reduced to one space dimension and applied to a Gaussian-type aperture distribution. The effect of a finite aperture was neglected. The one-dimensional integral was placed in a form suitable for Airy function representation.

The current distribution method given in this paper takes account of all phase errors caused by an off-axis dipole or tapered amplitude source. The machine integration was performed on the surface of the paraboloid without recourse to an aperture plane distribution. The analytical method presented here accounts for the finite two-dimensional aperture distribution. The solution is given in terms of familiar Bessel functions. An analytical solution is also given for the more complicated case of a primary source of finite size. The methods presented in this paper are:

- 1) Current distribution method: The formal solution is given in a form suitable for machine computation.

\* Manuscript received by the PGAP, December 1, 1959; revised manuscript received January 25, 1960. The work reported in this paper was performed by Lincoln Laboratory, a center for research operated by the Massachusetts Institute of Technology with the joint support of the U. S. Army, Navy, and Air Force.

† Electronic Communications, Inc., Timonium, Md. Formerly at M.I.T. Lincoln Lab., Lexington, Mass.

<sup>1</sup> R. L. Pease, "Paraboloidal Reflector Patterns," M.I.T. Lincoln Lab., Lexington, Mass., Tech. Rept. No. 184; August 5, 1958.

<sup>2</sup> F. B. Hildebrand, "The Alternation in the Radiated Field of a Paraboloid Due to a Shift in the Position of the Dipole Feed," Mass. Inst. Tech., Cambridge, Mass., Rad. Lab. Rept. No. 1078; February 20, 1946.

<sup>3</sup> J. W. Mauchly and R. M. Shower, "Report on the Mathematical Computation of Current Flow Lines in, and Field Patterns of, Paraboloid Reflectors," Dept. of Elec. Engrg., University of Pennsylvania, Philadelphia, Rept. PZ-1; July, 1942.

<sup>4</sup> K. S. Kelleher, and H. P. Coleman, "Off-Axis Characteristics of the Paraboloidal Reflector," Naval Res. Lab., Washington, D. C., NRL Rept. No. 4088; December 31, 1952.

- 2) Scalar diffraction theory: a) Analytical field patterns are derived as a series of related Bessel functions. Two cases are considered—(1) dipole and (2) plane aperture primary illumination. b) The method of stationary phase is applied to case (2) above.

The results of 1) and 2) are compared with the experimental results.

## II. CURRENT DISTRIBUTION METHOD<sup>5</sup>

The secondary pattern for the antenna reflector system of Fig. 1 may be obtained formally by the current distribution method. The field in the far zone is given by<sup>6</sup>

$$E_{\Theta}(\Theta, \Phi) = B \hat{i}_{\Theta} \cdot \mathbf{I} \quad (1)$$

$$E_{\Phi}(\Theta, \Phi) = B \hat{i}_{\Phi} \cdot \mathbf{I}, \quad (1a)$$

where

$$B = \frac{-j\omega\mu}{2\pi} \frac{\exp[-jkR]}{R} \left[ \left( \frac{\epsilon}{\mu} \right)^{1/2} \frac{P}{2\pi} \right]^{1/2} \quad (2)$$

$$\mathbf{I} = \int_{\mathcal{S}} \frac{[G(\theta', \phi')]^{1/2}}{\rho'} [\hat{n} \times (\hat{\rho}' \times \hat{e}')] \exp[-jk(\rho' - \hat{\rho}' \cdot \hat{i}_R)] dS \quad (3)$$

$$\hat{i}_R = \sin \Theta \cos \Phi \hat{i} + \sin \Theta \sin \Phi \hat{j} + \cos \Theta \hat{k}$$

$$\hat{i}_{\Theta} = \cos \Theta \cos \Phi \hat{i} + \cos \Theta \sin \Phi \hat{j} - \sin \Theta \hat{k}$$

$$\hat{i}_{\Phi} = \cos \Theta \hat{j} - \sin \Theta \hat{k}.$$

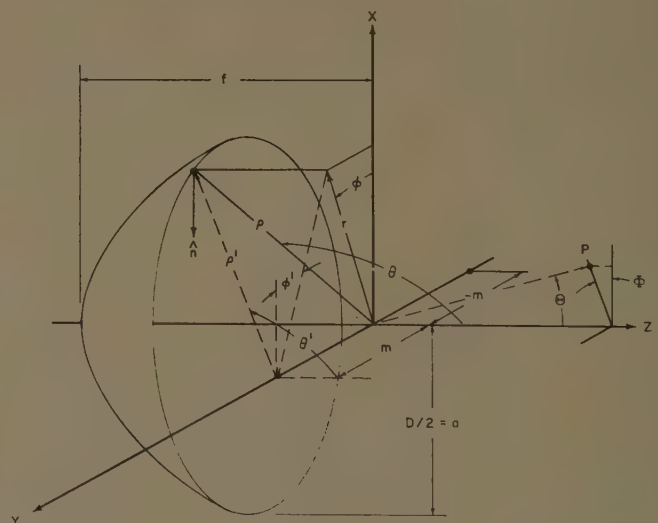


Fig. 1.

<sup>5</sup> The development in this section follows closely the work of R. L. Pease, *op. cit.*

<sup>6</sup> S. Silver, "Microwave Antenna Theory and Design," McGraw-Hill Book Co., Inc., New York, N. Y., sec. 6.8; 1949.



Note that primed vectors are referred to the origin at the offset feed point  $0'$  and unprimed vectors to the focus of the paraboloid at point  $0$ . Unit vectors are denoted by circumflexes and unnormalized vectors are denoted by arrows.

The unit vectors  $\hat{i}_R$ ,  $\hat{i}_\theta$  and  $\hat{i}_\phi$  refer to the far-field point. The reflector surface is given as a function of the variables  $\rho$  and  $\theta$ , where, for a paraboloid of focal length  $f$ ,

$$\rho = \frac{2f}{1 - \cos \theta} \quad (5)$$

The following assumptions are made in the evaluation of (3):

- 1) The reflector surface is in the far field of the primary source.
- 2) The surface currents are continuous at the reflector edge (*i.e.*, current flows to the shadow side of the reflector).
- 3) All edge effects are neglected.
- 4) Only the initial radiation from current element on the reflector is considered. Interaction of surface elements is neglected.
- 5) Back radiation from the primary source is neglected.

The determination of the field at the reflector is accomplished in two steps: 1) The direction cosines for the radial vector  $\rho'$  (Fig. 1) are determined as a function as the paraboloid coordinates  $\theta$  and  $\phi$ ; 2) the offset (*i.e.*, "primed") coordinates determined in 1) represent a mutually orthogonal set intersecting at  $0'$ . The far field at the reflector surface may be represented by a suitable vector combination of the offset direction cosines and the paraboloidal coordinates.

Application of simple trigonometry yields the rather awkward expressions

$$\rho = \frac{f}{1 - \cos \theta} \left[ 4 - 4 \left( \frac{m}{f} \right) \sin \theta \sin \phi (1 - \cos \theta) + \left( \frac{m}{f} \right)^2 (1 - \cos \theta)^2 \right]^{1/2} \quad (6)$$

$$\theta' = \arctan \frac{[(m/f)^2 (1 - \cos \theta)^2 - (m/f) \sin \theta \sin \phi (1 - \cos \theta) + 4 \sin^2 \theta]^{1/2}}{2 \cos \theta} \quad (7)$$

$$\phi' = -\arctan \frac{(m/f)(1 - \cos \theta) - 2 \sin \theta \sin \phi}{2 \sin \theta \cos \phi}, \quad (8)$$

where  $m$  is the primary feed offset and  $\rho'$ ,  $\theta'$ ,  $\phi'$  are shown in Fig. 1. The unit vector  $\hat{\rho}'$  may now be given in terms of its direction cosines, or

$$\hat{\rho}' = \sin \theta' \cos \phi' \hat{i} + \sin \theta' \sin \phi' \hat{j} + \cos \theta' \hat{k} \quad (9)$$

An elegant method for obtaining the far field of the primary source has been suggested by Pease.<sup>7</sup> Assump-

tion 1) above implies that the primary wave polarization  $\hat{e}'$  is at right angles to  $\hat{\rho}'$ . The primary wave polarization vector is further assumed to be coplanar with the source polarization that is in the  $\hat{z}$  direction. The vectors  $\hat{e}'$ ,  $\hat{z}$  and  $\hat{\rho}'$  are then coplanar and  $(\hat{z} \times \hat{\rho}')$  is at right angles to this plane. Hence,  $\hat{e}'$  is at right angles to both  $\hat{\rho}'$  and  $(\hat{z} \times \hat{\rho}')$ , or

$$\hat{e}' = \frac{\hat{\rho}' \times (\hat{z} \times \hat{\rho}')}{|\hat{\rho}' \times (\hat{z} \times \hat{\rho}')|} \quad (10)$$

$$\hat{e}' = \frac{\hat{z} - (\hat{\rho}' \cdot \hat{z}) \hat{\rho}'}{(1 - \sin^2 \theta' \cos^2 \phi')^{1/2}} \quad (11)$$

The outward normal  $\hat{n}$  to the surface  $S$  at  $P(\rho, \theta, \phi)$  and the elemental area  $dS$  may be evaluated by the standard methods with the result

$$\hat{n} = -\cos \frac{\theta}{2} \cos \phi \hat{i} - \cos \frac{\theta}{2} \sin \phi \hat{j} + \sin \frac{\theta}{2} \hat{k} \quad (12)$$

$$dS = \rho^2 \sin \theta \csc \frac{\theta}{2} d\theta d\phi \quad (13)$$

With the aid of (1) to (13), the far-field components in the  $H$ -plane (*i.e.*,  $\Phi = \pi/2$ ) are given by

$$E_\Theta \left( \Theta, \frac{\pi}{2} \right) = 4B \int_{-\pi/2}^{\pi/2} \int_{\theta_m}^{\pi} K_\Theta \left( \theta, \phi; \Theta, \frac{\pi}{2} \right) F \left( \theta, \phi; \Theta, \frac{\pi}{2} \right) d\theta d\phi \quad (14)$$

$$E_\Phi \left( \Theta, \frac{\pi}{2} \right) = 4B \int_{-\pi/2}^{\pi/2} \int_{\theta_m}^{\pi} K_\Phi \left( \theta, \phi; \Theta, \frac{\pi}{2} \right) F \left( \theta, \phi; \Theta, \frac{\pi}{2} \right) d\theta d\phi, \quad (15)$$

where

$$K_\Theta = \cos \Theta \sin \theta' \sin \phi' \cos \frac{\theta}{2} \cos \phi$$

$$- \sin \Theta \cos \theta' \cos \frac{\theta}{2} \cos \phi,$$

$$K_\Phi = \cos \theta \sin \frac{\theta}{2} - \sin \theta' \sin \phi' \cos \frac{\theta}{2} \sin \phi$$

<sup>7</sup> R. L. Pease, *op. cit.*, p. 3.





It is assumed that the amplitude of the aperture distribution is identical to the unperturbed field. Actual calculations show that the error introduced is of the order  $(m/f)^2$ .

Eq. (18), for both the  $x$ - and  $y$ -components of the far field may now be evaluated by the use of (20) and (26), whence, for dipole illumination,

$$E_x(\Theta, \Phi) \cong B' \int_0^{a/2f} \int_0^{2\pi} \exp \{ \} u du d\phi \quad (27)$$

$$E_y(\Theta, \Phi) \cong B' \int_0^{a/2f} \int_0^{2\pi} \left\{ \sin 2\phi \left[ \frac{u^2}{1+u^2} + \frac{u^2}{(1+u^2)^2} \right] - \sin 4\phi \frac{u^2}{(1+u^2)^2} \right\} \exp \{ \} u du d\phi \quad (28)$$

where

$$B' = \frac{jk}{4\pi R} \exp[-jkR],$$

$$\exp \{ \} = \exp \left\{ j2kf \left[ 1 - \frac{m}{f} \frac{u}{(1+u^2)^2} \sin \phi + u \sin \Theta \cos(\phi - \Phi) \right] \right\},$$

$a$  = aperture radius,

$$u = \cot \left( \frac{\theta}{2} \right).$$

The integration with respect to  $\phi$  in (27) and (28) may be carried out directly, since

$$\int_0^{2\pi} \exp[jg \sin(\phi - \Phi)] d\phi = 2\pi J_0(g) \quad (29)$$

and

$$\int_{\alpha}^{\alpha+2\pi} \exp[j(n\phi - g \sin \phi)] d\phi = 2\pi J_n(g). \quad (30)$$

Eqs. (27) and (28) are reduced to

$$E_x \cong 2\pi B' \int_0^{a/2f} J_0(g) u du \quad (31)$$

$$E_y \cong 2\pi B' \int_0^{a/2f} \sin 2\Phi \left[ \frac{u^2}{(1+u^2)^2} + \frac{u^2}{(1+u^2)} \right] J_2(g) u du + 2\pi B' \int_0^{a/2f} \sin 4\Phi \frac{u^2}{(1+u^2)^2} J_4(g) u du, \quad (32)$$

where

$$g = 2kf \frac{u}{(1+u^2)^2} \frac{m}{f} + 2kfu \sin \Theta.$$

Confining interest in the  $H$ -plane, then

$$E_y \cong 0, \quad \Phi = \frac{\pi}{2}.$$

The cross polarization is of second order in  $(m/f)$  and is neglected in this approximate analysis.

The integrand in (31) is an odd function such that all odd powers of  $u$  contribute to the far field. For analytical evaluation of (31) the  $u$  variation of the kernel will be replaced by a suitable approximation. Since the paraboloid subtends an angle somewhat less than 180 degrees at the focal point, then it follows from the binomial expansion

$$\frac{u}{(1+u^2)^2} \cong u(1-2u^2). \quad (33)$$

Eq. (31) is reduced to

$$E_x \left( \Theta, \frac{\pi}{2} \right) \cong 2\pi B' \int_0^{a/2f} J_0[2kfu \sin \Theta + 2kmu(1-2u^2)] \cdot u du. \quad (34)$$

The kernel of (34) is placed in the above form to facilitate its expansion in terms of  $J_\nu(2kfu \sin \theta)$  since<sup>9</sup>

$$J_0[2kfu \sin \Theta + 2kmu(1-2u^2)] = \sum_{\nu=0}^{\infty} (-1)^\nu \frac{[2kmu(1-2u^2)]^\nu}{\nu!} \times \left[ 1 + \frac{m}{2f} \frac{(1-2u^2)}{\sin \Theta} \right]^\nu J_\nu(2kfu \sin \Theta). \quad (35)$$

The expansion was carried out until the last term retained was two orders of magnitude less than the leading term (*i.e.*, terms in  $\nu=0, 1$  and the leading term for  $\nu=2$ ). After integration by parts,<sup>10</sup> noting

$$\int_0^z z^{\nu+1} J_\nu(z) dz = z^{\nu+1} J_{\nu+1}(z), \quad (36)$$

then with (34) and (35) it follows that

$$E_x \left( \Theta, \frac{\pi}{2} \right) \cong \Lambda_1(\beta) - [\alpha_1 + \alpha_2 \sin \Theta] \Lambda_2(\beta) - [\gamma_1 + \gamma_2 \sin \Theta] \Lambda_3(\beta), \quad (37)$$

where<sup>11</sup>

$$\Lambda_P(\beta) = \frac{P!}{(\beta/2)^P} J_P(\beta), \quad \beta = ka \sin \Theta$$

$$\alpha_1 = \frac{1}{4} \frac{m}{f} k^2 a^2 \left[ 1 - 2 \left( \frac{a}{2f} \right)^2 \right],$$

$$\gamma_1 = \frac{1}{12} \frac{m}{f} k^2 a^2 \left( \frac{a}{2f} \right)^2 \left\{ \frac{m}{f} \left[ 1 - 2 \left( \frac{a}{2f} \right)^2 \right] + \left( \frac{m}{2a} \right)^2 \beta^2 \right\},$$

<sup>9</sup> E. Jahnke and F. Emde, "Tables of Functions with Formula and Curves," Dover Publications, Inc., New York, N. Y., p. 144; 1945.

<sup>10</sup> N. W. McLachlan, "Bessel Functions for Engineers," Oxford University Press, New York, N. Y.; 1934.

<sup>11</sup> Jahnke and Emde, *op. cit.*, pp. 180-189.

$$\alpha_2 = \frac{1}{8} \frac{m}{f} k^2 a^2 \left\{ 1 - 4 \left( \frac{a}{2f} \right)^2 \left[ 1 - \left( \frac{a}{2f} \right)^2 \right] \right\},$$

$$\gamma_2 = \frac{1}{12} k^2 a^2 \left( \frac{a}{2f} \right)^2 \left\{ \frac{m}{f} + \left( \frac{m}{2a} \right)^2 \beta^2 \right\}.$$

It may be noted that for  $m=0$ , the field pattern reduces to the well-known formula

$$E_x = \Lambda_1(ka \sin \Theta). \quad (38)$$

The far-field pattern for the offset feed case becomes asymmetric around  $\Theta=0$ . This result is easily seen by noting that the terms

$$-\alpha_2 \sin \Theta \Lambda_2(ka \sin \Theta)$$

and

$$-\gamma_2 \sin \Theta \Lambda_3(ka \sin \Theta) \quad (38a)$$

are odd about  $\Theta=0$ . Shifting the feed from  $y=0$  to  $y=+m$  is mathematically represented by subtracting the odd terms given by (38a) from the symmetrical pattern given by (38). The result is a main beam shift toward the negative  $y$ -axis in the  $H$ -plane. As a further consequence of the odd-order phase effects given in (37), the side-lobe structure becomes asymmetrical. These results are shown graphically in Sec. VI.

#### IV. SCALAR DIFFRACTION THEORY (PLANE APERTURE ILLUMINATION)

Eq. (27) for dipole primary illumination may be modified for other amplitude distributions with the addition of the gain factor  $G^{1/2}$ .

For amplitude distributions other than the simple dipole, the normal procedure would be to consider the primary source concentrated at  $x=m$ , and modify the dipole amplitude variation. However, some phase error is introduced by neglecting the finite size of the primary source. A simple amplitude factor such as  $G^{1/2}$  cannot account for this error.

The procedure for obtaining the secondary pattern will be explained with the aid of Fig. 3.

The radiation pattern for a simple dipole source placed at  $y=+m$  was obtained in Sec. III. For an extended source of width  $b$ , polarized in the  $x$ -direction, it is necessary to replace the plane aperture by an equivalent "sheet" of simple dipoles. Then by the principle of superposition, the far field at point  $(\Theta, \pi/2)$  is the sum of all infinitesimal dipoles in the  $x$ - $y$  plane that extend from  $y=m-b/2$  to  $y=m+b/2$ . If the amplitude of the primary illumination varies along  $y$ , then this change is included by a multiplicative factor. As an example, consider a rectangular waveguide primary source shown in Fig. 4. Since the amplitude variation in the  $E$ -field is cosinusoidal, then the field at point  $P$  due to dipole element at  $y=y_1$  is

$$\cos \frac{\pi}{b} (y-m) E_x \left( \Theta, \frac{\pi}{2} \right) \Big|_{y=y_1}, \quad (39)$$

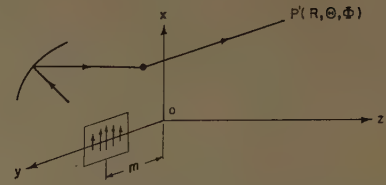


Fig. 3—Primary illumination of aperture of finite size.

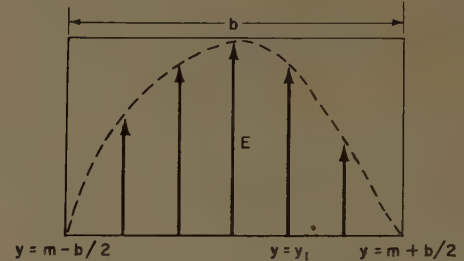


Fig. 4—Cross section of rectangular waveguide primary source.

where

$$m - \frac{b}{2} \leq y_1 \leq m + \frac{b}{2}.$$

Since the field is continuous over the width of the aperture, then the field at  $P$  due to a rectangular waveguide source is given by

$$E_{xw} \left( \Theta, \frac{\pi}{2} \right) = \int_{m-(b/2)}^{m+(b/2)} E_x \left( \Theta, \frac{\pi}{2} \right) \cos \frac{\pi}{b} (\xi - m) d\xi. \quad (39a)$$

To evaluate (39) with  $E_x(\Theta, \pi/2)$  as given by (37), the offset  $m$  must be replaced by the dummy variable  $\xi$ . The integration of (39) involves simple integrals of the form

$$\int \xi \cos \frac{\pi}{b} (\xi - m) d\xi. \quad (40)$$

The resultant field pattern is given by

$$E_{xw} = \Lambda_1(\beta) - [\alpha_{12} + \alpha_{22} \sin \Theta] \Lambda_2(\beta) - [\gamma_{12} + \gamma_{22} \sin \Theta] \Lambda_3(\beta), \quad (41)$$

where

$$\alpha_{12} = \frac{k^2 a^2}{16 f^2} \left\{ 1 - 4 \left( \frac{a}{2f} \right)^2 \left[ 1 - \left( \frac{a}{2f} \right)^2 \right] \right\} \times \left[ \left( m + \frac{b}{2} \right)^2 + \left( m - \frac{b}{2} \right)^2 - 6m \left( \frac{b}{\pi} \right)^2 \right],$$

$$\alpha_{22} = \frac{1}{4} \frac{m}{f} a^2 k^2 \left[ 1 - 2 \left( \frac{a}{2f} \right)^2 \right],$$



$$\begin{aligned}\gamma_{12} &= \frac{1}{24} \frac{k^2 a^2}{24 f^2} \left( \frac{a}{2f} \right) \left[ 1 - 2 \left( \frac{a}{2f} \right)^2 \right] \\ &\quad \times \left[ \left( m - \frac{b}{2} \right)^2 + \left( m - \frac{b}{2} \right)^2 - 6m \left( \frac{b}{\pi} \right)^2 \right] \\ &\quad - \frac{1}{48} \frac{\beta^2}{f} \left( \frac{a}{2f} \right)^4 k^2 \left[ \left( m + \frac{b}{2} \right)^3 \right. \\ &\quad \left. + \left( m - \frac{b}{2} \right)^3 - 6m \left( \frac{b}{\pi} \right)^2 \right], \\ \gamma_{22} &= \frac{1}{12} \frac{k^2 a^2}{f} \left( \frac{a}{2} \right)^2 - \frac{\beta^2}{96} \left( \frac{k^2 a^2}{2f^2} \right)^2 \\ &\quad \cdot \left[ \left( m + \frac{b}{2} \right)^3 + \left( m - \frac{b}{2} \right)^3 - 6m \left( \frac{b}{\pi} \right)^2 \right].\end{aligned}$$

It is expected that the results due to dipole illumination will be almost identical to those obtained for a waveguide primary source. The reason for this similarity may be seen crudely from the following.

In line with the derivation of (41), consider the far-field pattern as the superposition of the individual pattern due to a displaced dipole. Assume that the change of phase over any given side lobe may be neglected.<sup>12</sup>

Now consider the secondary pattern as the superposition of two dipoles located symmetrically about  $y = +m$ . The reader may verify that the resulting addition of the two patterns will have a slightly increased beamwidth with little change in side-lobe level.

## V. SCALAR DIFFRACTION THEORY (PLANE WAVE ILLUMINATION)

A more general, though less accurate, method will be employed in this section. This is the method of stationary phase. Although it is difficult to determine the accuracy of the stationary phase expression, the methods may be applied to any gain function that is bounded and slowly varying in the variable  $u = \cot(\theta/2)$ .

Asymptotic approximations for integrals of the type given in (27) are discussed in the literature.<sup>13</sup> The method is briefly summarized for convenience. Consider the integral

$$f(x) = \int_a^b g(t) \exp[ixh(t)] dt. \quad (42)$$

Application of DeMoivre's theorem to (42) yields

$$f(x) = \int_a^b g(t) \cos xh(t) dt + i \int_a^b g(t) \sin xh(t) dt. \quad (43)$$

<sup>12</sup> It has been shown by Pease, *op. cit.*, that the quadratic phase term for  $m=0$  is given by  $E_q \sim \exp \{ -j(ka \sin \Theta)^2 [4kf(1 - \cos \Theta)]^{-1} \}$  whence for  $\Theta < 7^\circ$  SBW,  $a/\lambda = 20$ ,  $f/\lambda = 22$ , then  $E_q \sim \exp [-j2\pi/15]$  or less than  $26.0^\circ$  phase change.

<sup>13</sup> A. Erdelyi, "Asymptotic Expansions," Dover Publications, Inc., New York, N. Y., p. 35; 1956.

Assume  $x$  large and  $h(t)$  real. If  $g(t)$  is bounded in  $(a, b)$ , then by Riemann's lemma,<sup>14</sup>

$$\int g(t) \begin{Bmatrix} \cos xh(t) \\ \sin xh(t) \end{Bmatrix} dt = O\left(\frac{1}{x}\right). \quad (44)$$

However, examination of (42) in the vicinity of the stationary point [*i.e.*,  $h'(t) = h'(t_0) = 0$ ] shows that, for  $x$  large,

$$f(x) \cong g(t_0) \exp[ixh(t_0)] \exp\left[-i\frac{\pi}{4}\right] \sqrt{\frac{2\pi}{x|h''(t_0)|}}. \quad (45)$$

As a first approximation, the value of integral (42) is due to the contributions near the stationary points. Near  $t = t_0$ , (42) becomes

$$f(x) \cong g(t_0) \exp[ixh(t_0)] \int_a^b \exp\left[\frac{ixh''(t_0)}{2}(t - t_0)^2\right] dt, \quad (46)$$

where  $a < t_0 < b$ .

If the limits in (46) include three standard deviations of the error function [*i.e.*, the kernel in (46)] then with less than one per cent error,

$$f(x) \cong g(t_0) \exp[ixh(t_0)] \exp\left[-i\frac{\pi}{4}\right] \sqrt{\frac{2\pi}{x|h''(t_0)|}}. \quad (47)$$

The stationary phase points may be interpreted physically as discrete sources. Hence, in the evaluation of the contribution due to the localized source, the effect of the remaining portions of the aperture is neglected.

The stationary phase integration will be concerned with primary sources polarized in the  $x$ -direction. Furthermore, their amplitude distributions will be different than the idealized dipole. The field in the aperture plane may be expressed as (*i.e.*, for point source illumination)

$$e_{TA} = [G(\theta, \phi)] e_A, \quad (48)$$

where

$e_{TA}$  = amplitude distribution due to tapered amplitude primary source,  
 $G^{1/2}$  = voltage gain function,  
 $e_A$  = dipole aperture field.

If the gain function is  $\phi$  independent, then it may be expanded as a series in  $u$ , or

$$G^{1/2} = \sum_{r=0}^{\infty} A_r g_r(u), \quad (49)$$

where

$$\left| \frac{A_{r+1} g_{r+1}(u)}{A_r g_r(u)} \right| < 1, \quad u \leq |u_{\max}|.$$

<sup>14</sup> H. Jeffreys and B. S. Jeffreys, "Methods of Mathematical Physics," Cambridge University Press, New York, N. Y.; 1946.

The integral for the  $x$ -component of the radiation field, (27) modified for the gain function (49), is

$$E_x\left(\Theta, \frac{\pi}{2}\right) \cong B' \sum_r A_r \int_{-\pi/2}^{\pi/2} d\phi \int_0^{a/2f} u g_r(u) \exp[\psi] du, \quad (50)$$

where

$$\psi = j \sin \phi [2kfu \sin \Theta + 2kmu(1 - 2u^2)].$$

The  $u$  integration in (50) is identical in form to (42). The asymptotic value of (43) is given by (47), and with this result (50) is reduced to

$$E_x\left(\Theta, \frac{\pi}{2}\right) = B' K(u_0) u_0 \sum_r A_r g_r(u) \times \int_{-\pi/2}^{\pi/2} \sin^{-1/2} \phi \exp[\psi(u_0)] d\phi, \quad (51)$$

where

$$\psi(u_0) = j2kf \sin \phi \left[ u_0 \left( \sin \Theta - \frac{m}{f} \right) + 2 \frac{m}{f} u_0^3 \right]$$

$$u_0 = \frac{\left( 1 - \frac{1}{2m} \sin \Theta \right)^{1/2}}{\sqrt{6}}$$

$$K(u_0) = \left( \frac{\pi}{24 | (m/f) u_0 | kf} \right)^{1/2} \exp \left[ -i \frac{\pi}{4} \right].$$

The integration in (51) is performed expanding  $\sin^{-1/2} \phi$  in a series of harmonics of  $\cos 2\phi$  or

$$\begin{aligned} \sin^{-1/2} \phi &= \left( \frac{1 - \cos 2\phi}{2} \right)^{-1/4} \\ &= 2^{1/4} \left( 1 + \frac{1}{4} \cos 2\phi + \frac{5}{32} \cos^2 2\phi \right. \\ &\quad \left. + \frac{45}{384} \cos^3 2\phi + \dots \right) \\ \sin^{-1/2} \phi &= 2^{1/4} \left( \frac{69}{64} + \frac{173}{512} \cos 2\phi + \frac{45}{512} \cos 4\phi \right. \\ &\quad \left. + \frac{15}{512} \cos 6\phi + \dots \right). \quad (52) \end{aligned}$$

Substitution of (52) in (51) yields

$$\begin{aligned} E_x\left(\Theta, \frac{\pi}{2}\right) &\cong 2^{1/4} B' K(u_0) \sum_r A_r g_r(u_0) \\ &\times \left\{ \frac{69}{64} \int_{-\pi/2}^{\pi/2} \exp[\psi(u_0)] d\phi + \frac{173}{512} \right. \\ &\times \int_{-\pi/2}^{\pi/2} \cos 2\phi \exp[\psi(u_0)] d\phi + \frac{45}{512} \\ &\times \int_{-\pi/2}^{\pi/2} \cos 4\phi \exp[\psi(u_0)] d\phi + \dots \left. \right\}. \quad (53) \end{aligned}$$

The electric field, in final form, becomes

$$\begin{aligned} E_x\left(\Theta, \frac{\pi}{2}\right) &= 2^{5/4} \pi B' K(u_0) \sum_r A_r g_r(u_0) \\ &\times \left\{ \frac{69}{64} J_0(2kfh) + \frac{173}{512} J_2(2kfh) \right. \\ &\left. + \frac{45}{512} J_4(2kfh) + \frac{15}{512} J_6(2kfh) + \dots \right\}, \quad (54) \end{aligned}$$

where

$$h = u_0 \left( \sin \Theta - \frac{m}{f} \right) + 2 \frac{m}{f} u_0^3.$$

The generality of the stationary phase method is seen from (54), which is arbitrary to the extent of the gain function  $G^{1/2}$ . As a practical example, consider the case of a rectangular waveguide primary source. Considering only the  $\theta$  amplitude variation, we get the gain function as

$$G^{1/2} = \frac{\cos [(\pi b/\lambda) \sin \theta]}{[(\pi b/\lambda) \sin \theta]^2 - (\pi^2/4)}, \quad (55)$$

where  $b$  is the  $H$ -plane waveguide width.

It is necessary to expand (55) in a convergent series in  $u = \cot(\theta/2)$  near the stationary phase point  $u = u_0$ . From (51), the value of  $u_0$  near  $\Theta = 0$  is  $u_0 = 1/\sqrt{6}$ . It follows that, near  $u_0 = 1/\sqrt{6}$ ,

$$\left. \frac{\pi b}{\lambda} \sin \theta \right|_{u_0} = \frac{2\pi b}{\lambda} \frac{u_0}{1 + u_0^2} \cong 1.63 \quad (56)$$

Note that the value of  $\theta$  that corresponds to  $u_0 = 1/\sqrt{6}$  (i.e.,  $\Theta(u = u_0) = 2 \cot^{-1} u_0$ ) determines a radial region near the edge of the aperture. Actually the stationary phase method applied in this section determines the far field by evaluating the contribution from annular rings of mean radius  $r_0$ , where

$$r_0 = 2fu_0. \quad (57)$$

Hence, as we look away from the broadside direction, the annular region moves toward the vertex of the paraboloidal reflector.

Returning to (55), we expand the numerator near

$$\zeta = \frac{\pi b}{\lambda} \sin \theta = \frac{\pi}{2}, \quad (58)$$

since from (56) it has this value (approximately) near  $u_0 = 1/\sqrt{6}$ . Since  $f \gg m$ , near  $\Theta = 0$ ,  $u_0$  will be of somewhat large variation. The expansion of the gain function will undoubtedly take place in a slowly converging series for a nonnegligible range of  $u_0$ . With this in mind,  $\cos \zeta$  is expanded near  $\zeta = \pi/2$

$$\begin{aligned} \cos \zeta &= \frac{(\pi/2) - \zeta}{1!} - \frac{1}{3!} \left( \frac{\pi}{2} - \zeta \right)^3 \\ &\quad + \frac{1}{5!} \left( \frac{\pi}{2} - \zeta \right)^5 + \dots, \quad (59) \end{aligned}$$



where

$$\zeta = \frac{\pi b}{\lambda} \sin \theta = \frac{2\pi b}{\lambda} \frac{u}{1+u^2}.$$

At  $u=u_0$ , the gain function  $G^{1/2}$  is given by

$$G^{1/2} = \frac{1}{1!} \frac{[(\pi/2) - \zeta(u_0)]}{\zeta^2 - (\pi^2/4)} - \frac{1}{3!} \frac{[(\pi/2) - \zeta(u_0)]^3}{\zeta^2 - (\pi^2/4)} + \dots$$

$$= \sum_r A_r g_r(u_0), \quad (60)$$

where

$$A_r = \frac{(-1)^{r+1}}{r!}, \quad r > 0$$

$$g_r(u_0) = \left( \frac{\pi}{2} - \zeta \right)^r / \left( \zeta^2 - \frac{\pi^2}{4} \right), \quad r = 1, 3, 5$$

$$A_r = 0, \quad r = 0$$

$$g_r(u_0) = 0, \quad r = 0, 2, 4.$$

The radiation pattern (54) is completed with the substitution of (60) for the  $r$  summation.

## VI. EXPERIMENTAL AND THEORETICAL RESULTS

The vertical and horizontal components of the  $H$ -plane radiation pattern (current distribution method) are given by (14) and (15). The power pattern is proportional to the sum of the squares of  $E_\Theta$  and  $E_\Phi$ , or

$$P\left(\Theta, \frac{\pi}{2}\right) \sim E_\Phi^2\left(\Theta, \frac{\pi}{2}\right) + E_\Theta^2\left(\Theta, \frac{\pi}{2}\right). \quad (61)$$

In the  $H$ -plane the spherical and Cartesian components of the radiation field are related in a simple manner

$$|E_\Phi| = |E_x| \quad (62)$$

$$|E_\Theta| = |E_y|. \quad (63)$$

Figs. 5–8 (next page) show the radiation pattern as a function of illumination offset for dipole and waveguide illumination. In comparing the individual patterns, we will define a standard beamwidth (SBW) as a half-power beamwidth for an equivalent paraboloid fed by a dipole source located at the focus. All results in this section are based on the constants

$$(f/D) = 0.573, \quad D = 48 \text{ inches}, \quad \lambda = 1.25 \text{ inches}. \quad (64)$$

The SBW for the above reflector is  $1.55^\circ$ . It follows that a feed offset of  $(m/f) = 0.027$  corresponds to a normalized value of secondary beam tilt of one SBW.

The major effects of the displacement of the primary feed from the focus will be discussed with reference to the rigorous solution. The approximate scalar diffraction expressions will then be compared with the results given by the current distribution method. Experimental results are given for comparison.

### A. Side-Lobe Variation

The side-lobe structure becomes asymmetrical around the main beam; the first side lobe near  $\Theta=0$  is higher than the corresponding side lobe on the other side of the main beam. For an offset of 0.32 SBW, the two side lobes adjacent to the main beam are down 16.8 and 19 db from the maximum value. As the feed is moved farther away from the focal axis, the side lobes become more asymmetrical. For example, at an offset of 1.85, SBW the side-lobe levels have changes to 15.2 and 23 db. In accordance with the discussion given in Sec. III, the results for a waveguide primary source are almost identical to those for dipole illumination. For all practical purposes, the results may be used interchangeably.

The beam deviation  $\delta$  is defined as

$$\delta = \frac{\text{feed tilt angle}}{\text{secondary main beam angle}}. \quad (65)$$

The value of  $\delta$  is a measure of the equivalent curvature of the reflecting surface. For example, if a plane sheet is illuminated with a point source, the angle of incidence equals the angle of reflection, hence  $\delta = +1$ . Similarly, for a paraboloid fed at the focus,  $\delta = 1$ , since the secondary beam is pointed along the focal axis. However, when the feed is moved off the focal point, higher-order phase distributions shift the secondary beam. Fig. 9 shows the variation of main beam angle with the primary feed position. The value of  $\delta$  is almost constant over the entire range of feed offsets. Since the value of  $(f/D)$  is large, then beam deviation is near unity. The theoretical value of  $\delta = 0.90$  compares favorably with Silver's value of 0.94.

### B. Cross Polarization

The cross-polarization component, which has a null at the maximum value of the vertical field pattern, is shown in Fig. 10. The two symmetrical main lobes shown in the figure have their maximum value of  $-27$  db (relative to the main polarization) when the main polarization is down 12 db from its maximum value. The maximum of  $-27$  db given for an offset of 0.32 SBW is increased slightly to  $-25$  db as the feed is displaced to 1.12 SBW. Note that the cross-polarization component aids in filling the deep nulls of the main field pattern.

### C. Directive Gain

Two major causes of gain change with offset are the variation of effective radiation area and the change in primary power intercepted by the reflector. A consistent gain calculation requires: 1) a knowledge of the relative far-field intensity, and 2) the actual power intercepted by the reflector. The calculation of directive gain with primary feed offset will be based on the two-dimensional  $H$ -plane radiation pattern. If we are to extend the results to three-space dimensions, it is necessary that the

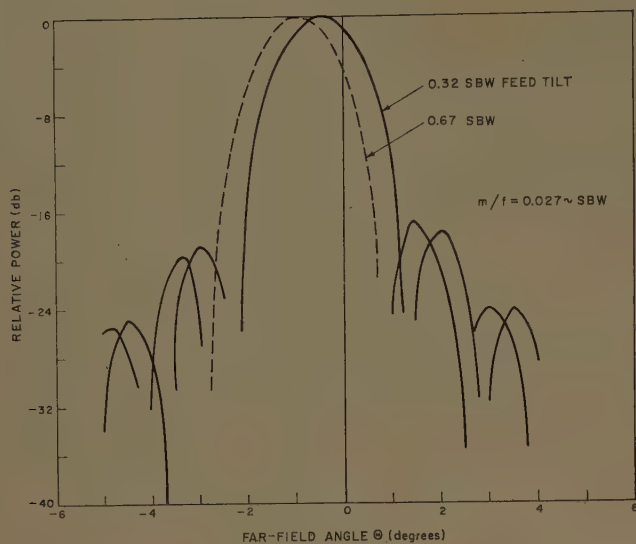


Fig. 5—Current distribution method radiation pattern (normalized, dipole illumination, H-plane).

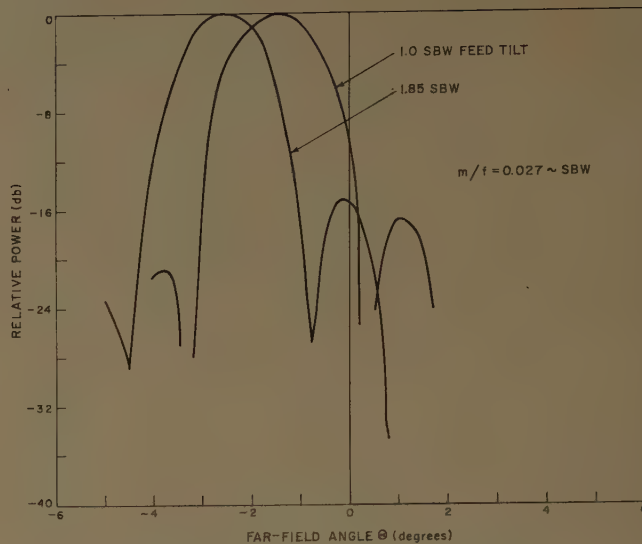


Fig. 6—Current distribution method radiation pattern (normalized, dipole illumination, H-plane).

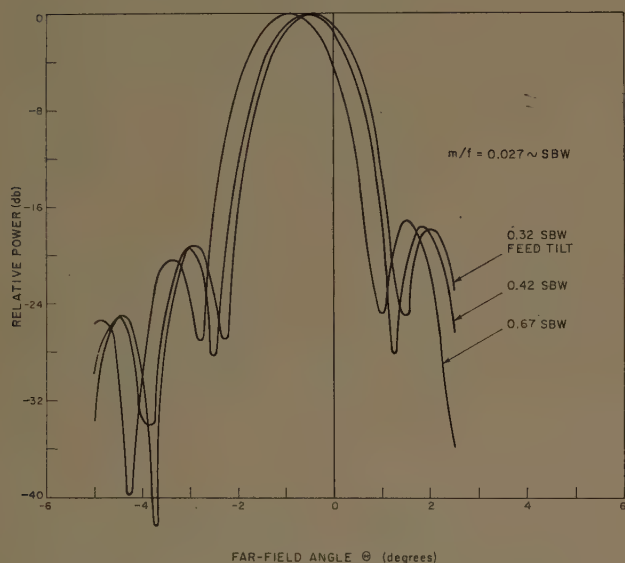


Fig. 7—Current distribution method radiation pattern (normalized, waveguide illumination, H-plane).

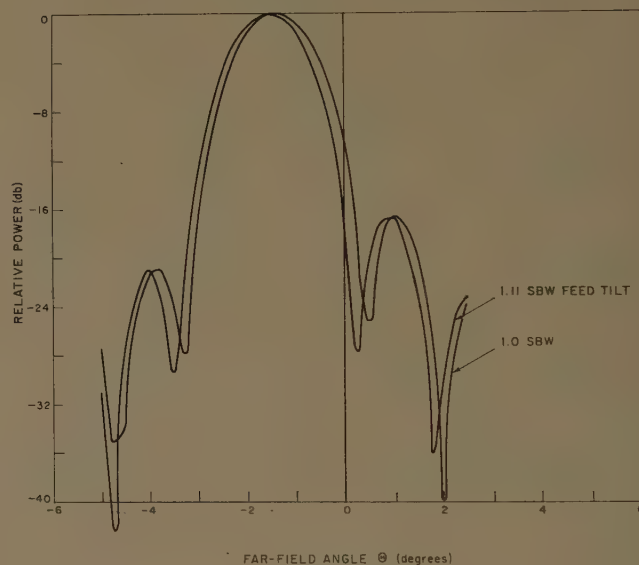


Fig. 8—Current distribution method radiation pattern (normalized, waveguide illumination, H-plane).

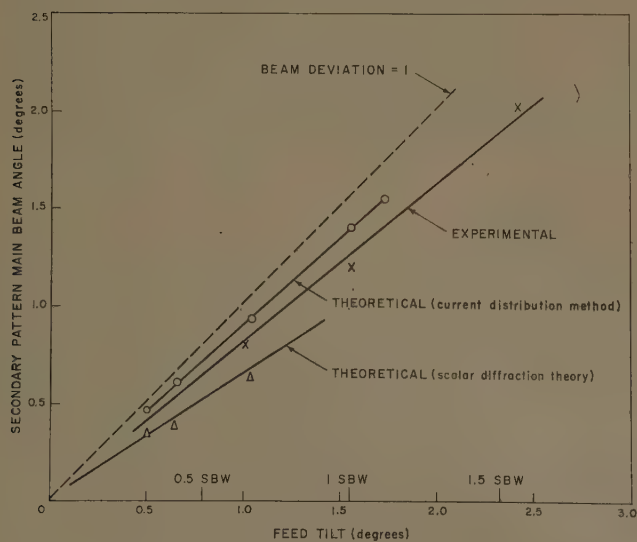


Fig. 9—Secondary beam position vs primary feed tilt (H-plane).

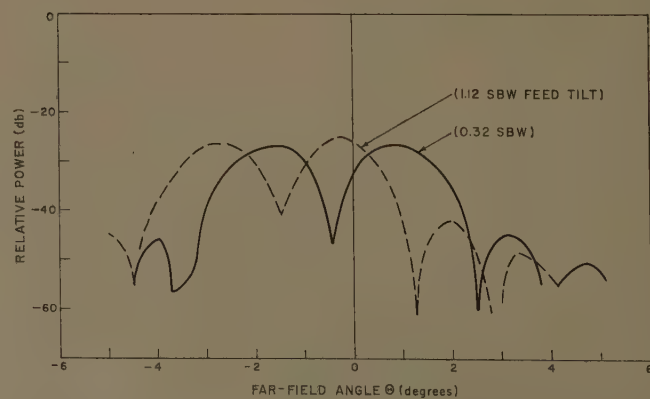


Fig. 10—Cross polarization in H-plane as function of feed tilt.



pattern be circularly symmetric. The directive antenna gain  $G_D$  is given by

$$G_D = \frac{P(\Theta_m)}{P_T/4\pi}, \quad (66)$$

where  $\Theta_m$  is the direction of the main beam and  $P_T$  is the total power intercepted by the reflector.

The variation of  $P_T$  with the offset distance  $m$  is given, approximately, by the variation of  $P_T$  for an infinitesimal dipole. The total power intercepted by the reflector is given by

$$P_T = B'' \int_0^{2\pi} \int_{\pi}^{\theta_1} \cos^2 \theta' d\theta d\phi, \quad (67)$$

where  $\theta'$  is given by (7) and  $\theta_1$  is the extremal value of  $\theta$ . Since the terms in  $(m/f)$  and  $(m/f)^2$  are small compared with unity, then by (7)

$$P_T = 2\pi B'' \int_{\pi}^{\theta_1} \cos^2 \theta \cdot \left[ 1 - \frac{1}{2} \left( \frac{m}{f} \right)^2 (1 - \cos \theta)^2 \right] d\theta. \quad (68)$$

Eq. (68) may be readily integrated, with the result

$$P_T = B''' \left[ 1 - \left( \frac{m}{f} \right)^2 I(\theta_1) \right], \quad (69)$$

where

$$\begin{aligned} I(\theta_1) &= 2[\theta_1 - \pi + \sin \theta_1 \cos \theta_1]^{-1} \\ &\times \left[ \frac{7}{8} (\theta_1 - \pi) - \frac{4}{3} \sin \theta_1 \right. \\ &\times \left. \left( 1 - \frac{21}{32} \cos \theta_1 + \frac{1}{2} \cos^2 \theta_1 - \frac{3}{16} \cos^3 \theta_1 \right) \right]. \end{aligned}$$

The evaluation of (69) for the values given in (64) yields the following approximate form

$$P_T = B''' \left[ 1 - 3.77 \left( \frac{m}{f} \right)^2 \right]. \quad (70)$$

The variation of  $P_T$  with the offset of the primary feed is shown in Fig. 11. For the offsets given in the figure, the variation of power intercepted by the reflector is almost negligible. With the aid of (70), the change in the theoretical value of  $G_D$  with offset is shown in Fig. 12. The loss of gain with offset is less than 0.88 db for offsets less than 2 SBW.

Fig. 13 shows the variation of directive gain with primary offset. It is readily seen that the change beamwidth is proportional to the offset, or

$$\frac{\Delta(BW)}{SBW} = K \frac{\theta_i}{SBW}, \quad (71)$$

where BW is the secondary pattern beamwidth,  $\theta_i$  is the primary offset angle and  $\theta_i$  is the arc tan  $(m/f)$ . The

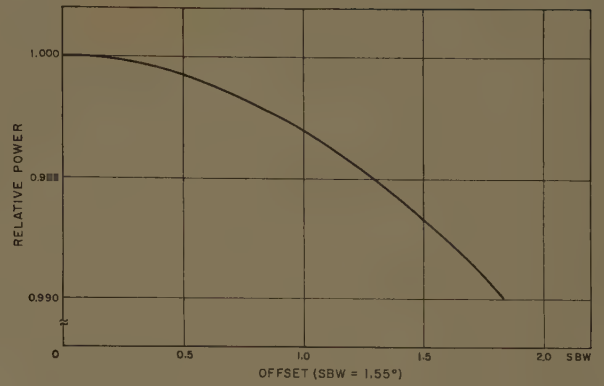


Fig. 11—Variation of primary illumination  $P_T$  with offset angle ( $H$ -plane).

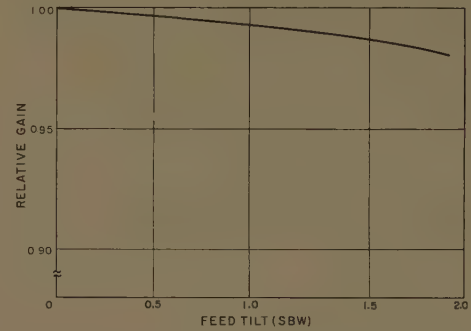


Fig. 12—Theoretical relative gain vs feed tilt in SBW (current distribution method,  $H$ -plane).

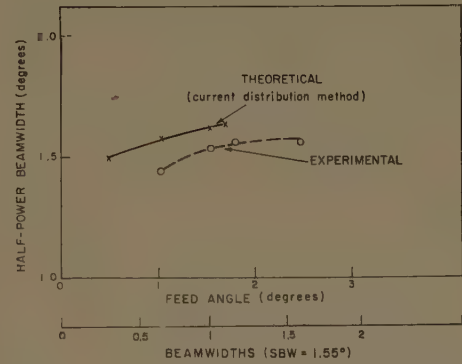


Fig. 13—Half-power beamwidth vs feed angle for single waveguide illumination ( $H$ -plane).

value of  $K$  is approximately 0.12. As expected from "the rule of thumb," the variation of beamwidth is slight.

#### D. Discussion of Scalar Diffraction Results

The major qualitative features as well as some important qualitative results are predicted by the approximate expression given in (37) and (41) and shown graphically in Figs. 14-16. Variation of half-power beamwidth and beam deviation agrees with the rigorous expressions based on the current distribution method. The most favorable agreement takes place at

small values of offset. At higher values of offset (e.g., 0.65 SBW), the side-lobe levels predicted by the scalar diffraction expansion are considerably higher than the rigorous solution. These differences are mainly due to: 1) the truncation of the Bessel function expansion, 2) the retention of only the linear and cubic phase terms, and 3) neglecting the cross-polarization component.

The results from the stationary phase evaluation of the scalar diffraction solution are shown in Figs. 18 and 20. The results indicate a rather low order of approximation, and are best when the nonlinearities are small; however, even at large offsets the stationary phase method is useful for a qualitative description of the phenomenon.

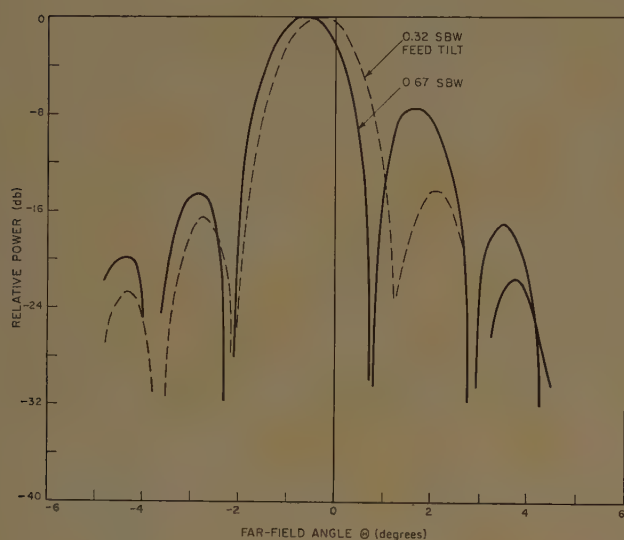


Fig. 14—Radiation pattern scalar diffraction theory (normalized, dipole illumination,  $H$ -plane).

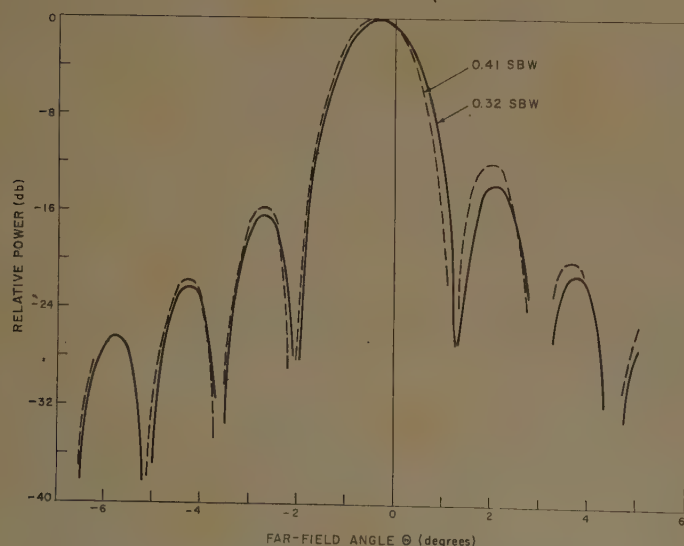


Fig. 15—Radiation pattern scalar diffraction theory (normalized, waveguide illumination,  $H$ -plane).

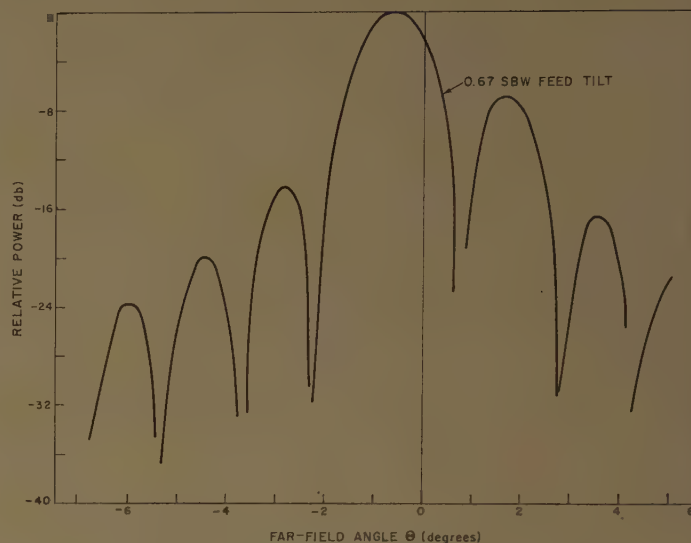


Fig. 16—Radiation pattern scalar diffraction theory (normalized, waveguide illumination,  $H$ -plane).

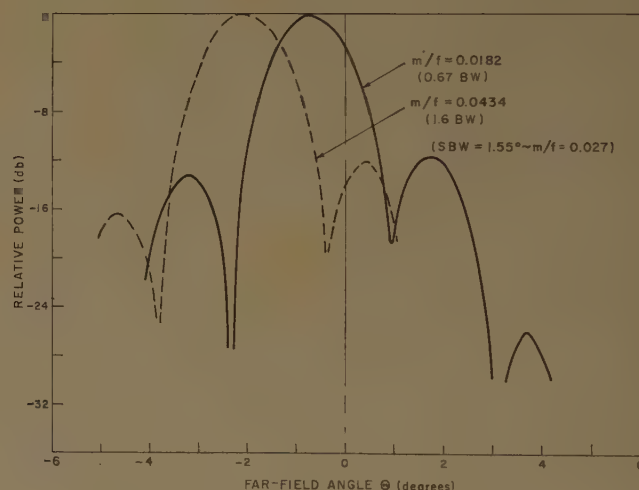


Fig. 17—Experimental reflector patterns ( $H$ -plane).

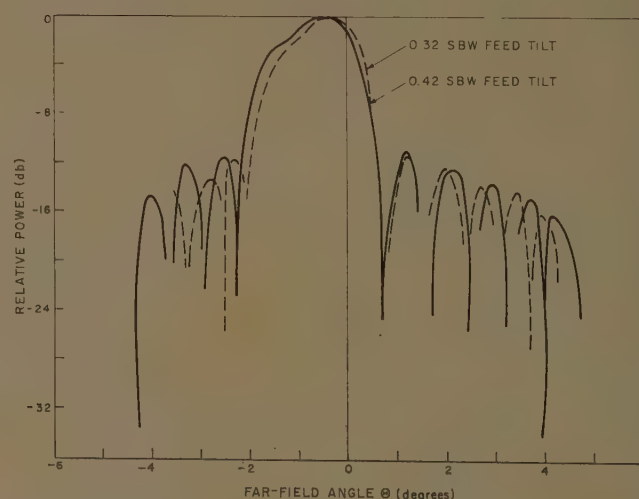


Fig. 18—Radiation pattern scalar diffraction theory (asymptotic expansion,  $H$ -plane).



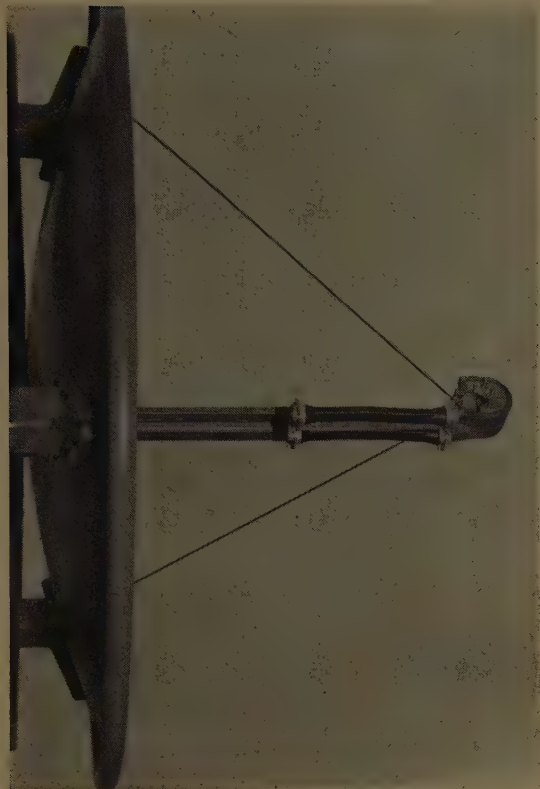


Fig. 19—Experimental waveguide fed paraboloidal reflector.

#### E. Experimental Measurements

The experimental waveguide fed paraboloid reflector antenna is shown in Fig. 19. It is illuminated by a standard X-band waveguide feed. The two waveguide feeds shown in the figure are located symmetrically with respect to the focal axis. The physical dimensions of the system are given by (64). The experimental results are

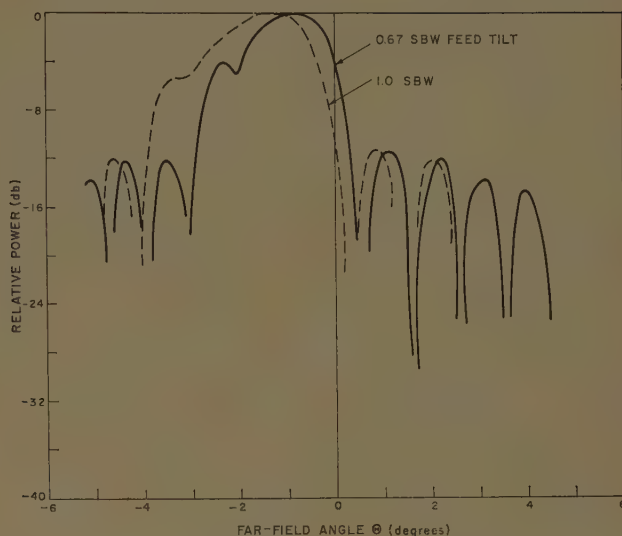


Fig. 20—Radiation pattern scalar diffraction theory (asymptotic expansion,  $H$ -plane).

shown in Figs. 9, 13 and 17. In general, the results predicted by the rigorous solution for side-lobe level are low and those predicted by scalar diffraction theory are high. The beam deviation shown in Fig. 9 is bracketed by the rigorous solution and the approximate scalar diffraction method.

#### ACKNOWLEDGMENT

The author expresses his appreciation to the many members of Lincoln Laboratory for their help and criticism. In particular, he wishes to thank Drs. R. L. Pease and S. J. Rabinowitz for the many illuminating discussions on paraboloidal reflector problems, also W. C. Danforth, Jr., who did the computations, and L. J. Ricardi for suggesting the problem.

# Unequally-Spaced, Broad-Band Antenna Arrays\*

D. D. KING†, R. F. PACKARD†, AND R. K. THOMAS†

**Summary**—Requirements for a broad-band, steerable linear antenna array are given. The limitations due to grating lobes of an equally-spaced array are discussed. Results are given of the study of several different unequally-spaced arrays which have two advantages:

- 1) fewer elements for comparable beamwidth;
- 2) grating lobes and minor lobes replaced by sidelobes of unequal amplitude which are all less than the main beam.

A scheme for controlling the cosine arguments in the radiation pattern formula is given which has resulted in one of the best patterns of this study of unequally-spaced arrays. The universal pattern factor was computed for an array having a set of spacings determined by this scheme. This array is capable of steering a beam  $\pm 90^\circ$  over a 2-to-1 frequency band with no sidelobe above  $-5$  db. It uses 21 elements, compared to 78 for an equally-spaced array of similar beamwidth.

The results obtained indicate that further study of the controlled cosine method and unequal spacing in general should result in better pattern characteristics.

## INTRODUCTION

### Unequal vs Equal Spacing

ANTENNA arrays are usually thought of as having equal spacings between elements. This is not necessary. Unequally-spaced arrays may be devised which have advantages in radiation pattern characteristics and in the number of elements required. Linear arrays with unequal spacing of the elements have been discussed in general terms in a report by Unz.<sup>1</sup> This paper gives the results of computations of the radiation patterns of certain unequally-spaced, symmetric arrays. The suitability of these arrays for broad-band, steerable arrays is demonstrated.

### Universal Pattern Factor

The radiation pattern characteristics of an array of any set of relative spacings may be given as a universal pattern factor. For equal spacings, these are the universal field pattern charts of Kraus<sup>2</sup> where the  $\psi$  scale is folded upon itself about  $\psi = 0.5$  turn. The same field pattern is repeated for values of  $\psi$  greater than one turn. For nonintegral, unequal spacings as considered in this study, the period of the universal pattern factor is large and the pattern cannot be folded upon itself for the range of values given. Kraus' parameter  $\psi$  has been re-

placed by a parameter  $Z$  which has been generalized to incorporate frequency bandwidth and beam steering angle.

Each universal pattern factor presented herein is given for  $Z$  ranging from 0 to 2. No sidelobes occur which are equal to the main lobe. For equally-spaced arrays, grating lobes equal to the main lobe would occur at  $Z = 1$  and  $Z = 2$ . Therefore, unequal spacings are advantageous for arrays whose pattern would include a maximum  $Z$  of 1 or more. By definition,

$$Z = S_{\min}(\sin \theta - \sin \theta_0),$$

where

$S_{\min}$  = the smallest of the set of unequal spacings in wavelengths,

$\theta_0$  = the angle to which the beam is steered,

$\theta$  = the azimuth angle measured from broadside.

The maximum  $Z$  for a given  $S_{\min}$  and  $\theta_0$  will correspond to  $\theta = 90^\circ$  or  $\theta = -90^\circ$ . For a minimum spacing of 1 wavelength, the maximum  $Z$  will be 1 for the beam broadside and 2 for the beam steered  $90^\circ$ . Such an unequally-spaced array would not have the grating lobes of an array with 1 wavelength equal spacings.

### Broad-Band Array

In this paper, the term "broad-band array" means an array of a specific length in meters whose elements are spaced such that the different radiation patterns at different frequencies in a band each have all sidelobes below an arbitrary level. As a practical consideration, it is assumed that the smallest spacing can be no less than 0.5 wavelength at the lowest frequency in the band. Therefore, for a 2-to-1 bandwidth, the smallest spacing will be no less than 1.0 wavelength at the highest frequency. Requiring beam steering of the array in addition would result in a larger maximum  $Z$ . Unequally-spaced arrays with sidelobes down over a large range of  $Z$  will be suitable broad-band arrays. Note that use of the parameter  $Z$  permits bandwidth and beam steering performance to be interchanged readily.

### Goals

The following characteristics were chosen as goals for the investigation reported herein:

- 1) array to have a single narrow main beam steerable up to  $90^\circ$  from broadside;
- 2) array to have all sidelobes below the main beam level;
- 3) array to be broad-band in the sense of retaining the above characteristics over a 2-to-1 frequency band;

\* Manuscript received by the PGAP, December 1, 1959; revised manuscript received, February 4, 1960. The research described in the paper has been sponsored by the Air Force Cambridge Res. Center, Air Res. and Dev. Command, Laurence G. Hanscom Field, Bedford, Mass., under Contract No. AF 19(604)-5234.

† Research Div., Electronic Communications, Inc., Timonium, Md.

<sup>1</sup> H. Unz, "Linear Arrays with Arbitrarily Distributed Elements," Electronics Res. Lab., Univ. of California, Berkeley, Rept. Ser. No. 60, Issue No. 168; November 2, 1956.

<sup>2</sup> J. D. Kraus, "Antennas," McGraw-Hill Book Co., Inc., New York, N. Y., pp. 519-534; 1950.



- 4) array elements to have a minimum spacing of one-half wavelength at the lowest frequency;
- 5) array to have fewer elements than an array of equal aperture having all elements spaced at half-wavelength intervals.

Certain additional characteristics were assumed for simplification of analysis:

- 1) all elements to be isotropic radiators;
- 2) each element to have equal amplitude illumination;
- 3) equal time phase to exist at each element with beam broadside;
- 4) array to be symmetrical about its center.

### METHOD OF ANALYSIS

The effect of unequal spacing in a linear array has been studied by computing the array radiation pattern. Two types of computations were made on an IBM model 650 digital computer:

- 1) universal pattern factor for a set of relative spacings;
- 2) radiation pattern and gain data for a specific element arrangement at a given relative frequency and with the beam steered in a given direction.

Data were computed by means of the formula

$$A = 20 \log_{10} \left[ \frac{c + 2 \sum_{k=1}^n \cos \left( 2\pi Z \frac{d_k}{\lambda} \right)}{2n + c} \right],$$

where

$A$  = the magnitude of the pattern factor in db;

$2n + c$  = the number of elements in the array;

note:  $c = 1$  for an odd number of elements;

$c = 0$  for an even number of elements;

$d_k/\lambda$  = the distance in wavelengths from the center of the array to the  $k$ th element;

$Z$  is as defined above.

Directive gain was computed from relative power pattern data by numerical integration with the interval chosen to be less than half of the half-power beam width.

Various trial sets of spacings, together with results and criteria for choosing sets of spacings, will be described. Five array configurations are illustrated in Fig. 1. This has been drawn at a relative frequency of 1.0; *i.e.*, the minimum spacing is about 1.0 wavelength.

### COMPUTATIONS

#### Logarithmic Spacing Scheme

To obtain the first set of unequal spacings for pattern computation, the elements in each half of an array were spread out in a logarithmic manner. This scheme is illustrated in Fig. 1. Ten elements are placed at equal numerical intervals over one logarithmic cycle. The smallest spacing is next to the center of the array, and

the distance to the  $k$ th element from the center is  $1 - \log(10 - k)$ . These relative spacings are then normalized so that the smallest equals one wavelength.

The first seven distances were used in computing the universal pattern factor of a 15-element array (Fig. 2). In Fig. 2 there are no sidelobes above  $-5$  db for  $Z$  up to 1.82. This means that this array could have its beam steered  $\pm 55^\circ$  and operate over a 2-to-1 band with no sidelobes above  $-5$  db.

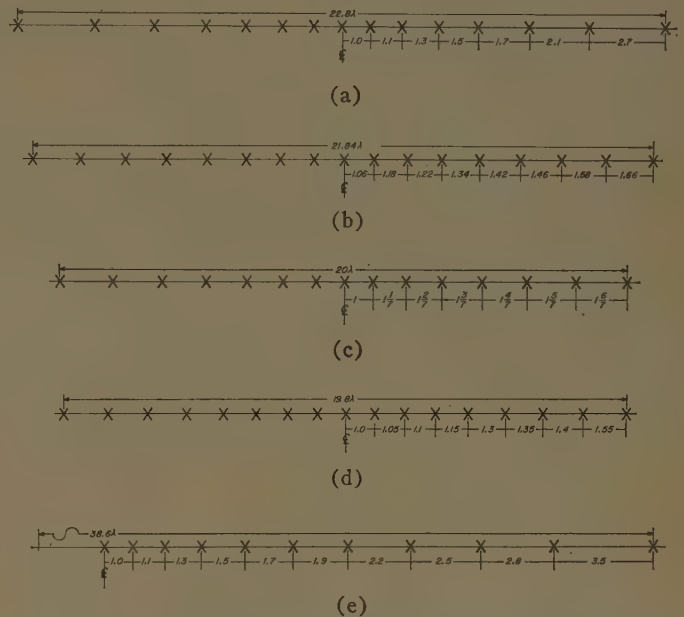


Fig. 1—Array configurations. Spacings drawn to scale with values given in wavelengths at relative frequency of 1.0. (a) Logarithmic spacings. (b) Prime number spacings. (c) Arithmetic progression spacings. (d) Elimination of multiples. (e) Controlled cosines spacings.

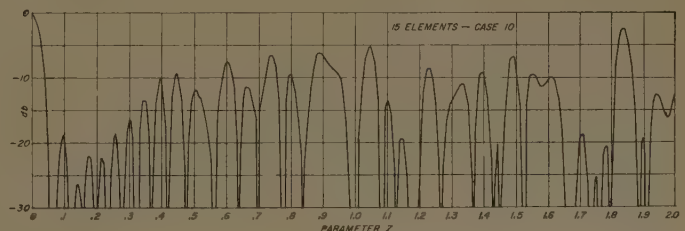


Fig. 2—Universal pattern factor for logarithmic spacing.

#### Nonmonotonic-Increasing Spacing Schemes

One pattern was computed for an array with reversed logarithmic spacings; *i.e.*, the spacings decreased monotonically from the center. The first sidelobe was only 4.8 db down. No universal pattern factor was computed for this case.

Another scheme investigated was one in which the spacings of the logarithmic case were chosen in a random sequence. A pattern factor for one random choice is shown in Fig. 3. The sidelobes appear to have slightly greater magnitude than for monotonic-increasing logarithmic spacing (Fig. 2). The random choice of spacings represented is 2.1, 1.3, 1.5, 1.7, 1.1, 1.0, 2.7.

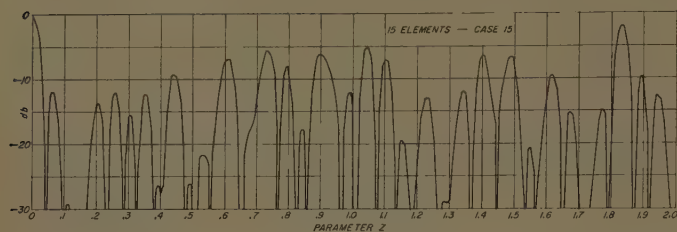


Fig. 3—Universal pattern factor for random logarithmic spacing.

In all other schemes, the spacings increase monotonically from the center. More study is needed to determine if this is a basic requirement.

#### Prime Number Spacing Scheme

Another attempt to choose spacings which were not multiples of some common factor was to derive a set of spacings from a sequence of prime numbers. The procedure is illustrated by the data in Table I. The resultant array factor (Fig. 4) has low sidelobes for  $Z$  less than 0.6 but is not outstanding beyond that. Note that the elements do not spread out as rapidly as in the logarithmic scheme. This prime number array has 17 elements for a total aperture of 21.84 wavelengths, whereas the logarithmic array has 15 elements for a total aperture of 22.88 wavelengths.

#### Arithmetic Progression Spacing Scheme

A trial set of distances was derived from spacings which formed an arithmetic progression. An initial spacing of 1 and a common difference of  $1/7$  was used to obtain a 15-element array. A plot of data computed for this case is shown in Fig. 5. Except for one lobe which reaches  $-5.8$  db at  $Z=0.61$ , all sidelobes are down 7 db or more.

#### Scheme for Elimination of Multiples

Distances were chosen for the computation of one pattern factor with the idea of eliminating the grating lobe by permitting no distance and no spacing between any two elements to be a multiple of one-half. The distances selected and the computed pattern factor are shown in Figs. 1 and 6. All lobes of Fig. 6 are below  $-5.8$  db out to  $Z=1.9$ . This means that this array could have its beam steered  $\pm 64^\circ$  and operate over a 2-to-1 band with no sidelobe above  $-5.8$  db.

This scheme resulted in the lowest sidelobes for low values of  $Z$ . In Fig. 6, all sidelobes are  $-17.5$  db or below for  $Z$  up to 0.58. Now, the pattern of an array with the beam broadside and at the one frequency at which the smallest spacing is 0.5 wavelength is represented by the universal pattern factor from  $Z=0$  to  $Z=0.5$ . This means that this array could be used at one frequency and without beam steering but with sidelobes 4.5 db below those of an equally-spaced array. This is achieved with equal amplitude illumination to each element, permitting maximum radiated power in very high-power

TABLE I  
PRIME NUMBER SPACING SCHEME

Element	Prime	Prime Doubled	Derived Spacing	Distance
1	53	106	1.06	1.06
2	59	118	1.18	2.24
3	61	122	1.22	3.46
4	67	134	1.34	4.80
5	71	142	1.42	6.22
6	73	146	1.46	7.68
7	79	158	1.58	9.26
8	83	166	1.66	10.92

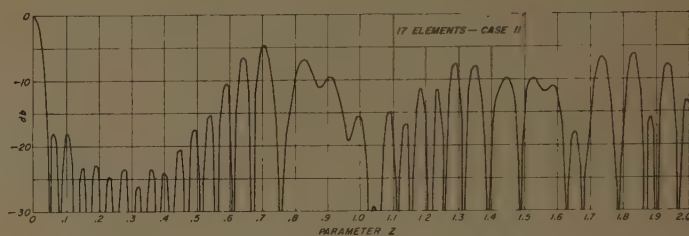


Fig. 4—Universal pattern factor for prime number spacing.

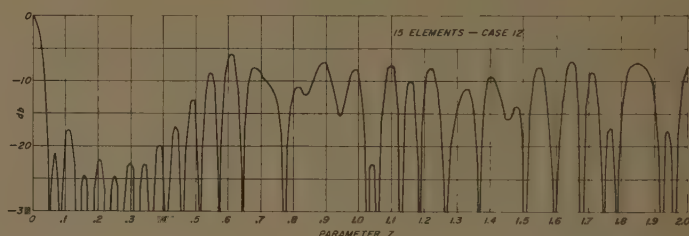


Fig. 5—Universal pattern factor for arithmetic progression spacing

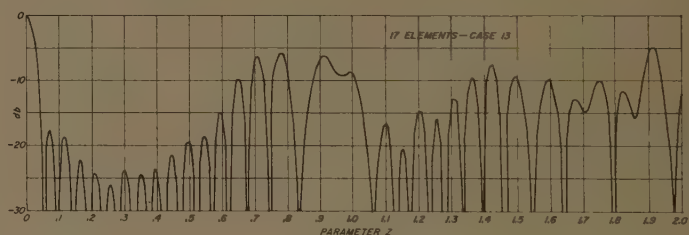


Fig. 6—Universal pattern factor for elimination of multiples.

arrays. Furthermore, only 17 elements are used instead of the 21 required for an equally-spaced array of equivalent aperture.

It should be possible to minimize sidelobes further over a restricted range of  $Z$  from 0 to 0.5. This method offers an alternative to that of tapering the amplitude illumination of an equally-spaced array.

#### Scheme for Control of Cosine Arguments

The core of the problem considered here is to minimize the sidelobes of a pattern factor for  $Z$  up to 2. A direct approach is to examine the pattern factor formula



$$A = 20 \log_{10} \left[ \frac{c + 2 \sum_{k=1}^n \cos \left( 2\pi Z \frac{d_k}{\lambda} \right)}{2n + c} \right]$$

The magnitude of  $A$  depends directly upon the sum of  $n$  cosine terms having arguments  $2\pi Z(d_k/\lambda)$ . Since the cosine function is periodic over the interval  $2\pi$ ,  $Z(d_k/\lambda)$  represents the number of periods, and the integral part of  $Z(d_k/\lambda)$  may be dropped. Now, the value of the cosine function varies from 1 to  $-1$  for arguments ranging over one period. Therefore, the  $n$  cosine terms will tend to have an average sum of zero if the fractional parts of  $Z(d_k/\lambda)$  are evenly spread over the range 0 to 1. A set of  $n$  distances ( $d_k/\lambda$ ) can be chosen easily so that this is true for one value of  $Z$ . The problem is to pick a set of distances such that for all  $Z$  in the range 0.05 to 2, the fractional parts of  $Z(d_k/\lambda)$  will spread evenly over the range 0 to 1. Then the sidelobes for all  $Z$  in the range 0.05 to 2 will be minimized.

A set of distances was devised that tended to have the above property. The data are given in Table II. The total aperture is much greater in this case, since the spacings chosen increase rapidly. Only 21 elements are used in an array 38.6 to 19.3 wavelengths long over a 2-to-1 band. It is not known if this rapid increase in spacing is necessary for the above criterion to be met.

The universal pattern factor for this case is shown in Fig. 7. Data for an array of equal spacings are given in Table III for comparison. An equally-spaced array has grating lobes, of amplitude equal to that of the main beam, at  $Z=1$  and  $Z=2$ . All other lobes are below  $-13$  db, however, making the equally-spaced array suited for applications requiring low sidelobes over narrow bands of operation. The controlled cosines method has successfully eliminated the 0-db-level grating lobes for  $Z$  up to 2, but at the expense of other sidelobes rising above  $-13$  db. The controlled-cosines array can have its beam steered  $\pm 90^\circ$  and operate over a 2-to-1 band with no sidelobe above  $-5$  db. The equally-spaced array cannot operate over a 2-to-1 band without having a 0-db-level grating lobe even if the beam is not steered from broadside at all.

### Beamwidth and Gain

The beamwidth of an unequally-spaced array is nearly the same as for a continuous, uniformly illuminated array of the same length. Beamwidths for both vary inversely as the aperture in wavelengths. A 22.9-wavelength logarithmic array has a broadside beamwidth of  $2.3^\circ$  vs  $2.2^\circ$  for a uniform array. A 38.6-wavelength controlled cosines array has a beamwidth of  $1.5^\circ$  vs  $1.3^\circ$  for a uniform array. The beamwidth increases as the beam is steered off broadside, reaching  $18.5^\circ$  at endfire for the controlled cosines case compared to  $17.4^\circ$  for uniform spacing.

The directive gain was computed for a few specific

TABLE II  
EFFECT OF SPACINGS ON COSINE ARGUMENTS

Element Number	Spacing	Distance ( $Zd_k$ for $Z=1$ )	$Z=.25$	$Zd_k$ $Z=.5$	$Z=2$
1	1.0	1.0	0.25	0.5	2.0
2	1.1	2.1	0.525	1.05	4.2
3	1.3	3.4	0.85	1.7	6.8
4	1.5	4.9	1.225	2.45	9.8
5	1.7	6.6	1.65	3.3	13.2
6	1.9	8.5	2.125	4.25	17.0
7	2.2	10.7	2.675	5.35	21.4
8	2.5	13.2	3.3	6.6	26.4
9	2.6	15.8	3.95	7.9	31.6
10	3.5	19.3	4.825	9.65	38.6

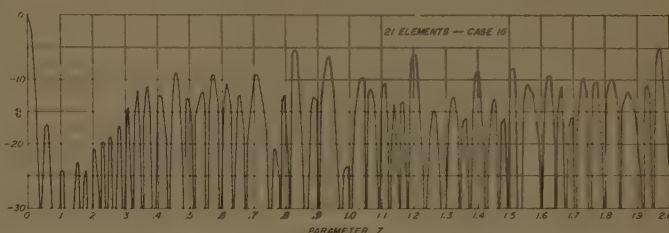


Fig. 7—Universal pattern factor for controlled cosines.

TABLE III  
COMPARISON OF ARRAY FACTORS OF TWO ARRAYS OF EQUAL APERTURE

	Array with Spacing Chosen by Controlled Cosines Method	Array with Equal Spacing
Spacing	Smallest spacing equals $\lambda/2$ at the lowest frequency.	All spacings equal $\lambda/2$ at the lowest frequency.
Total aperture	19.3 $\lambda$	19.5 $\lambda$
Number of elements	21	40
Bandwidth	Bandwidth Sacrificed for Low Sidelobes	
Beam steering range	1.09 to 1	1.3 to 1
Maximum side-lobe level	$\pm 30^\circ$	$\pm 30^\circ$
	- 9 db	-13 db
Bandwidth	Sidelobe Level Sacrificed for Bandwidth	
Beam steering range	2 to 1	2 to 1
Maximum side-lobe level	$\pm 90^\circ$	two 0-db grating lobes when steered $\pm 90^\circ$
	- 5 db	one 0-db grating lobe with beam broadside

cases. The calculated values are approximately equal to the theoretical gain which is  $2n+C$ , the number of elements, for an array of equal amplitude illumination. The directive gain of a 19-element array was calculated by pattern integration to be 18.2 (12.6 db). If the same aperture were used for an equally-spaced array with half-wavelength spacing, 45 elements would be accommodated with consequent gain of 45 (16.5 db). Reduced gain must be considered against the advantage of achieving a narrow beam over a broad band with a reduced number of elements.

## CONCLUSIONS

Preliminary calculations have been made for several arrays of unequally-spaced elements. Universal pattern factors have been computed and interpreted for broadside, steerable arrays. One of the best schemes devised for the spacing of elements resulted in an array capable of operation over a 2-to-1 band, beam steerable to  $\pm 90^\circ$  with sidelobes  $-5$  db or below.

In very high-power applications of single-frequency,

broadside arrays, use of unequal spacings is a possible method of reducing sidelobes which is more efficient than tapering the amplitude illumination.

Various points for further investigation have been indicated. In particular, derivation of other sets of distances by the controlled cosines method promises pattern improvement. The data obtained demonstrate the possible advantages of using unequally-spaced arrays. However, the potentialities of unequal spacing have not been explored in detail.

## Resonant Slots with Independent Control of Amplitude and Phase\*

BERNARD J. MAXUM†

**Summary**—The design of slot arrays requiring nonuniform phase distributions, such as those having shaped beam radiation patterns, are facilitated by the development of slots having independent amplitude and phase control. A "complex" slot (which is inclined and displaced) on the broad wall of a rectangular waveguide makes it possible to control the coupling characteristics over a range in phase from zero to  $2\pi$  and over a range in magnitude from zero to unity. The "voltage" across the slot as a function of its orientation is found and is related to the coupling parameters used in common array design. An experimental procedure for independently verifying the amplitude and phase characteristics is described. A typical complex slot array design is made and radiation patterns are included demonstrating the accuracy and usefulness of the design procedure.

## INTRODUCTION

A NARROW half-wave slot cut in a waveguide will, in general, interrupt the current sheet which exists on the inside surface of the waveguide. This interruption excites a time-varying electric field across the slot and a corresponding magnetic field along the slot. The result is a half-wave magnetic dipole. Energy is radiated from this resonant slot with an amplitude and phase partially dependent upon the component of the current sheet which would exist perpendicular to the slot at its center if the slot were not there.

It has been common practice in the past to orient the slots in such a manner as to interrupt only those currents which are either in-phase or in phase-quadrature to the wave in the guide. As a consequence of this practice, aperture distributions of slot arrays have been, for

the most part, limited to tapered amplitude distribution of equiphase slots.

The general slot under consideration in this paper, however, is not oriented in such a specific manner. Since it is inclined at an angle from the axis and displaced from the center of the waveguide, any phase and amplitude can be obtained. Included in this paper are the phase and amplitude characteristics of an inclined-displaced slot (hereinafter referred to as a complex slot). Also included is a design for an array of slots giving a  $\csc^{5/2}\phi \cos^{1/2}$  radiation pattern.

## DISCUSSION OF THE THEORY

The boundary value problem for the fields in the vicinity of a waveguide slot was solved by Stevenson<sup>1</sup> and Watson.<sup>2</sup> They determined the voltage  $V$  across the center of a resonant broadwall slot in terms of the angle of inclination  $\theta$  and the displacement  $x$ . When the excitation is assumed small, the voltage transformation ratio  $V/A$  is given by<sup>3</sup>

$$\frac{V}{A} = \left| \frac{V}{A} \right| e^{j\alpha} = \frac{8.10}{a} \left\{ \frac{\cos \left[ \frac{\pi}{2} \cos(i - \theta) \right]}{\sin(i - \theta)} e^{j\pi x/a} + \frac{\cos \left[ \frac{\pi}{2} \cos(i + \theta) \right]}{\sin(i + \theta)} e^{-j\pi x/a} \right\} \quad (1)$$

\* Manuscript received by the PGAP, May 4, 1959; revised manuscript received, February 10, 1960. This paper was presented at the 1958 URSI Spring Meeting, Washington, D. C., April 24-26, 1958; also published at Hughes Aircraft Co., Culver City, Calif., Tech. Memo. No. 573, December, 1957.

† Dept. of Elec. Engrg., University of California, Berkeley, Calif. Formerly at Hughes Aircraft Co., Culver City, Calif.

<sup>1</sup> A. F. Stevenson, "Theory of slots in rectangular waveguides," *J. Appl. Phys.*, vol. 19, pp. 24-38; January, 1948.

<sup>2</sup> W. H. Watson, "The Physical Principles of Waveguide Transmission and Antenna Systems," Clarendon Press, Oxford, Eng., pp. 96-98, 192-199; 1947.

<sup>3</sup> Stevenson, *op. cit.*, (27), (32), and (38); Watson, *op. cit.*, (66.1), (66.3), (64.2), and (66.1).



where

- $A$  = the amplitude of the dominant mode in the waveguide,
- $a$  = the inside broad dimension of the waveguide,
- $x$  = the displacement of the slot,
- $\theta$  = the inclination of the slot,

and the angle  $i$  is given by

$$i = \sin^{-1} \frac{\lambda}{2a} = \cos^{-1} \frac{\lambda}{\lambda_0} = \tan^{-1} \frac{\lambda}{2g} \quad (2)$$

The slot geometry is shown in Fig. 1.

In the derivation of 1), certain simplifying assumptions are necessary: 1) the walls of the waveguide are perfectly conducting and of negligible thickness; 2) the slot width is small compared with its length; 3) only the  $TE_{10}$  mode propagates. These assumptions are, for the most part, not fully realized in practice, and thus small deviations from the theoretical expressions are to be expected. The amplitude and phase characteristics of (1) are plotted in Fig. 2 as a function of the slot orientation with  $a = 0.9$  inch.

Usually, array design is based on slot coupling coefficients which relate the power radiated to the power in the guide. The coupling coefficient  $\gamma$  is approximately related to the voltage ratio  $V/A$  by

$$\left| \frac{V}{A} \right| \cong \sqrt{12.74 \frac{k k_0 b}{a}} \gamma \quad (3)$$

where  $k = 2\pi/\lambda$ ,  $k_0 = 2\pi/\lambda_0$  and  $a$  and  $b$  are the inside dimensions of the waveguide. [Eq. (3) is derived in Appendix I]. Approximations leading to (3) have been made, based upon the excitation being small. These approximations were found to result in an error of five per cent where  $\gamma = 0.1$ .

#### EXPERIMENTAL VERIFICATION

In the transmission line formulation, the general inclined-displaced slot may be represented by an equivalent  $T$  or  $\pi$  network located in the plane of the slot. Straightforward methods could then be used to measure the impedance parameters of this network. However, an alternate scheme, utilizing the transformation properties of a discontinuity in a waveguide, was developed. This technique allowed verification of the theoretical relations without the determination of the equivalent network representation.

The transformation of a wave as it passes a discontinuity, such as a slot in a waveguide, is given by Watson<sup>4</sup>

$$\Gamma' = \frac{ge^{i\delta} + (1 - 2g)\Gamma}{1 - ge^{i\delta}\Gamma} \quad (4)$$

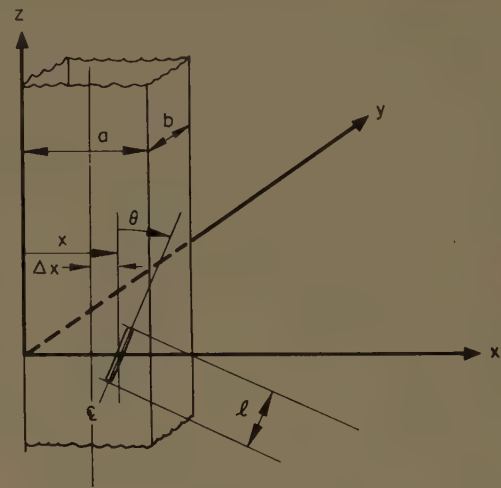


Fig. 1—The slot geometry.

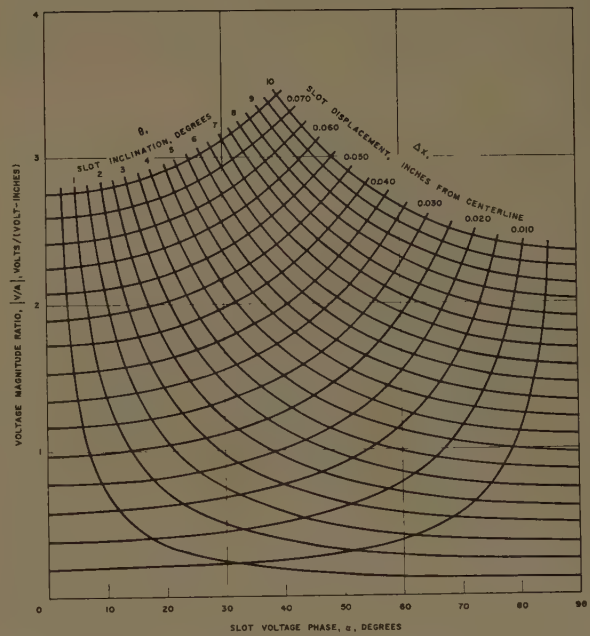


Fig. 2—Complex slot design characteristics.

where  $\Gamma'$  is the reflection coefficient just before the plane of the slot and  $\Gamma$  is the reflection coefficient just beyond the slot. The quantity  $g$ , discussed in Appendix I, is a measure of the magnitude of the disturbance and is real for resonant slots. The quantity  $\delta$  is a measure of the phase and is related to the phase of the radiated wave discussed in a subsequent part of this section [see (9)].

Following Watson's procedure for measuring phase, a calibrated short was placed beyond the slot. It was possible to find a position of this shorting termination such that the slot would not radiate. With the short at this position, the reflection coefficient is the same on either side of the slot. The reflection coefficients  $\Gamma$  and  $\Gamma'$  were set equal and (4) was solved. This equation became quadratic in  $\Gamma$  and was found to have a double root equal to  $e^{i\delta}$  for  $g \neq 0$ .

<sup>4</sup> Watson, *op. cit.*, p. 13, (16.6).

The admittance in terms of the reflection coefficient was taken from standard transmission line equations,

$$Y = \frac{\Gamma - 1}{\Gamma + 1}, \quad (5)$$

with  $\Gamma = e^{j\delta} = \cos \delta + j \sin \delta$ , (5) reduced to

$$Y = j \tan \frac{\delta}{2}. \quad (6)$$

The admittance of a shorted termination, also taken from standard transmission line equations, is given by

$$Y = j \cot \frac{\pi z}{\lambda_g} \quad (7)$$

where  $z$  is the distance from the short to the plane of the slot. Eqs. (6) and (7) were equated and  $\delta$  was extracted, giving

$$\delta = \pi - \frac{2\pi z}{\lambda_g}. \quad (8)$$

The quantity  $\delta$  is related to the slot voltage phase  $\alpha$  by Watson<sup>5</sup> as

$$\delta = 2\alpha - \pi. \quad (9)$$

The measured values of  $\delta$  from (8) are shown in Fig. 3 along with theoretical values calculated from (9) and (1).

To verify experimentally the magnitude relations, several methods were tried. Watson suggested finding  $g$  in (4) by measuring  $\Gamma'$  with a matched termination ( $\Gamma = 0$ ). Since  $\delta$  was previously determined independently and  $\Gamma'$  was measured,  $g$  was readily found from  $g = \Gamma'/e^{j\delta}$ . However, this method did not prove to be practical, since the voltage standing-wave ratio was too small to be measured accurately.

The same method as used with series and shunt slots was applied. First the position of the shorted termination, at which the slot did not radiate, was found. Next, the short was moved  $\lambda_g/4$  from that position. The input VSWR was measured, and  $g$  was calculated from the following relation:

$$g = \frac{1}{2r + 1} \quad (10)$$

where  $r$  is the VSWR. (This relation between the transformation magnitude and the measured VSWR is derived in Appendix II.) The resulting experimental value of  $g$  was compared with the theoretical value from (15) in Appendix I. This comparison is plotted in Fig. 4.

The resonant slot length was determined experimentally. This was done in the same conventional manner as if the slots were pure series or pure shunt. With the short in such a position as to render the slot

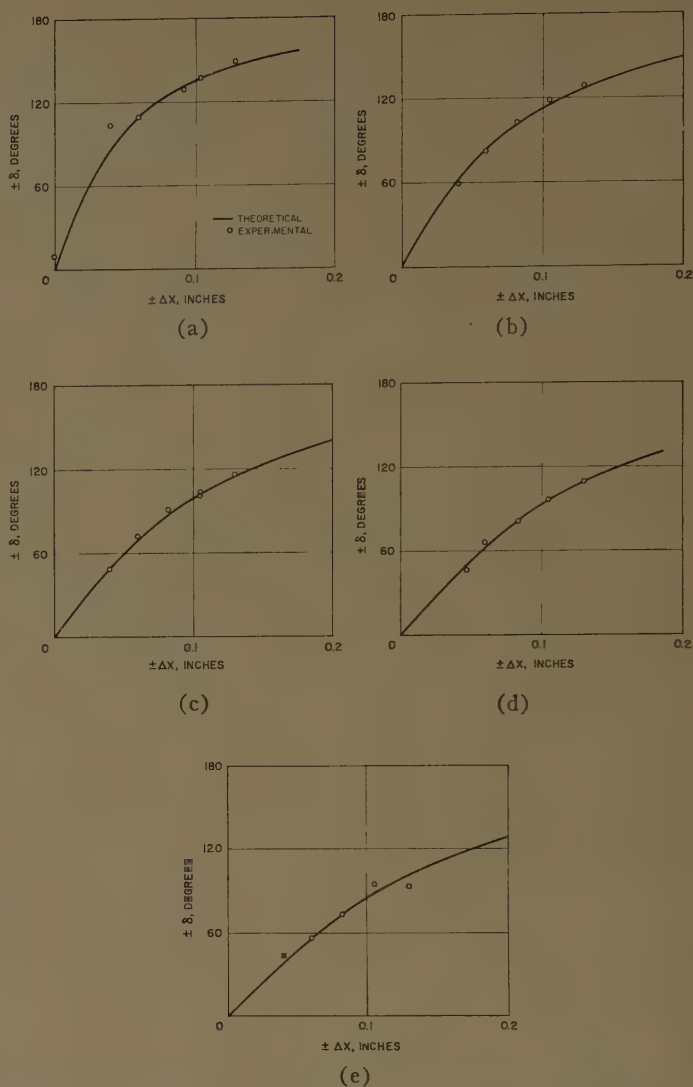


Fig. 3—Comparison of theoretical and experimental phase characteristics for complex slots: —, theoretical; O, experimental. (a)  $|\theta| = 7^\circ$ . (b)  $|\theta| = 11^\circ$ . (c)  $|\theta| = 14^\circ$ . (d)  $|\theta| = 16^\circ$ . (e)  $|\theta| = 18^\circ$ .

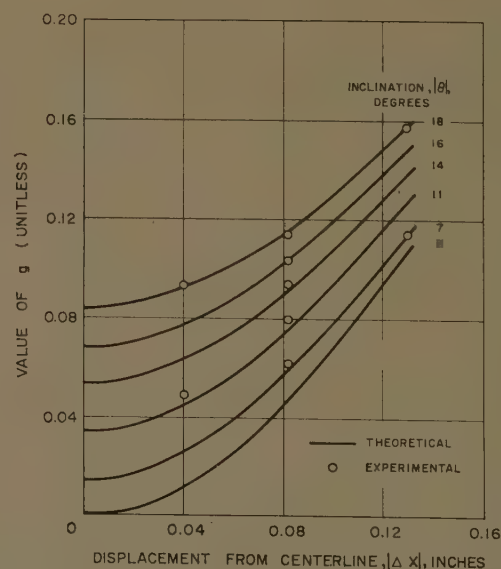


Fig. 4—Complex slot transformation magnitude characteristics.

<sup>5</sup> *Ibid.*, pp. 96-97, (66.1) and (66.8).



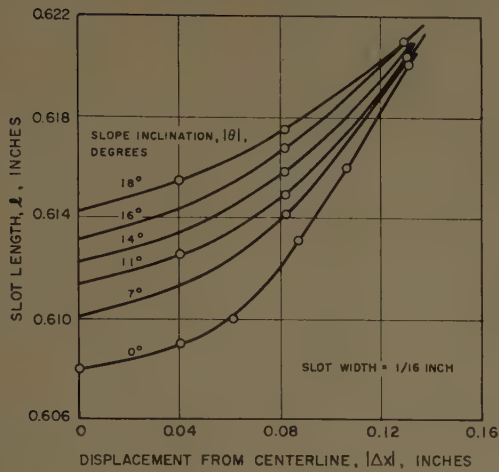


Fig. 5—Resonant slot length for complex slots.

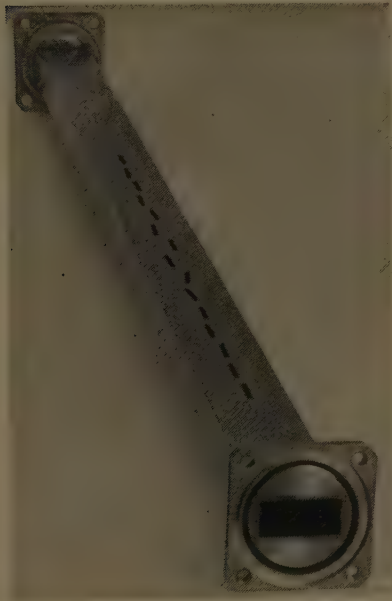


Fig. 6—A 15-element complex slot array in a  $1 \times \frac{1}{2}$ -inch waveguide. This array was constructed according to the tolerances shown below.

For $\Delta x \leq 0.009$ inch	$\pm 0.002$ inch
$0.010 \leq \Delta x \leq 0.019$	$\pm 0.003$ inch
$0.020 \leq \Delta x \leq 0.034$	$\pm 0.004$ inch
$0.035 \leq \Delta x$	$\pm 0.005$ inch
$\theta \leq 0^\circ 30'$	$\pm 2'$
$0^\circ 30' < \theta \leq 2^\circ$	$\pm 10'$
$2^\circ < \theta$	$\pm 20'$
all $l$	$\pm 0.005$ inch.

ineffective as a radiator, a null position was found on a slotted line in front of the slot. The short when moved  $\lambda_0/4$  would cause this null to move  $\lambda_0/4$  if the slot were resonant. These experimental results are plotted in Fig. 5.

The term "resonant" may seem to be inconsistent with previous usage. However, a more general criterion for resonance of a slot is not that one sees a pure resistance or pure conductance at the plane of the slot, but rather whether or not the transformation of the wave past the slot

exhibits a change in phase. The former criterion is consistent with the latter only in the case of pure series and pure shunt slots. The latter applies to complex slots in general, series and shunt slots being special cases.

The theoretical and experimental values of magnitude and phase checked so well that it was decided to design the first array from the theoretical relations.

#### SLOT ARRAY DESIGN PROCEDURE

Further verification of the theory was obtained by designing and testing a shaped-beam array of complex slots (see Fig. 6).

The aperture excitation of a discrete array of  $N$  radiating elements is given by

$$A_n = a_n e^{j\alpha_n} \quad (11)$$

where  $a_n$  is real and positive and  $n=0, 1, 2, \dots, N-1$ . The coupling coefficients required to give the distribution of (11) may be determined in terms of  $a_n$  and the power into the matched load  $P_L$  by<sup>6</sup>

$$\gamma_n = \frac{a_n^2(1 - P_L)}{K_{N-1} - K_n(1 - P_L)} \quad (12)$$

where

$$K_m = \sum_{n=0}^m a_n^2.$$

Previous work<sup>7</sup> had made available the aperture distribution for a 15-element array having  $\csc^{5/2}\phi \cos^{1/2}\phi$  radiation pattern. This information was used as the present design objective. Table I gives the aperture slot excitations  $a_n$  and  $\alpha_n$ <sup>7</sup> for this array.

The coupling coefficients  $\gamma_n$  were calculated from (12) for standard X-band waveguide ( $a=0.9$  inch,  $b=0.4$  inch),  $f=9375$  mc and with  $P_L$  set at 66 per cent. This large value of  $P_L$  was necessary in order to keep  $\gamma_n < 0.1$ . A longer array with a greater number of slots would, of course, enable one to reduce  $P_L$ . For example, for  $P_L=2$  per cent, 50 to 60 slots are required. The voltage ratios  $|V/A|_n$  were calculated from (3) and the inclination  $\theta_n$  and displacement  $\Delta x_n$  were read from Fig. 2, where

$$\Delta x_n = \frac{a}{2} - x_n. \quad (13)$$

The slot length was then taken from Fig. 5, for a width of  $1/16$  inch.

The radiation pattern of this array is shown in Fig. 7 superimposed on the computed pattern. Discrepancies

<sup>6</sup> M. G. Chernin and R. W. Bickmore, "A design method for very long linear arrays," 1956 IRE CONVENTION RECORD, pt. 1, pp. 225-229; and V. T. Norwood, "Note on a method for calculating coupling coefficients of elements in antenna arrays," IRE TRANS. ON ANTENNAS AND PROPAGATION, vol. AP-3, pp. 213-214; October, 1955.

<sup>7</sup> "Research Report on Development of AS-(x A-85)/APQ Flat Slab K-Band Bombing Radar Antenna," Hughes Aircraft Co., Culver City, Calif., Rept. No. 437-01-F, p. 40.

TABLE I  
TABULATION OF THE SLOT ARRAY DESIGN

$n$	$a_n$	$\alpha_n$ (degrees)	$\gamma_n$	$ V/A _n$	$\theta_n$ (degrees)	$\Delta x_n$ (inches)	$l_n$ (inches)
0	3.351	+ 4.00	0.00501	0.7104	+0.20	+0.018	0.608
1	2.163	-13.62	0.00209	0.4586	+0.38	-0.010	0.608
2	2.819	+44.42	0.00357	0.5994	+1.40	+0.009	0.609
3	7.233	+ 1.04	0.02406	1.5559	-0.12	-0.040	0.609
4	0.655	- 0.77	0.00020	0.1419	-0.008	+0.004	0.608
5	7.335	+43.98	0.02538	1.5980	-4.50	-0.029	0.610
6	10.285	+43.12	0.05252	2.2988	+6.60	+0.044	0.611
7	13.468	+12.50	0.09880	3.1530	-3.05	-0.084	0.614
8	11.666	+ 3.01	0.08021	2.8409	+0.62	+0.076	0.612
9	9.679	-13.09	0.05843	2.4247	+2.33	-0.061	0.611
10	7.655	-12.73	0.03794	1.9538	-1.77	+0.049	0.610
11	5.632	-17.57	0.02096	1.4522	+1.78	-0.035	0.609
12	4.198	-26.99	0.01179	1.0892	-1.83	+0.023	0.609
13	2.977	-24.44	0.00596	0.7744	+1.06	-0.015	0.608
14	1.000	0.00	0.00067	0.2596	0.00	+0.007	0.608

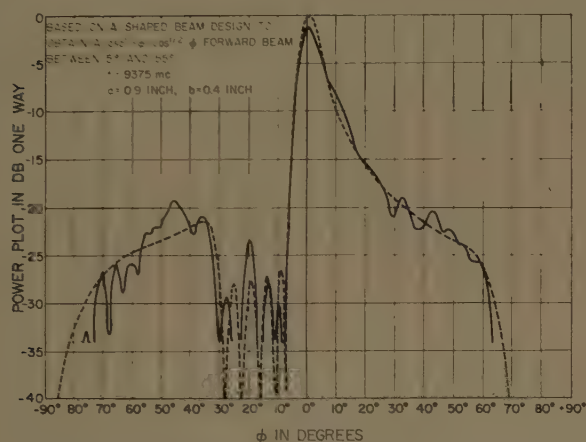


Fig. 7—Theoretical and experimental radiation patterns from a 15-element array of resonant complex slots: —, experimental; ---- theoretical.

are seen to be within  $\pm 2$  db over the region of major interest. Comparison of the two curves remained within  $\pm 3$  db over a 4.3 per cent frequency band centered at 9375 mc. The power into the load at 9375 mc was 66.3 per cent as compared with the design value of 66 per cent. The input VSWR at 9375 mc was 1.4 and remained below 1.5 over a  $\pm 4$  per cent band.

#### CONCLUSIONS

The expressions of Watson and Stevenson for complex slot characteristics have been reduced to a useful form by the assumption that the excitation is small. This assumption has resulted in relatively simple design equations which find direct application in the development of a very versatile radiating element. Although values for the relation between the slot voltage and its orientation are in error due to the small excitation assumption, the same assumption causes approximately equal but opposite error in the predicted relation between the slot voltage and the coupling coefficient. The error between the orientation and coupling is, therefore, very small.

This balancing of errors has been investigated only for coupling values of 0.1 and less. The possibility exists

that this effect might occur for larger coupling values as well. If this were the case, the range of validity of the design equation would be considerably extended.

Since Watson's method of measuring the magnitude characteristics was found impractical, an alternate experimental technique was used. A surprisingly simple relation was derived which related the measured variables with the magnitude characteristics. Since the theoretical values were so well verified by the experimental data, the shaped-beam array was designed theoretically and proved successful.

#### APPENDIX I

##### DERIVATION OF THE RELATION BETWEEN THE SLOT VOLTAGE AND THE COUPLING COEFFICIENT

Watson<sup>8</sup> introduces a quantity  $g$  which is related to the power radiated. The fraction of the power absorbed in the load (*i.e.*, that power radiated from the slot) when the line is terminated in a match is

$$1 - \frac{|1 - g|^2}{1 - |g|^2} \quad (14)$$

He writes this quantity  $g$  as<sup>9</sup>

$$g = \frac{-L|\zeta|^2}{K} \quad (15)$$

where  $L = a/(\pi b k k_0)$  and  $\zeta$  is given by

$$\zeta = K \frac{V}{A} \quad (16)$$

and  $K$  approaches a negative real constant  $-0.338$  for resonant slots with small excitation.

Squaring the absolute value of (16) and combining with (15) gives

$$\left| \frac{V}{A} \right|^2 = \frac{g}{LK^*} \quad (17)$$

<sup>8</sup> Watson, *op. cit.*, p. 14.

<sup>9</sup> *Ibid.*, p. 96, (66.7).



When the quantity  $\gamma^6$  is defined as the ratio of the radiated power  $P_r$  to the power beyond the slot  $P_0$ , the fraction of the power radiated becomes  $P_r/(P_r + P_0) = P_r/P_i$ , and from (14) may be written

$$1 - \frac{|1 - g|^2}{1 - |g|^2} = \frac{P_r}{P_r + P_0} = \frac{\gamma}{\gamma + 1}. \quad (18)$$

For small excitation,  $\gamma$  and  $g$  become small compared to unity. Eq. (18) under this condition reduces to

$$2g = \gamma \quad (19)$$

and from (17), there results for a resonant slot with small excitation

$$\left| \frac{V}{A} \right|^2 = -\frac{\gamma}{2LK}. \quad (20)$$

Therefore, the absolute value of the relative voltage is

$$\left| \frac{V}{A} \right| = \sqrt{-\frac{\gamma}{2LK}}. \quad (21)$$

Since  $K$  is real and negative, (21) is real and (3) results

$$\left| \frac{V}{A} \right| = \sqrt{12.74 \frac{kk_0 b}{a} \gamma}.$$

## APPENDIX II

### DERIVATION OF EQUATION (10)

When (4) is solved for  $g$ ,

$$g = \frac{\Gamma' - \Gamma}{\Gamma\Gamma'e^{-j\delta} - 2\Gamma + e^{j\delta}}. \quad (22)$$

With the short at a position  $\lambda_g/4$  from a minimum radiating position,  $\Gamma = -e^{j\delta}$  and  $\Gamma' = -[(r-1)/(r+1)]e^{j\delta}$  for a resonant slot. Eq. (22) then becomes

$$g = -\frac{e^{+j\delta} \left( \frac{r-1}{r+1} - 1 \right)}{\left( \frac{r-1}{r+1} \right) e^{j\delta} + 3e^{j\delta}} \quad (23)$$

which reduces to

$$g = \frac{1}{2r+1}. \quad (10)$$

## Mutual Coupling of Shunt Slots\*

A. F. KAY† AND A. J. SIMMONS†

**Summary**—Stevenson's method of analysis is extended to the case of a pair of shunt slots in the broad face of rectangular waveguide. The voltages in the slots are calculated including the effect of mutual coupling. Formulas suitable for calculation of mutual coupling are presented and the results of calculations for certain cases of overlapping quarter-wave spaced slots and nonoverlapping half-wave spaced slots are presented.

Measurement of the scattering matrix of the slot pairs inside the waveguide and the radiation patterns external to the waveguide for the overlapping case tend to confirm the results of the theory.

Calculations of the effect of mutual coupling on the patterns of three half-wave-spaced slot arrays indicate that mutual coupling is usually negligible for this type of slot.

### I. INTRODUCTION

THE task of the designer of a waveguide slot array antenna is to control the voltages in the individual slots in the array in order to obtain a desired radiation pattern. It is usually assumed that the field

in a narrow slot can be characterized by a single complex number  $V$ , representing the voltage across the center of the slot.<sup>1</sup> In the absence of mutual coupling the slot voltages may be calculated using transmission-line theory, with the slots represented by shunt or series elements. The transmission line theory can be used to take account of the coupling which takes place in the dominant or propagating mode. When the slots are close enough together, there is coupling caused by the fields external to the waveguide and also by higher-mode internal fields which act to change the voltages in the slots from those calculated by transmission line theory. This coupling, excluding the effects of dominant mode coupling, is what will be referred to in this paper as "mutual coupling."

The changes which are caused by this mutual coupling may be treated by representing the slots by  $\pi$  or  $T$  networks instead of simple series or shunt elements.

\* Manuscript received by the PGAP, May 29, 1959. The work reported in this article was sponsored by the Air Force Cambridge Research Center under Contract No. AF19(604)-3476.  
† Technical Res. Group, Somerville, Mass.

<sup>1</sup> A. F. Stevenson, "Theory of slots in rectangular waveguides," *J. Appl. Phys.*, vol. 19, pp. 24-38; January, 1948.

This treatment is of limited usefulness since it provides information only on the transmission line properties of the slots, permitting one to calculate impedance. The voltages in the slots, which are of primary interest, are not readily identifiable with voltages in the equivalent network. In the following study the voltages in the slots are considered basic, though the equivalent network may also be found from the results.

The special case of a pair of longitudinal shunt slots in the broad face of rectangular waveguide is treated. If one knows mutual coupling between pairs of slots, one can then use this information to calculate the effects of mutual coupling on arrays by treating the slots in pairs. Calculations have been carried out for quarter- and half-wave slot spacing, and experimental measurements have been made in order to check the theory. In the half-wave case, calculations have been carried out to predict the effect of mutual coupling on the pattern of various low-sidelobe arrays which were designed neglecting mutual coupling.

## II. CALCULATIONS OF MUTUAL COUPLING FROM THEORY

We start with the pair of slots and dimensions defined in Fig. 1. A dominant mode is incident from the left with voltage  $e^{-jU(z-z_1)}$ , where

$$U = 2\pi/\lambda_g = 2\pi\sqrt{1 - (\lambda/2a)^2}/\lambda, \quad (1)$$

and a matched load follows the slots on the right. All the assumptions made by Stevenson<sup>1</sup> are also made here. Briefly, the waveguide walls are infinitely thin perfect conductors, the slot is narrow and radiates only into a half space, and the guide dimensions are such that only the dominant TE<sub>01</sub> mode may propagate. The tangential electric field in the slots is assumed to have only an  $x$  component and to be equal to

$$\frac{V_i}{w_i} \cos \frac{\pi}{2l_i} (z - z_i) \quad i = 1 \text{ or } 2 \quad (2)$$

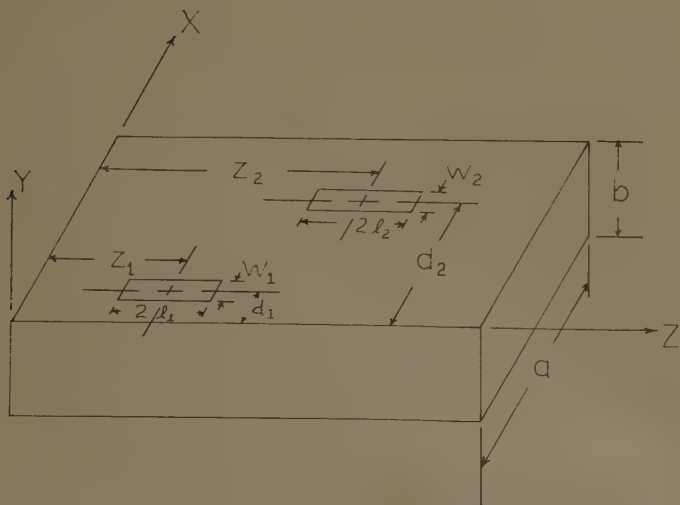


Fig. 1—Slot parameters.

where  $w_i$  and  $l_i$  are the slot width and half-length,  $z_i$  is the  $z$  coordinate of the slot center and  $V_i$  is defined by (2) and is called the voltage in the slot and is the quantity of greatest interest.

Following a suggestion by Stevenson,<sup>2</sup> the voltages in the pair of slots can be shown to be related by the equations

$$\zeta_1 = A_{11}V_1 + A_{21}V_2, \quad (3)$$

$$\zeta_2 = A_{12}V_1 + A_{22}V_2,$$

where

$$\zeta_i = \zeta_{i0} e^{-jU(z_i - z_1)},$$

and, for narrow slots ( $w_i \ll a$ ),

$$\zeta_{i0} = \frac{\pi^3}{a l_i \left[ \left( \frac{\pi}{2l_i} \right)^2 - U^2 \right]} \cos \left( \frac{\pi d_i}{a} \right) \cdot \cos(U l_i) \quad i = 1 \text{ or } 2. \quad (4)$$

The  $\zeta_i$  are analogous to "driving currents" and are proportional to the dominant-mode magnetic field at the position of the slot as in Stevenson's analysis.<sup>3</sup>

The coefficients  $A_{11}$  or  $A_{22}$  in (3) also relate the voltage in the slot to the incident field when only one slot is present, and are known from single-slot theory or from measurement. The coefficients  $A_{12} = A_{21}$  are coupling coefficients including both dominant-mode and mutual coupling. We subtract the portion of  $A_{12}$  which arises from dominant-mode coupling, in order to obtain a quantity expressing only the mutual coupling. To do this it is convenient to define a parameter  $\sum_0$  as

$$\sum_0 = j \left( \frac{\pi^2 k U b c_1 c_2 A_{12}}{2 \zeta_{10} \zeta_{20}} + \frac{c_1 c_2 e^{-jU(z_2 - z_1)}}{2} \right), \quad (5)$$

where

$$c_1 = \cos \left( \frac{\pi d_1}{a} \right), \quad c_2 = \cos \left( \frac{\pi d_2}{a} \right) \quad (6)$$

$$k = \frac{2\pi}{\lambda}.$$

The second term on the right of (5) cancels the dominant mode coupling associated with the first term. The additional factors present in this definition serve to simplify the later expressions involving  $\sum_0$  and in particular make all the terms depending on coupling inside the waveguide pure real.  $\sum_0$  vanishes when mutual coupling is negligible; therefore we call it the mutual coupling coefficient. The mutual coupling problem is now reduced to the problem of finding the values of  $\sum_0$  for given parameters of the slot pairs. In general,  $\sum_0$  may be divided into four parts,

<sup>2</sup> *Ibid.*, see (71).

<sup>3</sup> *Ibid.*, see (26).



$$\Sigma_0 = \frac{Ua^2 \left[ \left( \frac{\pi}{2l_1} \right)^2 - U^2 \right] \left[ \left( \frac{\pi}{2l_2} \right)^2 - U^2 \right]}{16 \cos(l_1 U) \cos(l_2 U) \cdot \{M + N + P + R\}}, \quad (7)$$

where  $M$ ,  $N$ ,  $P$ ,  $R$  are functions given in Appendix I. The physical significance of the four terms are as follows:  $M$ ,  $N$  and  $P$  are the internal coupling terms, and  $R$  is the external coupling term.  $M$  and  $P$  are zero except in the case where the ends of the slots overlap in the  $z$  direction in which case  $M$  represents the additional dominant-mode coupling caused by overlap, and  $P$  represents the additional higher-mode coupling.

For the purposes of computation we first treat the case in which  $l_1 = l_2 = \lambda/4$ , i.e., half-wave slots. The general expressions for  $M$ ,  $N$ ,  $P$ ,  $R$  may be simplified considerably for this case, and in fact we use these simplified expressions for  $M$ ,  $N$ ,  $P$  and  $R$  for all cases in which  $l \approx \lambda/4$  which is true for the resonant slots used in

practice. It is our belief, based on physical grounds, that while the self-coupling terms  $A_{11}$  and  $A_{22}$  depend markedly on the slot length, the mutual coupling is a slowly-varying function of slot length, and, since the inclusion of mutual coupling introduces in general only a small correction to the calculated slot voltages, a closely approximate value for  $\Sigma_0$ , calculated for the case  $l = \lambda/4$ , is sufficient in practice. This contention seems to be borne out by experiment, as will be shown in Section IV.

In order to check the theory experimentally, values of  $\Sigma_0$  were calculated for 12 cases with  $\lambda_g/4$  spacing (overlapping slots) and five cases of  $\lambda_g/2$  spacing at a frequency of 9364 mc using waveguide of internal dimensions  $a = 0.900$  inch,  $b = 0.400$  inch. The calculated results are presented in Fig. 2 and in Table I. For the

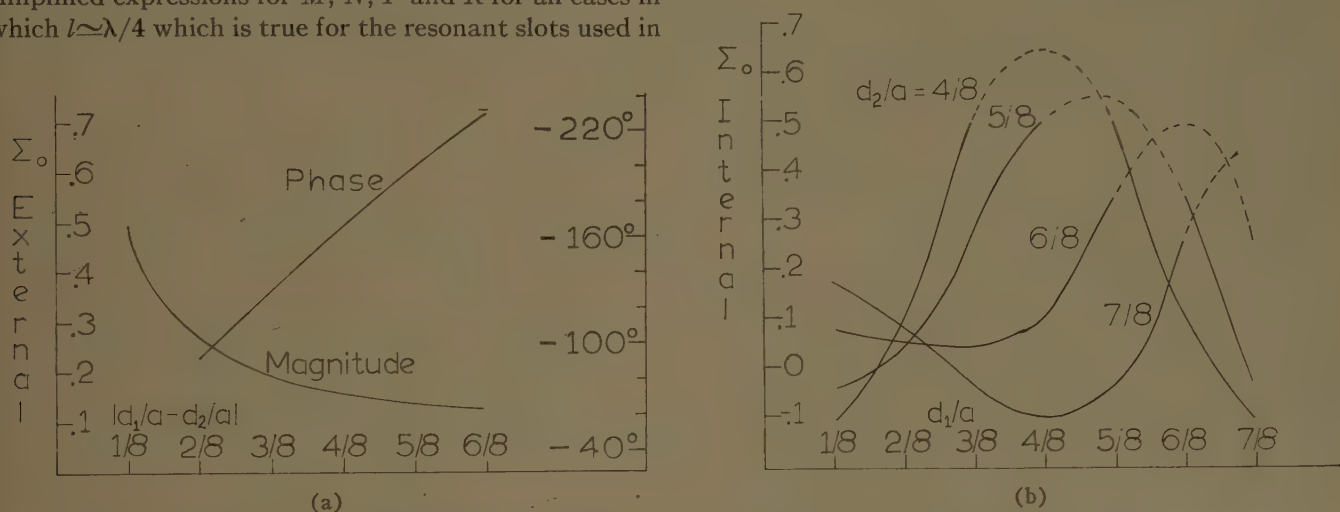


Fig. 2—Theoretical values of the mutual coupling coefficient  $\Sigma_0$ ,  $\lambda_g/4$  spacing. (a) External coupling, (b) internal coupling.

TABLE I  
CALCULATED VALUES OF  $\Sigma_0$

Case	$d_1/a$	$d_2/a$	$\Sigma_0$ External	$\Sigma_0$ Internal	$\Sigma_0$
$\lambda_g/4$ Spacing					
1	1/8	3/4	$-0.2250 + 0.0778j$	0.0764	$-0.1490 + 0.0778j$
2	1/4	3/4	$-0.2500 - 0.0628j$	0.0497	$-0.2000 - 0.0628j$
3	3/8	3/4	$-0.1870 - 0.2220j$	0.0371	$-0.1500 - 0.2220j$
4	1/2	3/4	$-0.0107 - 0.3690j$	0.0973	$0.0866 - 0.3690j$
5	5/8	3/4	$0.3550 - 0.4720j$	0.3470	$0.7020 - 0.4720j$
6	3/4	7/8	$0.3550 - 0.4720j$	0.2530	$0.6080 - 0.4720j$
7	5/8	7/8	$-0.0107 - 0.3690j$	-0.0364	$-0.0471 - 0.3690j$
8	1/2	7/8	$-0.1880 - 0.2220j$	-0.1090	$-0.2970 - 0.2220j$
9	3/8	7/8	$-0.2500 - 0.0628j$	-0.0438	$-0.2940 - 0.0628j$
10	1/8	7/8	$-0.1440 + 0.1730j$	0.1750	$0.0306 + 0.1730j$
11	1/2	5/8	$0.3550 - 0.4720j$	0.4940	$0.8490 - 0.4720j$
12	3/8	5/8	$-0.0107 - 0.3690j$	0.2700	$0.2590 - 0.3690j$
$\lambda_g/2$ Spacing					
1	1/8	3/4	$-0.0569 - 0.0196j$	0.00531	$-0.0516 - 0.0196j$
2	1/4	3/4	$-0.0598 + 0.00095j$	0.00571	$-0.0541 + 0.00095j$
3	3/8	3/4	$-0.0536 + 0.0365j$	0.00893	$-0.0446 + 0.0365j$
4	1/2	3/4	$-0.0414 + 0.0591j$	0.01600	$-0.0253 + 0.0591j$
5	5/8	3/4	$-0.0352 + 0.0735j$	0.02480	$-0.0105 + 0.0735j$

sake of comparison, of the importance of internal and external coupling we have plotted

$$\sum_0 \text{ external} = \frac{a^2 U^2 (k^2 - U^2)^2}{16 \cos^2 (Ul)} R, \quad (8)$$

$$\sum_0 \text{ internal} = \frac{a^2 U^2 (k^2 - U^2)^2}{16 \cos^2 (Ul)} (M + N + P). \quad (9)$$

The dashed portion of the curves in Fig. 2(b) indicate an estimate of where the curve lies, since in this region the slots intersect each other and the theory breaks down. It may be seen that  $\sum_0$  internal is of the same order of magnitude as  $\sum_0$  external for the  $\lambda_0/4$  spacing, the latter varying in phase while the former is of constant phase, independent of slot spacing. In the case of  $\lambda_0/2$  spacing,  $\sum_0$  external appears more important than  $\sum_0$  internal for most cases. With these values for  $\sum_0$ , (5) may be solved for  $A_{12}$  and the voltages in the slots found from (3). From these voltages may also be found the reflection and transmission coefficients inside the waveguide, as will be indicated in the next section.

### III. CALCULATION OF COUPLED-SLOT VOLTAGES AND SCATTERING MATRIX FROM SINGLE-SLOT DATA AND THE MUTUAL COUPLING COEFFICIENTS

The voltages in the slots may now be calculated from a knowledge of the single-slot behavior and the value of  $\sum_0$ . It is convenient to introduce a parameter  $\beta_i$  which expresses the relation of the voltage in the  $i$ th slot to the dominant-mode fields excited by the slot inside the waveguide. A slot with voltage  $V_i$  excites two dominant-mode waves of equal amplitude  $\beta_i$  traveling in opposite directions away from the slot. The complex amplitude of either wave referred to the slot center is given by

$$\beta_i = \frac{V_i \zeta_{i0}}{\pi^2 k U b}, \quad (10)$$

where  $i=1$  or  $2$ , which is the same as Stevenson's usage,<sup>4</sup> with slightly different notation, and shows that the dominant-mode amplitude is directly proportional to  $V_i$  and to the dominant-mode coupling factor,  $\zeta_{i0}$ . Eq. (10) is fundamental and holds, by superposition, regardless of whether other slots are present or not. If slot  $i$  is present alone, we use the notation of  $V_{i0}$  for  $V_i$  and  $\beta_{i0}$  for  $\beta_i$ .

Making use of (10) we can relate the self-coupling coefficient  $A_{11}$  or  $A_{22}$  to the admittance or the reflection coefficient of the single slot. For convenience, we characterize the single slot by its reflection coefficient,  $s_1$  or  $s_2$ , a quantity easily subject to measurement. We have first

$$s_1 = \beta_{10}, \quad s_2 = e^{ju(z_2 - z_1)} \beta_{20}, \quad (11)$$

where these reflection coefficients are referred to the centers of the respective slots. Next, using (3), with  $A_{12}$

set equal to zero, and (10), we have

$$A_{ii} = \frac{\zeta_{i0}^2}{\pi^2 k U b s_i}, \quad i = 1 \text{ or } 2. \quad (12)$$

We now have sufficient relations to calculate  $\beta_i$  and  $V_i$  in terms of  $\sum_0$  and  $s_i$ .

In two particular cases considered, we can show, after some manipulation, that for  $\lambda_0/4$  spacing

$$\beta_1 = \frac{s_1(1 + ys_2)}{1 + y^2 s_1 s_2}, \quad \beta_2 = \frac{js_2(ys_1 - 1)}{1 + y^2 s_1 s_2}, \quad (13)$$

where

$$y = \frac{2 \sum_0}{c_1 c_2} - 1. \quad (14)$$

For  $\lambda_0/2$  spacing

$$\beta_1 = \frac{s_1(1 - zs_2)}{1 - z^2 s_1 s_2}, \quad \beta_2 = \frac{s_2(zs_1 - 1)}{1 - z^2 s_1 s_2}, \quad (15)$$

where

$$z = \frac{2j \sum_0}{c_1 c_2} - 1. \quad (16)$$

In practice it has proved most convenient first to calculate  $\beta_1$  and  $\beta_2$  from (13) and (15), and then to find  $V_1$  and  $V_2$  using (10).

Also, knowing  $\beta_1$  and  $\beta_2$  it is a simple matter to calculate the interaction of the slots with the dominant mode in the waveguide, which is of interest for impedance calculations. This is most simply done in terms of the scattering matrix,

$$[S] = \begin{pmatrix} s_{11} & s_{12} \\ s_{21} & s_{22} \end{pmatrix}, \quad (17)$$

where, from the definition of  $\beta_1$  and  $\beta_2$ , it easily follows that

$$s_{11} = \beta_1 + \beta_2 e^{-ju(z_2 - z_1)}, \\ s_{12} = (1 + \beta_1) e^{-ju(z_2 - z_1)} + \beta_2. \quad (18)$$

The input reference terminals are at the center of slot 1, the output at slot 2. Similar expressions for  $s_{22}$  and  $s_{21}$  may be obtained by interchanging load and generator, in which case different values of  $\beta_1$  and  $\beta_2$  are obtained.

### IV. MEASUREMENTS ON PAIRS OF SLOTS

In order to find experimentally the effect of mutual coupling, two types of measurement were made. Internal measurement of the scattering matrix of pairs of slots was made and the array pattern of pairs of slots was measured externally. First, the scattering matrix and patterns of a series of single slots were measured at 9364 mc to provide values of  $s_1$  and  $s_2$ . The slots were exactly one-half-wavelength long (0.630 inch), with square ends; the ratio of width to length was 1:10. The slots were cut in pieces of waveguide 6 inches long and

<sup>4</sup> *Ibid.*, see (25).



flat metal ground planes approximately 6 inches square were clamped on each side to approximate the infinite conducting plane required in the initial assumptions. Measurement of the scattering matrix was made using a movable-short and Deschamps<sup>5</sup> graphical construction. Single-slot radiation patterns were also measured so that the element pattern could be subtracted from the total pattern of the pair of slots, leaving just the array pattern which depends only on the relative voltages in the two slots.

The results of these single-slot measurements are shown in Table II and Fig. 3.

TABLE II  
RESULTS OF SINGLE-SLOT MEASUREMENTS, HALF-WAVE SLOTS

Slot Position $d/a$	Reflection Coefficient $s_i$	Admittance $y_i$
1/8 or 7/8	$(0.339 \pm 0.002)e^{j(180.0 \pm 0.2)^\circ}$	1.029
2/8 or 6/8	$(0.238 \pm 0.002)e^{j(172.0 \pm 0.5)^\circ}$	$0.625e^{-j10.4^\circ}$
3/8 or 5/8	$(0.074 \pm 0.002)e^{j(146.4 \pm 2.1)^\circ}$	$0.157e^{-j87.2^\circ}$

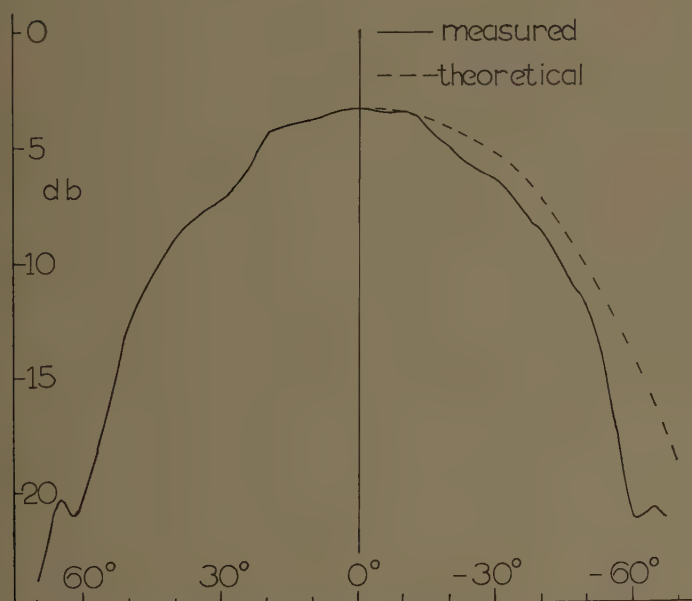


Fig. 3—Measured and theoretical  $H$ -plane patterns of a single slot at  $d/a = 3/4$ .

The case of quarter-wave spacing was studied in most detail, and the following experimental results apply in the most part to that case.

Fig. 4 (next page) shows some typical results for reflection coefficient measurements, comparing calculated results with and without inclusion of mutual coupling with measured values. It can be seen that the experimental results agree quite well with the theory and that there is in most cases a marked difference between the

two methods of calculation, indicating the effect of mutual coupling.

The transmission coefficient showed similar behavior, though this coefficient is not as much affected by mutual coupling, and the difference is therefore less striking than for the reflection coefficient.

In order to extend the results to the more practical case of nonhalf-wave slots, in particular to resonant slots approximately one-half-wave in length, a series of similar measurements were made for resonant slots. The resonant lengths for three slot positions were determined experimentally with the results given in Table III. Calculations were made using values of  $\sum_0$  proper for half-wavelength slots in order to check the hypothesis that  $\sum_0$  varies negligibly with slot length over the range of lengths used. Measurements and calculations are shown in Fig. 5. The agreement is considered quite good, especially in the case of  $s_{22}$ . Therefore it is assumed that the values of  $\sum_0$  calculated for half-wavelength slots may be used for calculations involving resonant slots.

Pattern calculations were also carried out. First the measured values of  $[S]$  were used in (18) to calculate  $\beta_1$  and  $\beta_2$ , then the slot voltages were calculated using (10), and finally the array patterns were calculated using these voltages. The slot voltages and array patterns were also calculated, neglecting mutual coupling, by using the measured values of single-slot admittance. Pattern measurements were then made, and the measured single-slot pattern was subtracted, leaving the experimental array patterns to compare with the calculated ones. Typical results are shown in Figs. 6 and 7, pp. 396–397. Fig. 7 is particularly interesting because one of the two slots was located on the waveguide centerline. The theoretical pattern neglecting mutual coupling is simply the pattern of the single noncentered slot since the centered slot does not couple to the dominant mode. Both experiment and theory indicate that the centered slot actually does have an induced voltage in this case. In order to calculate the voltage induced in the slot in this case, a limiting process must be applied to the previous formulas, since both  $\beta_i$  and  $\zeta_{i0}$  go to zero for slot  $i$  centered. The results are, if slot 1 is on the centerline,

$$\lim_{d_1 \rightarrow a/2} \frac{V_1}{V_2} = j \sum_0 Y_1' \quad (19)$$

where

$$Y_1' = \lim_{d_1 \rightarrow a/2} \frac{Y_1}{\cos^2 \frac{\pi d_1}{a}}, \quad (20)$$

where  $Y_1$  is the slot admittance.  $Y_1'$  is evaluated theoretically by Oliner<sup>6</sup> and we have used his theory, which

<sup>5</sup> G. A. Deschamps, "Determination of reflection coefficients and insertion loss of a waveguide junction," *J. Appl. Phys.*, vol. 24, pp. 1046–1050; August, 1953.

<sup>6</sup> A. A. Oliner, "The impedance properties of narrow radiating slots in the broad face of rectangular waveguide," *IRE TRANS. ON ANTENNAS AND PROPAGATION*, vol. AP-5, pp. 4–20; January, 1957.

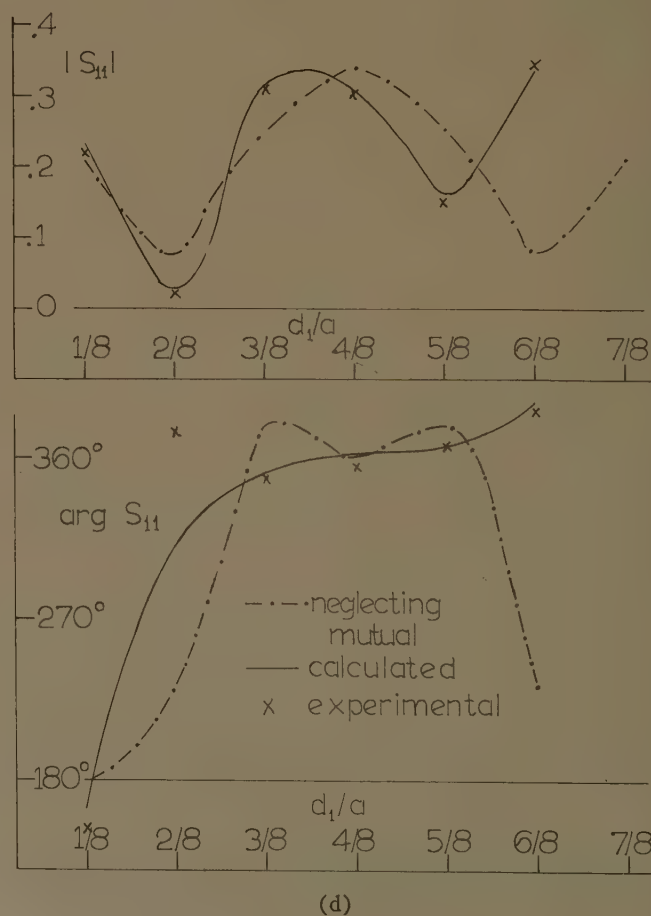
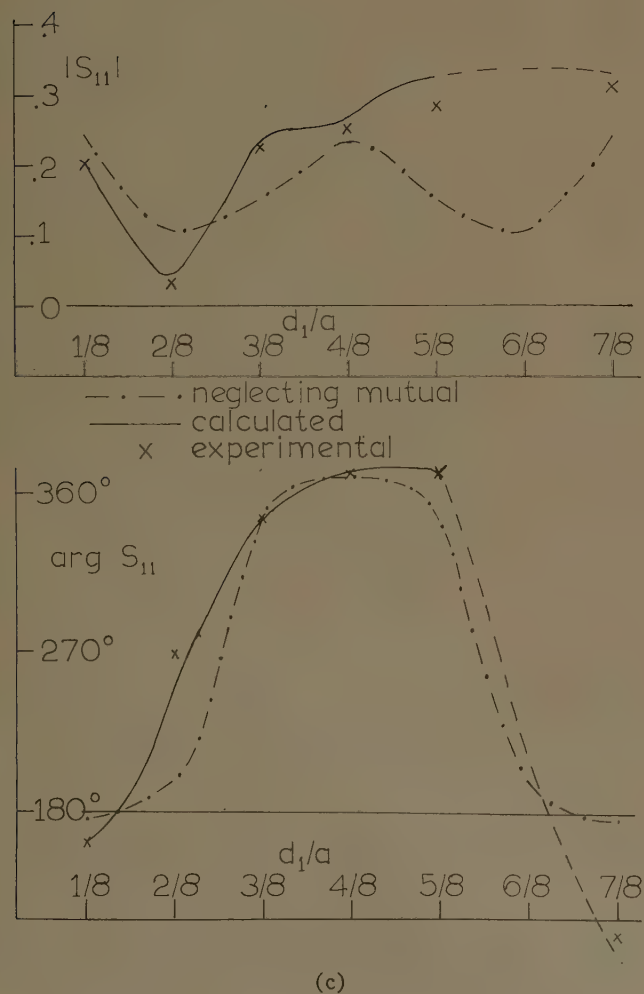
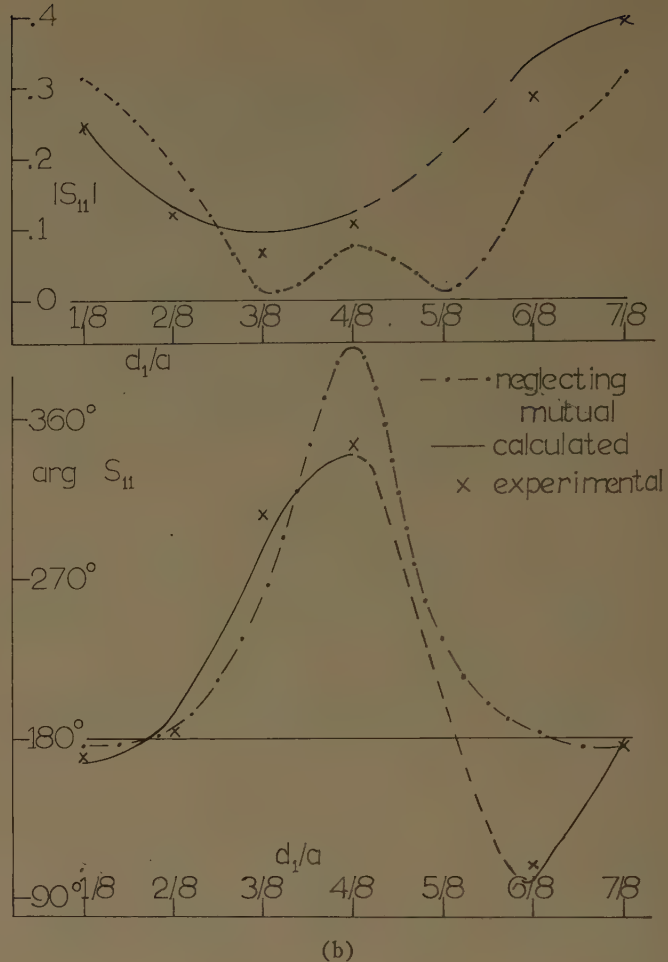
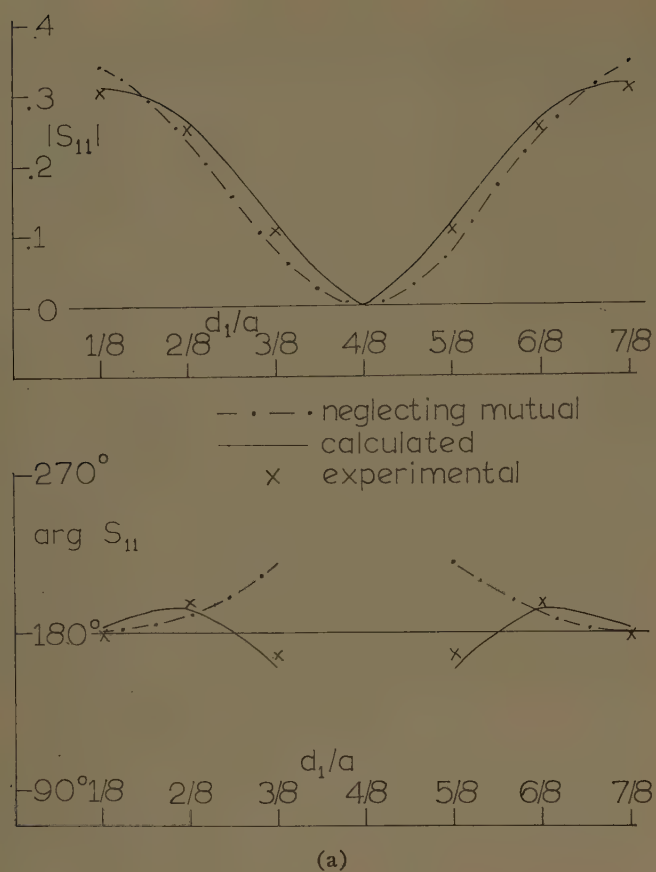
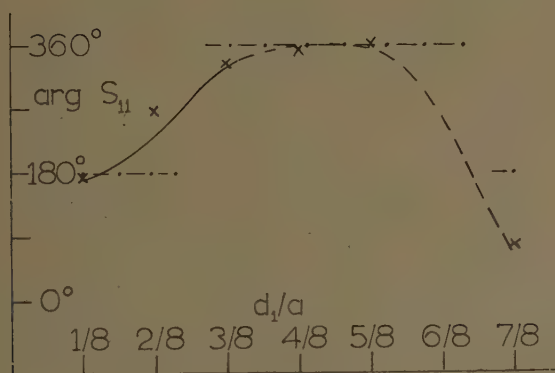
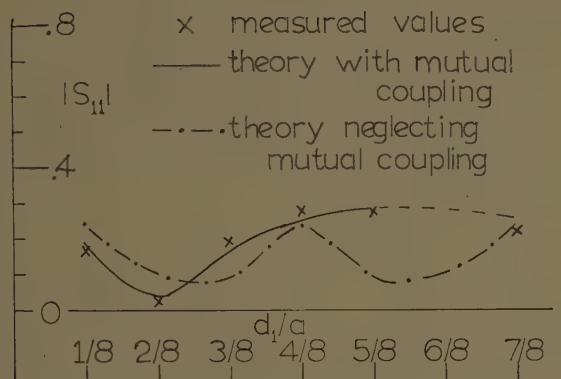


Fig. 4—Reflection coefficient. (a)  $d_2/a = 4/8$ . (b)  $d_2/a = 5/8$ . (c)  $d_2/a = 6/8$ . (d)  $d_2/a = 7/8$ .

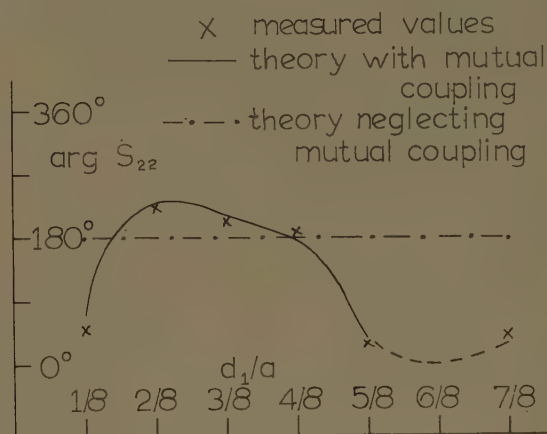
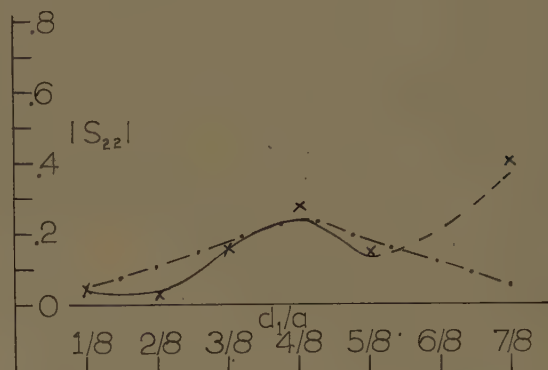


TABLE III  
RESULTS OF SINGLE-SLOT MEASUREMENTS, RESONANT SLOTS

$d/a$	Resonant Length ( $2l$ )	Normalized Conductance
1/8 or 7/8	0.630 inch	1.029
2/8 or 6/8	0.624 inch	0.609
3/8 or 5/8	0.606 inch	0.223



(a)



(b)

Fig. 5—Measured values of reflection coefficient, resonant slot-pairs.  $d_2/a = 3/4$ . (a)  $S_{11}$ , (b)  $S_{22}$ .

for our values of parameters gives a value

$$Y_1' = 0.890e^{-j44.0^\circ}.$$

Figs. 6 and 7 indicate quite clearly the distortion of array patterns by mutual coupling for slots spaced one-quarter-guide-wavelength.

Measurements of scattering matrix were also performed in a few cases with slots spaced one-half-guide-wavelength, but the results were somewhat inconclusive because the effects noted were at the limit of our measurement accuracy.

#### V. THE EFFECT OF MUTUAL COUPLING ON LOW-SIDELobe ARRAYS

In order to assess the effect of mutual coupling on low-sidelobe arrays, three half-wave spaced resonant arrays were designed using a Tchebycheff distribution<sup>7</sup>

<sup>7</sup> L. B. Brown and G. A. Scharp, "Tchebycheff Antenna Distribution, Beamwidth and Gains," Navord Rept. 4629; February, 1958.

and neglecting mutual coupling. Resonant slots were used.

The slot conductances were first calculated from the desired slot voltage distribution and the condition for a match to the input line. Then the slot displacements were calculated from the semi-empirical relation

$$\frac{G}{Y_0} = 1.22 \cos^2 \frac{\pi d}{a}, \quad (21)$$

where the constant 1.22 was determined as a best fit to the values on Table III.

Once the slot displacements were known, the mutual coupling coefficient  $\sum_0$  could be calculated for each pair of slots, and the actual voltages determined.

A matrix relation similar to (3),

$$[\xi] = [A][V], \quad (22)$$

may be written for  $N$  slots. If  $[A_0]$  and  $[V_0]$  represent

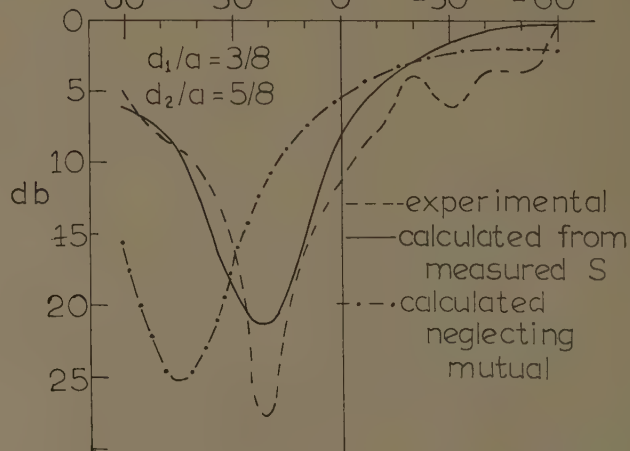
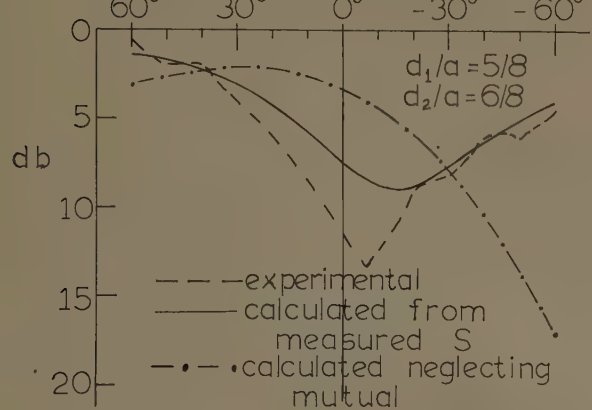
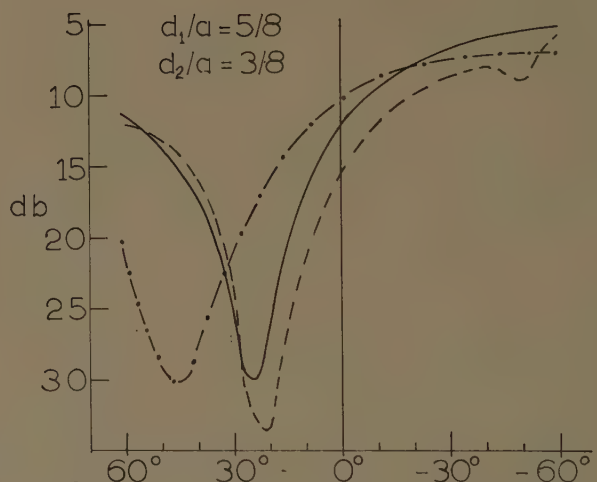
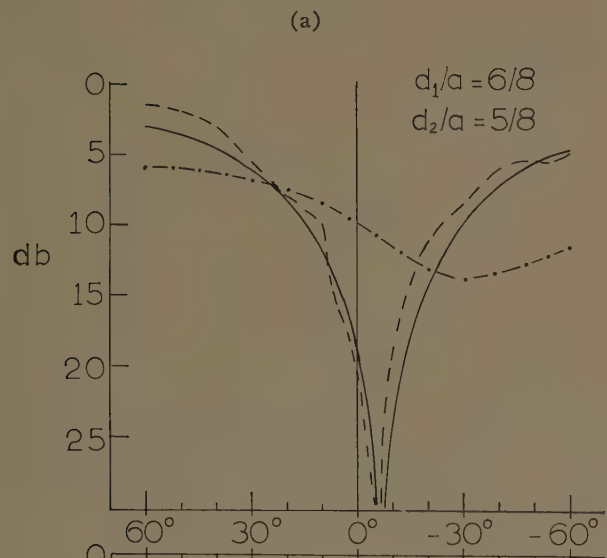
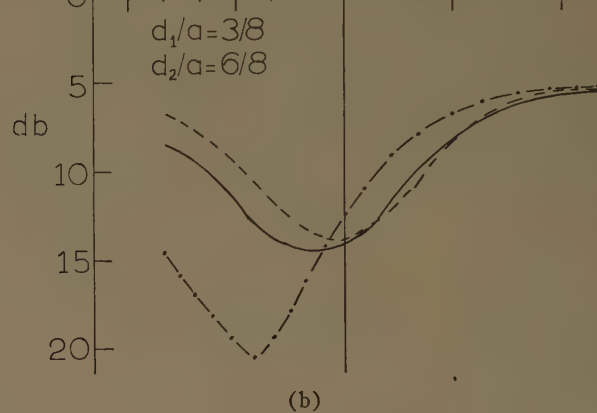
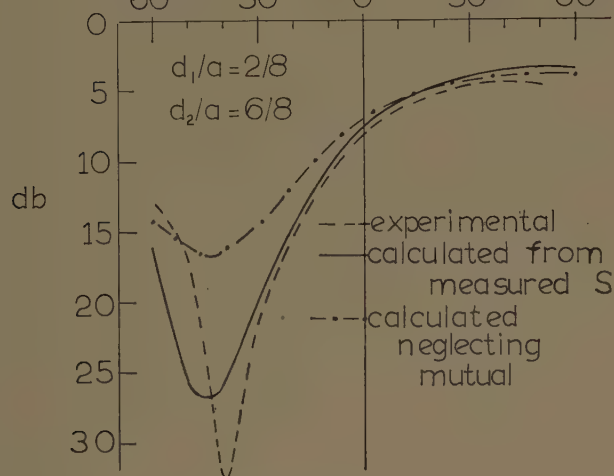
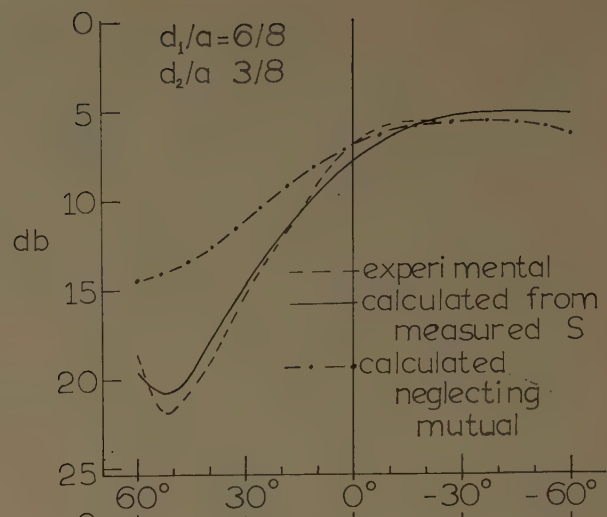
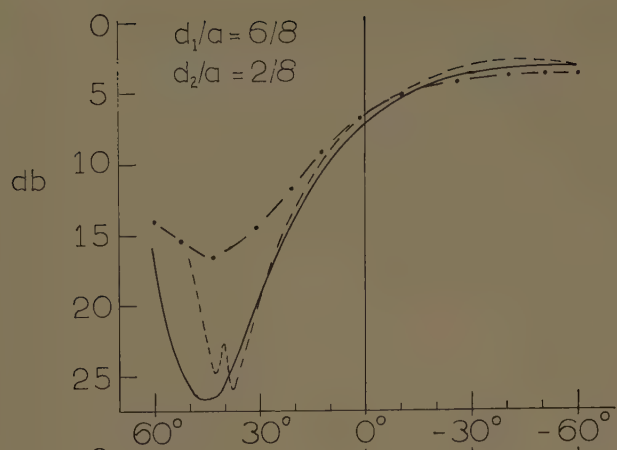


Fig. 6—Array patterns. (a)  $d/a:6/8$  and  $2/8$ . (b)  $d/a:6/8$  and  $3/8$ . (c)  $d/a:6/8$  and  $5/8$ . (d)  $d/a:5/8$  and  $3/8$ .



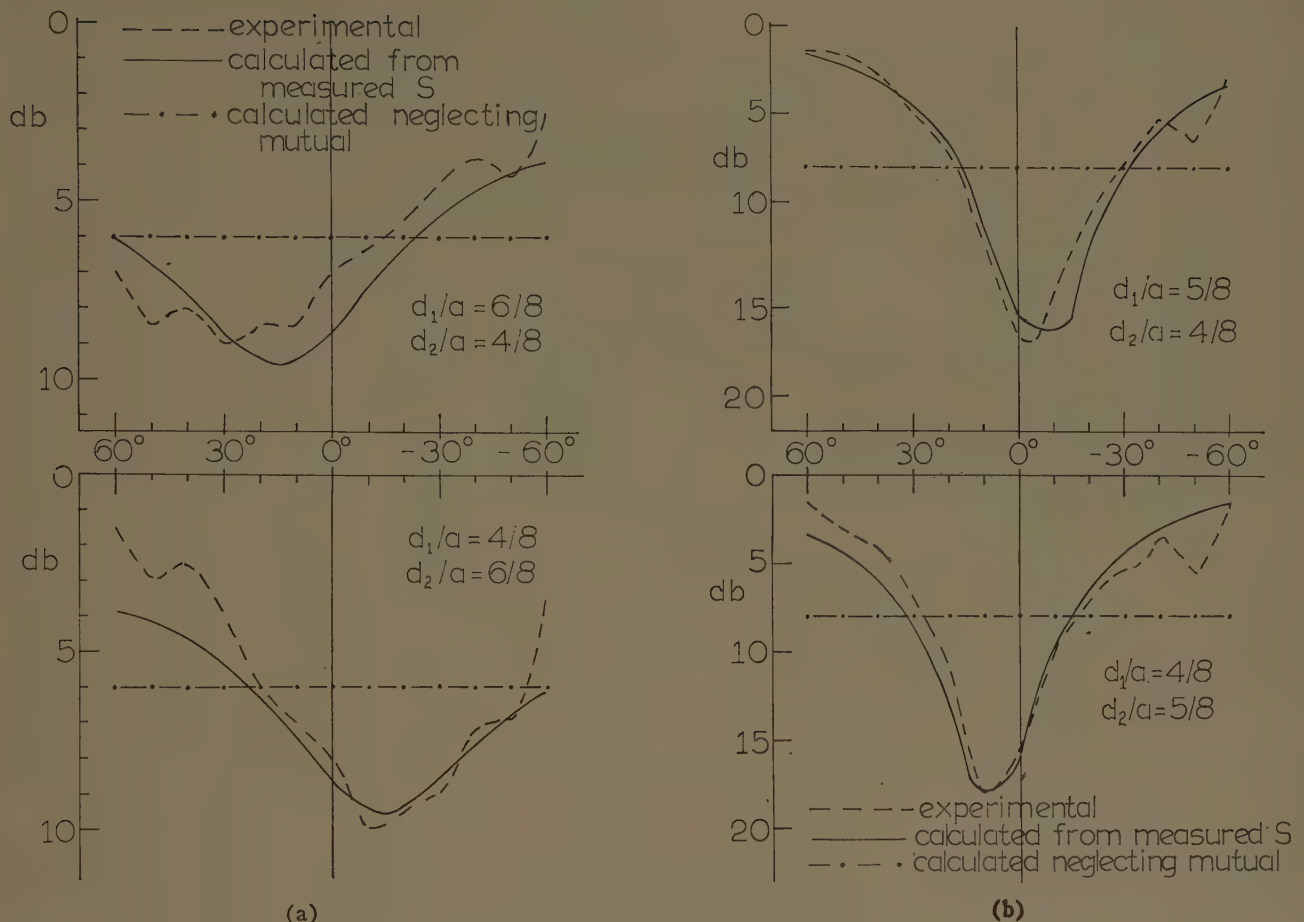


Fig. 7—Array patterns, one slot centered. (a)  $d/a:4/8$  and  $6/8$ . (b)  $d/a:4/8$  and  $5/8$ .

the matrix  $[A]$  and  $[V]$ , neglecting mutual coupling, then

$$[I] = [A_0][V_0] \quad (23)$$

also, since this equation is equivalent to the equations from which the slot array was calculated. Thus

$$[A_0][V_0] = [A][V]. \quad (24)$$

Letting

$$\begin{aligned} [A] &= [A_0] + [a] \\ [V] &= [V_0] + [v], \end{aligned} \quad (25)$$

and neglecting second-order products because the mutual coupling for  $\lambda_g/2$  spacing is small, we have

$$[A_0][v] = -[a][V_0]. \quad (26)$$

Furthermore, if we include only mutual coupling of nearest neighbors, the elements in  $[a]$  satisfy

$$a_{mn} = 0 \quad \text{unless} \quad m = n \pm 1. \quad (27)$$

Finally, using (5)

$$a_{m,m+1} = \frac{-2j\zeta_{m0}\zeta_{m+1,0}(\sum_0)_{m,m+1}}{\pi^2 k b c_m c_{m+1} U}, \quad (28)$$

where  $(\sum_0)_{m,m+1}$  means the mutual coupling term  $\sum_0$  for the  $m$ th and  $m+1$ st slots.

Using these relations, the  $N$  equations (26) may be solved explicitly after some manipulation for the  $N$  voltages  $v_n$ <sup>8</sup> and the new array voltages may be calculated. Table IV (next page) compares the original voltages, without mutual coupling and with mutual coupling, for three different low-sidelobe arrays. The effect of mutual coupling is to increase the magnitudes and introduce a slight phase error. The patterns of the three arrays were calculated to show the effect of mutual coupling on the sidelobe level and are shown in Fig. 8. The first sidelobe in each case was somewhat higher than the design level, while the other sidelobes were almost unaffected or slightly lower.

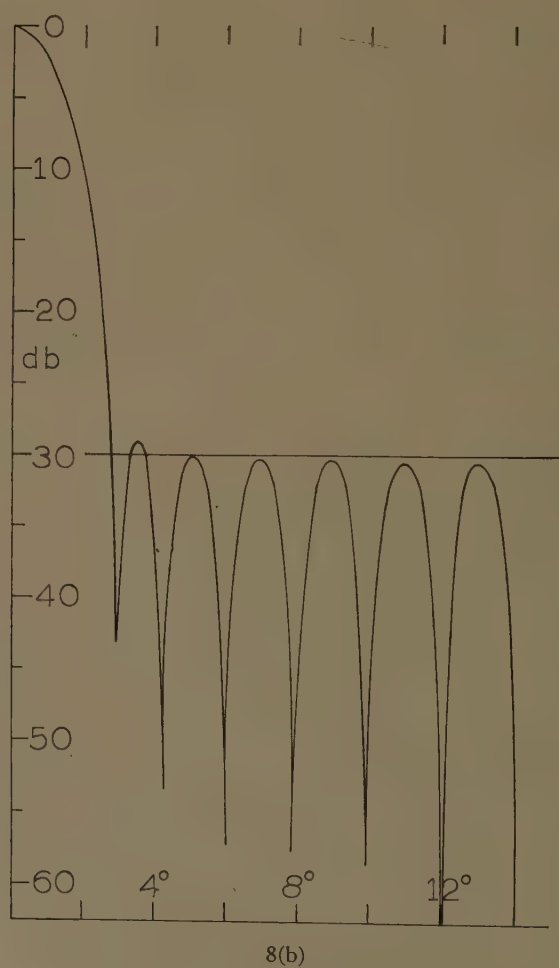
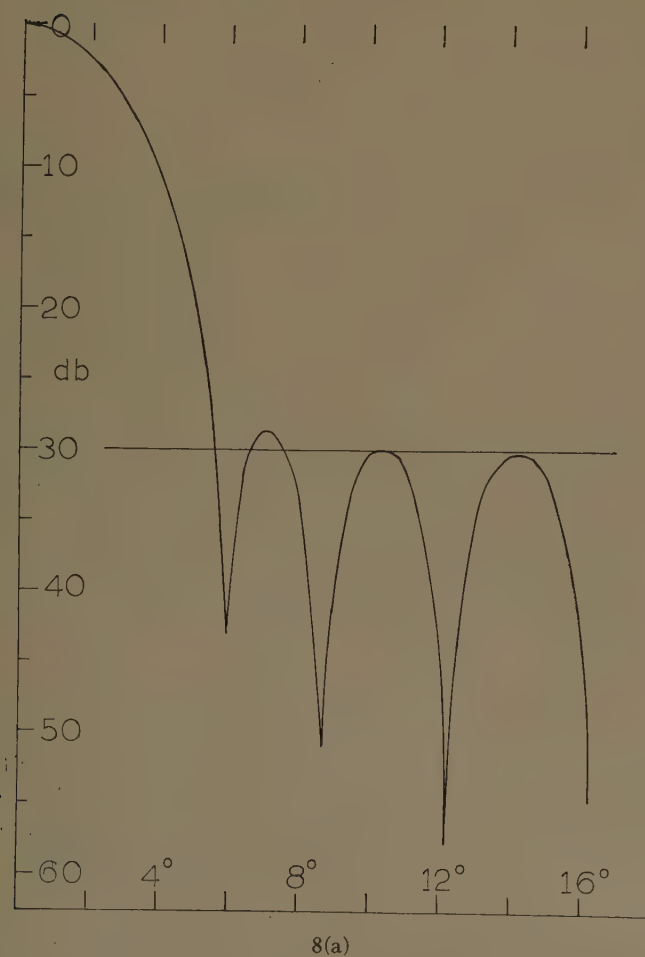
## VI. CONCLUSIONS

Mutual coupling between pairs of longitudinal shunt slots may be calculated, and its effect on the slot voltages determined, by means of the theory presented here. The effect for slots spaced one-quarter-guide-wave-length is significant, altering both impedance and pat-

<sup>8</sup> "Microwave Studies in Variable Index Lenses, Electronic Switching, and Effect of Mutual Coupling on Slot Arrays," Tech. Res. Group, Somerville, Mass., Final Rept. on Contract AF19(604)-4054, Section IIIC; February 4, 1959.

TABLE IV  
ARRAY VOLTAGES  
TCHEBYCHEFF RESONANT SLOT ARRAYS  
 $N$ =number of array elements  
 $S$ =design side lobe level

	Design Voltages <sup>7</sup>				Actual Voltages for Resonant Array Including Mutual Coupling					
	$N=20$ $S=30$	$N=40$ $S=30$	$N=40$ $S=50$		$(N=20, S=30)$		$(N=40, S=30)$		$(N=40, S=50)$	
					Real	Imaginary	Real	Imaginary	Real	Imaginary
$V1_0$	0.100000	0.100000	0.100000	$V1$	0.1057	-0.0019 $j$	0.1028	-0.0010 $j$	0.1069	-0.0024 $j$
$V2_0$	0.087706	0.043761	0.104745	$V2$	0.1019	-0.0046 $j$	0.0537	-0.0034 $j$	0.1215	-0.0060 $j$
$V3_0$	0.120094	0.052600	0.155383	$V3$	0.1356	-0.0048 $j$	0.0595	-0.0024 $j$	0.1766	-0.0075 $j$
$V4_0$	0.154975	0.062041	0.218193	$V4$	0.1744	-0.0054 $j$	0.0701	-0.0028 $j$	0.2476	-0.0104 $j$
$V5_0$	0.190517	0.071988	0.293642	$V5$	0.2137	-0.0053 $j$	0.0813	-0.0031 $j$	0.3329	-0.0138 $j$
$V6_0$	0.224646	0.082332	0.381723	$V6$	0.2511	-0.0047 $j$	0.0930	-0.0035 $j$	0.4323	-0.0176 $j$
$V7_0$	0.255221	0.092946	0.481895	$V7$	0.2845	-0.0038 $j$	0.1049	-0.0039 $j$	0.5453	-0.0217 $j$
$V8_0$	0.280221	0.103695	0.593049	$V8$	0.3115	-0.0027 $j$	0.1170	-0.0042 $j$	0.6705	-0.0259 $j$
$V9_0$	0.297934	0.114432	0.713502	$V9$	0.3306	-0.0018 $j$	0.1290	-0.0044 $j$	0.8059	-0.0301 $j$
$V10_0$	0.307117	0.125003	0.841018	$V10$	0.3404	-0.0012 $j$	0.1408	-0.0047 $j$	0.9490	-0.0339 $j$
$V11_0$		0.135254	0.972867	$V11$			0.1522	-0.0048 $j$	1.0965	-0.0371 $j$
$V12_0$		0.145026	1.105904	$V12$			0.1631	-0.0050 $j$	1.2449	-0.0394 $j$
$V13_0$		0.154167	1.236684	$V13$			0.1733	-0.0050 $j$	1.3903	-0.0408 $j$
$V14_0$		0.162530	1.361597	$V14$			0.1826	-0.0051 $j$	1.5279	-0.0393 $j$
$V15_0$		0.169979	1.477010	$V15$			0.1907	-0.0048 $j$	1.6546	-0.0369 $j$
$V16_0$		0.176389	1.579432	$V16$			0.1977	-0.0046 $j$	1.7673	-0.0354 $j$
$V17_0$		0.181654	1.665661	$V17$			0.2035	-0.0045 $j$	1.8619	-0.0336 $j$
$V18_0$		0.185684	1.732936	$V18$			0.2080	-0.0045 $j$	1.9355	-0.0318 $j$
$V19_0$		0.188410	1.779062	$V19$			0.2110	-0.0044 $j$	1.9858	-0.0304 $j$
$V20_0$		0.189785	1.802515	$V20$			0.2125	-0.0044 $j$	2.0114	-0.0296 $j$





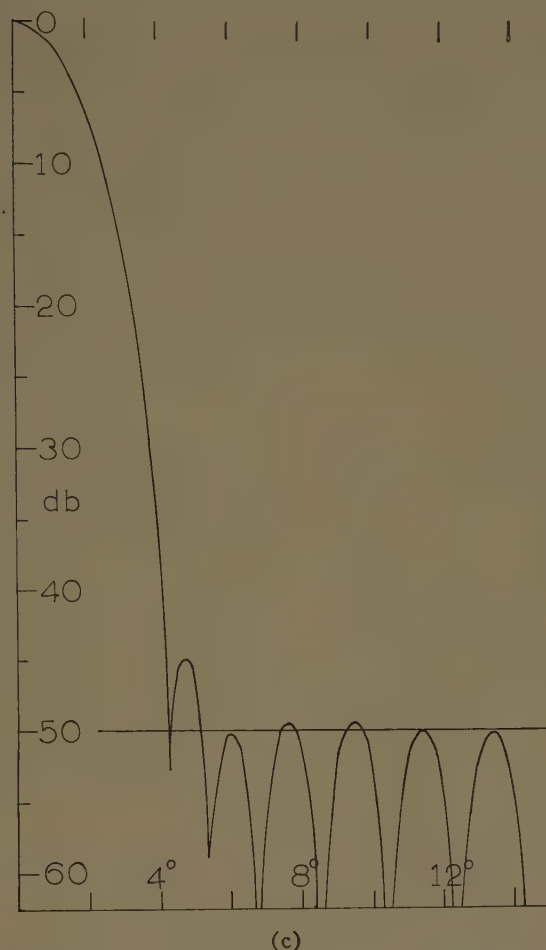


Fig. 8—Calculated array patterns. (a) 20-element array, designed for 30-dB sidelobes. (b) 40-element array, designed for 30-dB sidelobes. (c) 40-element array, designed for 50-dB sidelobes.

terms of the slot pairs to a marked degree. The effect for half-wave spaced slots is much smaller and shows up appreciably only in arrays designed for very low sidelobe levels, below 30 dB. The effect of errors caused by mutual coupling in these cases would probably be masked by errors caused by machining tolerances. The practice of antenna engineers in neglecting mutual coupling for this type of slot is, therefore, in general justified.

#### APPENDIX

The derivation of the basic equations follows the method of Stevenson,<sup>1</sup> modified to include two slots rather than one. Exact integral equations may be set up for the fields in the slot. These are reduced to algebraic equations using the approximation that the slot length-to-width ratio is large. Two simultaneous algebraic equations are obtained for the voltages in the slots, the coefficients of which are complicated integral expressions involving the free space and waveguide Green's functions. The details of the derivation may be found in a previous article.<sup>9</sup> The results for slots of length  $l_1$  and

$l_2$  are given with some errors in this first article, but they are corrected in a later article.<sup>10</sup> The results are as follows:

$$M = \frac{-4c_1c_2 \sin(U\Delta)}{Ua^2 \left[ \left( \frac{\pi}{2l_1} \right)^2 - U^2 \right] \left[ \left( \frac{\pi}{2l_2} \right)^2 - U^2 \right]} + \frac{4c_1c_2}{\pi^2 \left[ \left( \frac{\pi}{2l_2} \right)^2 - \left( \frac{\pi}{2l_1} \right)^2 \right]} \cdot \left\{ \frac{\left[ k^2 - \left( \frac{\pi}{2l_1} \right)^2 \right] \sin \left( \frac{\pi\Delta}{2l_1} \right)}{\left[ \left( \frac{\pi}{2l_1} \right)^2 - U^2 \right] \left( \frac{\pi}{2l_1} \right)} - \frac{\left[ k^2 - \left( \frac{\pi}{2l_2} \right)^2 \right] \sin \left( \frac{\pi\Delta}{2l_2} \right)}{\left[ \left( \frac{\pi}{2l_2} \right)^2 - U^2 \right] \left( \frac{\pi}{2l_2} \right)} \right\}, \quad (29)$$

<sup>9</sup> A. F. Kay, "Mutual Coupling of Shunt Slots in the Broad Face of Rectangular Waveguide," Tech. Res. Group, Somerville, Mass., Rept. No. 3 on Contract AF19(604)-1307; May, 1956.

<sup>10</sup> A. F. Kay and A. J. Simmons, "Mutual Coupling of Shunt Slots in the Broad Face of Rectangular Waveguide," Tech. Res. Group, Somerville, Mass., Final Rept. on Contract AF19(604)-2453; March, 1958.

$$N = \sum'_{m,n} \frac{\epsilon_{mn} \cos\left(\frac{m\pi d_1}{a}\right) \cos\left(\frac{m\pi d_2}{a}\right) \left[\left(\frac{m}{a}\right)^2 + \left(\frac{n}{b}\right)^2\right]}{\alpha_{mn} \left[\left(\frac{\pi}{2l_1}\right)^2 + \alpha_{mn}^2\right] \left[\left(\frac{\pi}{2l_2}\right)^2 + \alpha_{mn}^2\right]} \cdot \{e^{-\alpha_{mn}\Delta a} + e^{-\alpha_{mn}\Delta b} + e^{-\alpha_{mn}\Delta c} + e^{-\alpha_{mn}\Delta d}\}, \quad (30)$$

$$P = \sum'_{m,n} \frac{2\epsilon_{mn} \cos\left(\frac{m\pi d_1}{a}\right) \cos\left(\frac{m\pi d_2}{a}\right)}{\pi^2 \left[\left(\frac{\pi}{2l_2}\right)^2 - \left(\frac{\pi}{2l_1}\right)^2\right]} \cdot \left\{ \frac{\left[k^2 - \left(\frac{\pi}{2l_1}\right)^2\right] \sin\left(\frac{\pi\Delta}{2l_1}\right)}{\left[\left(\frac{\pi}{2l_1}\right)^2 + \alpha_{mn}^2\right] \left(\frac{\pi}{2l_1}\right)} - \frac{\left[k^2 - \left(\frac{\pi}{2l_2}\right)^2\right] \sin\left(\frac{\pi\Delta}{2l_2}\right)}{\left[\left(\frac{\pi}{2l_2}\right)^2 + \alpha_{mn}^2\right] \left(\frac{\pi}{2l_2}\right)} \right\}; \quad (31)$$

and, if  $l_1 = l_2$ ,

$$R = \frac{4abl^2}{\pi^5} \int_{-l}^l \left\{ \frac{e^{-jk r_1}}{r_1} + \frac{e^{-jk r_2}}{r_2} \right\} \left\{ \frac{l}{\pi} \left( k^2 + \left( \frac{\pi}{2l} \right)^2 \right) \cdot \cos\left(\frac{\pi u}{2l}\right) + \frac{1}{2} \left( k^2 - \left( \frac{\pi}{2l} \right)^2 \right) (u - l) \sin\left(\frac{\pi u}{2l}\right) \right\} du,$$

where

$$\begin{aligned} \Delta a &= |z_0 - l_1 - l_2|, \\ \Delta b &= |z_0 + l_2 - l_1|, \\ \Delta c &= |z_0 + l_1 - l_2|, \\ \Delta d &= |z_0 + l_1 + l_2|, \\ z_0 &= |z_2 - z_1|, \\ \Delta &= \begin{cases} \Delta a & \text{if } z_0 < l_1 + l_2 \text{ (slots "overlap")} \\ 0 & \text{if } z_0 > l_1 + l_2 \text{ (slots do not "overlap")}, \end{cases} \\ r_1 &= \sqrt{\delta^2 + (u + l + z_0)^2}, \\ r_2 &= \sqrt{\delta^2 + (u + l - z_0)^2}, \\ \delta &= |d_1 - d_2|, \end{aligned}$$

$$\begin{aligned} \alpha_{mn} &= \frac{2\pi}{\lambda} \sqrt{\left(\frac{m\lambda}{2a}\right)^2 + \left(\frac{n\lambda}{2b}\right)^2 - 1}, \\ \epsilon_{mn} &= \begin{cases} 4, & mn > 0 \\ 2, & mn = 0. \end{cases} \end{aligned} \quad (32)$$

$\sum'_{m,n}$  means summation over all combinations of non-negative integers  $m$  and  $n$  except  $m=n=0$  and  $m=1, n=0$ .

These formulas may be considerably simplified for half wavelength slots,  $l_1 = l_2 = l = \lambda/4$ . In this case it has been shown<sup>10</sup> that

$$M = \frac{4c_1 c_2}{(k^2 - U^2)} \left[ \frac{\sin(k\Delta)}{\pi^2 k} - \frac{\sin(U\Delta)}{a^2 U (k^2 - U^2)} \right], \quad (33)$$

$$N = \frac{1}{\pi^4} \sum'_{m,n} \frac{\epsilon_{mn} \cos\left(\frac{m\pi d_1}{a}\right) \cos\left(\frac{m\pi d_2}{a}\right)}{\alpha_{mn} \left[\left(\frac{m}{a}\right)^2 + \left(\frac{n}{b}\right)^2\right]} \cdot [e^{-\alpha_{mn}\Delta a} + 2e^{-\alpha_{mn}\Delta b} + e^{-\alpha_{mn}\Delta d}], \quad (34)$$

$$\begin{aligned} P \simeq \frac{2 \sin(k\Delta)}{k\pi^3} & \left\{ -ab [\log(1 - e^{-(\pi/b)(d_1+d_2)})] \right. \\ & \cdot (1 - e^{-(\pi/b)(d_1-d_2)}) (1 - e^{-(\pi/b)(2a-d_1-d_2)}) \\ & \cdot (1 - e^{-(\pi/b)(2a-|d_1-d_2|})] + \pi \left[ \frac{a^2}{3} + \frac{d_1^2 + d_2^2}{2} \right. \\ & \left. \left. - a \max\{d_1, d_2\} \right] - \frac{2a^2 c_1 c_2}{\pi} \right\}, \end{aligned} \quad (35)$$

and

$$R = -j \frac{abl}{\pi^4} \left\{ e^{-jk z_0} \left[ \int_{x'}^{x_0'} + \int_{y''}^{y_0''} \right] \frac{e^{-it}}{t} dt \right. \\ \left. + e^{+jk z_0} \left[ \int_{x''}^{x_0''} + \int_{y'}^{y_0'} \right] \frac{e^{-it}}{t} dt \right\}, \quad (36)$$

where

$$\begin{aligned} x_0' &= k(\sqrt{\delta^2 + z_0^2} - z_0), \\ x_0'' &= k(\sqrt{\delta^2 + z_0^2} + z_0), \\ x' &= k(\sqrt{\delta^2 + (2l + z_0)^2} - 2l - z_0), \\ x'' &= k(\sqrt{\delta^2 + (2l - z_0)^2} - 2l + z_0), \\ y' &= k(\sqrt{\delta^2 + (2l + z_0)^2} + 2l + z_0), \\ y'' &= k(\sqrt{\delta^2 + (2l - z_0)^2} + 2l - z_0). \end{aligned} \quad (37)$$

The simplification of the terms  $P$  and  $R$  is particularly important. The series expression for  $P$  in (31) is very slowly converging, but this may be converted to a rapidly converging series only the first term of which is included in (35), since it may be shown that in practice the error introduced by neglecting the remaining terms is less than 0.01 per cent. The integrals occurring in equation (36) for  $R$  may be expressed in terms of the well-tabulated Sine and Cosine Integrals.

Equations (33) through (36) were used in all the calculations of  $\sum_0$ . It was found that 26 terms of the series for  $N$  were more than enough for 1 per cent accuracy.



# A Wide-Band Transverse-Slot Flush-Mounted Array\*

E. M. T. JONES† AND J. K. SHIMIZU†

**Summary**—This paper describes the design analysis and measured performance of an antenna composed of an  $H$ -plane array of parallel waveguides having quarter-wavelength-thick transverse slots extending completely across the array. Each relatively wide nonresonant slot in this array radiates only a small amount of power, and the dimensions of the slots are relatively uncritical. The radiated  $H$  field from this antenna lies parallel to the transverse slots. The cosine of the angle between the direction of maximum radiation and the plane of the antenna is equal to the velocity of light divided by the phase velocity of propagation along the array.

An experimental antenna was built with a radiating aperture 9 inches wide and 20 inches long. The antenna was fed from a hog horn which yielded an approximately sinusoidal  $H$ -plane illumination over the 9-inch aperture width. The power coupled from the transverse slots was varied along the 20-inch length of the aperture to achieve a Taylor aperture distribution with  $-25$ -db  $E$ -plane sidelobes. At the design frequency of 11 kmc, the  $E$ -plane and  $H$ -plane beamwidths were  $5.4^\circ$  and  $7.3^\circ$ , while the  $E$ -plane and  $H$ -plane first-sidelobe levels were  $-24.7$  db and  $-24.2$  db, respectively, in close agreement with theoretical expectations. The direction of maximum radiation was within  $0.35^\circ$  of the design value at 11 kmc. Good radiation patterns were obtained with the antenna from 7.0 kmc, which is slightly above the cutoff frequency of the guides, to 11.4 kmc, which is slightly below the frequency at which spurious lobes are generated by the widely-spaced slots.

## INTRODUCTION

THIS PAPER describes the design and measured performance of a wide-band flush-mounted antenna consisting of an  $H$ -plane array of waveguides having quarter-wavelength-thick slots extending completely across the array.<sup>1,2</sup> A photograph of the experimental model of this antenna is shown in Fig. 1.



Fig. 1—Photograph of the experimental antenna.

\* Manuscript received by the PGAP, December 4, 1959; revised manuscript received, February 19, 1960.

† Electromagnetics Lab., Stanford Res. Inst., Menlo Park, Calif.

<sup>1</sup> R. S. Elliott, "Serrated waveguide—Part I: theory," IRE TRANS. ON ANTENNAS AND PROPAGATION, vol. AP-5, pp. 270-275; July, 1957.

<sup>2</sup> K. C. Kelly and R. S. Elliott, "Serrated waveguide—Part II: experiment," IRE TRANS. ON ANTENNAS AND PROPAGATION, vol. AP-5, pp. 276-283; July, 1957.

This antenna radiates a pencil beam whose  $H$  field lies parallel to the radiating slots. The elevation angle  $\theta_0$  of the beam measured from the surface of the antenna is related to the velocity of light  $c$  and the phase velocity  $v_\phi$  of propagation along the array by the expression

$$\cos \theta_0 = \frac{c}{v_\phi} \quad (1)$$

Because  $v_\phi$  changes with frequency, the antenna scans in the  $E$  plane with frequency.

The radiating slots in this antenna are made one-quarter wavelength thick, so that they will each couple only a small amount of power from the waveguides and at the same time introduce such a small reactive loading that they will not appreciably perturb the phase velocity of propagation in the waveguides. The amount of power coupled from each slot is proportional to the square of its width. Therefore, it is possible to design this antenna to have a wide variety of aperture distributions by appropriately adjusting the various slot widths.

The technique used to calculate the coupling from the slots in this array is an approximate one and hence cannot be expected to yield as precisely predictable radiation patterns as were achieved by Honey,<sup>3</sup> who used the exact transverse-resonance analysis technique. Nevertheless, the measured performance of this antenna agrees quite closely with the theoretical predictions and it is believed that the method of analysis employed here may be safely used to design this type of antenna to have a wide variety of useful radiation patterns.

## THEORETICAL ANALYSIS OF THE TRANSVERSE-SLOT ANTENNA

In order to design this type of antenna to have a specified aperture distribution, and therefore a specified radiation pattern, it is necessary to know the amount of power coupled out of each slot. In addition, there are local nonpropagating fields at both the inside and the outside ends of the coupling slots which increase the effective electrical thickness of the coupling apertures. Therefore, it is necessary to make the physical thickness  $l'$  less than one-quarter wavelength so that the effective electrical thickness of the slots will be one-quarter wavelength. In this paper, the amount of power coupled from each slot is determined by the approximate solution of the boundary value problem. The increase in electrical thickness of the coupling slots is determined approxi-

<sup>3</sup> R. C. Honey, "A flush-mounted leaky-wave antenna with predictable patterns," IRE TRANS. ON ANTENNAS AND PROPAGATION, vol. AP-7, pp. 320-329; October, 1959.

mately using appropriate equivalent circuits in the "Waveguide Handbook."<sup>4</sup>

In the theoretical analysis, it is assumed that the radiating surface of the antenna has infinite width and length, and that the width  $b'$  of the coupling slots does not vary in the direction of propagation. The results so obtained should be quite accurate for antennas whose width and length are on the order of 8 wavelengths or more, and for antennas whose slot widths do not change too rapidly along the array.

The amount of power coupled from each slot is determined in the following manner (the notation is illustrated in Fig. 2): waves propagating down each of the waveguides in the arrays will have transverse magnetic fields of the form

$$H_x(x) = H_x \sin \frac{\pi x}{a} \quad (2)$$

The dominant TEM mode will propagate in each of the slots. Thus the magnetic field  $H_x'$  at the inside edge of the coupling slot is constant with  $x$ . If one assumes that very little power is coupled from the waveguides by each coupling slot, it is seen that the average value of the waveguide transverse magnetic field, averaged over the distance  $a+t$ , must be equal to  $H_x'$  at the inside edge of the coupling slot. Therefore

$$H_x' = \frac{2}{\pi} \frac{a}{a+t} H_x \quad (3)$$

The dominant mode electric field  $E_x'$  at the outside edge of the coupling slot, one-quarter wavelength removed from the inside edge, is (in mks units)

$$E_x' = \eta H_x' \quad (4)$$

where  $\eta = 377$  ohms is the impedance of free space.

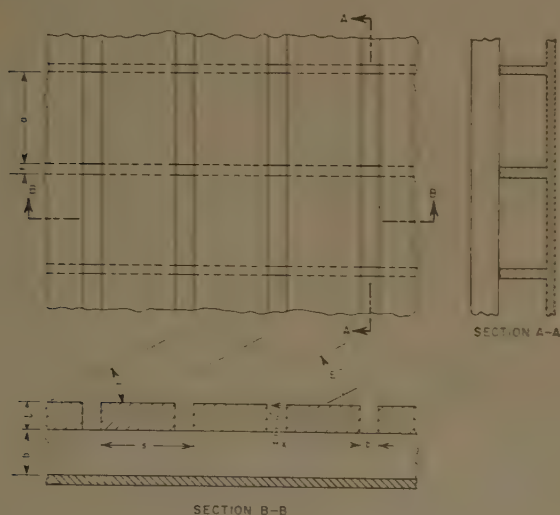


Fig. 2—Sketch illustrating the notation used in the analysis.

Maximum radiation from the array occurs at the angle  $\theta_0$ , defined by (1). Because the amount of power radiated from each slot is small, it is permissible to assume that each aperture radiates into a hypothetical tube of infinite width in the  $x$  direction and of height  $s \sin \theta_0$ . The strength of the electric field  $E''$  in this tube is determined by the condition that the voltage across the radiating aperture  $E'b'$  is equal to the voltage  $E''s \sin \theta_0$  across the tube. Therefore

$$E'' = \frac{E_x' b'}{s \sin \theta_0} \quad (5)$$

The peak power  $P$  radiated into one of the tubes of width  $(a+t)$  is

$$P = \frac{E''^2}{\eta} (a+t) s \sin \theta_0 \quad (6)$$

Substituting (3)–(5) into (6), one finds that

$$P = \eta \frac{4a^2 b'^2 H_x^2}{\pi^2 (a+t) s \sin \theta_0} \quad (7)$$

The peak power  $P_0$  transmitted along one of the waveguides in the array is

$$P_0 = \eta \frac{\lambda_g}{\lambda} \frac{ab H_x^2}{2} \quad (8)$$

Thus it is seen that

$$\frac{P}{P_0} = \frac{8}{\pi^2} \frac{\lambda}{\lambda_g} \frac{ab'^2}{(a+t)bs \sin \theta_0} \quad (9)$$

The neper attenuation  $\alpha_s$  of a wave in the feeding waveguides along a distance  $s$  is, by definition, equal to  $P/2P_0$ .

Therefore we have, finally,

$$\alpha_s = \frac{4}{\pi^2} \frac{\lambda}{\lambda_g} \frac{ab'^2}{(a+t)bs \sin \theta_0} \quad (10)$$

The effect of the local fields at either end of a coupling slot is conveniently represented by lumped susceptances located at the inside and outside edges of the slot. The local fields on the outside of a slot are similar to those existing on one side of an infinite grating of capacitive strips. Therefore, the equivalent lumped susceptance at the outer edge of the aperture is approximately equal to one-half the equivalent susceptance  $B_0$  of the capacitive grating. The expression for this susceptance is<sup>5</sup>

$$\frac{B_0}{Y_0'} \cong \frac{2b'}{\lambda} \ln \frac{2s}{\pi b'} \quad (11)$$

where  $Y_0'$  is the characteristic admittance of the TEM transmission line forming the thick slot.

<sup>4</sup> N. Marcuvitz, "Waveguide Handbook," McGraw-Hill Book Co., Inc., New York, N. Y.; 1951.

<sup>5</sup> *Ibid.*, p. 280.







11 kmc. The design elevation angle of the beam above the ground plane is  $36.6^\circ$  at 11 kmc so that no second-order lobes can be generated. The width of the slots was varied along the length of the array so that the amount of power radiated from each slot was different. The excitation of the slots was chosen to yield a far-field pattern with very nearly the narrowest possible beamwidth for a given maximum sidelobe level of  $-25$  db. The procedure for designing such arrays is described by Taylor.<sup>7</sup> The specified radiation pattern is given by

$$F(u) = \frac{\sin \pi u}{\pi u} \prod_{m=1}^2 \left\{ \frac{1 - \frac{u^2}{\sigma^2[A^2 + (m - \frac{1}{2})^2]}}{1 - \frac{u^2}{m^2}} \right\} \quad (16)$$

where

$$u = 2l/\lambda (\cos \theta - \cos \theta_0),$$

$2l$  = full length of the line source,

$\theta$  = angle of radiation measured from the plane of the aperture,

$\theta_0$  = angle of maximum radiation measured from the plane of the aperture,

$A^2 = 1.29177$ , since  $\cosh A$  is the inverse of the sidelobe voltage ratio and is equal to 17.7828, and

$\sigma^2 = 1.19336$ , a parameter given by Taylor for these requirements.

A plot of the theoretical radiation pattern of the antenna mounted in an infinite ground plane is shown in Fig. 6, together with the experimental pattern which was measured in a finite ground plane. The differences between the theoretical and experimental patterns are minor, thus verifying the design procedure. For example, the theoretical half-power beamwidth is  $5.5^\circ$  while the measured value is  $5.4^\circ$ . Similarly, the measured first-sidelobe level is  $-24.7$  db while the theoretical value is  $-25.5$  db. In the plane of the radiating aperture ( $\theta = 0$ ), the measured pattern is lower than the theoretical pattern, as expected, since at the horizon the pattern of a vertically-polarized antenna such as this one mounted in a finite horizontal ground plane is theoretically 6 db lower than the pattern of one mounted in an infinite plane. The sidelobes at elevation angles greater than  $90^\circ$  (which are shown in Fig. 9), corresponding to radiation back toward the feed, are probably caused by backward-traveling waves within the antenna reflected from the last slot. However, these lobes are below the unity gain level and should not be troublesome in practice. Comparison of the two patterns also reveals that there is probably a slight amount of phase error along the radiating aperture since there is a shoulder in the experimental pattern at the angular position of one of the first sidelobes of the theoretical pattern.

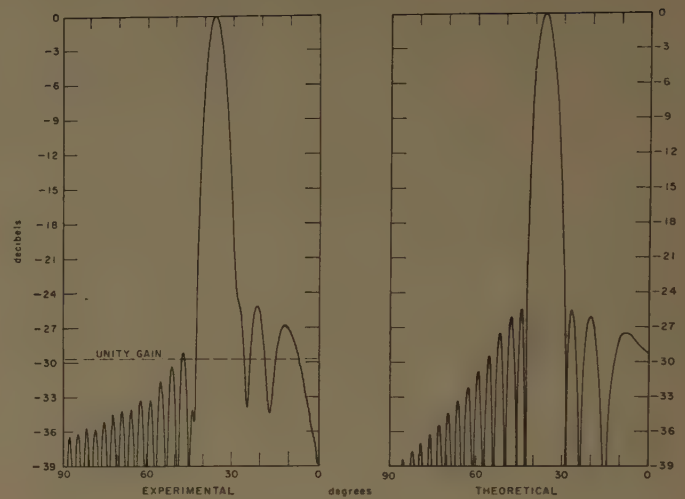


Fig. 6—Theoretical and experimental antenna radiation patterns.

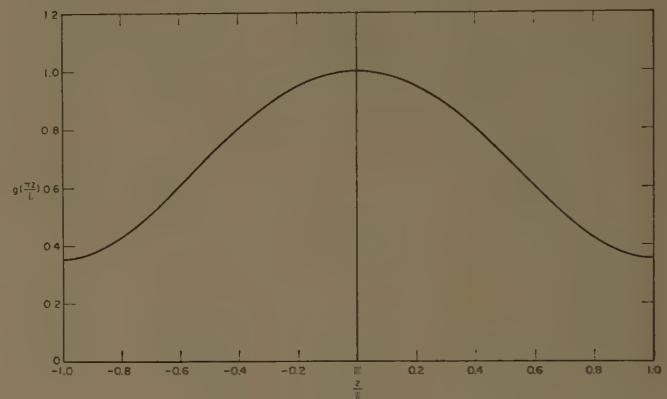


Fig. 7—Theoretical antenna aperture distribution.

The aperture distribution (normalized to a maximum value of unity) required to produce the theoretical radiation pattern is given by

$$g\left(\frac{\pi z}{l}\right) = \frac{1 + 0.4646 \cos \frac{\pi z}{l} - 0.0210 \cos \frac{2\pi z}{l}}{1.4436} \quad (17)$$

where  $z$  is zero at the center of the aperture. A plot of this aperture distribution is shown in Fig. 7.

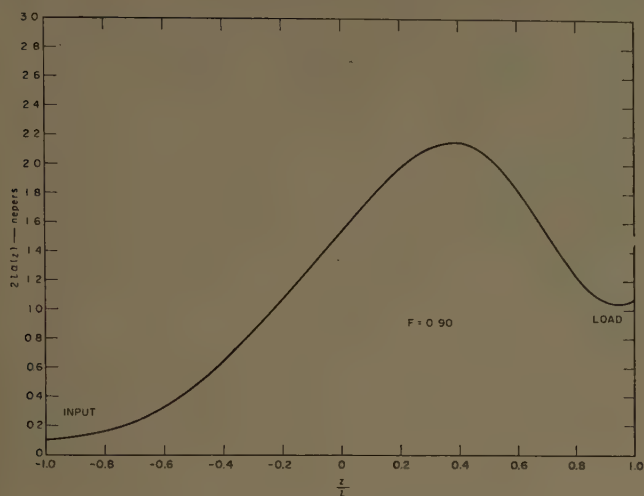
For an end-fed linear array the aperture distribution is related to the attenuation per slot  $s\alpha(z)$  along the array and is given by the following expression:

$$s\alpha(z) = \frac{1}{2} \frac{g^2\left(\frac{\pi z}{l}\right)}{\frac{1}{F} \int_{-l}^{+l} g^2\left(\frac{\pi \xi}{l}\right) d\xi - \int_{-l}^z g^2\left(\frac{\pi \xi}{l}\right) d\xi} \quad (18)$$

neper per slot

where  $\xi$  is the variable of integration along the aperture, and  $F$  is the fraction of the input power that is radiated by the antenna. For the experimental antenna,  $F = 0.90$

<sup>7</sup> T. T. Taylor, "Design of line-source antennas for narrow beamwidth and low side lobes," IRE TRANS. ON ANTENNAS AND PROPAGATION, vol. AP-3, pp. 16-28; January, 1955.

Fig. 8—Plot of  $2la(z)$  along the aperture.

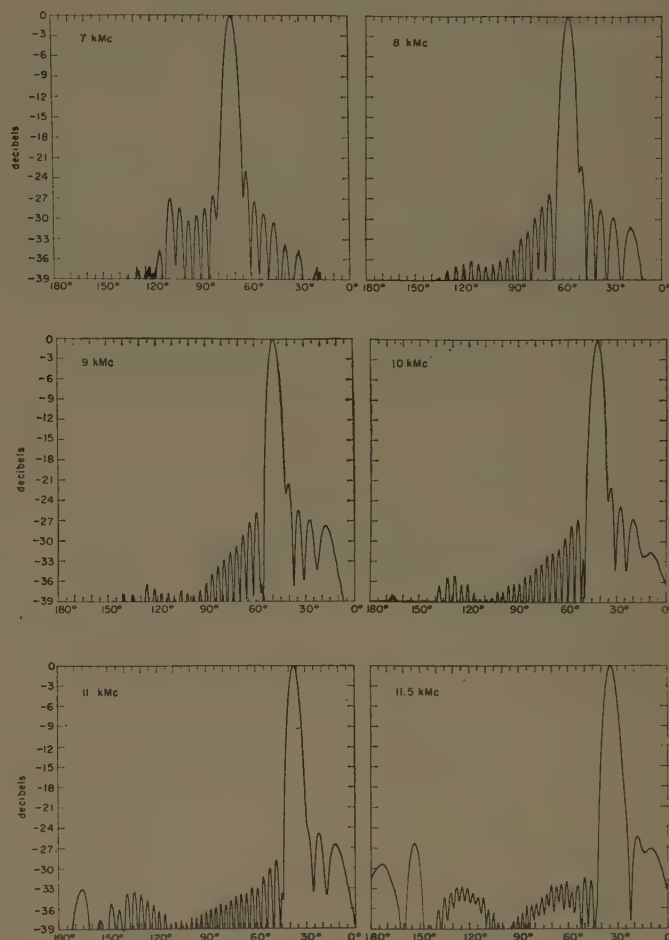
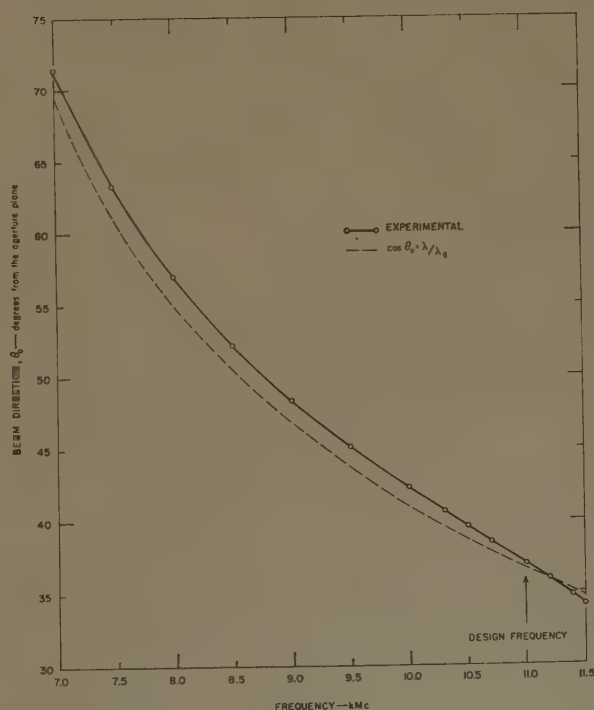
was chosen. A plot of  $2la(z)$  which is easily obtained from (18) is shown in Fig. 8.

An initial design for the antenna was made, using (10), (15),<sup>8</sup> and (18), with  $b$  held fixed at the value of 0.400 inch. Near the center of the radiating aperture,  $l'$  is substantially less than one-quarter wavelength. Therefore this design requires that if the outer surface of the antenna is to be flat, the bottom surfaces of the feeding waveguides must be curved.

Because it would be very difficult to curve the bottom surfaces of the waveguides, the  $b'$  values of the initial design were modified so that the distance from the bottom surface of each waveguide to the outer surface of the antenna was constant (*i.e.*,  $b + l' = \text{constant}$ ). The dimensions so obtained are shown in Fig. 3.

The measured  $E$ -plane radiation patterns of this antenna are shown in Fig. 9 at frequencies of 7, 8, 9, 10, 11, and 11.5 kmc. Patterns measured at 7.5, 8.5, 9.5, and 10.5 kmc, but not shown, are similar. From 7 to 11.5 kmc, the patterns show sidelobe levels that are nearly the same as those obtained at the design frequency. At 12 kmc, the measured pattern (not shown) is distorted because the slots are spaced on 0.545-wavelength centers, which is a great enough separation to allow them to generate spurious beams.

Fig. 10 shows a plot of the measured  $E$ -plane beam elevation angle compared with the angle predicted by (1) under the assumption that the phase velocity of propagation along the array is the same as that along an unloaded waveguide of the same width,  $a$ . At 11 kmc, the difference between the theoretical and experimental beam angles is only  $0.35^\circ$ . Surprisingly, inspection of the figure shows that even at frequencies far removed from

Fig. 9—Measured  $E$ -plane radiation patterns.Fig. 10—Measured  $E$ -plane beam elevation angle compared with theoretical.

<sup>8</sup> Actually, the values of  $l'$  were determined from the formula

$$l' = \frac{\lambda}{4} - \frac{2b'}{\pi} \left( 1 + 0.6 \ln \frac{2s}{\pi b'} + \ln \frac{b}{2b'} \right)$$

which differs from (15) by a maximum of 9 per cent for the largest values of  $b'$ . However, it is believed that (15) is the more accurate expression and should be used in future designs.

the design frequency, the beam elevation angle is very close to the theoretical value. Thus it appears that the actual thickness of the radiating slots is not a very critical dimension.

The  $E$ -plane 3-db beamwidth of the antenna is shown in Fig. 11 as a function of frequency. If the  $E$ -plane beam elevation angle were that given by the theoretical curve in Fig. 10, the ratio of projected aperture to wavelength would be constant. If, in addition, the aperture distribution were independent of frequency, the  $E$ -plane beamwidth would be independent of frequency. The constancy of  $E$ -plane beamwidth shown in Fig. 11 indicates that these two conditions are nearly satisfied in this antenna.

Fig. 12 shows the measured  $H$ -plane patterns of the antenna for the frequencies 7, 8, 9, 10, 11, and 11.5 kmc. Shown for comparison is the  $H$ -plane pattern of the hog horn alone measured at 11 kmc. The measured first-sidelobe level of  $-21.0$  db is consistent with the approximately sinusoidal aperture distribution of the hog horn. The variation in the shape and beamwidth of the  $H$ -plane patterns of the array is presumably due to

phase errors in the  $H$ -plane aperture illumination caused by multiple reflections set up in the hog horn between the parabolic reflecting surface and the ends of waveguides in the array.

The gain of the array, relative to an isotropic antenna, as a function of frequency is shown in Fig. 13. From about 8 kmc to 11.5 kmc, the gain of the antenna increases slightly because the  $H$ -plane beamwidth of the antenna decreases. Below 8 kmc, the gain drops sharply.

The VSWR of this antenna (shown in Fig. 14) is measured at the input to the throat of the hog horn, and is due primarily to reflections at the junction between the hog horn and the array waveguides. Shown for comparison is the approximate theoretical VSWR, which is the ratio of guide wavelength in the array waveguides to free-space wavelength.

The measured fraction  $F$  of the power radiated divided by the power transmitted down the guides is shown in Fig. 15.  $F$  was determined from the measured insertion loss,  $L$ , of the central waveguide of the array by means of the relation

$$F = 1 - \frac{1}{L}. \quad (19)$$

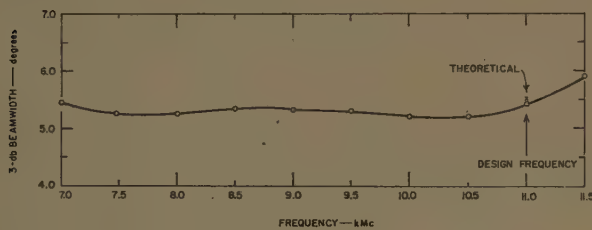


Fig. 11— $E$ -plane beamwidth vs frequency.

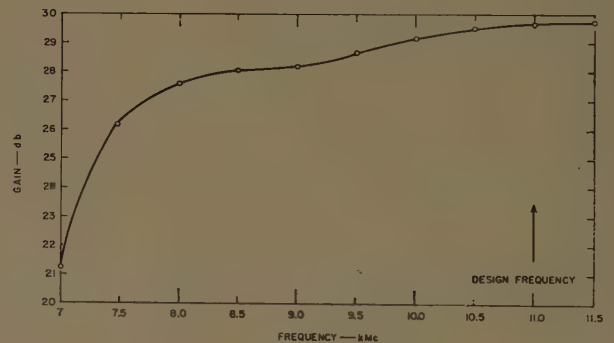


Fig. 13—Measured gain vs frequency.

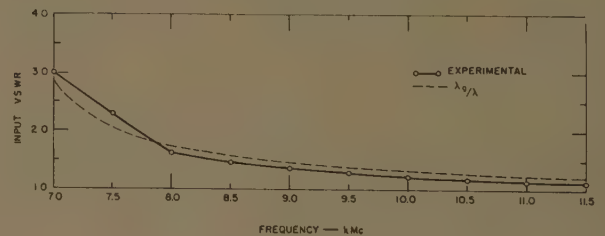


Fig. 14—Measured VSWR.

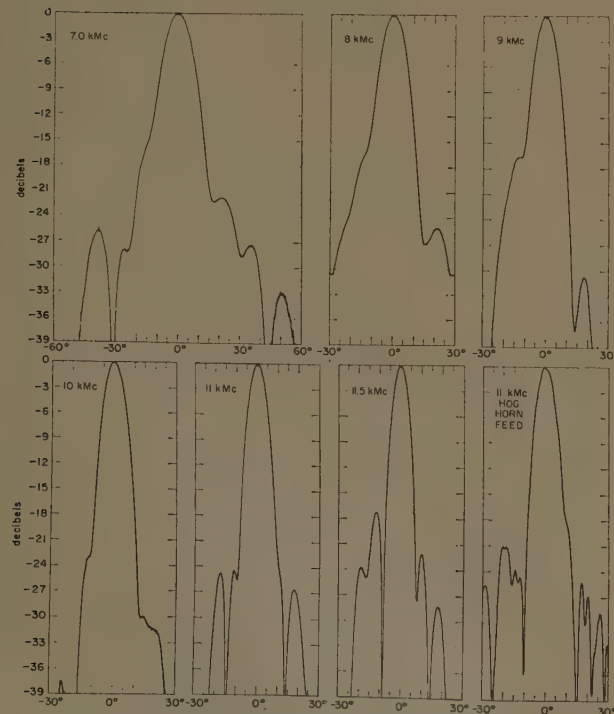


Fig. 12—Measured  $H$ -plane radiation patterns.

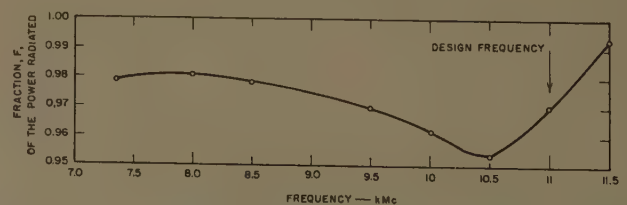


Fig. 15—Measured fraction  $F$  of the available power radiated by the antenna.



The insertion loss was measured as the ratio of the power received by a matched detector placed on the central waveguide of an array of nine waveguides with no radiating slots and the same length as the slotted array when fed by the hog horn, to the power received by the same matched detector placed at the end of the central waveguide of the array, with its matched load removed, and also connected to the hog horn. At the design frequency of 11 kmc, the measured insertion loss of the array was 15.3 db, corresponding to an  $F$  value of 0.97, which is 7 per cent higher than the theoretical  $F$  value of 0.90. Thus, the experimental antenna radiated 7 per cent more power than expected, which increases its gain by about 0.33 db. Some idea of the magnitude of the increase in power coupling from each slot in the antenna to cause it to radiate this increased power can be obtained by considering a hypothetical antenna with uniform-width slots designed to have an  $F$  value of 0.90. If this antenna were found to have a measured  $F$  value of 0.97, it would mean that each slot radiated 1.54 db more power than desired. Because the theoretical analysis presented here is most accurate for narrow slots, it is likely that the power radiated by the narrow slots in the experimental antenna is almost that predicted by the theory, while the power radiated by the wide slots

is at least 1.54 db greater than predicted by theory. Thus it appears likely that the actual aperture distribution of the experimental antenna is asymmetrical and has an amplitude at the load end of the antenna a few decibels higher than at the feed end. Honey<sup>9</sup> has shown that if one takes an aperture distribution yielding a Taylor radiation pattern with -35-db sidelobes, and superimposes on the aperture distribution a 10-db exponential taper, the altered radiation pattern will have only a 1 per cent wider beamwidth and -34-db sidelobes. Therefore, it is not surprising that the slight asymmetry in the aperture distribution of the antenna described here has very little effect on the radiation pattern.

#### CONCLUSION

The measured performance of the wide-band, transverse-slot, flush-mounted, antenna array agrees well in all essential points with the theoretical analysis. Therefore, it is believed that the analysis presented here may be safely used to design this type of antenna to have a wide variety of pattern shapes for various applications.

<sup>9</sup> R. C. Honey, L. A. Robinson, and J. K. Shimizu, "Antenna Design Parameters," Stanford Res. Inst., Menlo Park, Calif., Quart-Progr. Rept. 9, SRI Proj. 1954, Contract DA 36-039 SC-73106; March, 1959.

## Relation Between a Class of Two-Dimensional and Three-Dimensional Diffraction Problems\*

L. B. FELSEN† AND S. N. KARP‡

**Summary**—By means of a certain transformation, a relationship is demonstrated between a class of two-dimensional and three-dimensional scalar or electromagnetic diffraction problems. The basic three-dimensional configuration consists of a perfectly reflecting half plane excited by a ring source centered about the edge and having a variation  $\exp(\pm i\phi/2)$ , where  $\phi$  is the azimuthal variable; in addition, a perfectly reflecting rotationally symmetric obstacle whose surface is defined by  $f(\rho, z) = 0$  ( $\rho, z$  are cylindrical coordinates) may be superposed about the edge ( $z$  axis). This problem is shown to be simply related to the two-dimensional problem for the line source excited configuration  $f(y, z) = 0$ , where  $y$  and  $z$  are Cartesian coordinates. Various special obstacle configurations are treated in detail.

\* Manuscript received by the PGAP, May 25, 1959; revised manuscript received, December 22, 1959.

† Microwave Res. Inst., Polytechnic Inst. of Brooklyn, Brooklyn 1, N. Y.

‡ Inst. of Mathematical Sciences, New York University, New York, N. Y.

For the general case of arbitrary electromagnetic excitation, the above-mentioned transformation is used to construct the solution for the diffraction by a perfectly conducting half plane from the knowledge of appropriate scalar solutions, namely those which obey the same equations and boundary conditions, and have the same excitations, as the Cartesian components of the electromagnetic field.

#### INTRODUCTION

THIS paper deals with the relationship between a special class of two-dimensional and three-dimensional diffraction problems. The basic three-dimensional configuration consists of a perfectly reflecting half plane excited by a ring source centered at the edge of the plane, with the plane of the loop oriented perpendicular to the edge, as shown in Fig. 1(a); the strength of the source, either scalar or electromagnetic, varies as  $\sin(\phi/2)$  or  $\cos(\phi/2)$ , where  $\phi$  is the azimuthal

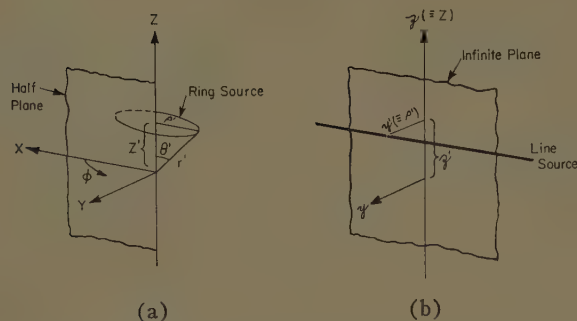


Fig. 1—Basic equivalent configurations: (a) three-dimensional and (b) two-dimensional.

angular variable. Via the transformation to be described below, the cylindrical coordinate  $\rho = r \sin \theta$  in Fig. 1(a) transforms into the  $y$  coordinate in Fig. 1(b), while the  $Z$  coordinate is preserved (the  $x$  coordinate does not occur in the two-dimensional problem). The three-dimensional configuration in Fig. 1(a) is thereby transformed into the two-dimensional one in Fig. 1(b) consisting of a uniform line-source parallel to a perfectly reflecting infinite plane. It is evident that any surface with rotational symmetry about the  $Z$  axis of Fig. 1(a), and described by the equation  $f(\rho, Z) = 0$ , is mapped by this transformation into the two-dimensional configuration  $f(y, Z) = 0$  in the presence of the infinite plane at  $y = 0$ . Some special structures in this category are listed in Fig. 2. We shall show how we can generate solutions for such ring-source-excited three-dimensional configurations involving an infinite half plane, from the knowledge of the two-dimensional results.

As a further application, it will be shown how the above-mentioned transformation can be employed to construct the electromagnetic field caused by an arbitrary source distribution in the presence of a perfectly conducting half-plane. The construction is carried out explicitly in terms of the solutions of the corresponding scalar Dirichlet and Neumann problems. The problem has been solved previously by Heins,<sup>1</sup> Senior,<sup>2</sup> and Vandakurov<sup>3</sup> for various dipole excitations through the use of methods which differ from each other and from the present one. The procedure we employ exhibits explicitly the modifications necessary in order to convert the scalar solutions into vector solutions. Thus, we start with the scalar wave functions corresponding to excitations which are Cartesian components of the arbitrarily prescribed vector excitation and which are assumed to be known. The vector solution is then constructed from these scalar solutions.

<sup>1</sup> A. E. Heins, "The excitation of a perfectly conducting half-plane by a dipole field," *IRE TRANS. ON ANTENNAS AND PROPAGATION*, vol. AP-4, pp. 294-296; July, 1956.

<sup>2</sup> T. B. A. Senior, "The diffraction of a dipole field by a perfectly conducting half-plane," *Quart. Mech. and Appl. Math.*, vol. 6, pp. 101-114; 1953.

<sup>3</sup> Yu. V. Vandakurov, "Diffraction by a perfectly conducting half-plane of electromagnetic waves emitted by an arbitrarily oriented electric and magnetic dipole," (Translated by M. D. Friedman, AFRCRC, Bedford, Mass.) *J. Exp. Theoret. Phys., USSR*, vol. 26, pp. 3-18. Tech. Translation No. 1; 1954.



(a) Sphere and cylinder.



(b) Cone and wedge.



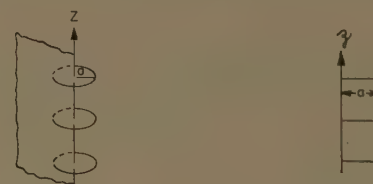
(c) Flat ring, and strip.



(d) Semi-infinite cylinder and semi-infinite plane.



(e) Infinite coaxial cylinders and infinite parallel planes.



(f) Array of disks and array of strips.

Fig. 2—Equivalent configurations: left column—three-dimensional; right column—two-dimensional.

## RELATION BETWEEN THREE- AND TWO-DIMENSIONAL PROBLEMS

### Scalar Problems

We define the even and odd Green's functions  $G_e(\mathbf{r}; \mathbf{r}', \theta')$  and  $G_o(\mathbf{r}; \mathbf{r}', \theta')$  appropriate to the ring-source-excited half plane in Fig. 1(a) as

$$G_{e,o}(\mathbf{r}; \mathbf{r}', \theta') = r' \sin \theta' \int_0^{2\pi} \begin{Bmatrix} \cos(\phi'/2) \\ \sin(\phi'/2) \end{Bmatrix} \mathcal{G}_{e,o}(\mathbf{r}, \mathbf{r}') d\phi',$$

$$\mathbf{r} = (r, \theta, \phi), \quad (1)$$

where  $\mathcal{G}_e(\mathbf{r}, \mathbf{r}')$  and  $\mathcal{G}_o(\mathbf{r}, \mathbf{r}')$  are the three-dimensional Green's functions satisfying the inhomogeneous wave equation

$$\left( \nabla_{r\theta}^2 + \frac{1}{r^2 \sin^2 \theta} \frac{\partial^2}{\partial \phi^2} + k^2 \right) G_{e,0}(r, \theta) = - \frac{\delta(r-r')\delta(\theta-\theta')\delta(\phi-\phi')}{r'^2 \sin \theta'} \quad (2a)$$

$$\nabla_{r\theta}^2 = \frac{1}{r^2} \frac{\partial}{\partial r} r^2 \frac{\partial}{\partial r} + \frac{1}{r^2 \sin \theta} \frac{\partial}{\partial \theta} \sin \theta \frac{\partial}{\partial \theta}, \quad (2b)$$

in the domain  $0 \leq r < \infty$ ,  $0 \leq \theta \leq \pi$ ,  $0 \leq \phi \leq 2\pi$ , with the boundary conditions on the half plane

$$\frac{\partial G_e}{\partial \phi} = 0, \quad G_0 = 0, \quad \text{at } \phi = 0, 2\pi, \quad (3a)$$

the edge condition<sup>4</sup>

$$G_{e,0} \text{ finite at } \rho = r \sin \theta \rightarrow 0, \quad (3b)$$

and also the

$$\text{radiation condition at } r \rightarrow \infty. \quad (3c)$$

One notes from (1) that  $G_e$  and  $G_0$  are excited by ring sources with  $\cos(\phi/2)$  and  $\sin(\phi/2)$  variation, respectively. Since the sets of functions  $w_e(\phi) = \cos(n\phi/2)$ ,  $n=0, 1, 2, \dots$ , and  $w_0(\phi) = \sin(n\phi/2)$ ,  $n=1, 2, \dots$ , each constitute a complete orthogonal set in the angular domain  $0 \leq \phi \leq 2\pi$  subject to the boundary conditions  $dw_e/d\phi=0$ ,  $w_0=0$  at  $\phi=0, 2\pi$ , these sources generate fields which vary everywhere as  $\cos(\phi/2)$  and  $\sin(\phi/2)$ , respectively. It follows that we may represent  $G_{e,0}$  as

$$G_{e,0}(r; r', \theta') = \begin{cases} \cos(\phi/2) \\ \sin(\phi/2) \end{cases} G(\varrho, \vartheta'), \quad \varrho = (r, \theta), \quad (4)$$

where  $G$  satisfies the following equation in view of (1), (2a) and (4):

$$\left( \nabla_{r\theta}^2 - \frac{1}{4r^2 \sin^2 \theta} + k^2 \right) G(\varrho, \vartheta') = - \frac{\delta(r-r')\delta(\theta-\theta')}{r'} \quad (5)$$

with boundary conditions as in (3b) and (3c).

We now introduce the transformation

$$G(\varrho, \vartheta') = \sqrt{\frac{\rho'}{\rho}} \bar{G}(\varrho, \vartheta'), \quad \rho = r \sin \theta, \quad 0 \leq \rho < \infty \quad (6)$$

into (5), and find that  $\bar{G}$  satisfies

$$\left( \frac{1}{r} \frac{\partial}{\partial r} r \frac{\partial}{\partial r} + \frac{1}{r^2} \frac{\partial^2}{\partial \theta^2} + k^2 \right) \bar{G}(\varrho, \vartheta') = - \frac{\delta(r-r')\delta(\theta-\theta')}{r'}. \quad (7a)$$

If  $r$  and  $\theta$  in (7a) are interpreted as cylindrical coordinates in a Cartesian  $(y, z)$  space where

$$y = r \sin \theta, \quad 0 \leq y < \infty, \\ z = r \cos \theta, \quad -\infty < z < \infty, \quad (7b)$$

then one notes that (7a), together with the boundary conditions in (8) below, represents exactly the formulation for the two-dimensional Green's-function problem in Fig. 1(b). This establishes the desired relationship between the ring-source-excited three-dimensional problem and the line-source-excited two-dimensional problem. To avoid confusion between the spherical and cylindrical coordinate interpretations of  $r$  and  $\theta$  in (5) and (7a), respectively, we shall henceforth employ the rectangular  $(y, z)$  coordinate notation for the equivalent two-dimensional problem [see Fig. 1(b)]. Concerning the boundary conditions on  $\bar{G}$  in (7a), we impose the radiation condition at infinity, as before; and on the infinite plane at  $y=0$ , we require in view of (3b), (6), and (7b),

$$\bar{G} = 0 \quad \text{at } y = 0. \quad (8)$$

Since this implies that  $\bar{G} \propto y$  as  $y \rightarrow 0$ , it follows that  $G \propto \sqrt{\rho}$  as  $\rho \rightarrow 0$ , in conformity with the familiar edge requirement.<sup>4</sup>

The basic transformation employed above can also be expressed as the following theorem and its converse which are verifiable by direct calculation.

*Theorem:* If

$$X = r \sin \theta \cos \phi; \quad Y = r \sin \theta \sin \phi; \quad Z = r \cos \theta; \quad (9a)$$

$$\rho \equiv y = r \sin \theta; \quad Z \equiv z = r \cos \theta,$$

$$\frac{\partial^2 \bar{u}}{\partial \rho^2} + \frac{\partial^2 \bar{u}}{\partial z^2} + k^2 \bar{u} = 0; \quad \bar{u} = \bar{u}(\rho, z) \equiv \bar{u}(y, z),$$

$$U(X, Y, Z) = \frac{1}{\sqrt{\rho}} \exp(\pm i\phi/2) \bar{u}(\rho, z),$$

then

$$\left( \frac{\partial^2}{\partial X^2} + \frac{\partial^2}{\partial Y^2} + \frac{\partial^2}{\partial Z^2} + k^2 \right) U(X, Y, Z) = 0. \quad (9b)$$

Conversely, if (9b) is true, and

$$U(X, Y, Z) = \frac{1}{\sqrt{\rho}} \exp(\pm i\phi/2) \bar{u}(\rho, z),$$

then  $\bar{u}_{\rho\rho} + \bar{u}_{zz} + k^2 \bar{u} = 0$ .

If the configuration also includes a surface of revolution  $S$  defined by  $f(\rho, Z) = 0$ , all previous considerations apply except that, in addition, the boundary conditions on  $S$  must be taken into account. Since the surface  $S$  is independent of the  $\phi$  coordinate, the boundary conditions need be imposed only on  $G(\rho, Z; \rho', Z')$  along the curve  $f(\rho, Z) = 0$ . Let us assume the linear homogeneous

<sup>4</sup> J. Meixner, "Die Kantenbedingung in der Theorie der Beugung Elektromagnetischer Wellen an Vollkommen Leitenden Ebenen Schirmen," *Ann. der Phys.*, Series 6, vol. 6, pp. 2-9; 1949. See also *Z. Naturforsch.*, vol. 3a, p. 506; 1948.



boundary condition

$$G = \alpha \frac{\partial G}{\partial n} \quad \text{on } S, \quad \alpha = \text{constant}, \quad (10)$$

where  $n$  is the direction of the normal into  $S$ . Then the condition on  $\bar{G}$  is found via (6) as

$$\bar{G} = \alpha \left[ \frac{\partial}{\partial n} - \frac{1}{2y} \left( \frac{\partial y}{\partial \bar{n}} \right) \right] \bar{G} \quad \text{on } \bar{S}, \quad (11)$$

where  $\bar{S}$  is the curve  $f(y, z)=0$  and  $\bar{n}$  the direction of the normal into  $\bar{S}$ . One notes from (10) and (11) that for  $\alpha=0$ ,

$$\bar{G} = 0 \quad \text{on } \bar{S} \quad \text{if} \quad G = 0 \quad \text{on } S, \quad (12a)$$

while for  $\alpha = \infty$ ,

$$\frac{\partial \bar{G}}{\partial \bar{n}} = \frac{1}{2y} \left( \frac{\partial y}{\partial \bar{n}} \right) \bar{G} \quad \text{on } \bar{S} \quad \frac{\partial G}{\partial n} = 0 \quad \text{on } S. \quad (12b)$$

Thus, a Dirichlet condition ( $\alpha=0$ ) on  $S$  always implies the same condition on  $\bar{S}$ , whereas a Neumann condition ( $\alpha = \infty$ ) on  $S$  leads generally to a mixed boundary condition on  $\bar{S}$ , unless the obstacles are confined completely to the planes  $z=\text{constant}$ , in which case  $(\partial y/\partial \bar{n}) = \pm (\partial y/\partial z) = 0$ .

We have therefore shown how the solutions for any two-dimensional Dirichlet-type diffraction problem can be taken over to yield the solution for a corresponding three-dimensional Dirichlet problem with an azimuthal field variation as in (4). Typical examples for which exact two-dimensional solutions are known include the cylinder [Fig. 2(a)], the wedge [Fig. 2(b)],<sup>5</sup> the slit [Fig. 2(c), with  $b \rightarrow \infty$ ], the semi-infinite parallel-plane region [Fig. 2(d)] and the infinite parallel-plane region [Fig. 2(e)]. Approximate solutions are available for the infinite array of strips [Fig. 2(f)], and others. The corresponding three-dimensional Dirichlet problems solved thereby via (4) and (6) are also shown in Fig. 2. Concerning the Neumann-type boundary condition, solutions for the two-dimensional problems in Figs. 2(c) and 2(f) imply those for the corresponding three-dimensional case, as noted above. Moreover, for the configurations in Figs. 2(d) and 2(e), a Neumann condition on the cylindrical surfaces implies an impedance-type boundary condition on the corresponding two-dimensional plane surface since on a plane  $y=\text{constant}$ ,  $(1/y)(\partial y/\partial \bar{n})$  is equal to a constant. This solution is known for the infinite parallel-plane case. Similarly, the Neumann condition  $\partial G/\partial r=0$  at  $r=a$  appropriate to a sphere of radius  $a$  has for its two-dimensional equivalent the known solution for a cylinder with  $(\partial \bar{G}/\partial \bar{n}) = (1/2a)\bar{G}$ , while that for a cone,  $\partial G/\partial \theta=0$  at  $\theta=\theta_0$ , leads to

a simple two-dimensional wedge problem with  $\partial \bar{G}/\partial \theta = (1/2)(\cot \theta_0)\bar{G}$ .<sup>6</sup>

### Electromagnetic Problems

Now we show how the fields radiated in the presence of a perfectly conducting half plane by electromagnetic ring-source distributions with variations  $\cos(\phi/2)$  or  $\sin(\phi/2)$  can be inferred from the solution for a scalar line source in the presence of an infinite plane. The latter solution can, of course, be expressed simply in terms of the free space result plus its image. Several other boundary value problems are also discussed.

**Longitudinal Electric Currents:** The configuration is shown in Fig. 3. A source variation  $\sin(\phi/2)$  is assumed



Fig. 3—Ring of longitudinal current elements.

since a tangential electric source current element of finite strength cannot exist on a perfectly conducting sheet. The vector electric field  $\mathcal{E}(\mathbf{r}; \mathbf{r}', \theta')$  and magnetic field  $\mathcal{H}(\mathbf{r}; \mathbf{r}', \theta')$  radiated by this distribution of currents of unit strength are given in terms of the Hertzian vector  $\mathbf{z}_0 G_0$  by

$$\begin{aligned} \mathcal{E}(\mathbf{r}; \mathbf{r}', \theta) &= -\frac{\mathbf{Z}}{ik} \nabla \times \nabla \times [\mathbf{z}_0 G_0(\mathbf{r}; \mathbf{r}', \theta')], \\ \mathcal{H}(\mathbf{r}; \mathbf{r}', \theta') &= \nabla \times [\mathbf{z}_0 G_0(\mathbf{r}; \mathbf{r}', \theta')], \end{aligned} \quad (13)$$

where  $\mathbf{Z}$  is the characteristic impedance of free space and  $\mathbf{z}_0$  is a unit vector along the  $z$  direction. A time dependence  $\exp(-i\omega t)$  is implied. Since  $G_0$  as given in (4) can be related to the two-dimensional problem in Fig. 1(b) via (6), (7a) and (8), we can write the solution as

$$\begin{aligned} \mathcal{E}(\mathbf{r}; \mathbf{r}', \theta') &= -\frac{\mathbf{Z}}{ik} \sqrt{\rho'} \nabla \times \nabla \times \left[ \mathbf{z}_0 \frac{\sin(\phi/2)}{\sqrt{\rho}} \bar{G}(\theta, \theta') \right], \\ \rho &= r \sin \theta, \\ \bar{G}(\theta, \theta') &= \frac{i}{4} [H_0^{(1)}(k\sqrt{(\rho - \rho')^2 + (z - z')^2}) \\ &\quad - H_0^{(1)}(k\sqrt{(\rho + \rho')^2 + (z - z')^2})], \end{aligned} \quad (14a)$$

$$- H_0^{(1)}(k\sqrt{(\rho + \rho')^2 + (z - z')^2})], \quad (14b)$$

<sup>5</sup> For a detailed discussion of the relationship between the two-dimensional wedge problem and the corresponding three-dimensional cone problem, see L. B. Felsen, "Radiation from Source Distributions on Cones and Wedges," Microwave Res. Inst., Polytechnic Inst. of Brooklyn, Brooklyn, N. Y., Rept. No. R-574-57, pp. 4-16; May, 1957.

<sup>6</sup> L. B. Felsen, "Field Solutions for a Class of Corrugated Wedge and Cone Surfaces," Microwave Res. Inst., Polytechnic Inst. of Brooklyn, Brooklyn, N. Y., Electronics Group Memo. 32; July, 1957.

and similarly for  $\mathcal{H}$ .  $H_0^{(1)}(w)$  in (14b) is the Hankel function of the first kind of order zero and argument  $w$ .

The electric field components along the  $\rho$ ,  $\phi$ ,  $z$  directions are given from (13) by

$$\begin{aligned}\mathcal{E}_\rho &= -\frac{\mathcal{Z}}{ik} \frac{\partial^2 G_0}{\partial z \partial \rho}, & \mathcal{E}_\phi &= -\frac{\mathcal{Z}}{ik\rho} \frac{\partial^2 G_0}{\partial z \partial \phi}, \\ \mathcal{E}_z &= -\frac{\mathcal{Z}}{ik} \left( \frac{\partial^2}{\partial z^2} + k^2 \right) G_0,\end{aligned}\quad (15)$$

so that one verifies that  $\mathcal{E}_z$  and  $\mathcal{E}_\rho$  vanish on the half plane as required. Since  $\bar{G} \propto \rho$  as  $\rho \rightarrow 0$  one obtains the proper edge behavior,<sup>4</sup>

$$\begin{aligned}\mathcal{E}_\rho &\propto \rho^{-1/2} \sin(\phi/2), & \mathcal{E}_\phi &\propto \rho^{-1/2} \cos(\phi/2), \\ \mathcal{E}_z &\propto \rho^{1/2} \sin(\phi/2),\end{aligned}\quad (16)$$

and analogously for  $\mathcal{H}_\rho$  and  $\mathcal{H}_\phi$ . [Note:  $\mathcal{H}_z = 0$  from (13).]

It is noted from (15) that if  $G_0$  vanishes on the cylindrical surfaces  $\rho = a, b$ , then  $\mathcal{E}_\phi$  and  $\mathcal{E}_z$  likewise vanish. Thus, by inserting for  $\bar{G}$  in (14a) the Dirichlet parallel-plane Green's function [see Fig. 2(e)], we can construct the electromagnetic solution for the ring-source-excited perfectly conducting coaxial-waveguide region whose center conductor is supported by a radial fin. The limiting cases  $a \rightarrow 0$  or  $b \rightarrow \infty$  are also admitted. By employing the parallel-plane eigensolutions we may also determine those  $E$ -mode functions in the coaxial waveguide whose  $\mathcal{E}_z$  component has an azimuthal variation  $\sin(\phi/2)$  (only the  $E$  modes are excited by the present source distribution since  $\mathcal{H}_z = 0$  as noted above); the cutoff wavelengths for these modes are identical with those for  $E$  modes in the parallel-plane waveguide.

**Longitudinal Magnetic Currents:** The physical configuration is as in Fig. 3, where the source distribution is now taken as a ring of unit strength magnetic currents with variation  $\cos(\phi/2)$ . From considerations dual to those in the preceding section, we write down the magnetic vector field  $\mathcal{H}$  for this case as

$$\begin{aligned}\mathcal{H}(r; r', \theta') &= -\frac{\mathcal{Y}}{ik} \sqrt{\rho'} \nabla \times \nabla \times \left[ z_0 \frac{\cos(\phi/2)}{\sqrt{\rho}} \bar{G}(\varrho, \vartheta') \right] \\ \mathcal{Y} &= \frac{1}{\mathcal{Z}},\end{aligned}\quad (17)$$

where  $\bar{G}$  is given in (14b). The corresponding expression for the electric field  $\mathcal{E}$  has a form dual to that given for  $\mathcal{H}$  in (13).

For the perfectly conducting coaxial waveguide with the radial fin [Fig. 2(e)], it is required that  $\partial G_0 / \partial \rho = 0$  at  $\rho = a, b$  [compare (15), with  $\mathcal{E}, \mathcal{Z}, G_0$  replaced by  $\mathcal{H}, \mathcal{Y}, G_0$ , respectively]. The corresponding parallel-plane problem, therefore, is one for which the impedance boundary condition [compare (12b)]

$$\frac{\partial \bar{G}}{\partial y} = \mp \frac{1}{2y} \bar{G} \text{ at } y = a, b \quad (18)$$

applies. By employing the parallel-plane eigensolutions satisfying (18), we can construct via (17) those  $H$ -mode functions whose  $\mathcal{H}_z$  field component varies like  $\cos(\phi/2)$  in the coaxial waveguide with the radial fin. Again, the cutoff wavelengths for these modes in the coaxial guide are identical with those for the  $H$  modes in the parallel-plane guide with the impedance-type boundary conditions (18).

**Radial Electric Currents:** The physical configuration for a ring of electric currents of unit strength directed radially with respect to some arbitrarily chosen origin along the edge of the half plane and varying like  $\sin(\phi/2)$  is shown in Fig. 4. The electric and magnetic fields re-



Fig. 4—Ring of radial current elements.

sulting from this current distribution are given in terms of a radial Debye potential function  $rG_0$  by

$$\begin{aligned}\mathcal{E}(r; r', \theta') &= -\frac{\mathcal{Z}}{ik} \nabla \times \nabla \times \left[ \frac{r}{r'} G_0(r; r', \theta') \right], \\ \mathcal{H}(r; r', \theta') &= \nabla \times \left[ \frac{r}{r'} G_0(r; r', \theta') \right]\end{aligned}\quad (19)$$

where  $r = r_0 \mathbf{r}$ ,  $r_0$  is the radial unit vector; and where  $G_0$  is related to  $\bar{G}$  in (14b) via (4) and (6) by  $G_0 = \sqrt{\rho'/\rho} \sin(\phi/2) \bar{G}(\varrho, \vartheta')$ .

One finds from (19) that the  $r, \theta, \phi$ -components of the electric field depend on  $G_0$  in (4) in the following manner:

$$\begin{aligned}\mathcal{E}_r &\propto \left( \frac{1}{r^2} \frac{\partial}{\partial r} r^2 \frac{\partial}{\partial r} + k^2 \right) G_0, & \mathcal{E}_\theta &\propto \frac{1}{r} \frac{\partial^2}{\partial r \partial \theta} G_0, \\ \mathcal{E}_\phi &\propto \frac{1}{r \sin \theta} \frac{\partial^2}{\partial r \partial \phi} G_0.\end{aligned}\quad (20)$$

It is verified readily that the edge conditions (16) are satisfied as  $\rho \rightarrow 0$ . Furthermore, one notes that if  $G_0$ , and therefore  $\bar{G}$ , vanishes on the conical boundary  $\theta = \text{constant}$ , then  $\mathcal{E}_r$  and  $\mathcal{E}_\phi$  likewise vanish. Thus, (19) remains valid when a perfectly conducting cone is superposed on the edge, with apex at the origin, as in Fig. 2(b), provided that one inserts for  $\bar{G}$  the corresponding two-dimensional Dirichlet solution for the wedge.

If a perfectly conducting sphere with radius  $a$  and centered at the origin is superposed onto the half plane



[Fig. 2(a)], one notes from (20) that the required boundary conditions are met if  $\partial G/\partial r = 0$  at  $r = a$ . The corresponding boundary condition on the cylinder in the equivalent two-dimensional problem is given, as before, by  $\partial \bar{G}/\partial \bar{n} = (1/2a)\bar{G}$ , leading again to a known boundary value problem.

**Radial Magnetic Currents:** The magnetic field radiated by a ring source of unit strength radial magnetic current elements as in Fig. 4 is obtained from an expression dual to that in (19) [a  $\cos(\phi/2)$  source variation is assumed]:

$\mathcal{H}(r; r', \theta')$

$$= -\frac{Y\sqrt{\rho'}}{ikr'} \nabla \times \nabla \times \left[ r \frac{\cos(\phi/2)}{\sqrt{\rho}} \bar{G}(\theta, \theta') \right] \quad (21)$$

with  $\bar{G}$  given in (14b). The corresponding expression for  $\mathcal{E}$  has a form dual to that for  $\mathcal{H}$  in (19).

If a perfectly conducting sphere with radius  $a$  is centered at the origin as in Fig. 2(a), the required boundary conditions on  $\mathcal{H}$  in (21) are satisfied if  $G = 0$  at  $r = a$ , leading to the equivalent two-dimensional Dirichlet problem for the cylinder. For a perfectly conducting conical boundary at  $\theta = \theta_0$  [Fig. 2(b)], the required boundary condition is  $\partial G/\partial \theta = 0$  at  $\theta = \theta_0$ , leading via (12b) to the previously-mentioned equivalent two-dimensional wedge problem with  $\partial \bar{G}/\partial \theta = (1/2)(\cot \theta_0)\bar{G}$ .

#### DIFFRACTION OF ELECTROMAGNETIC FIELDS BY A PERFECTLY CONDUCTING HALF PLANE

In the previous section we considered some electromagnetic problems arising from source distributions having a special angular dependence. However, our basic formulas [(9a) and (9b)] can also be used to good purpose in deducing the effect of a conducting half plane on general incident fields, as we shall see below.<sup>7</sup>

We consider the problem of diffraction of an arbitrary vector electromagnetic field by a perfectly conducting half plane. The half plane is defined by  $Y = 0, X > 0$  as in Fig. 1(a). We use two sets of coordinates, the Cartesian coordinates  $X, Y, Z$ , and the cylindrical coordinates  $\rho, \phi, Z$ , defined in (9a):

$$X = \rho \cos \phi, \quad Y = \rho \sin \phi; \quad 0 \leq \phi \leq 2\pi. \quad (22)$$

The total electric field  $\mathcal{E}$  is expressed by means of its Cartesian components  $\mathcal{E}_X, \mathcal{E}_Y, \mathcal{E}_Z$ , which must obey the inhomogeneous wave equations

$$\begin{aligned} (\nabla^2 + k^2)\mathcal{E}_X &= S_X; & (\nabla^2 + k^2)\mathcal{E}_Y &= S_Y; \\ (\nabla^2 + k^2)\mathcal{E}_Z &= S_Z, \end{aligned} \quad (23)$$

the divergence condition

$$\nabla \cdot \mathcal{E} = \frac{\partial \mathcal{E}_X}{\partial X} + \frac{\partial \mathcal{E}_Y}{\partial Y} + \frac{\partial \mathcal{E}_Z}{\partial Z} = 0 \text{ outside of source regions,} \quad (24)$$

<sup>7</sup> This problem was discussed by S. Karp, "An Analysis of Edge Behavior in Vector Diffraction Theory," presented at the Symposium on Electromagnetic Waves, University of Michigan, Ann Arbor; July, 1955. (Abstract appeared in IRE TRANS. ON ANTENNAS AND PROPAGATION, vol. AP-4, p. 579; July, 1955.)

and the following boundary conditions on the perfectly conducting half plane and at infinity:

$$0 = \mathcal{E}_X(X, 0, Z) = \mathcal{E}_Z(X, 0, Z) = \frac{\partial}{\partial Y} \mathcal{E}_Y(X, 0, Z); \quad X > 0.$$

$$\left[ \frac{\partial}{\partial Y} \mathcal{E}_Y(X, 0, Z) \equiv \frac{\partial}{\partial Y} \mathcal{E}_Y \right]_{Y=0} \quad (25)$$

$$\mathcal{E}_X, \mathcal{E}_Y, \mathcal{E}_Z, \text{ outgoing at infinity} \quad (26)^8$$

Moreover, we require the edge conditions<sup>4</sup>

$$\mathcal{E}_Z(\rho, \phi, Z) \rightarrow 0 \quad \text{as } \rho \rightarrow 0, \quad (27)$$

$$\text{no component of } \mathcal{E} \text{ or } (\nabla \times \mathcal{E}) \text{ is as singular as } 1/\rho \text{ at the edge.} \quad (28)$$

The functions  $S_X, S_Y, S_Z$ , in (23) represent the sources of the field, and are assumed to be given and to be confined to the interior of a finite region exterior to the half plane and its edge. Concerning (25) we note that the first two equalities express the boundary condition at a perfect conductor. The (redundant) condition  $\partial \mathcal{E}_Y/\partial Y = 0$  follows from (24) if we proceed to the limit  $Y \rightarrow 0$  for  $X > 0$ , while requiring that  $\mathcal{E}_X$  and  $\mathcal{E}_Z \rightarrow 0$ . The magnetic field  $\mathcal{H}$  corresponding to  $\mathcal{E}$  according to the Maxwell field equations is defined as  $\mathcal{H} = (1/ikZ)\nabla \times \mathcal{E}$ , where  $Z$  is the characteristic impedance of free space. To facilitate subsequent discussions, we introduce the incident field,  $\mathcal{E}_{\text{inc}}$ . This field is defined as that outgoing wave solution of (23) which is regular except at the sources of the field. Since  $\mathcal{E}$  and  $\mathcal{E}_{\text{inc}}$  have the same sources, we deduce from (23) that

$$(\nabla^2 + k^2)\nabla \cdot (\mathcal{E} - \mathcal{E}_{\text{inc}}) = \nabla \cdot \mathcal{S} - \nabla \cdot \mathcal{S} \equiv 0. \quad (23a)$$

Now the function  $\nabla \cdot (\mathcal{E} - \mathcal{E}_{\text{inc}})$  is an outgoing wave at infinity, as follows from the outgoing behavior of the Cartesian components of  $\mathcal{E}$  and  $\mathcal{E}_{\text{inc}}$ . Since it has no sources [by (23a)], it vanishes identically. Thus (24) can be replaced by:

$$\begin{aligned} \nabla \cdot \mathcal{E} &= \nabla \cdot \mathcal{E}_{\text{inc}} = 0 \quad \text{outside of sources} \\ \nabla \cdot \mathcal{E} - \nabla \cdot \mathcal{E}_{\text{inc}} &\equiv 0 \quad \text{everywhere.} \end{aligned} \quad (24a)$$

Our method of analysis will be based on an assumed knowledge of the solutions of certain scalar boundary value problems, in terms of which the electromagnetic solution will be expressed. In the scalar diffraction theory for a half plane, it is customary to solve problems of the type posed in (2a) and (3) and summarized below for convenience:

$$\nabla^2 \phi + k^2 \phi = \text{source term.} \quad (29)$$

$$\phi \text{ outgoing at } \infty. \quad (30)$$

$$\phi(X, 0, Z) = 0, \text{ or } \frac{\partial}{\partial Y} \phi(X, 0, Z) = 0, \text{ for } X > 0. \quad (31)$$

$$\phi \text{ finite as } \rho \rightarrow 0. \quad (32)$$

<sup>8</sup> If  $k = k_1 + ik_2, k_2 > 0$ , then we require instead that  $\mathcal{E}(\infty) = 0$ .



The pair of problems so expressed can be solved explicitly, as is well known. We can, therefore, directly construct a triplet of functions ( $E_x, E_y, E_z$ ), *i.e.*, a vector  $\mathbf{E}$ , say, which satisfies conditions (23), (25) and (26) and such that  $\mathbf{E}$  is finite at the edge of the screen. Despite this, the vector  $\mathbf{E}$  fails to be a solution of Maxwell's equations, since it does not satisfy the divergence condition (24).

It is known that near the edge, functions of the type of ( $E_x, E_y, E_z$ ) behave like

$$(C_1(Z)\sqrt{\rho} \sin \phi/2, C_2(Z) + C_3(Z)\sqrt{\rho} \cos \phi/2, C_4(Z)\sqrt{\rho} \sin \phi/2), \quad (33)$$

where the functions  $C_1, C_2, C_3$  and  $C_4$  depend on the particular excitation. Hence, conditions (27) and (28) are actually fulfilled. In fact they are over-fulfilled, since we can allow appropriate infinities of  $\epsilon_x$  and  $\epsilon_y$  at the edge.

We now proceed to show how to construct the vector  $\mathbf{e}$ , given the vector  $\mathbf{E}$ . To do this we define  $\mathbf{e} = \mathbf{e} - \mathbf{E}$ , and then note that we must have, in virtue of (23)–(28) and (24a),

$$(\nabla^2 + k^2)\mathbf{e} = 0, \quad \mathbf{e} \equiv (e_x, e_y, e_z), \quad (34)$$

$$\psi \equiv \nabla \cdot \mathbf{e} + \nabla \cdot \mathbf{E} - \nabla \cdot \mathbf{e}_{\text{inc}} = 0, \quad (35)$$

$$e_x(X, 0, Z) = e_z(X, 0, Z) = \frac{\partial}{\partial Y} e_y(X, 0, Z) = 0; \quad X > 0, \quad (36)$$

$$\mathbf{e} \text{ outgoing at } \infty, \quad (37)$$

$$e_z(\rho, \phi, Z) \rightarrow 0 \text{ as } \rho \rightarrow 0, \quad (38)$$

$$\mathbf{e}, (\nabla \times \mathbf{e}) \text{ not as singular as } \frac{1}{\rho} \text{ at } \rho = 0. \quad (39)$$

If such a vector  $\mathbf{e}$  can be found, then  $\mathbf{e} + \mathbf{E}$  will satisfy all the conditions imposed upon  $\mathbf{e}$ .

It is at this point that the basic formulas (9a) and (9b) are employed. Let us set

$$e_x = \frac{1}{\sqrt{\rho}} \sin(\phi/2) F_1(\rho, Z) \quad (40)$$

$$e_y = \frac{1}{\sqrt{\rho}} \cos(\phi/2) F_2(\rho, Z), \quad (41)$$

$$e_z \equiv 0, \quad (42)$$

where

$$\left( \frac{\partial^2}{\partial \rho^2} + \frac{\partial^2}{\partial Z^2} + k^2 \right) F_{1,2} = 0, \quad (43)$$

and where  $F_1$  and  $F_2$  are outgoing at infinity. Then (34), (36), (37) and (38) are fulfilled. We can exclude the possibility that  $F_1(0, Z) = 0$ , or  $F_2(0, Z) = 0$ , for then the functions  $F_1$  and  $F_2$  would be identically zero, since they are sourceless radiating-wave functions in the Cartesian  $\rho, Z$  plane. Thus,  $e_x \rightarrow \rho^{-1/2} \sin(\phi/2) F_1(0, Z)$ ,  $e_y \rightarrow \rho^{-1/2} \cos(\phi/2) F_2(0, Z)$  near  $\rho = 0$ , and this is the expected

form of edge singularity, and it is in accordance with (39), insofar as  $\mathbf{e}$  is concerned. Condition (39) also restricts the singularity of  $(\nabla \times \mathbf{e})$ , of course, but this will be attended to after the solution is obtained.

We now have to fulfill condition (35). To this end we note that the function  $\psi = \nabla \cdot \mathbf{e} + \nabla \cdot \mathbf{E} - \nabla \cdot \mathbf{e}_{\text{inc}}$ , with  $\mathbf{e}$  given in (40)–(42), is a scalar wave function which is outgoing at infinity. This follows from the fact that the Cartesian components of the vector  $(\mathbf{e} + \mathbf{E} - \mathbf{e}_{\text{inc}})$ , and therefore their derivatives as well, possess these properties. Furthermore, we know that  $\psi$  vanishes on the screen. [In fact,  $\nabla \cdot \mathbf{e} = 0$  on the screen by (36),  $\nabla \cdot \mathbf{E}$  vanishes there because of (25), while  $\nabla \cdot \mathbf{e}_{\text{inc}} = 0$  at the screen since the sources do not extend to the screen.] These properties of  $\psi$  ensure that it will vanish identically provided that it vanishes as the edge is approached radially. We shall therefore examine the behavior of  $\psi$  near the edge; as we shall see, the divergence will vanish there, provided the functions  $F_1$  and  $F_2$  are suitably chosen.

First, as mentioned above,  $\nabla \cdot \mathbf{e}_{\text{inc}} = 0$  near the edge. Next we observe from (33) that the singular part of the expansion of  $\nabla \cdot \mathbf{E}$  is given by the formula

$$\begin{aligned} & \left( \text{note: } \frac{\partial}{\partial X} (\sqrt{\rho} \sin(\phi/2)) \right) \\ &= -\frac{\partial}{\partial Y} (\sqrt{\rho} \cos(\phi/2)) = -\frac{1}{2\sqrt{\rho}} \sin(\phi/2) \Bigg) : \\ & \nabla \cdot \mathbf{E} \rightarrow \frac{-1}{2} C_1(Z) \frac{1}{\sqrt{\rho}} \sin(\phi/2) + \frac{1}{2} C_3(Z) \frac{1}{\sqrt{\rho}} \sin(\phi/2) \\ &= \frac{C(Z)}{\sqrt{\rho}} \sin(\phi/2) \end{aligned} \quad (44a)$$

where

$$C(Z) = \frac{1}{2} [-C_1(Z) + C_3(Z)]. \quad (44b)$$

Here the functions  $C_1, C_3$  are known from the solution of the scalar problems. We require, therefore, that the singular part of the expansion of  $\nabla \cdot \mathbf{e}$  be given by

$$\nabla \cdot \mathbf{e} \rightarrow -C(Z) \frac{1}{\sqrt{\rho}} \sin(\phi/2), \quad (45)$$

so that  $\nabla \cdot \mathbf{e} + \nabla \cdot \mathbf{E}$  will vanish as  $\rho \rightarrow 0$ . However, from (40), (41), (42) we have

$$\begin{aligned} \nabla \cdot \mathbf{e} \rightarrow & \left[ F_1(0, Z) \frac{\partial}{\partial X} \left( \frac{1}{\sqrt{\rho}} \sin(\phi/2) \right) \right. \\ & \left. + F_2(0, Z) \frac{\partial}{\partial Y} \left( \frac{1}{\sqrt{\rho}} \cos(\phi/2) \right) \right] \\ & + \frac{1}{\sqrt{\rho}} \sin(\phi/2) \cos \phi \frac{\partial}{\partial \rho} F_1(0, Z) \\ & + \frac{1}{\sqrt{\rho}} \cos(\phi/2) \frac{\partial}{\partial \rho} F_2(0, Z) \sin \phi. \end{aligned} \quad (46)$$

Since  $F_1(0, Z)$  and  $F_2(0, Z)$  do not both vanish, the bracketed term in (46) is  $0(\rho^{-3/2})$ ; on the other hand, the remaining part of the right side of (46) is  $0(\rho^{-1/2})$ . Eq. (45), therefore, implies that the bracketed term of (46) vanishes identically. But the coefficients of  $F_1$  and  $F_2$  in (46) are identical by the Cauchy-Riemann equations, since  $(X + iY)^{-1/2} = (1/\sqrt{\rho}) (\cos(\phi/2) - i \sin(\phi/2))$ . Hence, we conclude that

$$F_1(0, Z) + F_2(0, Z) = 0. \quad (47)$$

The uniqueness theorem for two-dimensional scalar waves then implies that  $F_1(\rho, Z) + F_2(\rho, Z) \equiv 0$  for all  $\rho$ , since the functions  $F_1$  and  $F_2$  are sourceless and outgoing. Therefore,  $(\partial/\partial\rho)F_1(0, Z) = -(\partial/\partial\rho)F_2(0, Z)$ . We now compare the second part of the right side of (46) with the right side of (45), and use the identity of  $(\partial/\partial\rho)F_1(0, Z)$  and  $-(\partial/\partial\rho)F_2(0, Z)$  to find

$$\begin{aligned} -C(Z) \sin \phi/2 &= \frac{\partial}{\partial\rho} F_2(0, Z) [\sin \phi \cos \phi/2 - \cos \phi \sin \phi/2] \\ &= \frac{\partial}{\partial\rho} F_2(0, Z) \sin \phi/2. \end{aligned} \quad (48)$$

Thus, we have to determine  $F_2(\rho, Z) = -F_1(\rho, Z)$  from the condition that

$$\frac{\partial}{\partial\rho} F_2(0, Z) = -C(Z). \quad (49)$$

But  $F_2(\rho, Z)$  is an outgoing wave function of  $\rho$  and  $Z(=z)$  if these are regarded as Cartesian coordinates. Therefore, we can solve (49) with (43) by a direct application of Green's theorem to the half-space region  $\rho \geq 0$ , utilizing the two-dimensional Neumann-type half-space Green's function, as follows:

$$\begin{aligned} F_2(\rho, Z) &= -\frac{i}{2} \int_{-\infty}^{\infty} C(z_0) H_0^{(1)}(k\sqrt{\rho^2 + (Z - z_0)^2}) dz_0 \\ &= -F_1(\rho, Z). \end{aligned} \quad (50)$$

We can now insert (50) into (40) and (41), and this gives us the solution for the required vector  $\mathbf{e}$ . Then  $\mathbf{E} = \mathbf{E} + \mathbf{e}$ , where  $\mathbf{E}$  is composed of the familiar scalar solutions, and  $\mathbf{e}$  is given by quadratures in terms of the quantity

$$C(Z) = \lim_{\rho \rightarrow 0} \frac{\sqrt{\rho}}{\sin \phi/2} \nabla \cdot \mathbf{E}. \quad (51)$$

If we use the fact that  $F_1(\rho, Z) = -F_2(\rho, Z)$ , it is easy to verify from (40), (41) and (42) that  $\nabla \times \mathbf{e}$  is  $0(\rho^{-1/2})$  at the edge, as required by (39). The analysis is therefore complete.

## Forward Scatter from Rain\*

L. H. DOHERTY† AND S. A. STONE†

**Summary**—The forward scatter of radio waves from rain has been observed over a 90-mile, 2720-mc path. The observations support the assumption of omnidirectional scattering from rain. On this link rain scatter may exceed the normal tropospheric scatter signal by 15 db. This latter signal may itself be increased by the presence of thunderstorms in the vicinity. Signal level distribution during rain and no-rain conditions are presented.

Among the effects of rain on a tropospheric scatter link are the increased fading rate and decreased bandwidth. The fading rate may increase by a factor of ten or more, and pulse-to-pulse fluctuations have been observed at a pulse repetition frequency of 600 pulses per second. Evidence for a decreased bandwidth is presented in the form of pulse photographs. The 1.5-μsec pulse is commonly broadened to 3 or 4 μsec and on occasions to lengths in excess of 20 μsec.

\* Manuscript received by the PGAP, October 26, 1959; revised manuscript received, January 25, 1960.

† Radio and Elec. Engrg. Div., Natl. Res. Council, Ottawa, Can.

## INTRODUCTION

GORDON<sup>1</sup> has made some calculations on the forward scatter from rain with particular reference to its value relative to transhorizon tropospheric scatter signal. His work was based on empirical relationships developed by workers in radar weather<sup>2</sup> and upon an estimate of the ratio of rain scatter volume to atmospheric scatter volume. The effective atmospheric scatter volume is limited, in the usual case, to a size which is small compared with the volume intersected by the

<sup>1</sup> W. E. Gordon, "The Scattering of Radio Waves by Turbulence in the Troposphere," School of Elec. Engrg., Cornell University, Ithaca, N. Y., Res. Rept. No. EE-163; September 15, 1953.

<sup>2</sup> J. S. Marshall, W. Hitschfeld, and K. L. S. Gunn, "Advances in radar weather," in "Advances in Geophysics," Academic Press, New York, N. Y., vol. 2; 1954. This article contains a survey of the field and a bibliography.

antenna beams. This results from the rapid decrease of scattered power with increasing scatter angle. In the rain-scatter case, the scattering cross section is independent of scattering angle, with the result that the volume is limited by either the volume of rain or the common volume of the antenna beams, whichever is smaller. In the case considered by Gordon he gave a value of 1000 as a possible ratio of the rain and atmospheric scatter volumes.

In the late spring of 1956, the National Research Council of Canada established an 11-cm radio link between Ottawa and Montreal in order to make some preliminary measurements of the forward scatter from rain. The link was operated throughout the summer of 1956, and the results were presented in a thesis by Stone.<sup>3</sup> Use was made of weather radar films provided by the Stormy Weather Group at McGill University. An important result of Stone's work was the recommendation that a second link be established over the same path, with the antennas swung sufficiently far off the Great Circle path so that little or no atmospheric scatter signal is received. The rain-scattered signal, being independent of scattering angle, would be received without attenuation. Operation of the two paths would make possible the separation of the signal on the normal Great Circle path into a tropospheric scatter component and a rain scatter component. Such a system was placed in operation between Ottawa and Montreal on June 1, 1958, and the following is an account of the observations on this link during the summer and early fall of 1958.

### THE PATH AND EQUIPMENT

The transmitter, with a 1.5- $\mu$ sec pulse output at 2720 mc is situated in Ottawa. The receiving equipment is 90 miles away at Dorval Airport, Montreal. The horizon is at 0° elevation at the transmitting end but, because of nearby obstructions, is elevated 40 minutes of arc at the receiving end.

The transmitted power is split between two antennas: one, horizontally polarized, is directly along the Great Circle path; the other, vertically polarized, is swung 10° to the south. At Montreal three antennas are each provided with a receiver. One of the antennas is directed along the Great Circle path at 0° elevation and forms with the horizontally polarized transmitting antenna a normal or direct path. Another antenna, vertically polarized, is pointing 8° south of 0° elevation. This, together with the vertically polarized transmitting antenna, forms the swung path.

McGill University's Stormy Weather Group operates a weather radar (AN-CPS9) which is located near the receiving site. The normal film record of the radar

screen shows precipitation echoes within a 100-mile radius centered on Dorval, and consequently covers the entire Ottawa-Montreal propagation path.

### CLASSIFICATION OF SIGNALS RECORDED DURING RAIN

Rain records on the two paths are shown in Fig. 1. The rise and fall of the signal levels correspond with the radar observed entry and exit of rain in the common volumes of the antenna beams. The hump on the falling side of the direct-path record corresponds with the movement of the storm over the receiving site. The recorded signal is being received through the sidelobes of the antenna. This effect, and its counterpart when rain is near the transmitting site, is observed frequently and is considered again in a later section. The lack of fluctuation in the two records when the rain-scattered signal is being received is due to the large value of the ratio of recording time constant to fading period. Thus the increased fading rate on the direct path appears as a decreased fading range.

Another manner in which rain affects the tropospheric scatter signal is shown in Fig. 2. The radar records give

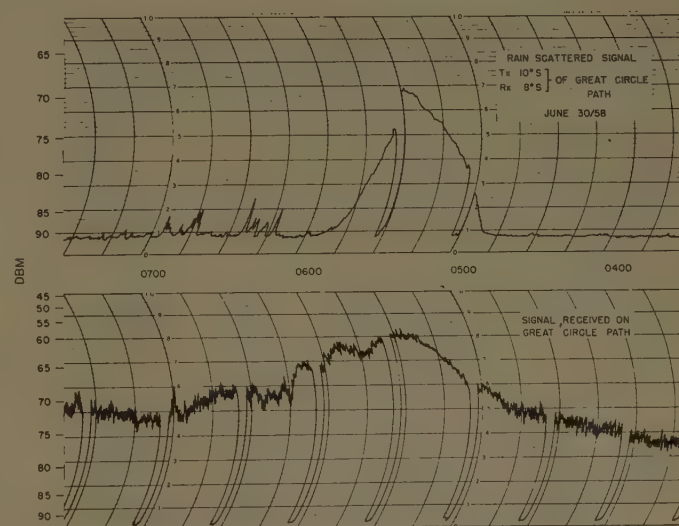


Fig. 1—Forward scatter from rain, June 30, 1958.

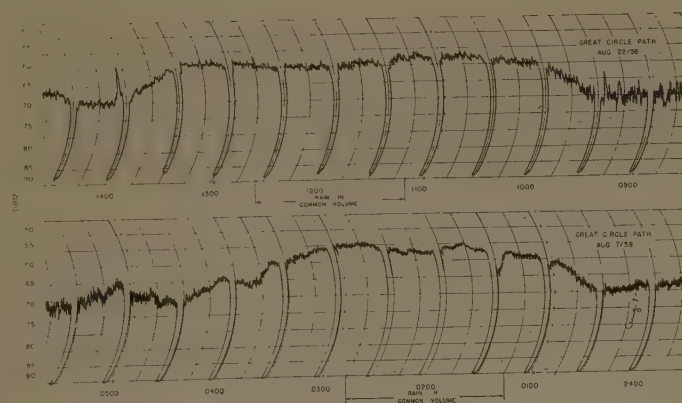


Fig. 2—Direct-path signal increases associated with rain.

<sup>3</sup> S. A. Stone, "Beyond-the-Horizon Propagation at Microwave Frequencies," M.Eng. thesis, Dept. of Elec. Engrg., McGill University, Montreal, Can.; 1958.



the periods when rain was present in the antenna beams, but it is observed that the direct-path signal rises before and falls after the appearance of rain in the common volumes. In this case the signal increase is not due to scatter from the raindrops but is due to an enhancement of the normal atmospheric scatter signal. A detailed examination of the meteorology has not been made, but the response of the type shown in Fig. 2 is usually associated with air mass or line thunderstorms rather than with frontal precipitation.

The classification of responses to rain is shown for 37 cases in Table I. In addition to the two types of response shown in Figs. 1 and 2 there are occasions when both these responses are present together, and other times when the direct-path signal shows no change when rain is present on the path. On four of the 37 occasions, a signal having the appearance of a super-refracted or layer-reflected signal was observed.

#### SIGNAL LEVELS DURING RAIN

The signals recorded during the period June 1 to October 31, 1958, have been analyzed in terms of a half-hour median. The periods of rain on the path, and the periods of super-refraction, have been separated from the total. Fig. 3 shows the cumulative probability distributions of half hour medians for these periods. A particular half-hour was classed as a "rain period" if the radar showed rain echo in any part of the common volume for at least 15 minutes of the half-hour. The super-refracted signal was classified from the nature of the fading.

From Fig. 3 it may be seen that during rain the half-hourly median is about 4 db higher at the 50 per cent level than the signals due to atmospheric scattering in the absence of rain. As mentioned in the previous section, this is due both to forward scatter from the rain and an increase in the atmospheric scatter signal associated with the meteorology which produces rain.

The power scattered from raindrops may be related to the rainfall rate according to the following expression:<sup>1</sup>

$$P_R = p\sigma\theta_R V$$

where

$p$  is the incident power density at the scattering volume (watts per square meter),

$\sigma = 4.6 \cdot 10^{-15} R^{1.6} \lambda^{-4}$  is the scattering coefficient per unit solid angle,

$R$  is the rainfall rate in millimeters per hour,

$\lambda$  is the wavelength in meters,

$\theta_R$  is the solid angle subtended by the receiving antenna at the scattering volume,

$V$  is the scattering volume in cubic meters.

The scattering coefficient has been established empirically from radar back scatter measurements. The volume  $V$  to be employed is either the volume filled by

TABLE I  
TYPE OF SIGNAL RESPONSE ON THE DIRECT PATH FOR  
THIRTY-SEVEN STORMS

Enhancement due to forward scatter from rain (Fig. 1)	7
Enhancement beginning before and ending after rain (Fig. 2)	9
As above, with additional enhancement due to forward scatter from rain	3
The super-refracted or layer-reflected signal	4
No noticeable effect	14
Total	37

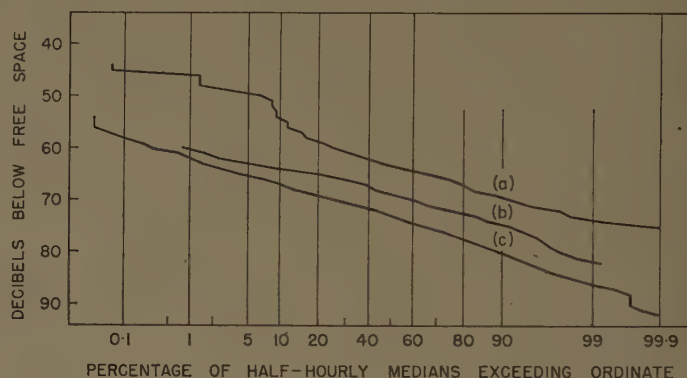


Fig. 3—Cumulative distributions of half-hourly medians during rain and no-rain conditions. (a) Super-refraction. (b) Rain on radar. (c) Remainder.

raindrops or the common volume of the antenna beams—whichever is the smaller.

Calculations using this expression have been performed for both the direct and swung paths for the common antenna volumes filled with rain and for the case of a north-south band of rain stretching across the common volumes. This latter situation is fairly common and the calculations have been performed for bands varying in thickness between 5 and 20 miles. The maximum signals received on the direct path during rainstorms have been examined from the point of view of rainfall rates required to produce them. In the frequency distribution of signal levels during rain the most probable corresponds to a rainfall rate of 4 mm per hour in the entire antenna volume, and to 12 mm per hour in a north-south band five miles thick. The rainfall rates corresponding to signal levels occurring one-quarter as often are about 12 and 40 mm per hour, respectively.

A comparison has also been made between maximum signals received on the direct and swung paths, and the results are shown in Fig. 4 for 49 rain storms. It is observed that the scatter of points has a reasonably well defined lower boundary. On this boundary the direct-path signal exceeds the swung-path signal by 5 db. The points lie near this boundary when a rain-scattered signal is predominant on both paths, and above the boundary when the normal scatter signal is large or is

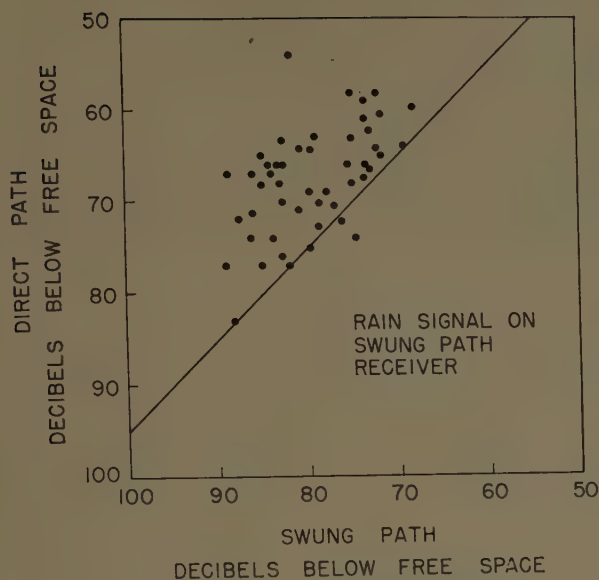


Fig. 4—Comparison of direct- and swung-path signals during rain.

enhanced as in Fig. 2. If it is assumed that the common volumes of the two paths are filled with rainfall of equal intensity, the calculated direct-path signal should exceed the swung-path signal by 8 db. These results, therefore, support the assumption of omnidirectional scattering from rain. The average scattering angle is about  $3^\circ$  for the direct path and about  $18^\circ$  for the swung path.

#### FADING RATE AND PULSE DISTORTION

Two important effects of rain on a tropospheric scatter system are the increase in fading rate and pulse distortion which occur in the presence of rain.

An increase in fading rate is a very obvious feature of the scatter signal as rain moves into the common volume. Autocorrelation coefficient calculations have been made on a number of occasions. Typically, under no-rain conditions the time correlation of the atmospheric scatter signal drops to a value of  $1/e$  in a time varying between  $1/4$  and 1 second. When rain is present in the common volume but is not significantly increasing the scattered power, the time falls to a value of about  $1/10$  second. When the rain-scattered component is predominant the value falls to about  $1/25$  second. In the latter case the equipment is probably limiting the speed of response. Examination of film records shows pulse-to-pulse fluctuations at a pulse recurrence frequency of 600 per second, and it is apparent that appreciable amounts of power are present in the fading spectrum at frequencies in excess of 200 cycles per second.

Pulse distortion is another commonly observed feature on the scatter link during rain. When rain is present in the common volume the path delays in the received signal are determined by the geometry of the common volume. For typical link parameters this can mean path delays increased by factors of two or three, and a reduction in effective bandwidth by the same factor. A

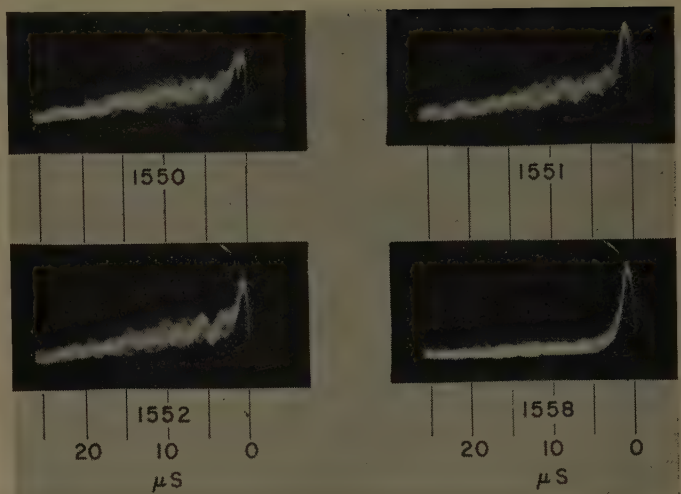


Fig. 5—Photographs of pulses received on direct path with rain near receiving terminal, October 10, 1958. Exposure— $1/50$  second.

more striking example of pulse delay is shown in Fig. 5. In the photographs taken at 1550, 1551, and 1552 hours, energy is arriving between 20 and 25  $\mu\text{sec}$  after the first arrival of the pulse. The photograph at 1558 shows the pulse with just a small amount of distortion at the trailing edge. The blurred feature of the delayed portions of these pulses is, of course, due to the extremely rapid fading of the rain-scattered component.

The extended tail of these pulses is due to scatter from rain near the receiving terminal. The energy is transmitted via the main beam of the transmitting antenna, scattered from an intense storm directly above or slightly in front of the receiving antenna, and received through the sidelobe of the receiving antenna. Sidelobes as much as 25 db below the main beam are more than counterbalanced by the distance factor appearing in the scattering formula.

#### CONCLUSIONS

The results of this experiment support the commonly made assumption of omnidirectional scattering from rain. Scattering at angles of  $3^\circ$  and  $18^\circ$  is the same within a factor of 3 db, and the results are consistent with relations derived from back-scattering (scattering angle equals  $180^\circ$ ) observations.

The passage of precipitation areas across or along the path may increase the signal level in one of two main ways. Energy may be scattered from the raindrops themselves. For heavy rain this increase may amount to 15 db, and in this area of the world the effect is confined to a few summer months. The scattered power per unit volume of rain varies as the fourth power of the frequency. Thus for links of the same path length the effect will tend to be 20 db greater in the X-band region (10,000 mc) and 20 db less in the 500z- to 1000-mc region. The ratio of rain-scattered power to atmospheric-scattered power increases with increasing distance, and at 200 miles is 20 db greater than for the 90-mile path of this paper. Beyond 200 miles the antenna common vol-



ume rises above the level at which weather occurs.

An increase in signal level may also occur without any rain-scattered component being present. This increase is associated with thunderstorms and not with frontal precipitation. Although the exact cause of this increase in signal level is not known, it is possibly a result of the mass of cold air diverging from the base of a thunderstorm. The boundary of this cold air may be as much as 50 miles from the center of the storm, and an elevated superrefracting layer will be formed above this ground-based cold air.

High fading rates are invariably associated with the passage of rain through the common volume, even when the rain-scattered component is negligible in comparison with the normal atmospheric-scattered signal. Presumably this is a result of high wind speeds and increased turbulent velocities associated with the rain. When the rain-scattered component is significant, very high frequency components are present in the fading spectrum. This is a result of the increase in size of the volume contributing to the scattering, and the relatively high velocity of fall possessed by the larger drops.

The pulse distortion which can occur as a result of rain scatter is of a very different order of magnitude than that encountered normally on a scatter link. Thus the 1.5- $\mu$ sec pulse used in this experiment is frequently stretched to 3 and 4  $\mu$ sec, and occasionally to 10 to 20  $\mu$ sec in length. This effect could presumably have very serious consequences for some scatter-communication systems.

#### ACKNOWLEDGMENT

The authors are much indebted to Prof. J. S. Marshall, Prof. W. Hitschfeld, and Prof. K. L. S. Gunn of the Stormy Weather Group, McGill University, for making available to us the film records from their weather radar, and for their helpful discussions and generous interest.

We are also indebted to D. Rocheleau, who played a prominent part in the operation and maintenance of the experimental equipment, and to Mrs. J. Burrell, who performed the reduction of the radio data and assisted in the reading of the radar films.

## Solution of a Reflection Problem by Means of a Transmission Line Analogy\*

B. L. JONES† AND P. C. PATTON†

**Summary**—Through the use of a transmission line analogy, a problem related to the reflection of electromagnetic energy from a periodic acoustic disturbance is solved. This solution agrees well with a numerical solution of a wave equation of the Mathieu form, which has been derived from a different model of the same problem. Subsequent experimental research has given results in good agreement with the theoretical solutions.

#### INTRODUCTION

THE propagation of an acoustic wave through air causes the index of refraction of the air in the vicinity of the wave to vary with both position and time. In order to investigate the propagation of an electromagnetic wave through the acoustically disturbed air, it is necessary to consider this variable index of refraction  $\eta = \eta(x, y, z, t)$  in deriving the wave equation from Maxwell's equations.

To simplify the problem, it is assumed that both the acoustic disturbance and the electromagnetic wave are plane waves traveling in the  $x$  direction. The index of refraction  $\eta(x, t)$  depends only upon  $x$  and  $t$ . Furthermore, the acoustic wave may be considered to be constant in time since the velocity of propagation of the electromagnetic wave is much greater than that of the acoustic wave. The problem is to determine the nature of reflected electromagnetic energy from the acoustic disturbance, under the assumptions that  $\eta$  is a function only of  $x$ , and that the acoustic wave is stationary in time.

#### DERIVATION OF THE WAVE EQUATION

If the electromagnetic wave is a plane polarized wave traveling in the  $x$  direction (through an acoustic disturbance), then Maxwell's curl equations in mks units reduce to

$$-\frac{\partial \bar{H}}{\partial x} = \epsilon(x) \frac{\partial \bar{E}}{\partial t} \quad (1)$$

\* Manuscript received by the PGAP, December 15, 1959; revised manuscript received, February 18, 1960. This work was performed under contract with the office of Naval Res., No. Nonr 1670(00), Subcontract FW1001 to the Bell Helicopter Corp.

† Midwest Res. Inst., Kansas City, Mo.



and

$$\frac{\partial \bar{E}}{\partial x} = -\mu \frac{\partial \bar{H}}{\partial t}, \quad (2)$$

in which  $\bar{H}$  is the magnetic vector and  $\bar{E}$  is electric field strength. The variable index of refraction due to the acoustic disturbance is given by

$$\frac{\epsilon(x)}{\epsilon_0} = [\eta(x)]^2 = \eta_0^2 [1 + \delta \sin kx]^2, \quad (3)$$

where  $\eta_0$  is the index of refraction of air when no acoustic wave is present,  $k$  is  $2\pi$  divided by the acoustic wavelength, and  $\delta \ll 1$ .

Differentiating (1) with respect to  $t$  and (2) with respect to  $x$  yields

$$\frac{\partial^2 \bar{E}}{\partial x^2} = \mu \epsilon(x) \frac{\partial^2 \bar{E}}{\partial t^2}; \quad (4)$$

differentiating (1) with respect to  $x$  and (2) with respect to  $t$  yields

$$\frac{\partial^2 \bar{H}}{\partial x^2} = \frac{1}{\epsilon(x)} \frac{\partial \epsilon}{\partial x} \frac{\partial \bar{H}}{\partial x} + \mu \epsilon(x) \frac{\partial^2 \bar{H}}{\partial t^2}. \quad (5)$$

Eqs. (4) and (5) reduce to the usual form of the wave equation when  $\epsilon(x)$  is replaced by  $\epsilon = \text{constant}$ .

General solutions to (4) and (5) do not exist. Moreover the usual traveling-wave solution of the form  $f(x \pm vt)$  is not a solution of these equations. This fact does not mean that the solution cannot be expressed in terms of traveling waves, but rather that the traveling waves would not have the simple form  $f(x \pm vt)$ .

For special forms of the function  $\epsilon(x)$ , solutions of (4) and (5) have been proposed;<sup>1,2</sup> however, these solutions are not adaptable to periodic forms of  $\epsilon(x)$ . Approximate solutions to (4) have been suggested,<sup>3</sup> but their application is tedious and there is no satisfactory error analysis of the approximation method involved.

#### USE OF A TRANSMISSION LINE ANALOGY

The foregoing difficulties have led to an attempt to extend the analogy between wave propagation in a transmission line and propagation of a plane wave through a dielectric medium<sup>4</sup> to the case of propagation of an electromagnetic wave through a medium with continuously varying index of refraction. A result

<sup>1</sup> D. E. Kerr, "Propagation of Short Radio Waves," Rad. Lab. Ser., vol. 13, ch. 2, McGraw-Hill Book Co., Inc., New York, N. Y.; 1951. See also R. Yamada, "On radio wave propagation in a stratified atmosphere," *J. Phys. Soc. Japan*, vol. 10, pp. 71-77; January, 1955.

<sup>2</sup> P. S. Epstein, "Reflection of waves in an inhomogeneous absorbing medium," *Proc. Nat. Acad. Sci.*, vol. 16, pp. 627-637; October, 1930. See also A. W. Friend, "Theory and practice of tropospheric sounding by radar," *Proc. IRE*, vol. 37, pp. 116-138; February, 1949.

<sup>3</sup> V. A. Bailey, "Reflection of waves by an inhomogeneous medium," *Phys. Rev.*, vol. 96, pp. 865-868; November, 1954. See also references contained therein.

<sup>4</sup> J. D. Ryder, "Networks, Lines and Fields," Prentice-Hall, Inc., New York, N. Y., pp. 426-432; 1955.

[see (6) below] of the theory of uniform lossless transmission lines has been used as a starting point, and has been modified by the substitution of a variable  $\eta(x)$  for the constant  $\eta$  of the theory of uniform transmission lines. The variable index of refraction defined in (3) indicates that the corresponding acoustic disturbance is a sine wave of small amplitude and frequency.

Eq. (6) is based on a solution obtained for (4) and (5) when  $\eta(x)$  is constant.<sup>5</sup> However, for small values of  $\delta$ ,  $\eta(x)$  does not vary much from the value  $\eta_0$ ; thus the results using (6) should be a fairly good approximation to the exact solution. Use of a medium-sized digital computer permitted solutions for many different values of  $\delta$  and  $k$ , and results from this approach proved to be useful.

#### TRANSMISSION LINE EQUATIONS

For a uniform transmission line of characteristic impedance  $Z_0$  (see Fig. 1) terminated in the impedance

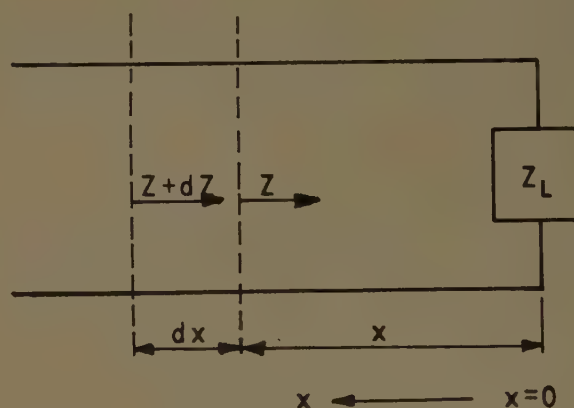


Fig. 1—The transmission line.

$Z_L$ , the impedance at a point a distance  $x$  from the end of the line is

$$Z = Z_0 \frac{Z_L + jZ_0 \tan\left(\frac{\omega_r x}{v}\right)}{Z_0 + jZ_L \tan\left(\frac{\omega_r x}{v}\right)}. \quad (6)$$

At a point  $\Delta x$  nearer the sending end, the impedance is

$$Z + \Delta Z = Z_0 \frac{Z + jZ_0 \tan\left(\frac{\omega_r \Delta x}{v}\right)}{Z_0 + jZ \tan\left(\frac{\omega_r \Delta x}{v}\right)}, \quad (7)$$

in which  $Z_0$  is the constant characteristic impedance in the interval  $\Delta x$ .  $Z + \Delta Z$  is independent of the nature of the line and loads on the sending side of the point at which it is determined.

<sup>5</sup> W. C. Johnson, "Transmission Lines and Networks," McGraw-Hill Book Co., Inc., New York, N. Y., pp. 152-155; 1950.

Now letting  $\Delta x$  be the differential length  $dx$ , (7) becomes

$$Z + dZ = Z_0 \frac{Z + jZ_0 \left( \frac{\omega_r dx}{v} \right)}{Z_0 + jZ \left( \frac{\omega_r dx}{v} \right)} \quad (8)$$

Clearing fractions, (8) becomes

$$\begin{aligned} ZZ_0 + jZ^2 \frac{\omega_r}{v} dx + Z_0 dZ + jZ dZ \frac{\omega_r}{v} dx \\ = ZZ_0 + jZ_0^2 \frac{\omega_r}{v} dx. \end{aligned} \quad (9)$$

Neglecting the term involving the product of two differentials and dividing by  $dx$  yields

$$Z_0 \frac{dZ}{dx} + j \frac{\omega_r}{v} (Z^2 - Z_0^2) = 0. \quad (10) \quad \text{but}$$

If the transmission line is lossless, then  $Z_0$  will be a real quantity; however,  $Z$  may be complex. If  $Z = R + jX$ , (10) becomes

$$\begin{aligned} Z_0 \left( \frac{dR}{dx} + j \frac{dX}{dx} \right) \\ + j \frac{\omega_r}{v} (R^2 + 2jRX - X^2 - Z_0^2) = 0. \end{aligned} \quad (11)$$

Upon separating (11) into its real and imaginary parts, we obtain

$$Z_0 \frac{dR}{dx} - 2 \frac{\omega_r}{v} RX = 0 \quad (12) \quad \text{and}$$

and

$$Z_0 \frac{dX}{dx} + \frac{\omega_r}{v} (R^2 - X^2 - Z_0^2) = 0. \quad (13)$$

#### PARAMETERS FOR THE ACOUSTIC WAVE

To make the transmission line problem analogous to that of wave propagation through a lossless dielectric medium, the following substitutions are made:<sup>6</sup>

$$Z(x) = \sqrt{\frac{\mu}{\epsilon(x)}}, \quad (14)$$

which is the normalized impedance, and

$$v = \sqrt{\frac{1}{\mu \epsilon(x)}}. \quad (15)$$

The magnetic permeability  $\mu$  will be assumed constant and equal to  $\mu_0$ , ( $x$ ) is given by (3), and

$$Z_0 = \sqrt{\frac{\mu_0}{\epsilon_0}} \frac{1}{(1 + \delta \sin kx) \eta_0}. \quad (16)$$

The characteristic impedance of air with no acoustic wave present is

$$R_0 = \sqrt{\frac{\mu_0}{\epsilon_0}} \frac{1}{\eta_0}; \quad (17)$$

therefore

$$Z_0 = \frac{R_0}{1 + \delta \sin kx}. \quad (18)$$

Also,

$$v = \frac{1}{\sqrt{\mu_0 \epsilon_0}} \frac{1}{(1 + \delta \sin kx) \eta_0}, \quad (19)$$

but

$$v_0 = \frac{1}{\sqrt{\mu_0 \epsilon_0}} \frac{1}{\eta_0}; \quad (20)$$

then

$$v = \frac{v_0}{1 + \delta \sin kx}. \quad (21)$$

If (18) and (21) are substituted in (12) and (13), the following results are obtained:

$$R_0 \frac{dR}{dx} - 2 \frac{\omega_r}{v_0} (1 + \delta \sin kx)^2 RX = 0, \quad (22)$$

$$\begin{aligned} R_0 \frac{dX}{dx} + \frac{\omega_r}{v_0} (1 + \delta \sin kx)^2 \\ \left[ R^2 - X^2 - \frac{R_0^2}{(1 + \delta \sin kx)^2} \right] = 0. \end{aligned} \quad (23)$$

#### DIGITAL COMPUTER EQUATIONS

Since (22) and (23) are nonlinear, solution by analytical means is not feasible. Instead, the equations were set up for numerical solution by Milne's method<sup>7</sup> for solving a system of two simultaneous first-order differential equations. The following substitutions were made:

$$q = \frac{R}{R_0},$$

$$u = \frac{X}{R_0},$$

$$\bar{x} = \frac{\omega_r}{v_0} x,$$

<sup>6</sup> S. Ramo and J. R. Whinnery, "Fields and Waves in Modern Radio," John Wiley and Sons, Inc., New York, N. Y., pp. 250-254; 1948.

<sup>7</sup> W. E. Milne, "Numerical Solution of Differential Equations," John Wiley and Sons, Inc., New York, N. Y., pp. 60-61; 1953.

$$M = \frac{kv_0}{\omega_r} \quad (24)$$

and the approximation

$$(1 + \delta \sin kx)^2 \approx 1 + 2\delta \sin kx, \quad (25)$$

where  $\delta \ll 1$ , was made. The effect of these substitutions is to reduce the equations to dimensionless form. The results are

$$\frac{dq}{d\bar{x}} = 2qu(1 + 2\delta \sin M\bar{x}) \quad (26)$$

and

$$\frac{du}{d\bar{x}} = 1 - (q^2 - u^2)(1 + 2\delta \sin M\bar{x}). \quad (27)$$

Now let  $q = 1 + y$ ; then

$$\frac{dy}{d\bar{x}} = 2u(1 + y)(1 + 2\delta \sin M\bar{x}), \quad (28)$$

and

$$\frac{du}{d\bar{x}} = 1 - ((1 + y)^2 - u^2)(1 + 2\delta \sin M\bar{x}). \quad (29)$$

At  $\bar{x} = 0$ , let  $R = R_0$  and  $x = 0$ , yielding the initial conditions  $y(0) = 0$  and  $u(0) = 0$ .

#### THE REFLECTED ELECTROMAGNETIC ENERGY

To determine the amount of energy reflected from the acoustic wave, it was necessary to calculate the voltage reflection coefficient  $\rho$  as a function of  $y$  and  $u$  in (28) and (29). Let

$$\rho = \frac{z - 1}{z + 1}, \quad (30)$$

in which  $z = Z/Z_0$ . From (22)  $R_0 \approx Z_0$ ; therefore,

$$z \approx \frac{Z}{R_0} = 1 + y + ju. \quad (31)$$

Then

$$\rho = \frac{y + ju}{y + 2 + ju}. \quad (32)$$

The ratio of reflected power to power transmitted,  $|\rho|^2$ , is then

$$|\rho|^2 = \frac{(y^2 + 2y + u^2)^2 + 4u^2}{((2 + y)^2 + u^2)^2}. \quad (33)$$

#### DIGITAL COMPUTER RESULTS

To solve (28) and (29) numerically, Milne's method was programmed for the IBM 650 Magnetic Drum Calculator. The computed results were used to calculate  $|\rho|$  at  $\bar{x} = 20\pi$  for these values of the parameters:  $2\delta = 1.0 \times 10^{-6}$  and  $M = 2.0$ . The value of  $|\rho|$  obtained

using this method was  $7.64 \times 10^{-6}$ , which compares favorably with an analytic approximation of  $7.85 \times 10^{-6}$ , and with a Mathieu equation numerical solution (discussed below) of  $7.91 \times 10^{-6}$ , also done on the IBM 650. This agreement was satisfactory for the purpose at hand. Further numerical results indicated peaks in  $|\rho|$  at values of  $M = 2, 1, 2/3, 1/2, 2/5, 2/6, 2/7, 2/8, 2/9, 2/10$ . This manner of behavior for  $|\rho|$  was, of course, expected from the Mathieu equation solution of the scattering problem, which was studied to further substantiate these results.

#### THE MATHIEU EQUATION SOLUTION

In considering the Mathieu equation approach to the reflection problem, it is necessary to assume not only the Maxwell equations (cgs units) but also the equations

$$\begin{aligned} \bar{D} &= \epsilon \bar{E}, \\ \bar{B} &= \mu \bar{H}. \end{aligned} \quad (34)$$

As before,  $\mu$  is a constant  $\mu_0$ , but  $\epsilon = \epsilon(x, t)$  is calculated to be

$$\epsilon(x, t) = \eta_0^2 [1 + 2\delta \sin (\omega_a t - kx)], \quad (35)$$

where  $\omega_a$  is the frequency of the acoustic wave. Since the acoustic wave is assumed to be stationary, the time dependence of  $\eta$  may be dropped, and the wave equation may be written as

$$-\frac{\partial^2 \bar{E}}{\partial x^2} = -\frac{\epsilon \mu}{c^2} \frac{\partial^2 \bar{E}}{\partial t^2}. \quad (36)$$

Considering only the plane wave case

$$\bar{E} = E_0 e^{j\omega_r t}, \quad (37)$$

(36) becomes

$$\frac{\partial^2 \bar{E}}{\partial x^2} + \frac{\mu \epsilon}{c^2} \omega_r^2 \bar{E} = 0, \quad (38)$$

and by (35)

$$\frac{\partial^2 \bar{E}}{\partial x^2} + \frac{\mu_0 \omega_r^2}{c^2} \eta_0^2 [1 + 2\delta \sin kx] \bar{E} = 0, \quad (39)$$

where  $k = 2\pi/\lambda_a$  and  $\lambda_a$  is the wavelength of the acoustic disturbance.

Substituting  $\eta_0 = \mu_0 = 1$  and  $kx = M\bar{x}$ , where  $M = \lambda_r/\lambda_a$ , then  $\omega_r/c = 2\pi/\lambda_r$  and (39) becomes

$$\frac{d^2 \bar{E}}{d\bar{x}^2} + \bar{E}(1 + 2\delta \sin M\bar{x}) = 0. \quad (40)$$

The solution to (40) may be written as

$$\bar{E} = A(x)e^{-i\bar{x}} + B(x)e^{i\bar{x}} = f_1(\bar{x}) + f_2(\bar{x}). \quad (41)$$



Then

$$|\rho| = \left| \frac{f_2}{f_1} \right| = \left| \frac{B(x)}{A(x)} \right|. \quad (42)$$

To separate (41) into real and imaginary parts, it is assumed that  $\bar{E} = \bar{E}_r + j\bar{E}_i$ , in which  $\bar{E}_r$  and  $\bar{E}_i$  are the real and imaginary parts of  $\bar{E}$ . Now the problem is to solve the set of equations

$$\begin{aligned} \bar{E}_r'' + \bar{E}_r(1 + 2\delta \sin M\bar{x}) &= 0 \\ \bar{E}_i'' + \bar{E}_i(1 + 2\delta \sin M\bar{x}) &= 0, \end{aligned} \quad (43)$$

with boundary conditions

$$\begin{aligned} \bar{E}_r(0) &= 1, & \bar{E}_r'(0) &= 0; \\ \bar{E}_i(0) &= 0, & \bar{E}_i'(0) &= -1. \end{aligned} \quad (44)$$

From (42) an equation for  $|\rho|$  in terms of  $\bar{E}_r$ ,  $\bar{E}_r'$ ,  $\bar{E}_i$ , and  $\bar{E}_i'$ , may be written

$$|\rho| = \sqrt{\frac{[\bar{E}_r + \bar{E}_i']^2 + [\bar{E}_i - \bar{E}_r']^2}{[\bar{E}_r - \bar{E}_i']^2 + [\bar{E}_i + \bar{E}_r']^2}}. \quad (45)$$

Using this method of solution, the value of  $|\rho|$  for  $\bar{x} = 20\pi$ ,  $2\delta = 1.0 \times 10^{-6}$ ,  $M = 2.0$  mentioned above ( $7.91 \times 10^{-6}$ ), was found.

#### CONCLUSION

Although the fundamental equations for both methods of solution of the scattering problem were derived from Maxwell's equations, the mathematical models involved were essentially different. The Mathieu equation solution was approximated analytically and was calculated numerically on a digital computer. Agreement of the various answers was considered good. Subsequent experimental work gave answers which substantially agreed with the calculated values of  $|\rho|$ , and which also indicated reflections at experimental equipment configurations corresponding to  $M = 2, 1, 2/3, 1/2$ , etc. A paper describing theoretical conclusions as well as detailed results from the scattering experiments will be published in the near future.

#### LIST OF SYMBOLS

- $\eta$  = index of refraction
- $\bar{H}$  = magnetic vector
- $\bar{E}$  = electric field strength
- $\epsilon(x)$  = dielectric permittivity at  $x$
- $\mu$  = magnetic permeability
- $\epsilon_0$  = dielectric permittivity of free space
- $\eta_0$  = index of refraction of air when no acoustic wave is present
- $\lambda_a$  = acoustic wavelength
- $k = 2\pi/\lambda_a$
- $\omega_a$  = frequency of acoustic wave
- $Z_0$  = characteristic impedance at a point on a transmission line
- $Z$  = impedance at any point on a transmission line
- $\Delta Z$  = difference between  $Z$  at  $x$  and at  $x + \Delta x$
- $j = \sqrt{-1}$
- $\lambda_r$  = electromagnetic wavelength
- $\omega_r$  = frequency of electromagnetic signal
- $v$  = velocity of propagation of wave along transmission line
- $R$  = real part of  $Z$
- $X$  = imaginary part of  $Z$
- $\mu_0$  = magnetic permeability of free space
- $R_0$  = characteristic impedance of air with no acoustic wave present
- $v_0$  = velocity of propagation of electromagnetic wave through undisturbed air
- $g$  = dimensionless; resistance  $R$  per unit of  $R_0$
- $u$  = dimensionless; reactance  $X$  per unit of  $R_0$
- $\bar{x} = \omega_r x / v_0$
- $M$  = dimensionless; ratio of  $\lambda_r$  to  $\lambda_a$
- $y$  = dimensionless; defined as  $g - 1$
- $c$  = velocity of propagation of electromagnetic air in vacuum.

#### ACKNOWLEDGMENT

Acknowledgment is made to Eugene Denman of Midwest Research Institute, whose derivation of the wave equation of Mathieu form for the reflection problem is presented here, and to Paul Smith of Carnegie Institute of Technology for studies (28) and (29) on the analog computer.

# Experimental Swept-Frequency Tropospheric Scatter Link\*

W. E. LANDAUER†

**Summary**—An experimental swept-frequency tropospheric scatter link, with a path length of 194 miles, has been established in France between Cholet and Corbeville. The transmitter (designed by Compagnie Générale de Télégraphie Sans Fil) sweeps in a nearly linear manner from 3100 to 3600 mc and back to 3100 mc at about 10 cps. The average transmitted power is 250 watts. The receiver and data display (designed by Airborne Instruments Laboratory) sweep in synchronism with the transmitter. The synchronizing signal is derived from the carrier frequency of a broadcast station (Paris-Inter). The receiver is designed to track swept signal amplitudes down to about 4 db above noise level, and after severe fades, to reacquire signals larger than 6 db above noise level in about 1 to 2 milliseconds. Received signal amplitude is presented as a simultaneous function of frequency and time.

Preliminary data obtained from the link indicate that privileged transmission frequencies exist at all times in this band at which the transmission level is about 10 db above median. The preliminary data gathered from the link are described, as well as general design features of the system.

## INTRODUCTION

A LARGE amount of data has been collected that describes the time variation of signal amplitude received over tropospheric scatter links operating at fixed frequencies. The frequency-swept link described here was set up to obtain data concerning the variation of received signal level as simultaneous functions of frequency and time, and to determine whether a cross-correlation exists between the frequency and time variation.<sup>1,2</sup>

## GENERAL DESCRIPTION OF THE LINK

The transmitter for the link was designed and constructed by the Département de Physique Appliquée of the Compagnie Générale de Télégraphie Sans Fil (CSF). The average power output of the transmitter is 250 watts. The transmitted frequency is swept from 3100 to 3600 mc and back to 3100 mc in a triangular fashion, 10 times a second. The rate of 10 per second was chosen to measure signal strength at each frequency in the band an average of twenty times a second. This rate is high compared to the fade rates<sup>3</sup> that were ex-

pected over the scatter path. First data obtained over the link show that this was a conservative assumption: slow fades at a fixed frequency occurred at rates of about 0.5 to 1 cps. Each frequency in the band under study is therefore sampled at a rate that is high compared to the fade rate; the measurement of received signal strength at the receiver terminal of the link can be considered as a simultaneous record of fading properties at all frequencies in the band between 3100 and 3600 mc.

The superheterodyne receiver for this link—designed and constructed by Airborne Instruments Laboratory (AIL)—was 194 miles from the transmitter site. A voltage-tuned local oscillator sweeps through the required band of frequencies in synchronism with the frequency sweep of the transmitter. An AFC loop actuated by received signals corrects the local oscillator frequency to keep the IF signal within the receiver IF pass band.

The transmitting and receiving antennas are two identical parabolic reflectors with diameters of 8 meters and focal lengths of about 3 meters. Antenna feeds giving horizontal and vertical polarization, as well as two beamwidths for each polarization (one with a 45.1-db gain at midband, the other with a 42.1-db gain at midband) are available to achieve flexibility in data gathering. Antenna positions are adjustable through  $\pm 3.0^\circ$  in azimuth and  $\pm 2.5^\circ$  in elevation. Fig. 1 shows the antenna mounted at the transmitter end of the link.

Flexibility in the link exists in antenna beamwidths and polarizations, in the band of frequencies swept

\* Manuscript received by the PGAP, November 9, 1959; revised manuscript received, February 12, 1960. This work was supported under Signal Corps Contract DA-36-039-sc-73276.

† Airborne Instruments Lab., a division of Cutler-Hammer, Inc., Deer Park, N. Y.

<sup>1</sup> J. H. Chisholm, L. P. Rainville, J. F. Roche, and H. G. Root, "Measurement of the bandwidth of radio waves propagated by the troposphere beyond the horizon," *IRE TRANS. ON ANTENNAS AND PROPAGATION*, vol. AP-6, pp. 377-378; October, 1958.

<sup>2</sup> A. B. Crawford, D. C. Hogg, and W. H. Kummer, "Studies in tropospheric propagation beyond the horizon," *Bell Sys. Tech. J.*, vol. 38, pp. 1067-1178; September, 1959.

<sup>3</sup> On a scatter link one generally observes slow fades of major amplitude variation (many decibels) with a superimposed much higher rate of fades of relatively small amplitude (a few decibels). The fade rate (as used above) refers to the slow fade rates. Alan T. Waterman, Jr., in "A rapid beam-swinging experiment in trans-horizon propagation," *IRE TRANS. ON ANTENNAS AND PROPAGATION*, vol. AP-6, pp. 338-340, October, 1958, reports occasional discontinuities occurring in less than  $\frac{1}{2}$  of a second. This implies that the sweep speed in this experiment may have been too low to observe certain phenomena on the link, though the observed results up to this time do not give any such indication.



Fig. 1—Transmitting antenna.



through, and in the display and recording of data. Initially the link provided operation of the sweep either through 500 mc or through 10 mc. In addition, the receiver and transmitter can be operated at any fixed frequency in the band to provide the more conventional type of scatter data. Data taken in the winter of 1958-1959 showed that the signal behavior over 100 to 200 mc of the band does not appear to differ from the behavior over the full 500-mc band. Since sweeping over a reduced bandwidth increases the depth of fade which the receiver can track, a 200-mc mode has been incorporated into the system.

Two displays are available for observing and recording the received signal strengths. An A-scope type of presentation shows received signal strength as a function of frequency, with the horizontal deflection proportional to frequency in the interval between 3100 and 3600 mc. Fig. 2 shows such a display. The sweep for the horizontal (frequency) scale is provided by the same triangular voltage that is used to tune the local oscillator. Fig. 2 illustrates the display of a single sweep of the receiver from 3100 to 3600 mc. It is also possible to use this same display to view the superpositions of receiver outputs during repeated sweeps of the local oscillator. In this manner, an envelope of received signal amplitudes as a function of frequency and time can be obtained.

The second method of data display (Fig. 3) is a frequency-time-intensity oscilloscope presentation, usually referred to as an FTI display. Here intensity is a measure of signal amplitude, horizontal deflection corresponds to frequency, and vertical deflection corresponds to time. A vertical line in this display, showing signal intensity as a function of time at a fixed frequency, is the type of data observed on conventional scatter links. Fig. 3 shows three frames, each of about 27-second duration, photographed with a Polaroid-Land camera. Future data will be taken by using a moving film camera, where the film motion replaces the vertical deflection of the CRT. In this way, patterns with variable time scales can be obtained.

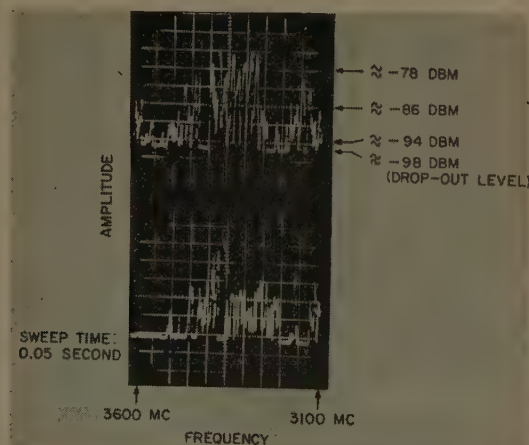


Fig. 2—A-scope presentation of one receiver sweep period.

## EQUIPMENT IN THE LINK

### Synchronization

The transmitter and receiver use voltage-tunable devices (a CSF carcinotron and a GE voltage-tunable magnetron, respectively) to determine the transmitted and received frequencies. In both transmitter and receiver, a triangular voltage with a frequency of 10 cps is applied to the voltage-tunable elements. To synchronize the frequency of these triangles, the inflection points of the triangles at both transmitter and receiver are derived by using auxiliary receivers tuned to the 164-kc signal of radio station Paris-Inter. By dividing this frequency by 8100, synchronizing pulses for the inflection points of the triangles are obtained at each end of the link, with the inflection points occurring at a rate of 164 kc/8100 kc or about 20 cps. This makes the triangle frequency about 10 cps.

Although the frequencies of the two triangles are synchronized by the 164-kc signal, the phase of the two tuning triangles is generally incorrect. That is, the inflection points of the transmitter frequency sweeps (as observed at the receiver site) do not coincide with the inflection points of the local oscillator frequency at the receiver. This phase difference is caused by the different starting times of the transmitter and receiver and by the difference in distance from the source of the synchronizing signal to the transmitter and to the receiver. Therefore, the first step during operation of the equipment is to make the inflection points of the sweeps coincide at the receiver. This is accomplished at the receiver in the following manner: a blanking voltage is derived from the A scope to suppress the 164-kc input to the dividing circuit exactly long enough to shift the phase of the tri-

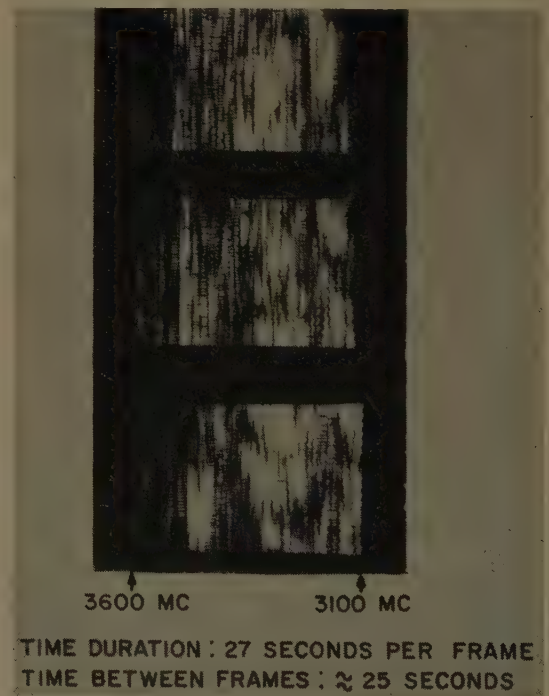


Fig. 3—FTI displays.



angle by a suitable amount. Alignment accuracy of  $\pm 3$   $\mu$ sec is obtained.

### Transmitter

Fig. 4 is a photograph and Fig. 5 is a simplified block diagram of the transmitter. The loop antenna at the top of the receiver cabinet receives the 164-kc synchronizing signal from Paris-Inter.

Two servoloops are shown in the transmitter block diagram. Loop 1 slaves the frequency of the transmitting carcinotron to a reference law of frequency variation provided by a voltage-controlled oscillator in loop 2. Loop 2 serves only to fix the sweep-inflection frequency accurately, with the use of two crystal oscillators.



Fig. 4—Transmitter.

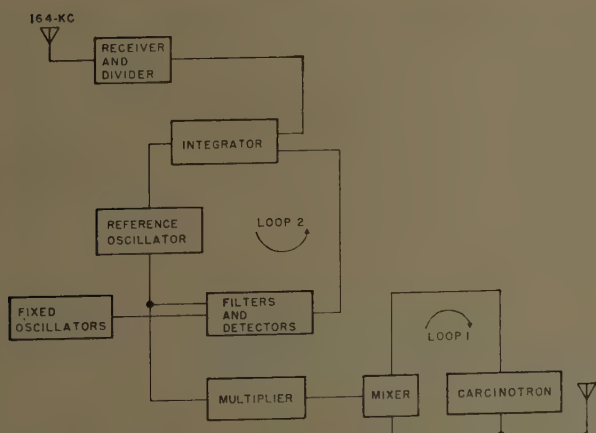


Fig. 5—Block diagram of transmitter.

The tuning voltage applied to the carcinotron consists of the sum of two voltages:

- 1) The basic triangular sweep. This is derived by integrating (and then amplifying) the square-wave output from the divider synchronized by the 164-kc signal. This voltage may result in deviations of about  $\pm 30$  mc from the desired linear frequency variation.
- 2) A correction voltage is supplied by loop 1 as a result of comparing the carcinotron frequency with the reference law of frequency.

The reference law of frequency is generated in a voltage-tunable low-frequency (27.25- to 31.75-mc) oscillator that has an extremely linear characteristic of frequency vs voltage. The output of the reference oscillator is applied to a multiplier that converts frequencies centered at 29.5 mc to frequencies centered at 236 mc. The actual reference signal is obtained by applying the output of the multiplier to a crystal mixer harmonic generator, where the 14th harmonic is the appropriate reference frequency for the carcinotron.

The linearity of sweep obtained with this system is such that the peak-to-peak deviation from a straight line between 3100 and 3600 mc is less than 7 mc. Power output over the band varies less than  $\pm 1.5$  db from the nominal output value of 250 watts.

### Receiver

Fig. 6 is a photograph and Fig. 7 is a simplified block diagram of the receiver. As in the transmitter, there is an auxiliary receiver for the 164-kc synchronizing signal. This signal is divided down to form a square wave that is integrated to form a triangular voltage that tunes the local oscillator in the receiver. The local oscillator is a voltage-tunable magnetron manufactured by the General Electric Company. The output of the oscillator is applied to a balanced mixer. A low-noise traveling-wave tube is used as preamplifier to improve the receiver noise figure.

The IF bandwidth of the receiver—and therefore its resolution—was 2 mc when the preliminary data to be discussed were obtained. To improve receiver sensitivity and resolution, this has subsequently been narrowed to about 300 kc. Even though the receiver and transmitter tuning triangles are synchronous and the tuning characteristics (frequency as a function of time) are nearly linear for both transmitter and receiver, the two laws of frequency variation are not sufficiently identical to keep the intermediate frequency within the pass band of the IF amplifier at all times. An AFC circuit is therefore provided that can lock the two frequencies together by applying a correction voltage to the local oscillator.

Since the AFC loop is operated by the received signal, a severe fade may result in loss of tracking. To facilitate the resumption of tracking after a fade, a low-frequency sine wave signal is superimposed on the tri-

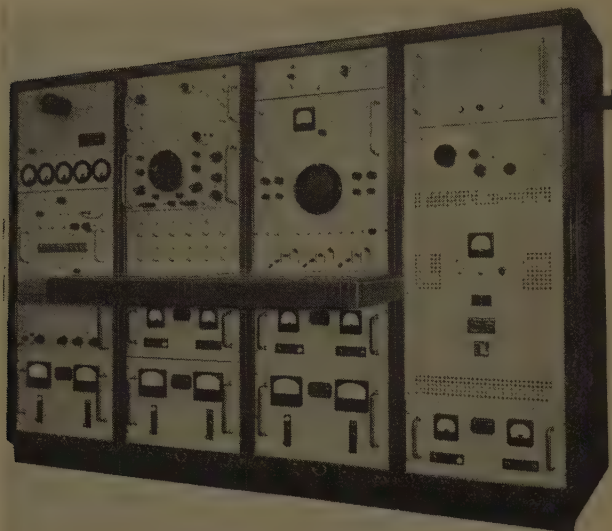


Fig. 6—Receiver.

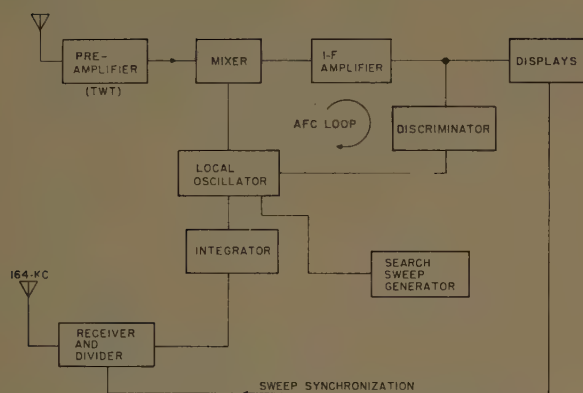


Fig. 7—Simplified block diagram of receiver.

angular tuning voltage applied to the voltage-tunable magnetron. In the absence of tracking, the local oscillator frequency is continuously "wobbled" from linearity by an amount slightly greater than the expected peak-to-peak deviation in the receiver and transmitter frequency laws. This wobble is about  $\pm 10$  mc. As soon as the mixer output frequency falls within the IF pass band, the AFC loop will lock and provide, as part of its correction voltage, a signal that cancels the low frequency sine wave. Audio frequencies near 300 cps were used as wobble frequencies during the initial link operation.

The output of the IF amplifier is detected and applied to a direct-coupled audio amplifier with adjustable bandwidths (range about 500 cps to 80 kc). The signals from this amplifier are shown on either the A scope or FTI displays discussed above.

#### DATA

The link was placed in operation in November, 1958 and preliminary propagation data were obtained for about one week. With the receiver IF bandwidth at 2

mc and a total swept band of 500 mc, the receiver could maintain frequency lock under swept conditions down to signal levels of  $-97$  to  $-100$  dbm. Using the receiver modifications mentioned above—that is, reduction of IF bandwidth to 300 kc and reduction of the band of frequencies covered to 200 mc—the receiver can maintain frequency lock under swept conditions for signals down to about  $-110$  dbm.

#### A-Scope Presentation

The A-Scope presentation shown in Fig. 2 is typical of those obtained under good operating conditions.

Fig. 2 shows signals received on a single sweep as the link frequency is varied from 3100 to 3600 mc. A straight line near the bottom of the display represents a severe fade, where the receiver AFC could no longer track. This level is at about  $-98$  dbm. The duration of each loss of tracking during the particular sweep shown is less than 3 milliseconds. This means that in this case the AFC loop was capable of reclosing each time it had opened within less than one cycle of the audio search sweep frequency used to wobble the local oscillator frequency.

The relatively low signal levels and poor tracking shown in the region between 3500 to 3600 mc were typical of much of the data obtained during link operation. This phenomenon is not fully understood and requires further investigation.

The upper trace of Fig. 2, especially in the region of very strong signals near the center of the band, shows an almost periodic variation of the received signal strength as a function of frequency. The periodicity in this amplitude pattern—the peaks (or nulls) repeat about every 17 mc—is not caused by the measuring equipment used on the link.

A possible explanation for the periodicity is obtained by considering the simplified case of two-ray propagation between the end-points of the link (the two rays being formed by the upper and lower half-power points of the antenna gain pattern).

If the phase of the two rays arriving at the receiver is such as to give a certain vector sum at the receiving site, then at a frequency removed from the one under consideration by  $1/T$ , where  $T$  is the difference in propagation time along the two-ray paths, the phase relationship between the two arriving vectors will again be the same as at the original frequency. Thus, the peaks (or nulls) in the pattern will be separated in frequency by  $1/T$ . For a 17-mc separation,  $T$  is about  $0.06 \mu\text{sec}$ , which is a reasonable value for the path geometry.<sup>4</sup>

<sup>4</sup> An expression for differential delay is given on p. 1163 of Crawford, Hogg, and Kummer.<sup>2</sup> Many interesting bandwidth data are presented in this paper based on narrow band experiments. For a bandwidth defined by a correlation coefficient of 0.6, the authors give, at frequencies near 4000 mc, and with 28-foot antennas, bandwidths varying from about 5 to more than 12 mc. This compares favorably with the 17 mc measured between nulls on the link described in the present paper.



This periodicity is much less distinct—perhaps completely lacking—when the signal level has dropped as shown in the lower half of Fig. 2. These data were taken within seconds of the upper set. They show the existence of a fairly rapid fluctuation in the median level of the signal. The fluctuation of signal strength here as a function of frequency is much more rapid than in the upper trace. This may be characteristic of lower signal levels.

### Fixed Frequency Signal Variation

Fig. 8 shows an A-scope presentation for fixed-frequency operation of the link. In the top trace, the total trace period is 50 seconds and in the bottom trace the total trace period is 10 seconds. The maximum fluctuation rate shown in the photograph is about 1 to 2 cps for the fine structure variation in amplitude. Strong variations occur at a much lower rate, about 1 in 10 to 15 seconds, as is shown fairly clearly in the upper trace.

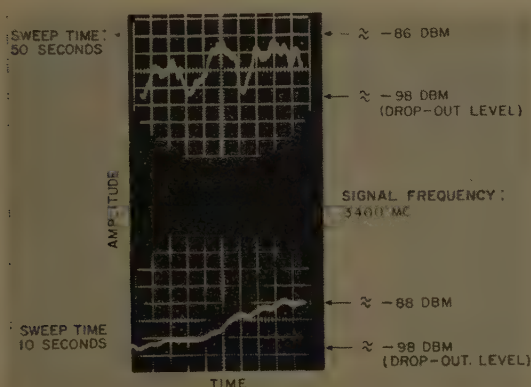


Fig. 8—Amplitude variations at a fixed frequency.

### FTI Display

Fig. 3 shows three typical FTI displays, each representing a time duration of about 27 seconds with about 25 seconds between successive frames. The direction of increasing frequency is right to left. The return trace in this display has been blanked and actually only one-half of the available data is presented. The rasters show the frequency range and the time duration for the maxima of the transmission (the light regions) as well as for the minima (the black regions). The range of signal levels presented in these rasters is between  $-98$  and  $-78$  dbm, with a median estimated at about  $-88$  dbm.

These contours show that transmission is privileged at certain frequency bands within the entire band for periods up to 20 seconds. These privileged frequency bands may be as wide as 20 mc, somewhat wider than the coherent bandwidths expected for this link. More important than the width of the band is the slowness of the fluctuations of the peaks of these signals. When the signal fades at a given frequency (as shown by the

transition from a bright vertical streak in Fig. 3 to a dark or black region) there is not generally a contiguous region of frequencies where the signals become correspondingly stronger.

A better understanding of the amplitude of the privileged frequencies is obtained from the A-scope display in Fig. 2. We see that in the 500-mc region displayed, there are some frequencies where the signal is above  $-78$  dbm, whereas, over the entire range, the median is estimated to be below  $-90$  dbm. In other words there are privileged frequencies in this band where the signal strength of the transmission over the link is better than 10 or perhaps 15 db above the median for that band. In this respect, Fig. 2 is typical of the results obtained. It is not necessary to use a 500-mc band to obtain a high probability of having a frequency in the band where the transmission is privileged by 10 to 15 db above the median of the band.

The high probability of finding a signal 10 db or more above the median within a band of frequencies covering 500 mc would indicate that the distribution of amplitude as a function of frequency is not a Rayleigh distribution. For even if the correlation bandwidth is as small as 5 mc (*i.e.*, if there are 100 independent channels in the 500-mc band), the probability of a signal in one of these channels being 10 db above median is 9.5 per cent. The observed probability is much greater, and the number of independent channels appears much smaller than 100. Crawford, Hogg, and Kummer<sup>2</sup> point out that scatter links showing very slow fade rates—as observed here—are often not Rayleigh distributed. Whether this also relates to the lack of Rayleigh distribution in amplitude as a function of frequency remains to be determined as additional data are taken on this link.

### POSSIBLE APPLICATION

The preliminary results obtained make it interesting to speculate about the properties of a scatter link designed to seek an optimum transmission frequency. If such a system were used, transmission levels of about 10 to 15 db above the median appear to be continuously available. To achieve similar performance in a conventional scatter link—that is, to keep the received signal level 10 db above median 99 per cent of the time—would require an increase in transmission power of about 28 db. Even with a triple diversity scatter system, an increase in transmitted power of about 15 db would be required to duplicate the performance of an optimum frequency-seeking system. Of course an optimum frequency-seeking system requires a rather wide bandwidth and some sort of a closed loop linking the transmitter and receiver. However, in many applications where this kind of system would be most desirable, bandwidth is ordinarily available, and the closed loop system is easily implemented.



## FUTURE PROGRAM

At the conclusion of data taking, a year from now, many of the questions raised by the initial data should be resolved, especially those pertaining to the nature of the signal peaks—that is, their time and frequency characteristics. A gross comparison will be made between the statistics of the peak signals and those of the minimum signals. As has been mentioned previously, a variety of climatic and antenna-feed conditions will be covered during the course of the data taking.

## ACKNOWLEDGMENT

The combined efforts of many people at AIL, at CSF, and at the Signal Corps made possible the successful establishment of this scatter link. At CSF the transmitter and antenna portions of the link were developed through the efforts of Alexis, Biggi, Broussaud, and Simon. Major contributions to the receiver design were made at AIL by Barna, Bridgeman, Franceschini, Lebenbaum, and Greene. H. Zweigbaum of the Signal Corps provided helpful counsel during the program.

## Energy Density in Continuous Electromagnetic Media\*

A. TONNING†

**Summary**—After a discussion of various types of linear electromagnetic media, a general expression for the energy density for a lossless medium is derived by evaluation of the total influx of energy to a volume element. The result reduces to the commonly used expression only if the medium is nondispersive. The physical significance of the extra energy term resulting from the dispersion is discussed, and a general expression for the stored energy of an electric network is given.

### I. INTRODUCTION

THE merit of a macroscopic description of electromagnetic phenomena in matter is its simplicity, as compared with the more complete microscopic description. When the various field quantities are replaced by their respective volume averages the effects of the complicated array of atoms and electrons constituting the medium may be represented by a few parameters which are taken to be continuous functions of position; the medium itself is regarded as a continuum which is fully characterized by these parameters. A description of this kind is, evidently, satisfactory only in cases where the large-scale effects of the presence of matter is all that is desired, while the details of the physical phenomena occurring on an atomic scale may be neglected. Since the averaging process is linear, any linear relation between the microscopic fields remains valid for the macroscopic fields as well. This is not true, however, for relations involving quantities which are nonlinear functions of the fields such as those appearing in the

momentum energy tensor. These quantities have a well defined meaning in vacuum, but there is no reason to suppose that the same interpretation is valid when the true fields are replaced by their volume averages. During the averaging process a large amount of information on the field distribution is clearly lost and it is not at all evident that the various physical quantities of importance are expressible in terms of the macroscopic fields.

In this discussion we shall confine our attention entirely to the energy relations and thus derive an expression for the energy density of a continuous, linear, time-invariant medium. It will be shown that the commonly used expression is incomplete and that it is, in general, necessary to add a term which reduces to zero in the case of frequency independent media.

### II. GENERAL FIELD RELATIONS—EXAMPLES OF LOSSLESS MEDIA

In terms of the macroscopic fields, Maxwell's equations are (mks units)

$$\left. \begin{aligned} \nabla \times \mathbf{E} + \frac{\partial \mathbf{B}}{\partial t} &= 0, \\ \nabla \times \mathbf{H} - \frac{\partial \mathbf{D}}{\partial t} &= \mathbf{J}, \\ \nabla \cdot \mathbf{D} &= \rho, \\ \nabla \cdot \mathbf{B} &= 0. \end{aligned} \right\} \quad (1)$$

In addition, the fields satisfying these equations must satisfy certain relations imposed upon them by the

\* Manuscript received by the PGAP, April 28, 1959; revised manuscript received, February 1, 1960.

† Norwegian Defense Res. Est., Bergen, Norway.

presence of the medium. These relations are the macroscopic characteristics of the medium. Let us introduce a vector  $\mathbf{D}'$  by writing

$$\frac{\partial \mathbf{D}'}{\partial t} = \mathbf{J}.$$

The current density  $\mathbf{J}$  determines  $\mathbf{D}'$  within an additive constant. When a convenient choice of this constant is made, it is seen from the equation of continuity that

$$\nabla \cdot \mathbf{D}' + \rho = 0.$$

Hence the second and third equations in (1) may be written

$$\begin{aligned} \nabla \times \mathbf{H} - \frac{\partial}{\partial t} (\mathbf{D} + \mathbf{D}') &= 0, \\ \nabla \cdot (\mathbf{D} + \mathbf{D}') &= 0. \end{aligned}$$

We shall assume that the current density  $\mathbf{J}$ , and hence also  $\mathbf{D}'$ , is uniquely determined by the electric field  $\mathbf{E}$ . In this case we introduce no further restriction on the medium by replacing the sum  $(\mathbf{D} + \mathbf{D}')$  by  $\mathbf{D}$ . This is equivalent to setting  $\mathbf{J}$  and  $\rho$  in (1) equal to zero, which is done in the following.

We shall assume, without discussion, that the energy flux in the medium is given by the same expression as for vacuum, viz

$$\mathbf{S} = \mathbf{E} \times \mathbf{H}. \quad (2)$$

The influx of energy to a unit volume during time  $dt$  is accordingly

$$-\nabla \cdot \mathbf{S} dt = \left( \mathbf{H} \cdot \frac{\partial \mathbf{B}}{\partial t} + \mathbf{E} \cdot \frac{\partial \mathbf{D}}{\partial t} \right) dt. \quad (3)$$

A part of this energy is in general converted into heat and lost while another part is stored in the medium and may be recovered in the form of electromagnetic energy. Particularly interesting are the media in which the process of building up an electromagnetic field is a reversible process. These are called lossless media. The mathematical criterion of reversibility is that the right-hand side of (3) is always a complete differential of a function  $u$  of  $\mathbf{E}$ ,  $\mathbf{H}$ ,  $\mathbf{D}$ , and  $\mathbf{B}$ .

$$\left( \mathbf{H} \cdot \frac{\partial \mathbf{B}}{\partial t} + \mathbf{E} \cdot \frac{\partial \mathbf{D}}{\partial t} \right) dt = du. \quad (4)$$

$u$  may also depend on the time derivatives of the fields. It does not, however, depend on time explicitly. Since the fields are functions of time, we shall for the sake of brevity write  $u = u(t)$ .

The net energy absorbed by the unit volume from  $t_0$  to  $t$  is

$$-\int_{t_0}^t \nabla \cdot \mathbf{S} dt = u(t_0) - u(t). \quad (5)$$

It is evident that if the fields and an appropriate number of their derivatives have the same values at the instants  $t_0$  and  $t_1$ , the net absorbed energy is zero. Thus *the power absorption during a complete cycle of field variation is always zero*. If the fields are zero for  $t = -\infty$ ,  $u(t)$  will tend to a limit as  $t \rightarrow -\infty$ , and since  $u$  is only determined by (4) within an additive constant, we may always assume that this limit is zero. With this convention,  $u(t)$  is the electromagnetic energy absorbed by a volume element during the building up of the fields in the medium. As we have seen,  $u(t)$  is also the energy we may extract from the medium by reducing the macroscopic fields to zero.

The definition of a lossless medium given above is unconventional. It may, therefore, be worth while to consider a few examples and to show that the definition is equivalent to ordinary conceptions of a lossless medium.

The simplest type of electromagnetic medium is characterized by

$$\mathbf{D} = \epsilon \mathbf{E}, \quad \mathbf{B} = \mu \mathbf{H}. \quad (6)$$

By insertion in (3) it is seen directly that the right-hand side is a complete differential of the function

$$u = \frac{1}{2} (\mathbf{H} \cdot \mathbf{B} + \mathbf{E} \cdot \mathbf{D}). \quad (7)$$

For nonisotropic media  $\epsilon$  and  $\mu$  are dyadics and the right-hand side of (3) may be written

$$\begin{aligned} -\nabla \cdot \mathbf{S} dt &= \frac{1}{2} d(\mathbf{H} \cdot \mathbf{B} + \mathbf{E} \cdot \mathbf{D}) \\ &+ \frac{1}{2} \left[ \mathbf{H}(\underline{\mu} - \tilde{\mu}) \frac{\partial \mathbf{H}}{\partial t} + \mathbf{E}(\underline{\epsilon} - \tilde{\epsilon}) \frac{\partial \mathbf{E}}{\partial t} \right] dt, \end{aligned} \quad (8)$$

where  $\tilde{\mu}$  is the transpose of  $\underline{\mu}$ .

The second term is not a complete differential for arbitrary functions  $\mathbf{H}$  and  $\mathbf{E}$  unless

$$\underline{\mu} - \tilde{\mu} = 0, \quad \underline{\epsilon} - \tilde{\epsilon} = 0. \quad (9)$$

Hence  $\underline{\epsilon}$  and  $\underline{\mu}$  are symmetrical for a lossless medium. In that case the energy density is again given by (7).

Media characterized by the relations

$$\begin{aligned} \mathbf{B} &= \underline{\mu} \cdot \mathbf{H} + \xi \cdot \mathbf{E}, \\ \mathbf{D} &= \underline{\gamma} \cdot \mathbf{H} + \epsilon \cdot \mathbf{E}, \end{aligned} \quad (10)$$

have been studied by Tellegen.<sup>1</sup> The condition of losslessness requires that  $\underline{\mu}$  and  $\underline{\epsilon}$  be symmetrical, and that  $\xi = \tilde{\gamma}$ . Here again it is found that the energy density is given by (7).

<sup>1</sup> B. D. H. Tellegen, "The Gyrator, a new network element," *Phillips Res. Repts.*, vol. 3; April, 1948.

The examples discussed so far represent very special types of linear media characterized by the fact that the vectors  $\mathbf{B}$  and  $\mathbf{D}$  at an arbitrary instant of time are uniquely determined by the values of  $\mathbf{H}$  and  $\mathbf{E}$  at the same instant. In general  $\mathbf{B}(t)$  and  $\mathbf{D}(t)$  will also be influenced by the values of  $\mathbf{H}$  and  $\mathbf{E}$  prior to the time  $t$ . In such cases the relation between  $\mathbf{E}$  and  $\mathbf{D}$  may take the form

$$\mathbf{D}(t) = \int_{-\infty}^t K(t - \tau) \cdot \mathbf{E}(\tau) d\tau, \quad (11)$$

where the kernel  $K(\tau)$  defines the electric properties of the medium. It is convenient to carry out the discussion of such media in terms of time-harmonic fields. Let us introduce

$$\mathbf{E}(t) = \text{Re} \{ \hat{\mathbf{E}} e^{j\omega t} \}, \quad (12)$$

with similar notations for the other field quantities. The complex field amplitudes  $\hat{\mathbf{E}}, \hat{\mathbf{D}}, \dots$  are in general functions of  $\omega$ . The relation (11) may now be written

$$\hat{\mathbf{D}} = \epsilon \cdot \hat{\mathbf{E}}, \quad (13)$$

where  $\epsilon$  is a function of  $\omega$ , *i.e.*, the medium is *dispersive*. The frequency dependent permittivity  $\epsilon(\omega)$  is, in fact, the Fourier transform of  $K(\tau)$ . The great advantage of carrying out the discussion in the frequency rather than in the time domain is that this permits us to reduce the integral relation (11) to the algebraic relation (13).

By the relation (11), the value of  $\mathbf{D}$  at a given point in space is uniquely determined by the value of  $\mathbf{E}$  at the same point. We may easily conceive of media for which the value of  $\mathbf{D}$  at a given point is influenced by the values of  $\mathbf{E}$  at other points of space. An example of this type of medium is an electron beam. In the most general case, therefore, the simple integral in (11) must be replaced by quadruple integrals extended over space-time.

In the following discussion we shall avoid the introduction of explicit relations between  $\mathbf{D}$  and  $\mathbf{B}$  on one side and  $\mathbf{E}$  and  $\mathbf{H}$  on the other. Therefore the results will be valid for the most general linear, time-invariant, lossless medium. The discussion is carried out in terms of time-harmonic fields, in which case the condition of losslessness assumes a particularly simple form. In terms of the complex field amplitudes, we have, for the left-hand side of (3),

$$\begin{aligned} -\nabla \cdot \mathbf{S} dt &= -\frac{1}{2} \text{Re} \nabla \cdot (\hat{\mathbf{E}} \times \hat{\mathbf{H}}^*) dt \\ &\quad -\frac{1}{2} \text{Re} \nabla \cdot (\hat{\mathbf{E}} \times \hat{\mathbf{H}} e^{j2\omega t}) dt, \end{aligned} \quad (14)$$

where the asterisk denotes the complex conjugate. The criterion of losslessness requires that the above be a complete differential, which will be the case only if its integral, taken over a complete cycle of the fields, is zero. Since the fields are periodic, it is here sufficient to integrate over one period, and we find that for a lossless

medium we have

$$\text{Re} \{ \nabla \cdot (\hat{\mathbf{E}} \times \hat{\mathbf{H}}^*) \} = 0, \quad (15)$$

which is a well known result.

From (15) and the complex Maxwell's equations

$$\begin{aligned} \nabla \times \hat{\mathbf{E}} + j\omega \hat{\mathbf{B}} &= 0, \\ \nabla \times \hat{\mathbf{H}} - j\omega \hat{\mathbf{D}} &= 0, \end{aligned} \quad (16)$$

it follows that

$$\text{Im} (\hat{\mathbf{E}}^* \cdot \hat{\mathbf{D}} + \hat{\mathbf{H}}^* \cdot \hat{\mathbf{B}}) = 0. \quad (17)$$

Hence, for a lossless medium the function

$$\bar{w} = 1/4 (\hat{\mathbf{E}}^* \cdot \hat{\mathbf{D}} + \hat{\mathbf{H}}^* \cdot \hat{\mathbf{B}}) \quad (18)$$

must be real for arbitrary complex vectors  $\hat{\mathbf{E}}$  and  $\hat{\mathbf{H}}$ , and for arbitrary real frequencies  $\omega$ .

It follows that if the electric and magnetic properties of the medium are given by a permittivity tensor  $\epsilon$  and a permeability tensor  $\mu$ , respectively, then  $\epsilon$  and  $\mu$  must be Hermitian for a lossless medium.

### III. DERIVATION OF A GENERAL EXPRESSION FOR THE ENERGY DENSITY IN THE CASE OF HARMONICALLY VARYING FIELDS

In the preceding section we defined the energy density of a lossless medium as the energy absorbed by the medium during the build-up of the electromagnetic field. This definition is not directly applicable to harmonically varying fields, because these are not zero for  $t = -\infty$ . We shall avoid this difficulty by evaluating the energy density for the case when the fields are given by (12) with  $\omega$  a complex constant

$$\omega = \omega_0 + j\sigma, \quad (19)$$

where  $\omega_0, \sigma$  are real, and  $\sigma$  is negative and numerically small. The fields are then zero for  $t = -\infty$ . After having found the energy density for this case we shall take the limit of the expression when  $\sigma \rightarrow 0$  as the energy density for a harmonically varying field. This seems to be a satisfactory procedure, since fields that are harmonic in the strictest sense never appear in a physical experiment.

From (3), the energy density is found to be

$$\begin{aligned} u &= - \int_{-\infty}^t \nabla \cdot \mathbf{S} dt = \frac{1}{2} (\mathbf{H} \cdot \mathbf{B} + \mathbf{E} \cdot \mathbf{D}) \\ &\quad + \frac{1}{2} \int_{-\infty}^t dt \left[ \mathbf{H} \cdot \frac{\partial \mathbf{B}}{\partial t} - \mathbf{B} \cdot \frac{\partial \mathbf{H}}{\partial t} + \mathbf{E} \cdot \frac{\partial \mathbf{D}}{\partial t} - \mathbf{D} \cdot \frac{\partial \mathbf{E}}{\partial t} \right]. \end{aligned} \quad (20)$$

$\bar{w}$  as given by (18) is clearly the time average of the first term in (20) for harmonically varying fields. We shall see, however, that this expression is incomplete since it neglects the contribution from the integral to the right in (20).



A simple calculation shows that

$$\mathbf{E} \cdot \frac{\partial \mathbf{D}}{\partial t} - \mathbf{D} \cdot \frac{\partial \mathbf{E}}{\partial t} = -\omega_0 e^{-2\sigma t} \text{Im} (\hat{\mathbf{E}}^* \cdot \hat{\mathbf{D}}). \quad (21)$$

Assuming that the fields are analytic functions of frequency, and writing

$$\hat{\mathbf{D}}(\omega_0) = \hat{\mathbf{D}}_0, \quad (22)$$

we have

$$\hat{\mathbf{D}}(\omega) = \hat{\mathbf{D}}_0 + j\sigma \frac{\partial}{\partial \omega_0} \hat{\mathbf{D}}_0, \quad (23)$$

where the higher order terms in the Taylor expansion have been neglected since  $\sigma$  is small. From (21) and (23) we then find

$$\mathbf{E} \cdot \frac{\partial \mathbf{D}}{\partial t} - \mathbf{D} \cdot \frac{\partial \mathbf{E}}{\partial t} = -\omega_0 e^{-2\sigma t} \text{Im} \left[ (\hat{\mathbf{E}}_0^* \cdot \hat{\mathbf{D}}_0) - j\sigma \left( \hat{\mathbf{E}}_0^* \cdot \frac{\partial \hat{\mathbf{D}}_0}{\partial \omega_0} - \hat{\mathbf{D}}_0 \cdot \frac{\partial \hat{\mathbf{E}}_0^*}{\partial \omega_0} \right) \right]. \quad (24)$$

The analogous expression for the magnetic fields is obtained from (24) by replacement of  $\mathbf{E}$  by  $\mathbf{H}$  and  $\mathbf{D}$  by  $\mathbf{B}$ . When the two expressions are added and the condition of losslessness (18) is remembered, we obtain the following expression for the integrand to the right in (20):

$$I = -\omega_0 \sigma e^{-2\sigma t} \text{Re} \left\{ \hat{\mathbf{E}}_0^* \cdot \frac{\partial \hat{\mathbf{D}}_0}{\partial \omega_0} - \frac{\partial \hat{\mathbf{E}}_0^*}{\partial \omega_0} \cdot \hat{\mathbf{D}}_0 + \hat{\mathbf{H}}_0^* \cdot \frac{\partial \hat{\mathbf{B}}_0}{\partial \omega_0} - \hat{\mathbf{B}}_0 \cdot \frac{\partial \hat{\mathbf{H}}_0^*}{\partial \omega_0} \right\},$$

and consequently

$$-\int_{-\infty}^t I dt = \frac{\omega_0}{2} \text{Re} \left\{ \hat{\mathbf{E}}_0^* \cdot \frac{\partial \hat{\mathbf{D}}_0}{\partial \omega_0} - \frac{\partial \hat{\mathbf{E}}_0^*}{\partial \omega_0} \cdot \hat{\mathbf{D}}_0 + \hat{\mathbf{H}}_0^* \cdot \frac{\partial \hat{\mathbf{B}}_0}{\partial \omega_0} - \hat{\mathbf{B}}_0 \cdot \frac{\partial \hat{\mathbf{H}}_0^*}{\partial \omega_0} \right\}, \quad (25)$$

where we have put  $\sigma = 0$ .

Here the sum in the brackets is real. This is seen by differentiating (18), which must be valid for every real value of  $\omega_0$ ,

$$\text{Im} \left\{ \frac{\partial \hat{\mathbf{E}}_0^*}{\partial \omega_0} \cdot \hat{\mathbf{D}}_0 + \hat{\mathbf{E}}_0^* \cdot \frac{\partial \hat{\mathbf{D}}_0}{\partial \omega_0} + \frac{\partial \hat{\mathbf{H}}_0^*}{\partial \omega_0} \cdot \hat{\mathbf{B}}_0 + \hat{\mathbf{H}}_0^* \cdot \frac{\partial \hat{\mathbf{B}}_0}{\partial \omega_0} \right\} = 0,$$

and noting that nothing is altered in the above if we take the complex conjugate of the first and third terms, changing their signs simultaneously.

The total stored energy in a unit volume element averaged over one period is accordingly

$$\bar{u} = \bar{w} + s, \quad (26)$$

where  $\bar{w}$  is given by (18) and

$$s = \frac{\omega}{4} \left[ \hat{\mathbf{E}}^* \cdot \frac{\partial \hat{\mathbf{D}}}{\partial \omega} - \frac{\partial \hat{\mathbf{E}}}{\partial \omega} \cdot \hat{\mathbf{D}}^* + \hat{\mathbf{H}}^* \cdot \frac{\partial \hat{\mathbf{B}}}{\partial \omega} - \frac{\partial \hat{\mathbf{H}}}{\partial \omega} \cdot \hat{\mathbf{B}}^* \right]. \quad (27)$$

The expression (26) may evidently also be written

$$\bar{u} = \frac{1}{4} \left[ \hat{\mathbf{E}}^* \cdot \frac{\partial}{\partial \omega} (\omega \hat{\mathbf{D}}) - \frac{\partial \hat{\mathbf{E}}}{\partial \omega} \cdot \omega \hat{\mathbf{D}}^* + \hat{\mathbf{H}}^* \cdot \frac{\partial}{\partial \omega} (\omega \hat{\mathbf{B}}) - \frac{\partial \hat{\mathbf{H}}}{\partial \omega} \cdot \omega \hat{\mathbf{B}}^* \right]. \quad (26a)$$

The result (27) may be written in more compact form if we make use of the fact that  $\bar{w}$ , as given by (18), is a nonanalytic function of frequency. Therefore, its derivative along the imaginary frequency axis is different from its derivative along the real axis. Writing

$$\omega = \lambda + j\sigma \quad (\lambda \text{ and } \sigma \text{ real}),$$

$$\bar{w} = \bar{w}_r + j\bar{w}_i$$

( $\bar{w}_r$  and  $\bar{w}_i$  real, and  $\bar{w}_i = 0$  on the real  $\omega$  axis),

we find from (27) that

$$s = \omega \frac{\partial}{\partial \sigma} \bar{w}_i. \quad (28)$$

If the electromagnetic properties of the medium are given by a permittivity tensor  $\underline{\epsilon}$  and a permeability tensor  $\underline{\mu}$ , we have from (27)

$$s = \frac{\omega}{4} \hat{\mathbf{E}}^* \left( \frac{\partial}{\partial \omega} \underline{\epsilon} \right) \mathbf{E} + \frac{\omega}{4} \hat{\mathbf{H}}^* \left( \frac{\partial}{\partial \omega} \underline{\mu} \right) \cdot \hat{\mathbf{H}}. \quad (29)$$

Here it is evident that  $s$  is zero if  $\epsilon$  and  $\mu$  are independent of frequency. Even for more general types of media,  $s$  will be nonzero only if the medium is dispersive. For that reason it seems appropriate to call  $s$  the density of *dispersion energy*.

In many cases we are free to prescribe the frequency dependence of  $\mathbf{E}$  and  $\mathbf{H}$ . In particular, when  $\mathbf{E}$  and  $\mathbf{H}$  are independent of frequency, the expression (26) takes on the concise form

$$\bar{u} = \bar{w} + \omega \frac{\partial}{\partial \omega} \bar{w} = \frac{\partial}{\partial \omega} (\omega \bar{w}). \quad (30)$$

#### IV. PHYSICAL SIGNIFICANCE OF THE DISPERSION ENERGY

Consider again the case in which the electromagnetic properties of the medium may be expressed by two tensors  $\underline{\epsilon}$  and  $\underline{\mu}$ . From (26a) it follows that the mean energy density may be written

$$\bar{u} = \frac{1}{4} \hat{\mathbf{E}}^* \cdot \frac{\partial}{\partial \omega} (\omega \underline{\epsilon}) \cdot \hat{\mathbf{E}} + \frac{1}{4} \hat{\mathbf{H}}^* \cdot \frac{\partial}{\partial \omega} (\omega \underline{\mu}) \cdot \hat{\mathbf{H}}. \quad (31)$$

Since the energy density cannot be negative, we find that, for any lossless medium the tensors  $\partial/\partial\omega(\omega\epsilon)$  and  $\partial/\partial\omega(\omega\mu)$  must be positive definite (or semidefinite) for every real  $\omega$ . This condition is satisfied by the  $\epsilon$  and  $\mu$  derived from the common models of lossless media, e.g., the permittivity given by (33) or (34). From the losslessness of the medium it follows that the tensors must be Hermitian. The tensors  $j\omega\epsilon$  and  $j\omega\mu$  are therefore characterized by the same properties as the impedance matrices of lossless electric networks.

Let us consider the still more specialized case of a medium which is isotropic and homogeneous. The tensors then reduce to scalars. Suppose that a plane electromagnetic wave is propagating in the medium. The intrinsic impedance of the medium and the wave number are, respectively,

$$Z = \sqrt{\frac{\mu}{\epsilon}}, \quad k = \omega\sqrt{\epsilon\mu}.$$

Under these conditions the expression (31) for the energy density is reduced to

$$\bar{u} = \frac{1}{2} |\hat{E}|^2 \sqrt{\frac{\epsilon}{\mu}} \frac{dk}{d\omega}. \quad (32)$$

On the other hand, the density of power flow is given by the Poynting vector

$$|S| = \frac{1}{2} \sqrt{\frac{\epsilon}{\mu}} |\hat{E}|^2.$$

Hence, the velocity of energy flow is

$$v = \frac{|S|}{\bar{u}} = \frac{d\omega}{dk},$$

which is the well known expression for group velocity. It is thus seen that the velocity of energy propagation is equal to the group velocity. Clearly this will not be found to be the case if the dispersion energy is neglected. Pelzer<sup>2</sup> has derived an expression for the energy density equivalent to (32) by requiring that the velocity of energy propagation is the group velocity.

A few simple models of dispersive media will be considered in order to gain some insight into the physical significance of the dispersion energy.

The propagation of plane electromagnetic waves in ionic crystals has been discussed by Huang and others.<sup>3</sup> The electric field will cause the ions to vibrate around

their equilibrium positions, thus giving rise to a mechanical wave which will be propagated in conjunction with the electromagnetic wave. The permittivity of a crystal of this type is

$$\epsilon = a - \frac{(b - a)\omega_0^2}{\omega_0^2 - \omega^2}, \quad (33)$$

where  $a$ ,  $b$ , and  $\omega_0^2$  are characteristic constants of the crystal. Huang discusses the various modes of propagation and gives explicit expressions for the mechanical and electromagnetic energy. When our expression for the dispersion energy is compared with Huang's results, it is found that the maximum value of the density of kinetic energy of the ions is equal to the density of dispersion energy. On the other hand the term  $1/4 \epsilon |\hat{E}|^2$  is not equal to the electric field energy. From (33) it is evident that this term may even become negative for frequencies in the neighbourhood of  $\omega_0$ , and it appears to have no clear physical significance. The sum of the density of mechanical and electric energy given by Huang is equal to our expression (32), as, of course, it must be.

A medium with a simpler structure is a gas of free electrons in vacuum. If the plasma frequency is denoted by  $\omega_p$ , the electric permittivity is

$$\epsilon = \epsilon_0 \left( 1 - \frac{\omega_p^2}{\omega^2} \right), \quad (34)$$

where  $\epsilon_0$  is the permittivity of vacuum. Since (34) is a special form of (33), the remarks made above are valid in this case also. When we evaluate the energy density associated with a plane wave from (32) we find

$$\bar{u} = \frac{1}{2} |\hat{E}|^2 \epsilon_0, \quad (35)$$

i.e., the energy density associated with a plane wave in this type of medium is, for a given electric field, independent of the plasma frequency; it will have the same value as in vacuum.

In the two examples discussed above the dispersion energy was closely associated with the kinetic energy of the charge carriers. This is not always the case. A medium may be dispersive even if all its stored energy is electromagnetic field energy. As an example of this type of medium, let us consider a so-called artificial dielectric, e.g., an array of metal spheres of infinite conductivity arranged in a three-dimensional lattice in vacuum. If the positions of the spheres are fixed, the stored energy is clearly electromagnetic. On the other hand macroscopic field quantities may be introduced in the ordinary manner as volume averages, over volumes sufficiently large to contain a number of spheres. The permittivity obtained in this way will depend on the number of spheres per unit volume, on their diameter, and on the

<sup>2</sup> H. Pelzer, "Energy density of monochromatic radiation in a dispersive medium," *Proc. Roy. Soc. (London) A*, vol. 208, pp. 365-366; September, 1951.

<sup>3</sup> K. Huang, "On the interaction between the radiation field and ionic crystals," *Proc. Roy. Soc. (London) A*, vol. 208, pp. 352-365; September, 1951.

wavelength of the incident radiation. Therefore, the medium is dispersive and contains a dispersion energy which in this case must be purely electromagnetic.

The simple examples mentioned above suffice to show that, in general, the dispersion energy cannot be identified as any particular form of energy. If we refuse to consider the microstructure of the medium, confining our attention entirely to its macroscopic properties, it does not seem possible to assign any separate significance to the various terms of which the energy density  $\bar{u}$  consists. However, the sum  $\bar{u}$  has a clear physical significance as the energy per unit volume that may be extracted from the medium by reduction to zero of the macroscopic electromagnetic fields. The interesting outcome of this discussion is, therefore, that neither the electromagnetic energy nor the kinetic energy of the charge-carriers is determined by the macroscopic fields. These quantities can only be found by considering the microstructure of the medium, *i.e.*, the type of mechanism which is the source of its macroscopic properties. Accordingly, in a theory which is strictly macroscopic, these quantities have no place. The macroscopic theory is not concerned with the various forms in which energy may be stored in the medium. Its concern is the amount of energy that has been absorbed by or may be extracted from the medium.

## V. THE ENERGY OF AN ELECTRIC NETWORK

The results obtained above will now be applied for the evaluation of the stored energy of an electric network. Let the network be a waveguide junction, as indicated in Fig. 1. It is bounded by a surface of infinite conductivity, perforated by a number of transmission lines. The cross sections of the transmission lines are of arbitrary form and may be simply connected, as for ordinary rectangular or circular waveguides or multiply connected, as for coaxial lines or double-wire shielded lines. The only assumptions made about the medium in the interior of the junction are that it is linear and that it is independent of time. The medium in the transmission lines is assumed to be characterized by a scalar permittivity  $\epsilon$  and a scalar permeability  $\mu$ , both independent of frequency and both homogeneous in the direction parallel with the transmission lines. The fields in the transmission lines will be referred to the reference planes  $T_1, T_2, \dots$ , perpendicular to the axes of the guides. The volume bounded by the junction, the walls of the transmission lines, and the terminal planes is denoted by  $V$ . Let the tangential component of the electric field  $\mathbf{E}$  on the reference planes be given. The field is monochromatic, having a frequency  $\omega$ . The tangential component of the magnetic field  $\mathbf{H}$  over the reference planes may then be found by solving Maxwell's equations throughout the region  $V$ .

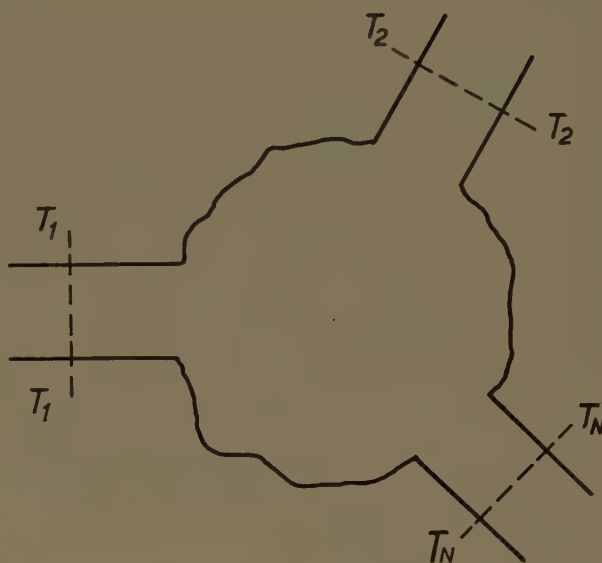


Fig. 1—Waveguide junction.

In order to find an expression for the stored energy, Maxwell's equations are differentiated with respect to frequency

$$\begin{aligned}\nabla \times \frac{\partial \hat{\mathbf{E}}}{\partial \omega} + j \frac{\partial}{\partial \omega} (\omega \hat{\mathbf{B}}) &= 0, \\ \nabla \times \frac{\partial \hat{\mathbf{H}}}{\partial \omega} - j \frac{\partial}{\partial \omega} (\omega \hat{\mathbf{D}}) &= 0,\end{aligned}\quad (36)$$

and we obtain

$$\begin{aligned}j \nabla \cdot \left( \hat{\mathbf{E}}^* \times \frac{\partial \hat{\mathbf{H}}}{\partial \omega} - \hat{\mathbf{H}}^* \times \frac{\partial \hat{\mathbf{E}}}{\partial \omega} \right) \\ = \frac{\partial}{\partial \omega} (\omega \hat{\mathbf{B}}) \cdot \hat{\mathbf{H}}^* - \omega \hat{\mathbf{B}}^* \frac{\partial \hat{\mathbf{H}}}{\partial \omega} + \frac{\partial}{\partial \omega} (\omega \hat{\mathbf{D}}) \cdot \hat{\mathbf{E}}^* - \omega \hat{\mathbf{D}}^* \frac{\partial \hat{\mathbf{E}}}{\partial \omega}.\end{aligned}$$

On comparing this with (28), and integrating over the volume  $V$ , the stored energy of the network is found,

$$\begin{aligned}U &= \int_V \bar{u} dV \\ &= j \frac{1}{4} \int_{T_1 + T_2 + \dots} \left( \hat{\mathbf{E}}^* \times \frac{\partial \hat{\mathbf{H}}}{\partial \omega} - \hat{\mathbf{H}}^* \times \frac{\partial \hat{\mathbf{E}}}{\partial \omega} \right) \cdot n dS,\end{aligned}\quad (37)$$

where the surface integral is taken over the terminal planes of the network. Let the network excitation be given by the tangential component of the magnetic field over the terminal planes  $T_1, T_2, \dots$ , and let this tangential component be kept independent of frequency. Then (37), is equivalent with

$$U = -j \frac{1}{4} \frac{\partial}{\partial \omega} \int_{T_1 + T_2 + \dots} (\hat{\mathbf{H}}^* \times \hat{\mathbf{E}}^*) \cdot n dS.\quad (39)$$



As is well known, terminal voltages and currents may be defined by expanding the fields in terms of the normal modes of the transmission lines, and by then identifying the voltage  $V_i$  and current  $I_i$  with the coefficient of expansion for the electric and magnetic fields respectively. Only the modes propagated by the transmission lines are coupled to each other through the junction. Hence, if the sum of the number of modes propagated is  $N$ , we have an  $N$  terminal pair network. The electric and magnetic fields at the terminal planes are characterized by the  $N$  dimensional column vectors  $\mathbf{v}$  and  $\mathbf{i}$  respectively.<sup>4</sup> Since the network is linear, these vectors are related by

$$\mathbf{v} = \mathbf{Z}\mathbf{i} \quad (39)$$

where the impedance matrix  $\mathbf{Z}$  is square, and is of  $N$ th order. It may be shown that

$$\int_{T_1+T_2+\dots} (\hat{\mathbf{H}}^* \times \hat{\mathbf{E}}^*) \cdot \mathbf{n} = \tilde{\mathbf{i}}^* \mathbf{Z} \mathbf{i}. \quad (40)$$

<sup>4</sup> For further details see C. G. Montgomery, R. H. Dicke, and E. M. Purcell, "Principles of Microwave Circuits," McGraw-Hill Book Co., Inc., New York, N. Y.; 1948.

Hence,  $\mathbf{i}$  being independent of frequency,

$$U = \frac{1}{4j} \tilde{\mathbf{i}}^* \left( \frac{\partial}{\partial \omega} \mathbf{Z} \right) \mathbf{i}. \quad (41)$$

This formula is well known for more special types of networks, and is usually taken to be the electromagnetic field energy.<sup>4</sup> However, this interpretation is not correct if the network includes dispersive media. In that case the field energy is not determined by the impedance matrix and the excitation of the network, but is also dependent on the structure of the medium.  $U$ , as given by (41), is the amount of energy that may be extracted from the network by connecting suitable load impedances to the network terminals.

#### ACKNOWLEDGMENT

The author gratefully acknowledges his debt to Tor Schaug-Pettersen and to Professor B. D. H. Tellegen for suggestions and illuminating discussions on the subject of this paper, and to Tore Wessel-Berg and P. Th. Hiis for carefully reading the manuscript. Finally, thanks are due to the Norwegian Defence Research Establishment for granting permission to publish the paper.

# communications

## Resonant Antenna Array with Tilted Beam\*

ELISABETH M. RUTZ†

THE described antenna array is a resonant waveguide array. The radiation maximum is tilted off broadside; this beam tilt is obtained by a constant phase difference between the admittances of successive radiating elements.

In microwave antennas in which the radiating elements are fed in cascade from an RF transmission line, the phase of the field radiated by each of the radiating elements is determined by three factors: 1) the position of the radiating element along the transmission line; 2) the phase velocity in the line; and 3) the admittance of the radiating element. The direction of the radiation maximum is determined by the relative phase of radiation of the array elements. A phase difference of the radiation of adjacent array elements will result in a tilt of the main beam.

The described linear array is a slotted waveguide array, the radiators are longitudinal shunt slots. In the array the radiating elements are fed in phase; a difference in phase of the admittances of successive slots results in a phase difference of the radiation of successive elements. Advantage is taken of the fact that the field across a longitudinal shunt slot is proportional to the slot admittance.<sup>1</sup>

At microwave frequencies, in-phase excitation of the

radiating elements is obtained in resonant arrays; this means that the radiators are spaced at intervals of a half guide-wavelength. For the required additional 180° phase-shift the slots are placed on alternate sides of the axis of the waveguide. A short-circuiting plunger which is placed approximately one-fourth guide-wavelength from the center of the last radiating slot terminates the array. There is no attenuation in a line loaded with elements which are spaced at half-wave intervals; the wave reflected at the short-circuit termination will give in-phase excitation. Power dissipation in a matched termination is avoided; this fact is especially important in comparatively short arrays.

A five-slot waveguide array at C-band frequencies was designed to test the principle; the design parameters are given in Fig. 1. The center element of the array is resonant; the elements toward the input terminals become increasingly shorter than the resonant length, and the symmetrical elements become increasingly longer. The constant phase difference between the admittances of successive radiating elements is 32°.

To obtain impedance match, the sum of the conductances of the radiating elements has to be equal to the characteristic admittance of the transmission line and the sum of the susceptances has to be zero. Since the conductance of the shunt slots off resonance decreases, their distance from the center of the waveguide has to be increased to assure that for uniform illumination each slot represents a conductance to the waveguide of  $G = G_0/5$ , where  $G_0$  is the characteristic admittance of

\* Manuscript received by the PGAP, February 18, 1960.

† Emerson Research Labs., a division of Emertron, Inc., Silver Spring, Md.

<sup>1</sup> R. J. Stegen, "Waveguide Slot Measurement Techniques," Hughes Aircraft Co., Los Angeles, Calif., Technical Memo. No. 262; December, 1951.

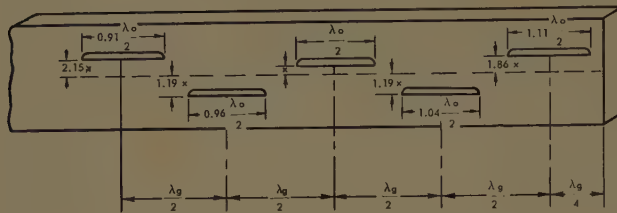


Fig. 1—Resonant array with tilted beam.

the waveguide. The susceptances of the radiating elements which are symmetrical to the array center are conjugate; the sum of the susceptances, therefore, becomes zero.

The described antenna array has the low loss characteristics of resonant arrays. The angle which the radiation maximum forms with the normal to the linear array is  $7^\circ$ , as shown in Fig. 2. The phase of the radiation of the shorter elements is advanced compared to the phase of the radiation of the longer elements; therefore, the radiation maximum is tilted towards the side of the array with the longer elements.

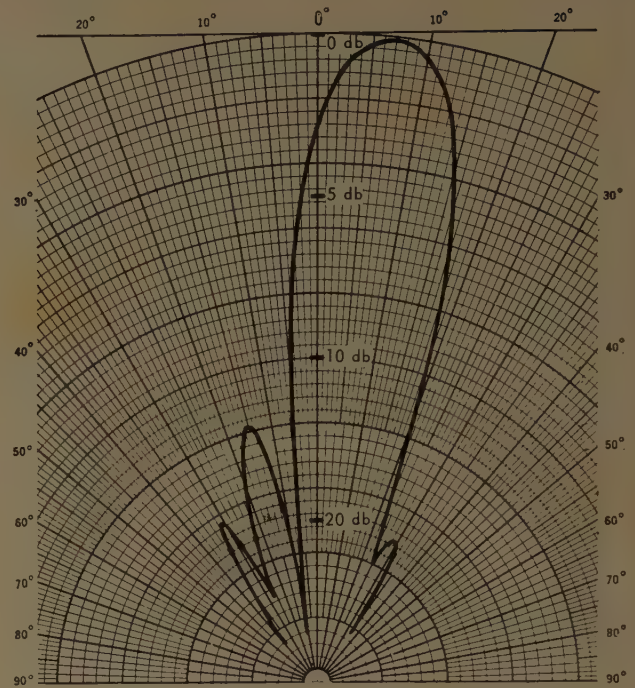


Fig. 2—H-plane pattern of five slots resonant array.

## Van Atta Reflector Array\*

E. D. SHARP† AND M. A. DIAB‡

**Summary**—The Van Atta reflector array is an array in which the elements are interconnected to reradiate received energy back in the direction of arrival. Scattering cross section measurements on a four-by-four Van Atta array of sixteen dipoles are presented. This array reflects over a wider angle than the typical corner reflector, but is sensitive only to incident waves in the frequency band of and having the polarization of the dipoles.

**D**R. L. C. Van Atta has devised a method of interconnecting the elements of an antenna array so that the incident energy is reradiated back in the direction of arrival.<sup>1</sup> An antenna array can be made into a reflector array by a simple interconnection of the radiators. The radiators that are equidistant from the array center are interconnected in pairs with lines of equal length. Equal line lengths are needed so that an equal phase delay occurs in each interconnecting line. The Van Atta array is capable, in principle, of reflecting

a wave incident at any angle from end-fire to broadside, but its performance is limited in practice by the directivity of the radiators.

To understand how the array operates, imagine a plane wave incident upon a linear array. The plane wave induces signals in each element having the phase shown in Fig. 1. After the energy has traveled through the equal-length interconnecting lines, the relative phases of the reradiated waves are reversed, as shown in Fig. 2. A study of the figure shows that the relative phases of these waves are of the correct value to cause the antenna to reradiate back in the direction from which the plane wave arrived. The same reasoning applies to a two-dimensional array, the interconnections of which are shown in Fig. 3.

The scattering cross section of the Van Atta reflector array can be derived from the definition<sup>2</sup>

$$\sigma = 4\pi R^2 \frac{P_R^s}{P_i} \quad (1)$$

\* Manuscript received by the PGAP, February 18, 1960. The work reported in this paper was done at Rome Air Development Center, Rome, N. Y.

† Stanford Research Institute, Menlo Park, Calif.

‡ Rome Air Development Center, Rome, N. Y.

<sup>1</sup> Electromagnetic Reflector, U. S. Patent No. 2908002, Serial No. 514040; October 6, 1959.

<sup>2</sup> D. E. Kerr, "Propagation of Short Radio Waves," M.I.T. Rad. Lab. Series, vol. 13, McGraw-Hill Book Co., Inc., New York, N. Y., p. 33; 1951.



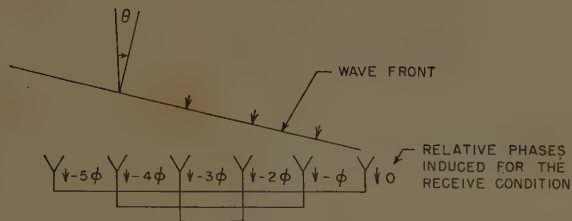


Fig. 1—Phasing of the array for the receive condition.

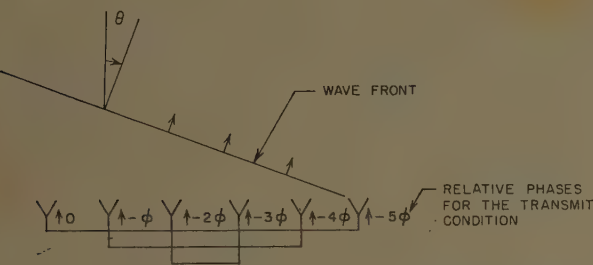


Fig. 2—Phasing of the array for the transmit condition.

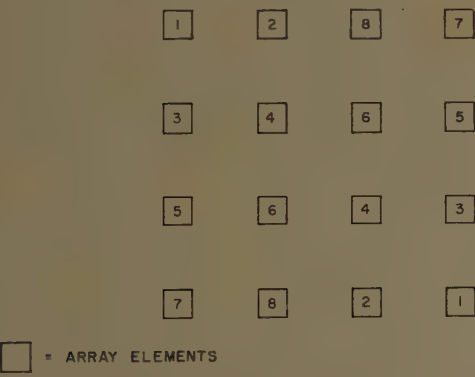


Fig. 3—Interconnections for a two-dimensional Van Atta array.

where

- $\sigma$  is the scattering cross section,
- $P_i$  is the power density of the plane wave incident upon the reflector, and
- $P_R^s$  is the reflected power density at a receiver a distance,  $R$ , away from the reflector.

The power received by a Van Atta array is equal to the product of the effective area,  $A_e$ , of the array and the incident power density,  $P_i$ . If there are no reflective or dissipative losses in the array, all of the received power is reradiated and the reflected power density at the receiver a distance,  $R$ , from the array is

$$P_R^s = \frac{A_e P_i G}{4\pi R^2} \tag{2}$$

where  $G$  is the gain of the array. For any antenna the gain and effective area are related by

$$G = 4\pi A_e / \lambda^2 \tag{3}$$

where  $\lambda$  is the free-space wavelength. Eliminating  $A_e$  from (2) by use of (3) and substituting the result into (1), the scattering cross section of the Van Atta array is

$$\sigma = \frac{G^2 \lambda^2}{4\pi} \tag{4}$$

At Rome Air Development Center a four-by-four array of sixteen half-wavelength dipoles mounted one-quarter wavelength above a reflector was constructed and interconnected with equal line lengths, as shown in Fig. 3. The scattering cross section of this array was measured and compared to a flat plate of the same aperture area.<sup>3,4</sup> A scattering cross section pattern taken at 2850 mc, the resonant frequency of the dipoles, in the plane perpendicular to the dipole axis, is shown in Fig. 4. The approximate theoretical scattering cross section in the same plane is also shown in Fig. 4.

The theoretical scattering cross section of the array can be derived by noting that the gain of an array is defined<sup>5</sup> as

$$G = \frac{4\pi \Phi_{\max}}{P} \tag{5}$$

where  $\Phi_{\max}$  is the radiation intensity at the peak of the beam and  $P$  is the total radiated power. For an array of  $n$  half-wavelength dipoles excited with currents of equal amplitudes, spaced one quarter-wavelength above a conducting plane, and with the beam positioned in the plane of Fig. 4 at the angle of incidence  $\theta$ , the radiation intensity at the peak of the beam is

$$\Phi_{\max} = (n^2 60 |I_0|^2 / \pi) \sin^2 \left( \frac{\pi}{2} \cos \theta \right) \tag{6}$$

where  $I_0$  is the peak current at the dipole terminals, and where  $\sin (\pi/2 \cos \theta)$  is the  $H$ -plane pattern of a dipole plus its image in the conducting plane. The total power radiated by this array is the sum of the powers radiated by each dipole,

$$P = n |I_0|^2 R_{in} / 2, \tag{7}$$

where  $R_{in}$  is the input radiation resistance of one dipole. Therefore, the gain of the antenna is

$$G = (480 n / R_{in}) \sin^2 \left( \frac{\pi}{2} \cos \theta \right). \tag{8}$$

Because of mutual coupling between dipoles, the input radiation resistance of each dipole is a function of the angle of incidence and the dipole position in the array. As an approximation, these particular mutual coupling effects are neglected and the input radiation resistance

<sup>3</sup> Eugene D. Sharp, "Properties of the Van Atta Reflector Array," Rome Air Development Center, N. Y., RADC Technical Rept. 58-53, AD-148684; April, 1958.  
<sup>4</sup> J. A. Fusca, "Compact reflector has ECM potential," *Aviation Week*, vol. 70, pp. 66-69; January 5, 1959.  
<sup>5</sup> S. A. Schelkunoff and H. T. Friis, "Antenna Theory and Practice," John Wiley and Sons, New York, N. Y., p. 179, 335; 1952.

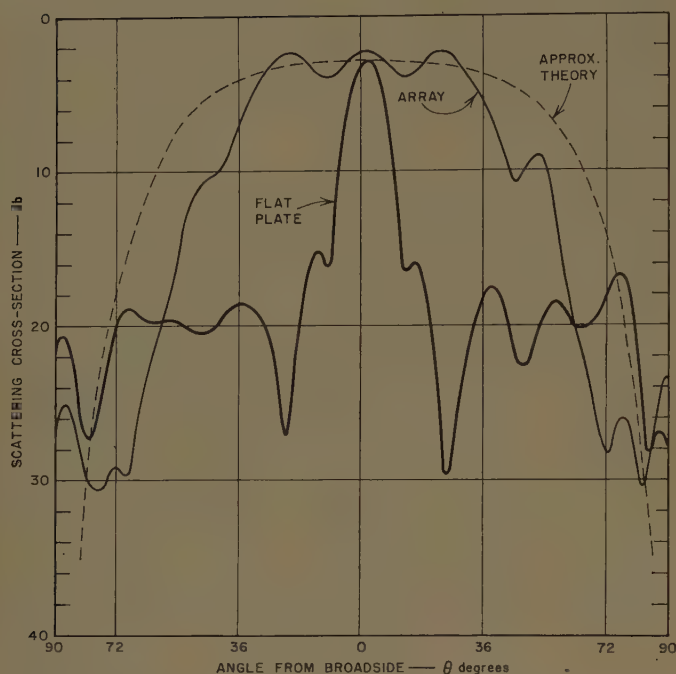


Fig. 4—Scattering cross section pattern of a Van Atta array of half-wave dipoles in a plane perpendicular to the dipole axes.

is assumed to be a constant and equal to that for an infinite array of half-wavelength dipoles spaced one-half wavelength apart and radiating normal to the array,  $R_{in} = 153$  ohms.<sup>6</sup> Substituting this value of input radiation resistance into (8) and using the relation that the aperture area of such an array of dipoles is  $A = n\lambda^2/4$  [to eliminate  $n$  in (8)] and then substituting the result into (4), the approximate theoretical scattering cross section of the array tested is

$$\sigma = (4\pi A^2/\lambda^2) \left[ \sin \left( \frac{\pi}{2} \cos \theta \right) \right]^4 \quad (9)$$

which is plotted in Fig. 4, normalized to the scattering cross section of the flat plate. It can be seen from (9) that the approximate theoretical scattering cross section is proportional to the element power pattern squared, considering the element to be a dipole plus its image.

The measured scattering cross section decreases faster than the approximate theoretical value at large angles of incidence. In part, the discrepancy between the

theory and measurement is due to the assumption that the input radiation resistance of the dipoles is a constant. Calculations of the input impedance of half-wavelength dipoles in a large array show that in the plane measured, the input radiation resistance increases as the angle of incidence increases.<sup>7</sup> For example, at  $\theta = 45^\circ$ ,  $R_{in} \approx 173$  ohms but at  $\theta = 0^\circ$ ,  $R_{in} \approx 153$  ohms. Since the input radiation resistance would enter (9) as the factor  $(1/R_{in})^2$ , a correction of 1.1 db should be subtracted from the approximate theoretical value shown in Fig. 4. Another effect causing the measured value to be low is the mismatch between the dipoles and interconnecting transmission lines. As the angle of incidence increases, the reactive part of the dipole input impedance increases; e.g., if we again take a specific value at  $\theta = 45^\circ$ , we find that the input reactance is nearly equal to the input resistance, causing a mismatch loss of about 1 db at each end of the interconnecting lines, and thus giving a second correction of about 2 db to be subtracted from the theoretical value shown in Fig. 4. Correcting the approximate theory at  $\theta = 45^\circ$  by subtracting a total of 3.1 db makes the agreement between theory and experiment better. Another effect, which is large in a small array, is the variation of input reactance and resistance with dipole position in the array; this variation causes phase errors in the received and re-radiated signals, further decreasing the array gain and scattering cross section.

The Van Atta array tested compared favorably with the corner reflector.<sup>8</sup> The Van Atta array maintained a high scattering cross section over a 50 per cent larger angle than the typical corner reflector and, for the same scattering cross section, the Van Atta array is somewhat smaller in cross sectional area. The corner reflector is not limited to any particular frequency band or polarization, while the Van Atta array is limited to the frequency band and polarization of the radiating elements; however, these limitations may not be too severe for many applications. The Van Atta array can be made to reflect a wave of any polarization by arranging that half the radiators be vertically polarized and half horizontally polarized or by using circularly polarized radiators. The frequency band of operation can be made quite large by use of wide-band radiators such as the conical helix and other frequency-independent antennas.

<sup>7</sup> P. S. Carter, Jr., "Mutual impedance effects in large beam scanning arrays," to be published in IRE TRANS. ON ANTENNAS AND PROPAGATION.

<sup>8</sup> S. D. Robertson, "Targets for microwave navigation," *Bell Sys. Tech. J.*, vol. 26, pp. 852-869; October, 1947.

<sup>6</sup> H. A. Wheeler, "Radiation resistance of an antenna in an infinite array or waveguide," *Proc. IRE*, vol. 36, pp. 478-487; April, 1948.

# A Circular Loop Antenna with Nonuniform Current Distribution\*

J. E. LINDSAY, JR.†

**Summary**—An analysis for the far field of a filamentary loop antenna with nonuniform current distribution is presented. In order to obtain a possible current distribution, an analogy between a circular transmission line and a parallel-wire transmission line is made. This analogy yields a standing wave of current similar to that found on a lossy parallel-wire line.

Considering only the far field of the antenna, the differential expressions for magnetic flux density are set up and the resulting equation is solved. The solution gives the magnetic flux density at a distant point from the antenna.

Loops with uniform current and loops with sinusoidal current distributions are shown to be special cases of the general solution. To verify the validity of the assumed current distribution, the experimental patterns of a loop  $1\lambda$  long are compared with calculated patterns. Results indicate that the field solutions are probably applicable to loops many wavelengths long.

## NEED FOR INVESTIGATION

NO PROBLEM is encountered in evaluating the radiation characteristics of a loop which is small with respect to the wavelength of operation. Here one assumes a uniform current distribution, and the field intensity expressions are easily formulated [1]. For a larger loop, a more realistic current distribution must be found. It is for this condition of operation that field expressions are sought.

A search through the available literature shows a limited amount of information on loop antennas whose dimensions are appreciable with respect to wavelength [1–6]. Certain papers assume a current distribution which is sinusoidal [3–5]. Glinski, however, pointed out in his paper that the assumption of a sinusoidal current distribution led to a noticeable deviation from experimental results for loops as small as  $\frac{1}{2}\lambda$  [2]. In order to obtain more realistic results, Glinski assumed a current distribution similar to that found on a lossy parallel-wire transmission line. To simplify his analysis, he retained only the first few terms of an infinite series expansion of the differential field expressions. This restriction, however, limits his results to loops of  $\frac{1}{2}\lambda$  or less. The work to follow assumes the current distribution of a lossy, uniform transmission line, and then proceeds to an exact solution for loops of all sizes when they possess such a current distribution.

## FORMULATION OF THE CURRENT DISTRIBUTION<sup>1</sup>

We will consider the circular loop to be a deformation of a shorted parallel-wire transmission line. Let  $s$  be the distance measured along the line (or the loop) from the shorted end. The current distribution is given by  $I(s) = I_L \cosh \gamma s$ , where  $\gamma$  is the propagation constant of the line and  $I_L$  is the current at the shorted end. In terms of an angular measurement  $\zeta$  (from the shorted end) the current on the loop may be given by

$$I(\zeta) = I_L \cosh \gamma R \zeta, \quad (1)$$

with  $R$  as the radius of the loop.

## OBTAINING THE FAR FIELD EXPRESSIONS

The  $e^{j\omega t}$  factor will be dropped for brevity but is implied as being present in the equations to follow.

As indicated in Fig. 1, two differential current elements,  $I_1 d\zeta_1$  and  $I_2 d\zeta_2$ , are located  $\zeta$  radians from the load end of the loop, and the differential magnetic vector potential expressions are formulated in terms of these elements. Since only the far field effects will be considered, the distances  $r_0$ ,  $r_1$  and  $r_2$  are very nearly parallel. These conditions yield

$$dA = \mu \frac{I_L e^{-j\beta r_0} \cosh \gamma R \zeta}{4\pi r_0} [d\zeta_1 e^{j\beta \Delta r_1} + d\zeta_2 e^{j\beta \Delta r_2}]. \quad (2)$$

Upon taking the curl of (2), discarding near-field terms, expanding the exponential terms by a Fourier-Bessel series, and finally integrating with respect to  $\zeta$ , one obtains the following magnetic fields:

$$B_\phi = -2\gamma R F(r_0) \sinh \gamma R \pi \left\{ \frac{jC_1}{(\gamma R)^2} + j \sum_{n=1}^{\infty} \frac{D_n + C_{(n+1)}}{(\gamma R)^2 + (2n)^2} - \sum_{n=1}^{\infty} \frac{A_n + B_{(n-1)}}{(\gamma R)^2 + (2n-1)^2} \right\} \quad (3a)$$

$$(\gamma R)^2 \neq -k^2,$$

\* Manuscript received by the PGAP, March 21, 1959; revised manuscript received January 21, 1960. A summary of the contents of a thesis submitted to the Faculty of the Graduate School of the University of Colorado in partial fulfillment of the requirements for the degree Master of Science, Department of Electrical Engineering.

† Elec. Engrg. Dept., University of Colorado, Boulder.

<sup>1</sup> Recent measurements of the current distribution on a slotted tubular semicircular loop above a ground plane show the lossy transmission line analogy to be quite accurate. A loss value of  $\alpha R = 0.11$  nepers was calculated for a  $\frac{1}{2}\lambda$  semiloop. This compares closely to the 0.1-neper value assumed in this paper.





### EXPERIMENTAL VERIFICATION FOR A LOOP $1\lambda$ IN CIRCUMFERENCE

Three major cuts in the far zone field pattern were chosen for comparison of experimental with calculated patterns. They are:

$$\text{Cut 1: } \phi = 0, \quad 0 \leq \theta \leq 2\pi$$

$$\text{Cut 2: } \phi = \frac{\pi}{2}, \quad 0 \leq \theta \leq 2\pi$$

$$\text{Cut 3: } \theta = \frac{\pi}{2}, \quad 0 \leq \phi \leq 2\pi.$$

Refer to Fig. 1 to visualize these cuts.

The patterns are normalized with respect to the pattern corresponding to Cut 2. A value of  $\alpha R = 0.1$  nepers was chosen for the calculated patterns. The comparative results are shown in Figs. 2-4 for Cuts 1, 2, and 3 respectively. (In Cut 3 it was impossible to keep the feed line normal to the polarization of the illuminating  $E$  field, resulting in a poor comparison for Cut 3 in Fig. 4.)

### CONCLUSIONS

It might be pointed out that the series converges quite rapidly. In fact, only one term of each series was used to calculate the given curves. It appears that the

above results will allow prediction of the radiation characteristics of the loop whose circumference is many wavelengths.

### ACKNOWLEDGMENT

The author wishes to acknowledge with gratitude the time, effort, and encouragement given by Professor Carl Johnk of the University of Colorado in conferences on the project. Senior Research Engineer Donald R. Dubbert of the Denver Research Institute of the University of Denver gave many helpful suggestions.

This research was carried on at the Denver Research Institute under a Contract with the Bureau of Aeronautics, Department of the Navy, Washington 25, D.C.

### BIBLIOGRAPHY

- [1] D. Foster, "Loop antenna with uniform current," *PROC. IRE*, vol. 32, pp. 603-607; October, 1944.
- [2] G. Glinski, "Note on circular loop antennas with non-uniform current distribution," *J. Appl. Phys.*; July, 1947.
- [3] L. L. Libby, "Special aspects of balanced shielded loops," *PROC. IRE*, vol. 34, pp. 641-646; September, 1946.
- [4] J. Mueller-Strobel and J. Patry, "Berechnung des Stromes der Rahmenempfangsantenna," *Schweizer Arch.*, pp. 193-202; July, 1947.
- [5] J. B. Sherman, "Circular loop antennas at ultra-high frequency," *PROC. IRE*, vol. 32, pp. 534-537; September, 1944.
- [6] E. M. Williams, "Radiating characteristics of short wave loop aeriels," *PROC. IRE*, vol. 28, pp. 480-484; October, 1940.

## Pattern Synthesis Using Weighted Functions\*

P. A. BRICOUT†

**Summary**—An increase in the accuracy of the synthesis of a pattern by a collinear array of equispaced radiators is obtained by expanding, in trigonometric series, the function to be generated, multiplied by a weight function  $1 + \mathcal{E}(x)$ . When  $\mathcal{E}(x)$  is a polynomial, an exponential function, a trigonometric function of the variable or a product of these, the changes in the coefficients of the expansion can be computed accurately, by using simple formulas.

To evaluate the method, a numerical example related to the synthesis of a dissymmetrical pattern with sharp cutoff requirements is given and it is shown that, using the same number of terms (*i.e.*, the same number of physical radiators), the accuracy of the synthesis and/or the slope of the pattern can be increased by a factor of approximately 20 per cent.

### INTRODUCTION

THE synthesis of a very dissymmetrical pattern by a collinear array of equispaced radiators normally requires a relatively large number of elements,

especially when sharp cutoff in a prescribed direction is required.

The conventional method is based on the expansion in series of the desired pattern in terms of harmonics of the phase function  $\psi$ , whose coefficients are given by Fourier's formula.

The decrease of the relative error when the number of terms increases is relatively slow and the purpose of this paper is to investigate if it is possible to increase the accuracy given by a limited number of terms, or otherwise to make the best use of the aperture of the antenna.

This problem is mathematically possible for two reasons. First, it is well known that Fourier's coefficients, giving the smallest possible value to the integral of the square of the error taken with an equal weight at all points of the pattern when the series is infinite, are *not the best for a limited expansion*. Second, the excellent performance of Tchebycheff polynomials  $T_n(x)$  is because of the fact that they synthesize the impulse

\* Manuscript received by the PGAP, February 26, 1960. The work reported here has been carried out under Wright Air Dev. Ctr. Contract AF33(600)37292.

† Emerson Res. Labs., Silver Spring, Md., a division of Emertron, Inc. Formerly with Litton Industries, College Park, Md.

function at  $x = \pm 1$  with a variable weight and it is known that they give to the integral

$$\int_{-1}^{+1} \frac{T_n(x)^2}{\sqrt{1-x^2}} dx \quad (x = \cos \psi)$$

its minimum value. It is obvious that the weight is infinite for the value  $x = \pm 1$  ( $\psi = 0$ ) corresponding to the main lobe and larger than unity at any other point.

It is then logical to give a larger weight to the points of the pattern where the accuracy requirements are more stringent, but this can be done in an infinite number of ways and should not result in too much deterioration of the pattern at any other point.

It can also be proven that the coefficients<sup>1</sup> of a limited expansion in  $\sin n\psi$  and  $\cos n\psi$  can be chosen so that the weighted square of the error integrated over the whole range of the variable is minimum.

The solution of this problem gives an expansion which has the maximum possible accuracy for a limited number of terms.

Contrary to the conventional Fourier formulas, which always give the same value for a given coefficient, disregarding the number of terms of the expression, all coefficients will now have values depending on the length of the expansion. The methods of Fejer's sums and of  $\sigma$  factor<sup>2</sup> are known ways for improving the accuracy of a limited series but a more direct and effective approach is now proposed.

#### PRINCIPLE OF THE METHOD

Let  $f(\psi)$  be the desired pattern expression in terms of the phase angle  $\psi$  and approximated by a limited trigonometric series of  $n$  harmonics.

$$\begin{aligned} f(\psi) \simeq & a_0 + a_1 \cos \psi + a_2 \cos 2\psi + a_3 \cos 3\psi + \dots \\ & + a_n \cos n\psi + \\ & + b_1 \sin \psi + b_2 \sin 2\psi + b_3 \sin 3\psi + \dots \\ & + b_n \sin n\psi. \end{aligned}$$

The synthesis is required only for  $\psi_0 < \psi < \psi_1$  and no radiation [ $f(\psi) = 0$ ] is desired outside of this interval. But a sharp cutoff at  $\psi = \psi_0$  and  $\psi = \psi_1$  is more difficult to obtain when the number of terms is smaller and it is well known that the sharp edges of the discontinuous functions are smoothed by the approximations.

To compensate, let us expand instead of  $f(\psi)$

$$f(\psi)w(\psi) = f(\psi)[1 + h\epsilon(\psi)]$$

the weight function  $w(\psi)$  being chosen so that:

- 1)  $\epsilon(\psi)$  is approximately proportional to the relative error of the limited expansion in series;
- 2) the mean value of  $\epsilon(\psi)$  in the interval  $\psi_0 < \psi < \psi_1$  is equal to zero.

$h$  is an undetermined constant which shall be chosen for maximum accuracy.

The expression of  $hf(\psi)\epsilon(\psi)$  using conventional Fourier formulas gives a new set of coefficients proportional to  $h$ , which can be written:

$$\bar{a}_p = h\lambda_p, \quad \bar{b}_p = h\mu_p$$

and are to be added to the first ones ( $a_p, b_p$ ). Let the original and the corrected expressions be symbolized by

$$\sum_n (a_p, b_p), \quad \sum_n (\bar{a}_p, \bar{b}_p) = h \sum_n (\lambda_p, \mu_p).$$

The best value for  $h$  is found, according to the method of least squares, by writing that the integral of the square of the error of the corrected expansion is a minimum or

$$\delta \int_{\psi_0}^{\psi_1} \left[ f(\psi) - \sum_n (a_p + \bar{a}_p, b_p + \bar{b}_p) \right]^2 d\psi = 0.$$

The expression of the integrand is

$$\begin{aligned} & \int_{\psi_0}^{\psi_1} \left[ f(\psi) - \sum_n (a_p, b_p) \right]^2 d\psi \\ & - 2h \int_{\psi_0}^{\psi_1} \left[ f(\psi) - \sum_n (a_p, b_p) \right] \times \sum_n (\lambda_p, \mu_p) d\psi \\ & + h^2 \int_{\psi_0}^{\psi_1} \left[ \sum_n (\lambda_p, \mu_p) \right]^2 d\psi = K - 2Bh + Ah^2. \end{aligned}$$

$K$  and  $B$  being positive, since they are the integrals of squares, the trinomial has a minimum for

$$h = \frac{B}{A} = \frac{\int_{\psi_0}^{\psi_1} \left[ f(\psi) - \sum_n (a_p, b_p) \right] \times \sum_n (\lambda_p, \mu_p) d\psi}{\int_{\psi_0}^{\psi_1} \left[ \sum_n (\lambda_p, \mu_p) \right]^2 d\psi}.$$

All numerical computations can be made exactly, using relatively simple formulas, in the very general case where the desired pattern can be expressed in terms of polynomials, exponential functions, and the product of both types of functions of the multiples of the variable. All integrals of the type

$$\int x^h \begin{cases} \sin mx \\ \cos mx \end{cases} dx \quad \int e^{\lambda x} \begin{cases} \sin mx \\ \cos mx \end{cases} dx$$

are known and can be expressed in finite terms.

#### NUMERICAL EXAMPLE

The expansion of the trapezoid

$$f(x) = 1 - \frac{2}{\pi} x \quad -\frac{\pi}{4} < x < \frac{\pi}{4}$$

$$f(x) = 0 \quad x < -\frac{\pi}{4}, \quad x > \frac{\pi}{4}$$

where  $x$  is an angle in radians (converted in degrees on the figures), by the conventional Fourier series limited

<sup>1</sup> D. Jackson, "The Theory of Approximation," Amer. Math. Soc., New York, N. Y., ch. 3; 1930.

<sup>2</sup> C. Lanczos, "Applied Analysis," Prentice-Hall, Inc., New York, N. Y., ch. 4; 1956.



TABLE I

$$f(x) = 1 - \frac{2}{\pi}x \quad -\frac{\pi}{4} < x < \frac{\pi}{4}$$

$$f(x) = 0 \quad x < -\frac{\pi}{4}, x > \frac{\pi}{4}$$

$$w(x) = 1 + h \left( \frac{2}{\pi} - \cos 2x \right) \quad h = 0.33021$$

$p$	Fourier Coefficients		Corrections		Weighted Coefficients	
	$a_p$	$b_p$	$\Delta a_p$	$\Delta b_p$	$a_p$	$b_p$
0	0.25		0		0.25	
1	0.45016	-0.06150	-0.01352h	-0.01648h	0.45570	-0.06694
2	0.31831	-0.10132	-0.04736h	-0.02471h	0.30267	-0.10948
3	0.15005	-0.10687	-0.27557h	-0.06552h	0.05905	-0.12851
4	0	-0.07958	-0.10610h	-0.00562h	-0.03504	-0.08144
5	-0.09003	-0.03355				

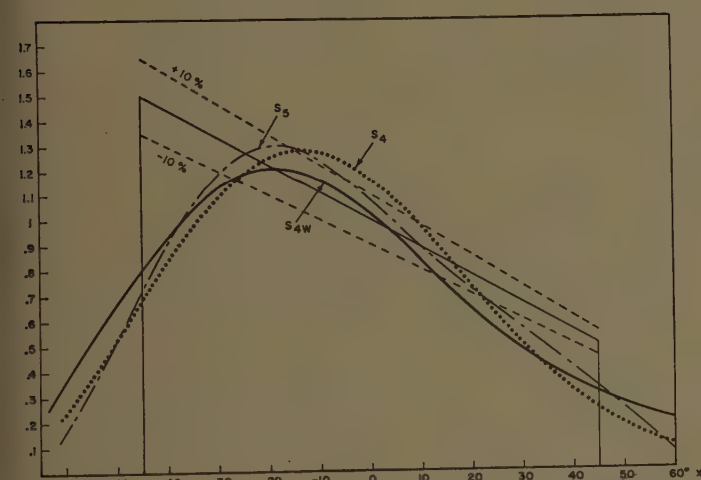


Fig. 1—Approximations to the trapezoid (solid thin line) by the Fourier expansion limited to the first 4 harmonics  $S_4$  (dotted line), by the same weighted  $S_{4w}$  (solid heavy line) and by the Fourier expansion of 5 harmonics  $S_5$  (mixed line).

to the first four harmonics ( $S_4$ ) or to the first five ( $S_5$ ), given on Table I and Fig. 1. The approximation is poor and the accuracy of the expansion is better than  $\pm 10$  per cent within only 26.1 per cent of the  $(-\pi/4, \pi/4)$  interval for  $S_4$  and 44.4 per cent for  $S_5$ .

The weight function

$$w(x) = 1 + h \left( \frac{2}{\pi} - \cos 2x \right)$$

which increases sharply at the ends of the interval and is smaller than unity for  $x=0$ , is then applied and the  $\lambda_p$ ,  $\mu_p$  and  $h$  are computed as explained.

Table I and Fig. 1 show the results. The weighted expansion of four harmonics  $S_{4w}$  is nearer to the trapezoid than the two uncorrected  $S_4$  and  $S_5$  and its error is smaller than  $\pm 10$  per cent within 51.1 per cent of the  $(-\pi/4, \pi/4)$  interval (as compared to 26.1 per cent and 44.4 per cent for  $S_4$  and  $S_5$ ). This means practically that 9 suitably fed and equispaced radiators can give a slightly better accuracy than 11 equispaced radiators

whose intensities and phases are found by the conventional Fourier analysis.

For evaluating the method in an unfavorable case, let us try to synthesize with isotropic sources the theoretical pattern expressed in phase angle  $\psi$  by

$$e = E(1 + e^{-\lambda\psi}) \text{ for } \psi_0 < \psi < \psi_1$$

$$e = 0 \text{ for } \psi < \psi_0, \psi > \psi_1$$

$$\begin{cases} E = 0.5 \\ \lambda = 0.0314 \\ \psi \text{ in degrees} \end{cases}$$

This pattern synthesizes the  $P = \operatorname{cosec}^2 \psi \cos^{1/2} \psi$  pattern with less than 4 per cent error within the range  $7.5^\circ < \psi < 114.5^\circ$  of the variable. The sharpest possible cutoff is required at the ends of interval.

As a first approximation, let us expand the desired pattern in Fourier series using the conventional formulas. The coefficients have been computed up to the tenth harmonic and are found in the left side of Table II. Fig. 2 shows the desired pattern and the approximation obtained with six, eight, and ten harmonics, using these coefficients. The approximation increases slowly with the number of terms (approximately as  $1/n$ ). Let us try to improve the expansion containing eight harmonics only, for better accuracy and sharper cutoff. The largest errors occur at edges of the pattern and some ripples proportional to  $C \sin 8(\psi - \psi_r)$  are found on the Fourier pattern.

A composite weight function, plotted on Fig. 3,

$$w(\psi) = 1 + ae^{-A(\psi - \psi_0)} + be^{B(\psi_1 - \psi)} - kc \sin(\psi - \psi_r),$$

whose values are opposite to the errors to be compensated and where  $a=b=1.1$ ,  $k=1.025$  has been chosen and expanded, using conventional formulas. The new coefficients are found in Table II and the new approximations are compared to classical ones in Fig. 4.

The product of the required pattern by the weight function is now expanded in series and this gives a new set of coefficients, which are a second-order approxima-

TABLE II

$p$	Fourier Coefficients		Corrected Coefficients	
	$a_p$	$b_p$	$a_p$	$b_p$
0	0.16769		0.19093	
1	0.20692	0.27535	0.21220	0.29031
2	-0.02976	0.16462	-0.02738	0.16356
3	0.02287	0.03811	0.04079	0.03927
4	0.05200	0.09285	0.06172	0.11277
5	-0.01787	0.07645	-0.02367	0.08360
6	0.00713	0.02378	0.01199	0.02430
7	0.02566	0.05556	0.03222	0.07144
8	-0.01254	0.04908	0.01263	0.02731
9	0.00332	0.01661		
10	0.01628	0.03938		

Errors:	Fourier		Corrected
	8 harmonics	10 harmonics	8 harmonics
Mean quadratic error	0.0866	0.0619	0.0597
Maximum absolute error	-0.1878	-0.1305	+0.1124

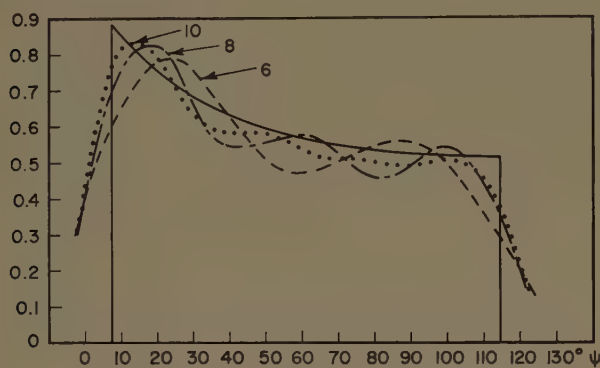


Fig. 2—Approximation to the theoretical pattern by Fourier expansion limited to the first 6, 8, and 10 harmonics. The theoretical pattern is drawn in solid line.

tion. When the undetermined factor is changed, the difference between each new set and the first approximation is increased proportionally. The change in the coefficients resulting from this adjustment can be easily computed. As the exponential weight function vanishes very quickly, its effect is limited to the edges of the pattern, and the integrals

$$\int_{\psi_0}^{\psi_1} e^{-A\psi} \begin{cases} \sin m\psi \\ \cos m\psi \end{cases} d\psi \quad \int_{\psi_0}^{\psi_0} e^{B\psi} \begin{cases} \sin m\psi \\ \cos m\psi \end{cases} d\psi$$

depend only on one of their limits and are given by simple formulas of the type

$$\frac{C_1[\sin m\psi_1 \pm \sin m\psi_0] \pm m[\cos m\psi_1 \pm \cos m\psi_0]}{C_3 + m^2},$$

$$\frac{C_1[\cos m\psi_1 \pm \cos m\psi_0] \pm m[\sin m\psi_1 \pm \sin m\psi_0]}{C_3 + m^2}.$$

The new coefficients are found in Table II and the new approximation is compared to classical ones (Fig. 3).

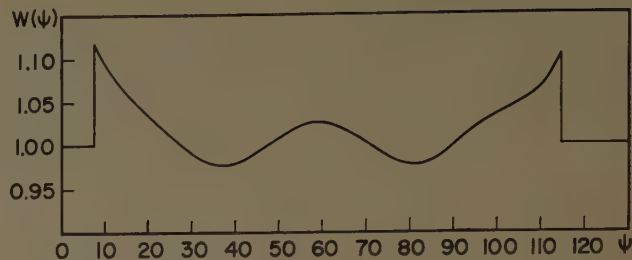


Fig. 3—Weight function  $w(\psi)$  used for increasing approximation.

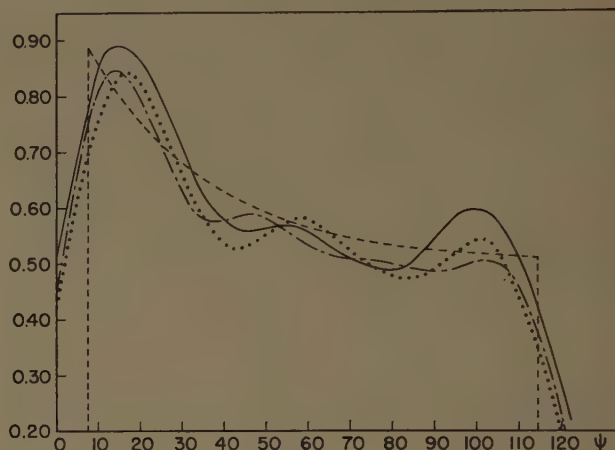


Fig. 4—Comparison of approximations to theoretical pattern (interrupted line). Conventional Fourier expansions limited to the first 8 harmonics (dotted line) and the first 10 harmonics (mixed line). Corrected expansion limited to the first 8 harmonics (solid line).

The corrections apply to all coefficients but are different for each of them. The largest changes occur for underlined values. The weight functions must be made very small to avoid overcorrections. Fig. 3 shows, at enlarged scale, the approximation given by the Fourier expansions and by the corrected expansion.

The mean quadratic error of the corrected 8-term expansion is 31 per cent smaller than the 8-term and slightly better than the 10-term Fourier expansions. This means that 17 radiators can be made as effective as 21, using a proper feed. The method is general and avoids the solutions of large sets of simultaneous equations.

## CONCLUSION

A mathematical method for increasing the accuracy of pattern synthesis by using weighted functions has been explained and exemplified.

The corrections to conventional Fourier coefficients are obtained by simple formulas and it is possible to obtain the optimum performance for a given aperture of the array.

# On the Excitation of Electromagnetic Surface Waves on a Curved Surface\*

JAMES R. WAIT†

**Summary**—The excitation and propagation of surface waves on a spherical inductive boundary are considered. The source is taken to be a vertical electric dipole. The circumferential attenuation rates of the various modes are discussed where it is indicated that the dominant mode is very similar to the trapped surface wave for a plane inductive boundary. The results appear to conflict with those of Barlow, but are in sympathy with some numerical data of Elliott for the circumferential attenuation rate of the dominant mode.

## INTRODUCTION

A SURFACE wave in electromagnetic theory is usually associated with a disturbance gliding along an interface between two dissimilar media. When the interface is plane and the lower medium exhibits the property of surface reactance, it is known that a wave may be excited which travels along the interface without radiation.<sup>1</sup> Examples of such surfaces are dielectric coated plane conductors and corrugated or comb structures. For excitation by a vertical electric dipole, for example, the existence of such a trapped surface wave requires that the surface be inductive.<sup>2</sup> Any loss in the structure produces attenuation.

The influence of curvature of the surface may be expected to modify the characteristics of the electromagnetic field. A physical discussion of the influence of curvature has been given by Barlow.<sup>3,4</sup> He indicates that radiation from the surface wave is accompanied by a backward tilt of the equiphase surfaces resulting in a departure from a pure radial distribution of the field. He states this has much of the same result as a physical obstacle in the space outside the surface, because it sets up an interference pattern. On the basis of Barlow's physical argument, the resulting reflected field provides for an increased rate of power flow outwards. While this seems like an interesting idea, it is not at all convincing to this writer. Furthermore, the radial solution adopted by Barlow involves Hankel functions of the first and second kind and thus does not satisfy the radiation condition at infinity. Nevertheless, Barlow's conclusions are not unreasonable from a physical viewpoint. However, from a quantitative standpoint, it would appear that his results cannot be accepted.

## SPHERICAL MODEL

It appears to the present writer that the simplest model for discussing the influence of curvature is a spherical surface which is excited by a radial electric dipole source. In terms of a spherical coordinate system  $(r, \theta, \phi)$ , the spherical surface which is defined by  $r=a$  exhibits an inductive reactance. That is, the boundary condition

$$E_\theta = -iXH_\phi \text{ at } r = a \quad (1)$$

is assumed where  $X$ , the surface reactance, is a positive real number. The source is a vertical electric dipole at  $r=a$  and  $\theta=0$ . Because of symmetry, the only non-vanishing field components are  $E_\theta$ ,  $E_r$  and  $H_\phi$ . A formal solution to this problem has been previously given by Wait.<sup>5</sup> Essentially it is an extension of the Van der Pol-Bremmer theory for a homogeneous dielectric sphere.<sup>6</sup>

For present purposes, the relevant solution (for a time factor  $\exp i\omega t$ ) may be written in the following form:

$$E_r = E_0 F$$

where

$$F = \frac{\pi^{1/2}\theta}{(\sin \theta)^{1/2}} e^{-i\pi/4} \left(\frac{ka}{2}\right)^{1/6} \cdot \sum_s \frac{\exp[-it_s(ka/2)^{1/3}\theta]}{t_s - q^2} \frac{w(t_s - y)}{w(t_s)} \quad (2)$$

where  $E_0$  is a reference field to be described below,<sup>7</sup> and where

$$q = \left(\frac{ka}{2}\right)^{1/3} \frac{X}{120\pi}, \quad y = (kh) \left(\frac{2}{ka}\right)^{1/3},$$

$$h = r - a, \quad k = 2\pi/\text{wavelength},$$

and  $t_s$  are roots of

$$\frac{dw(t)}{dt} - qw(t) = 0 \quad (3)$$

\* J. R. Wait, "Radiation from a vertical antenna over a curved stratified ground," *J. Res. NBS*, vol. 56, pp. 230-240; July, 1956. For a similar treatment, see also K. Furutsu, "On the excitation of waves of proper solutions," *Proc. URSI Symp. on Electromagnetic Theory*; to be published.

<sup>6</sup> B. Van der Pol and H. Bremmer, "The diffraction of electromagnetic waves from an electrical point source round a finitely conducting sphere, with applications to radiotelegraphy and the theory of the rainbow; the propagation of radio waves over a finitely conducting spherical earth," *Phil. Mag.*, vol. 24, pp. 141-176, July, 1937; vol. 24, pp. 825-864, November, 1947; vol. 25, pp. 817-834, June, 1938; vol. 27, pp. 261-275, March, 1939.

<sup>7</sup>  $E_0$  is the radiation field of the dipole if it were placed on the surface of a perfectly conducting plane source.

\* Manuscript received by the PGAP, February 6, 1960.

† Natl. Bureau of Standards, Boulder, Colo.

<sup>1</sup> H. M. Barlow and A. L. Cullen, "Surface waves," *Proc. IEE*, vol. 100, pt. III, pp. 329-347; November, 1953.

<sup>2</sup> J. R. Wait, "Excitation of surface waves on conducting, stratified, dielectric-clad, and corrugated surfaces," *J. Res. NBS*, vol. 59, pp. 365-377; December, 1957.

<sup>3</sup> H. M. Barlow, "The power radiated by a surface wave circulating around a cylindrical surface," *Proc. IEE*, vol. 106, pp. 180-185; March, 1959.

<sup>4</sup> H. M. Barlow, "Surface waves supported by curved boundaries," *Proc. URSI Symp. on Electromagnetic Theory*, June, 1959; to be published.



where  $w(t)$  is an Airy integral function.<sup>8</sup> The above expression for the radial electric field at height  $h$  above the spherical surface is valid under the assumptions that

$$(ka/2)^{1/3} \gg 1, \quad X \ll 120\pi \text{ ohms, and } h \ll a.$$

These conditions, which are not overly restrictive, greatly simplify the mathematics, yet the important features of the problem are retained.

#### THE DOMINANT SURFACE WAVE MODE

It is first desirable to search for the root of the above equation which, in the limit of  $ka \rightarrow \infty$ , corresponds to the trapped surface wave mode on a flat reactive surface. Replacing  $w(t)$  by the first term of its asymptotic expansion (valid when the real part of  $t$  is large), the root determining equation reduces to

$$(t^{1/4} - qt^{-1/4}) \exp(\frac{2}{3}t^{3/2}) = 0. \quad (4)$$

The real part of this vanishes when

$$t = t_0 \cong q^2$$

which is the required solution. This corresponds to a wave which varies azimuthally in the manner

$$\begin{aligned} \exp - i \left[ ka\theta + \left( \frac{ka}{2} \right)^{1/3} \theta t_0 \right] \\ \cong \exp [-ika\theta(1 + X^2/2\eta_0^2)] \\ \cong \exp [-iks \sqrt{1 + X^2/\eta_0^2}] \end{aligned} \quad (5)$$

where  $s = a\theta$  is the distance measured along the surface from the source. This wave propagates along the surface in an unattenuated fashion and has a phase velocity  $c/\sqrt{1 + X^2/\eta_0^2}$  in accordance with expected behavior for a flat surface.<sup>1</sup>

The next most obvious step is to consider higher-order inverse powers of  $t$  in the asymptotic expansion of the Airy function  $w(t)$ . This leads to a solution of the following form:

$$t_0 \cong q^2 \left[ 1 + \frac{1}{2q^3} - \frac{5}{32q^6} + \dots \right]. \quad (6)$$

Consequently,

$$\begin{aligned} F \cong e^{-i\pi/4(2\pi ks)^{1/2}} \frac{X}{\eta_0} \left( 1 + \frac{5}{16q^3} + \dots \right) \\ \times \exp \left[ -iks(X^2/2\eta_0^2) \left( 1 + \frac{1}{2q^3} - \frac{5}{32q^6} + \dots \right) \right]. \end{aligned} \quad (7)$$

In the limiting case of a flat earth (*i.e.*,  $q \rightarrow \infty$ ), this reduces to

$$F \cong e^{-i\pi/4(2\pi ks)^{1/2}} (X/\eta_0) \exp [-iks(X^2/2\eta_0^2)] \quad (8)$$

<sup>8</sup> In terms of Hankel functions of order one-third,

$$w(t) = \exp(-2\pi i/3)(-\pi t/3)^{1/2} H_{1/3}^{(2)} \left[ \left( \frac{2}{3} \right) (-t)^{3/2} \right].$$

which agrees with a previous analysis.<sup>2</sup>

Eq. (6) indicates that the influence of curvature is to retard the phase of the surface wave as a result of the correction factor  $(1 + 1/2q^3 \dots)$  which is greater than unity. It is interesting to note, however, that this correction factor, which is obtained from an asymptotic development of the Airy function, is always real even if a large number of terms are retained. Thus, in this asymptotic sense, the curvature does not produce attenuation. To obtain the attenuation constant it is necessary to return to

$$w'(t) - qw(t) = 0 \quad (9)$$

where the prime indicates differentiation with respect to  $t$ . A perturbation method is quite convenient here since a first-order solution for  $t_0^{(1)}$  may be obtained from the asymptotic solution. Then a second-order solution  $t_0^{(2)}$  is obtained by expanding  $w'(t)$  and  $w(t)$  in a Taylor expansion about  $t_0^{(1)}$ . Thus

$$\begin{aligned} [w'(t_0^{(1)}) - qw(t_0^{(1)})] \\ + (t - t_0^{(1)})[w''(t_0^{(1)}) - qw'(t_0^{(1)})] \cong 0 \end{aligned} \quad (10)$$

where higher-order terms in  $(t - t_0^{(1)})$  have been neglected. Using

$$w''(t) - tw(t) = 0,$$

it follows that

$$t_0^{(2)} \cong t_0^{(1)} - \frac{w'(t_0^{(1)}) - qw(t_0^{(1)})}{t_0^{(1)}w(t_0^{(1)}) - qw'(t_0^{(1)})}. \quad (11)$$

In this way a second-order approximation may be obtained from a first-order approximation. The process may be repeated and it appears to converge. Using this method, the root  $t_0$  does become complex although the imaginary part is extremely small. The real and imaginary parts of  $t_0$  are plotted in Figs. 1 and 2 as a function of  $q$  where they are indicated by the label  $ka \rightarrow \infty$ . If  $ka$  is not extremely large, it is not permissible to use the Airy approximation adopted in this paper. The case where  $(ka/2)^{1/3}$  is not large compared with one, requires that the root  $t_0$  be calculated from an equation involving spherical Hankel functions of complex order. For certain values of  $ka$  and  $X$ , such results have been reported by R. S. Elliott.<sup>9</sup> They were obtained on a high-speed digital computer. Using the numerical data from Elliott's paper,<sup>9</sup> the corresponding values<sup>10</sup> of  $\text{Re } t_0$  and  $\text{Im } t_0$  are shown for  $ka = 60, 120, 480$  and  $960$  as a func-

<sup>9</sup> R. S. Elliott, "Spherical surface wave antennas," IRE TRANS. ON ANTENNAS AND PROPAGATION, vol. AP-4, pp. 422-428, July, 1956; "Azimuthal surface waves on circular cylinders," J. Appl. Phys., vol. 26, pp. 368-376, April, 1955.

<sup>10</sup> Elliott's  $\gamma$  is related to  $t_0$  by  $\gamma a = ka + (ka/2)^{1/3} t_0$ ; also his parameter

$$\sqrt{\frac{\epsilon_0}{\epsilon}} \frac{\theta_G}{\theta_G + \theta_T} \tan k(a - b)$$

is equivalent to  $X/120\pi$ .

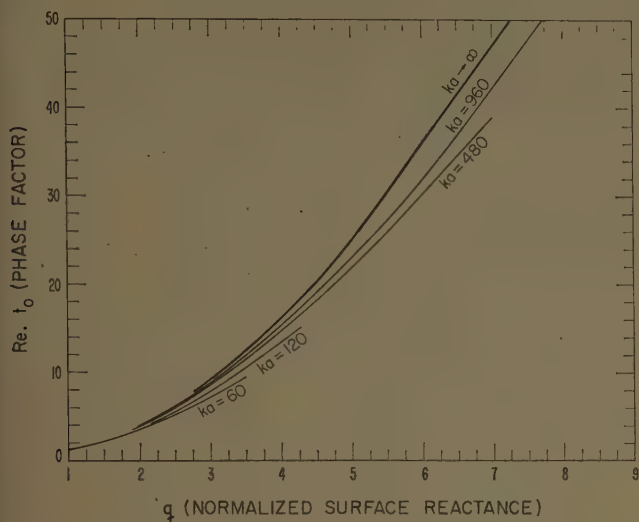


Fig. 1—Phase factor  $\text{Re } t_0$  as a function of  $q$ , the normalized surface reactance.

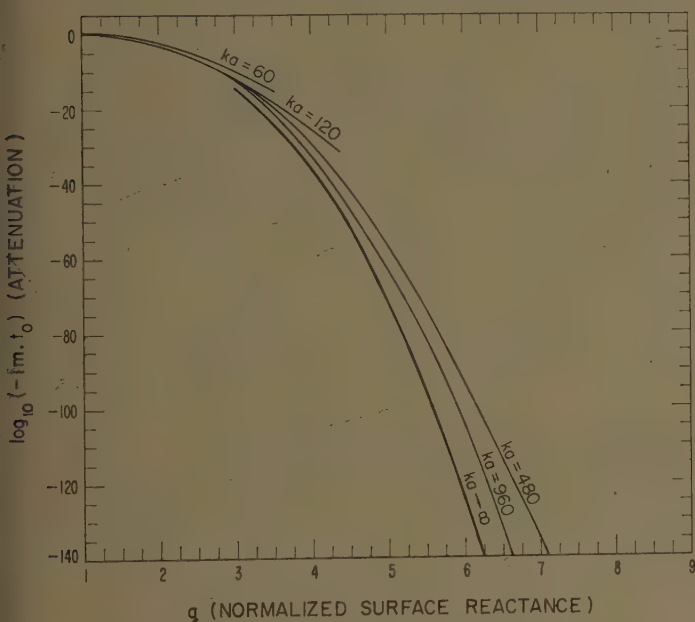


Fig. 2—Attenuation factor  $-\text{Im } t_0$  as a function of  $q$ , the normalized surface reactance.

tion of  $q$  (which is simply related to  $X$ ). It appears that  $ka = \infty$  curves are asymptotic to the curves for large but finite  $ka$ .

#### OTHER MODES

In addition to the root  $t_0$ , there are other roots (not mentioned by Elliott<sup>9</sup>), denoted  $t_1, t_2, \dots$ , etc., which have relatively large imaginary parts corresponding to large attenuation. These roots, which are also solutions of (9), may be obtained from the corresponding solutions for  $q=0$  and  $q=\infty$ .

For  $q=0$ , the roots  $t=t_s^0$  are solutions of

$$w'(t_s^0) = 0, \quad (12)$$

whereas, for  $q=\infty$ , the roots  $t=t_s^\infty$  are solutions of

$$w(t_s^\infty) = 0. \quad (13)$$

Writing

$$t_s^0 = \left(\frac{3x_s}{2}\right)^{2/3} e^{-i\pi/3} \quad \text{and} \quad t_s^\infty = \left(\frac{3y_s}{2}\right)^{2/3} e^{-i\pi/3},$$

it is seen that  $x_s$  and  $y_s$  are the roots of

$$J_{2/3}(x_s) - J_{2/3}(x_s) = 0 \quad (14)$$

and

$$J_{1/3}(y_s) + J_{1/3}(y_s) = 0, \quad (15)$$

respectively. Thus

$t_0^0 = 1.0199 e$	$t_0^\infty \sim \infty$
$t_1^0 = 3.2482 e$	$t_1^\infty = 2.3381 e$
$t_2^0 = 4.8201 e$	$t_2^\infty = 4.0879 e$
$t_3^0 = 6.1633 e$	$t_3^\infty = 5.5206 e$
$t_4^0 = 7.3722 e$	$t_4^\infty = 6.7867 e$

where  $e = e^{-i\pi/3}$ . The root for  $s=0$  corresponds to the surface wave described above. The numbering of the nonzero orders is arranged so the imaginary part of  $t_s$  continuously increases.

Noting again that  $w''(t) - tw(t) = 0$  for any  $t$  and that  $w'(t_s) - qw(t_s) = 0$ , it is seen that the differential equation for the  $t_s$ , for any  $q$ , is

$$\frac{dt_s}{dq} = \frac{1}{t_s - q^2}. \quad (16)$$

Solving this under the initial conditions,

$$t_s = t_s^0 \quad \text{at} \quad q = 0$$

and

$$t_s = t_s^\infty \quad \text{at} \quad q = \infty.$$

Fock,<sup>11</sup> as well as Van der Pol and Bremmer,<sup>6</sup> has shown that

$$t_s(q) = t_s^0 + \frac{1}{t_s^0} q - \frac{1}{2(t_s^0)^3} q^2 + \left( \frac{1}{3(t_s^0)^2} + \frac{1}{2(t_s^0)^5} \right) q^3 - \left( \frac{7}{12(t_s^0)^4} + \frac{5}{8(t_s^0)^7} \right) q^4 + \dots \quad (17)$$

and

$$t_s(q) = t_s^\infty + \frac{1}{q} + \frac{t_s^\infty}{3} \frac{1}{q^3} + \frac{1}{4q^4} + \frac{(t_s^\infty)^2}{5} \frac{1}{q^5} + \dots \quad (18)$$

<sup>11</sup> V. A. Fock, "Diffraction of radio waves around the earth's surface," *J. Phys. USSR*, vol. 9, pp. 256-266; April, 1945.

The series involving powers of  $q$  may be used for  $s=0, 1, 2, 3 \dots$  and it includes the "surface wave" root  $t_0$ . The series involving powers of  $1/q$  may only be used for  $s=1, 2, 3 \dots$  since the initial value is an awkward infinity. As described above, the root  $t_0$  for large but finite  $q$  is obtained from the series of the form

$$t_0 \sim q^2 \left[ 1 + \frac{1}{2q^3} - \frac{5}{32q^6} + \dots \right] \quad (19)$$

or more adequately from values given in Figs. 1 and 2.

For a purely inductive surface, where  $q$  is a real positive quantity, the imaginary part of  $t_0$  is very much less than the imaginary parts of  $t_1, t_2, t_3, \dots$ , etc. Thus, in most cases of practical interest, the field in the vicinity of a curved reactive surface is determined by the surface wave mode.

#### HEIGHT-GAIN FUNCTIONS

It is also of interest to examine briefly the height-gain function. It is given by

$$G = \frac{w(t_0 - y)}{w(t_0)} \quad (20)$$

being the ratio of the field at height  $h$  to the field on the surface. It is possible to obtain numerical values by using tables of the Airy function (or the related Hankel function of order one-third) of complex argument.

For reasonably low heights (*i.e.*,  $y \ll 1$ ) the height-gain function may be approximated by

$$G \cong \exp(-yq) = \exp\left(\frac{-khX}{120\pi}\right) \quad (21)$$

which corresponds to the behavior over a flat boundary whose surface reactance is  $X$ . The field in this case decays rapidly above the surface. However, for greater

heights the function  $G$  must eventually change from a decreasing to an increasing function if the surface is curved. This is to allow for leakage as suggested by Barlow.<sup>3,4</sup> This is also quite evident from the asymptotic expansion of the function  $w(t_0 - y)$ , given by

$$w(t_0 - y) \cong \frac{1}{(y - t_0)^{1/4}} \exp\left[-i \frac{2}{3} (y - t_0)^{3/2} - i \frac{\pi}{4}\right]. \quad (22)$$

This is valid when  $y - \text{Re } t_0 \gg 1$ . Furthermore, since

$$(y - t_0)^{3/2} \cong y^{3/2} - \frac{3}{2} t y^{1/2}$$

and  $-\text{Im } t \ll \text{Re } t$ , it follows that

$$|w(t_0)G| \cong \frac{1}{y^{1/4}} \exp(-y^{1/2} \text{Im } t_0). \quad (23)$$

Thus at large heights (but still  $h \ll a$ ),  $G$  is increasing in magnitude since  $\text{Im } t_0 < 0$ . However, the function  $G$  does not continue to increase when  $h$  becomes comparable or large compared to the radius  $a$ ; then the field has a radiation character.

#### FINAL REMARKS

The model adopted in the present paper appears to be an adequate first approximation for studying the influence of curvature on surface wave propagation. It is shown that it is not necessary to introduce a wave "reflected from outer space" in the manner suggested by Barlow. Furthermore, the results in the present paper seem to confirm the earlier analysis of Elliott. Barlow<sup>4</sup> had questioned the attenuation rates computed by Elliott and thought that they were too small.

#### ACKNOWLEDGMENT

The author would like to thank A. Conda for assistance in the numerical aspects of the problem.



## Note on "The Excitation of Electromagnetic Surface Waves on a Curved Surface"\*

H. M. BARLOW†

SINCE the field associated with a pure surface wave must by its very nature extend to an infinite distance from the supporting surface, any physical obstacle outside the surface necessarily produces radiation. It does this by setting up a field reflected from the obstacle. In practice, a perfectly homogeneous medium extending to infinity outside the supporting surface is impossible to achieve, and consequently it is important to consider the effect on the behavior of the wave of a discontinuity deliberately introduced into the surrounding medium. Barlow,<sup>1</sup> referenced by Wait,<sup>2</sup> attempts to examine that problem in relation to the particular case of a surface wave circulating in azimuth around a highly reactive cylindrical surface. Previously,

no consideration had been given to the mechanism by which an obstacle outside the surface modified the field distribution, but the analysis for which Elliott<sup>3</sup> was originally responsible and which has now been confirmed by Wait, using a somewhat different approach, emphasizes the exceedingly low level of radiation which would be expected to arise when the medium is perfectly homogeneous and the surface is only slightly curved.

Some preliminary experiments made here very recently seem to indicate a substantially higher level of radiation than would be expected from the Elliott-Wait theory, and while it is yet too early to draw any conclusions from this work, there is an implication that reflected fields from obstacles outside the surface do play an important part in a practical case.

\* Manuscript received by the PGAP, February 15, 1960.

† Elec. Engrg. Dept., University College, London, Eng.

<sup>1</sup> H. M. Barlow, "Surface waves supported by cylindrical surfaces," *Proc. URSI Symp. on Electromagnetic Theory*, June, 1959; *IRE TRANS. ON ANTENNAS AND PROPAGATION*, vol. AP-7, pp. 147-153; December, 1959.

<sup>2</sup> J. R. Wait, "On the excitation of electromagnetic surface waves on a curved surface," this issue, p. 445.

<sup>3</sup> R. S. Elliot, "Spherical surface wave antennas," *IRE TRANS. ON ANTENNAS AND PROPAGATION*, vol. AP-7, pp. 422-428, July, 1959; "Azimuthal surface waves on circular cylinders," *J. Appl. Phys.*, vol. 26, pp. 368-376; April, 1955.

## The Structure of HF Signals Revealed by an Oblique Incidence Sweep Frequency Sounder\*

D. J. DOYLE†, E. D. DUCHARME†, AND G. W. JULL†

THE current interest<sup>1-3</sup> in sweep-frequency pulse sounding at oblique incidence lies not only in its application in furthering basic studies of the ionosphere, but also in its potential importance as a means to obtain improvement in present HF prediction services. The technique by which multipath and signal structure are examined across the HF band through the

use of narrow sounding pulses permits unambiguous identification of propagation modes and indicates the frequency dependence of ionospheric signals. Of particular interest are studies of transmissions near the MUF (maximum usable frequency) in the region of predominantly specular reflection, and just above the MUF in the region where extensions of the band have been observed.

The intent of this communication is to present a description of preliminary oblique sounding trials that are designed to investigate the signal structure dependence on frequency over a 960-km East-West circuit between Halifax, Nova Scotia, and Ottawa, Ontario. The sounding transmitter in Halifax delivers narrow (10-μsec width), shaped pulses of 100-kw peak power, and a 10-cps PRF, into a rhombic antenna. The transmitter is step-tuned regularly through the HF band from 1 to

\* Manuscript received by the PGAP, February 12, 1960. The work was carried out under PCC No. D48-28-01-07 of the Defence Research Board.

† Defence Res. Telecommunications Est., Ottawa, Ont., Can.

<sup>1</sup> E. Warren and E. L. Hagg, "Single-hop propagation of radio waves to a distance of 5300 km," *Nature*, vol. 181, pp. 34-35; January, 1956.

<sup>2</sup> G. W. Jull and W. L. Hatton, "Ionospheric studies at oblique incidence over a 600 mile circuit," *Canadian IRE Convention Record*, pp. 110-113; October, 1958.

<sup>3</sup> P. G. Sulzer, "Sweep frequency pulse transmission measurements over a 2400 km path," *J. Geophys. Res.*, vol. 60, pp. 411-420; December, 1955.



Fig. 1—Three-dimensional model illustrating signal strength and multipath dependence on frequency (14:37 EST June 12, 1958). (a) Model shown as a conventional oblique ionogram with the regular ionospheric modes noted:  $E_L$  and  $F_{1L}$  denote low angle rays for the  $E$ - and  $F_1$ -layer signals, respectively.  $E_H$  and  $F_{1H}$  denote high angle rays for the  $E$ - and  $F_1$ -layer signals, respectively.  $O$  and  $X$  denote ordinary and extraordinary ray components for the  $F_1$ -layer signals. (b) Model illustrating signal strength dependence on frequency with additional modes noted:  $F_D$ —additional stratification caused by a traveling wave disturbance.  $F_S$ —scatter from the base of the  $F_1$  layer.  $E_S$ —extension of  $E$ -layer signals beyond the  $E$ -layer MUF.

25 mc, and remains on each 100-kc step for one second. A wide-band (100-kc) logarithmic receiver situated at Shirley Bay, near Ottawa, is similarly step-tuned through the band in synchronism with the sounding transmitter. The relatively high power of the transmitter permits studies on signals above the MUF, in spite of the wide receiver bandwidth. A prearranged program ensures reception of the sounding signals, while synchronism of the transmitter PRF with the time base of the receiver display units is maintained through the use of two highly stable crystal oscillators. The sounding program is repeated every five minutes. Along with the normal recording of the receiver signals as oblique ionograms, the signals can be photographed from an "A" display, using a 35-mm camera.

A three-dimensional model has been constructed from "A" display recordings taken during one sweep so that the frequency dependence of ionospheric mode fine structure can be clearly illustrated. This model is illustrated in plan view in Fig. 1(a) in the conventional form of an oblique ionogram, with frequency as the abscissa and path delay time as the ordinate. The signal level dependence with frequency for the various propagation modes is illustrated in Fig. 1(b). (The signal levels on the model are as received and no correction has been made for system gain variations with frequency.) The modes identified in Fig. 1 are characteristic of observations during a summer day on this circuit. There are a number of important fine structure features which are best understood with reference to this three-dimensional ionogram.

- 1) The  $E$ -layer transmission mode controls the circuit MUF, and an important feature of the  $E$ -layer transmission is the relative strength of the  $E$ -layer high angle ray ( $E_H$  in Fig. 1), which is observed to extend 3.5 mc below the circuit MUF. Very little, if any, ionospheric focusing of the low and high ray is seen to take place at the circuit MUF.

- 2) The  $F_1$ -layer rays exhibit a multiplicity of additional modes which are not to be expected on the basis of first-order magneto-ionic theory. In addition to the regular ordinary and extra-ordinary polarization components, several additional modes exist which can be explained with some degree of certainty. The first is the additional set of high angle signals  $F_D$  which have been identified as an additional stratification at  $F_1$ -layer heights caused by a traveling disturbance moving across the transmission path. Vertical sounding observations at Ottawa, which confirm this, show a similar stratification during the period of oblique recording. The second mode  $F_S$  which can be identified is scatter from the bottom of the  $F_1$  layer.

During the period of observation the  $E$ -layer signals were found to have a strong scatter component, which has two important effects on the frequency dependence of the signals. Fig. 2(a) illustrates the median signal level observed on five consecutive five-minute sounding runs following the observations on Fig. 1. (The  $E$  layer shows relatively little change during this recording period.) The rise in signal level from 10 to 12.5 mc results from a decrease in the nondeviative absorption with frequency. It is observed that the  $E$ -layer high angle ray (ordinary ray component) is not more than 10 db below the strength of the low angle ray over the frequency band from 10 to 12.5 mc. There is clearly no pronounced focusing at the MUF (13.4–13.7 mc). The delay times associated with these modes are shown in Fig. 2(b). Above the MUF, the signal strength decreases at the rate of approximately 34 db/mc over the narrow range of 500 kc; at higher frequencies the decrease was much less. Heavy interference prevented measurements between 14.8 and 16.5 mc, but comparatively low-level scatter signals are observed above 16.5 mc. The delays associated with this scatter are shown in Fig. 2(b), with a duration of scatter delays up



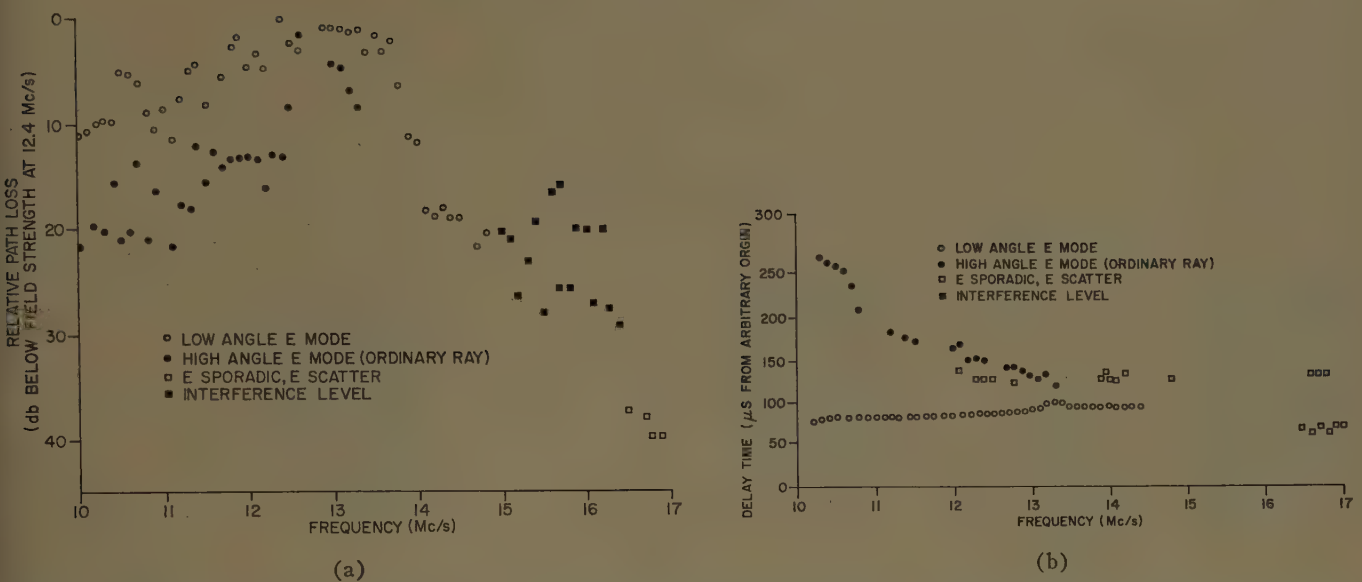


Fig. 2—Frequency dependence of *E*-layer signals (14:37–15:02 EST, June 12, 1958). (a) Median signal level dependence on frequency. (b) Signal delay time dependence on frequency.

to 70  $\mu$ sec. It appears that the delay times associated with the last arriving scatter signals may be caused by sporadic *E* transmission as these signals can also be observed below the MUF.

By way of contrast, for *E*-layer transmissions that show rather less scatter signal components above the MUF, a signal level falloff above the MUF of some 45–50 db/mc has been observed over a frequency range of greater than 1 mc. Moreover, the high ray strength was lower than the low ray strength by greater than 20 db for all frequencies except those very close to the MUF. In this case, there is occasionally pronounced signal enhancement near the MUF, although focusing of the low and high *E* rays is not a general occurrence for observations that use narrow pulses. Similar lack of focusing has been noted by Salaman.<sup>4</sup>

<sup>4</sup> R. K. Salaman, "An Experimental Study of Pulse Amplitude Focussing Near the MUF," presented at URSI-IRE Spring Meeting, Washington, D. C.; 1959.

It would clearly be of great value in improving the utilization of the *HF* band if operators of circuits could be provided with information on the frequency and time dependence of the signal strength and multipath duration. While it would not be necessary, or indeed feasible, to provide information with the detail illustrated on the three-dimensional model, it is believed at present that, with some loss in resolution, information can be made available to communicators if oblique sounding techniques similar to those described are used.

The authors acknowledge the assistance of EMI-Cossor Electronics Ltd., Dartmouth, Nova Scotia in obtaining these results. The research group of EMI-Cossor Electronics engaged in ionospheric studies has constructed the oblique sounding system and has operated the sounding transmitter. They also acknowledge the value of helpful discussion on these trials with W. L. Hatton of the Defence Research Telecommunications Establishment, Ottawa.



# Contributors

L. H. Doherty (S'42-A'46-M'53-SM'58) was born in Montreal, Can. on August 22, 1922. He received the B. Eng. degree from



L. H. DOHERTY

McGill University, Montreal, Can., in 1944, and the Ph.D. degree in electrical engineering from Cornell University, Ithaca, N. Y. in 1953. He joined the staff of the National Research Council of Canada in 1944, and was employed in radio wave propagation research in Ottawa, Ontario, and Suffield, Alberta. In 1948, while undertaking graduate studies, he was appointed research associate at Cornell University, and worked in the fields of radio astronomy, antennas, and radio wave propagation. In 1953 he rejoined the National Research Council, and has been engaged in radio wave propagation research since that date.

Dr. Doherty is a member of Sigma Xi.

S. Edelberg, for a photo and biography please see p. 350 of the May, 1960 issue of these TRANSACTIONS.

Leopold B. Felsen (S'47-A'53-M'54-SM'55) was born in Munich, Germany, on May 7, 1924. He received the B.E.E., M.E.E., and D.E.E. degrees from the Polytechnic Institute of Brooklyn, Brooklyn, N. Y., in 1948, 1949, and 1952, respectively.



L. B. FELSEN

He entered the United States in 1940, and during World War II was concerned with work on electronic ballistic calibration devices in the U. S. Army. Since 1948, he has been with the Microwave Research Institute of the Polytechnic Institute of Brooklyn and presently holds the position of research associate professor. His research work has been concerned chiefly with problems in electromagnetic diffraction, multimode propagation, and microwave network and measurement techniques. He has also been teaching graduate courses in the electrical engineering department.

Dr. Felsen is a member of the USA Commission 6 of URSI and of Eta Kappa Nu, Tau Beta Pi, and Sigma Xi.

Bernard L. Jones was born in Kansas City, Missouri, on May 7, 1924. He received the B.S. degree in electrical engineering



B. L. JONES

from the University of Kansas in 1947. He did postgraduate studies in physics at the University of Kansas, Lawrence, until 1948. He was a research engineer for Aluminum Company of America from 1949 to 1955. In 1955 and 1956, he was on the electrical engineering staff of Jones-Hettelsater Construction Company. Since 1956, Mr. Jones has been on the staff of Midwest Research Institute, Kansas City, Missouri.

Edward M. T. Jones (S'45-A'51-M'55-SM'56) was born in Topeka, Kans., on August 19, 1924. He received the B.S.E.E. degree in 1944 from Swarthmore College, Swarthmore, Pa., and the M.S. and Ph.D. degrees in electrical engineering in 1948 and 1950, respectively, from Stanford University, Stanford, Calif.



E. M. T. JONES

He was a Radar Maintenance Officer in the U. S. Navy from 1944 to 1946, and from 1948 to 1950, he was a Research Associate at Stanford. In 1950, he joined the staff of Stanford Research Institute, Menlo Park, Calif., and in 1957, became Head of the Microwave Group of the Electromagnetics Laboratory. His fields of specialty include microwave filters and antennas, stripline components, and parametric amplifiers.

Dr. Jones is a member of the Scientific Research Society of America, Sigma Tau, and Sigma Xi.

Samuel N. Karp was born in Brooklyn, N. Y., on February 13, 1924. He received the A.B. degree from Brooklyn College in 1944 and the M.Sc. and Ph.D. degrees in 1945 and 1948, respectively, from Brown University, Providence, R. I.

During his stay at Brown University, he served as a research assistant and later as a research associate working in compressi-

ble fluid theory, especially the theory of oscillating airfoils. In 1948 he joined the Mathematics Research Group at New York

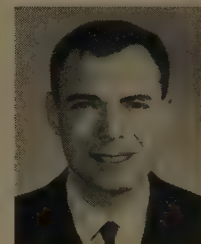


S. N. KARP

University as a senior research scientist working on problems of electromagnetic theory. He is now an associate of mathematics, as well as a member of the Division of Electromagnetic Research of the Institute of Mathematical Sciences at N.Y.U.

Dr. Karp is a member of Pi Mu Epsilon, Sigma Xi, the American Mathematical Society, and the American Physical Society.

Alan F. Kay (M'55) was born in Newark, N. J., in 1925. He received the B.S. degree from the Massachusetts Institute of Technology, Cambridge, in 1948, and the Ph.D. degree from Harvard University in 1951, both in mathematics.



A. F. KAY

Since 1951 he has worked on microwave and antenna problems. In 1957 he was elected vice-president of Technical Research Group, Inc., Syosset, N. Y., where he has been employed for the last six years. He assisted in the founding of the microwave and antenna laboratory at TRG located in Somerville, Massachusetts.

Dr. Kay is a member of SIAM and AMS.

D. D. King (M'46-SM'57-F'59) was born on August 7, 1919, in Rochester, N. Y. He received the B.A. degree in engineering sciences in 1942 and the Ph.D. degree in physics in 1946, both from Harvard University, Cambridge, Mass.



D. D. KING

He was a teaching fellow in physics and communication engineering in 1943, serving as a staff member of the pre-radar Officer's Training School at Cruft Laboratory, Harvard. He was a research associate there during 1945, a research fellow

in electronics in 1946, and assistant professor of applied physics in 1947. In 1948, he was appointed associate professor of physics in the Institute for Cooperative Research of The Johns Hopkins University, Baltimore, Md.; in 1950 he became assistant director and in 1955, director of the Radiation Laboratory. He became Vice-President of research at Electronic Communications, Inc., Timonium, Md., in 1956.

Dr. King is a member of Sigma Xi and the American Physical Society.

Walter E. Landauer was born on October 11, 1923 in Stuttgart, Germany. He received a B.E.E. degree from the Cooper Union School of Engineering, New York, N. Y., in 1947 and the M.S. degree in electrical engineering from Columbia University, New York, N. Y., in 1949.

Mr. Landauer was a teaching assistant in electrical engineering at Columbia University from 1947 to 1949. He has also, at various times, taught at the Polytechnic Institute of Brooklyn, Brooklyn, N. Y., and at Cooper Union.

He joined Airborne Instruments Laboratory, Deer Park, N. Y., in 1949 and is, at present, a group leader in the Ground Data Handling section of that company. In his assignments with AIL, he has at various times worked in development of active countermeasures equipment, was project engineer for the development of radiation monitoring equipment for use on nuclear-powered vessels, and was responsible for the development of the swept tropospheric scatter link described in this issue. He is currently engaged in the development of a large-scale, digital, ground-based data handling system.

Mr. Landauer is a member of the AIEE and a registered professional engineer in the State of New York.

Bernard J. Maxum was born in Breerton, Wash., on November 4, 1931. He received the B.S.E.E. degree from the University of Washington, Seattle, in 1955, the M.S.E.E. degree on a Hughes Fellowship from the University of Southern California, Los Angeles, in 1957, and is currently pursuing the Ph.D. degree on a Ford Foundation Fellowship at the University of California, Berkeley.

He has taught at the University of Southern California, the University of Washington, and at the University of California,

Berkeley. From 1955 to 1958, he worked at Hughes Aircraft Company, Culver City, Calif., on antenna array design and research in slotted waveguides and ferrites. He was employed at Boeing Airplane Company, Seattle, from 1958 to 1959, engaged in work on two-dimensional array antennas and plasma research.

Mr. Maxum is a member of Sigma Xi and Tau Beta Pi.

S. Nishida, for photograph and biography please see p. 352 of the May, 1960 issue of these TRANSACTIONS.

A. A. Oliner (M'47-SM'52), for a photo and biography please see p. 443 in the October, 1959 issue of these TRANSACTIONS.

Richard F. Packard (A'54-M'59) was born on September 14, 1927, in Lewiston, Me. He attended Bates College, Lewiston, and is currently enrolled at McCoy college, The Johns Hopkins University, Baltimore, Md., where he has completed most of the course requirements for the B.S. degree in mathematics.

From 1946 to 1949, he served in the U. S. Navy as an electronics technician. He worked for the Raytheon Manufacturing Company, Waltham, Mass., and for Massachusetts Institute of Technology's Lincoln Laboratory, Lexington, Mass., in a similar capacity for two years. From 1953 to February, 1959, he was an engineer at the Martin Company, Baltimore, doing antenna and radome development. In February, 1959, he joined the staff of the Research Division, Electronic Communications, Inc., Timonium, Md., where he has worked on direction finders and antenna arrays.

Peter C. Patton (A'55-M'58) was born in Wichita, Kans., on June 11, 1935. He received the A.B. degree in engineering and applied physics from Harvard University, Cambridge, Massachusetts, in 1957 and the M.A. degree in mathematics from the University of Kansas, Lawrence, in 1959.

From 1957 to 1959 he was a research assistant in the mathematics department

at the University of Kansas. In 1959 he became a member of the Systems Engineering Section of Midwest Research Institute, Kansas City, Missouri.

Mr. Patton is a member of Pi Mu Epsilon.

Sheldon S. Sandler was born in Cleveland, Ohio on December 17, 1932. He received the B.S.E.E. degree from Case Institute of Technology, Cleveland, in 1954. Under a Thomas A. Edison Fellowship at Yale University, he received the M.E. degree in electrical engineering, in 1955. From 1955 to 1956, he was a research associate in the Department of Physics, Horizon's Inc., Cleveland, Ohio. From

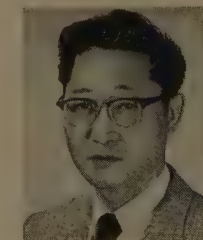


S. S. SANDLER

1956 to 1958, he was engaged in graduate study in the Department of Engineering and Applied Physics, Harvard University, Cambridge, Mass. receiving the M.A. degree in 1958. From 1958 to September 1959, he was a staff member of the Antenna group of M.I.T. Lincoln Laboratory, Lexington, Mass. Currently he is associated with Electronic Communications Inc., Timonium, Maryland, investigating wave propagation in ferrites at microwave frequencies.

Mr. Sandler is a member of Tau Beta Pi and Eta Kappa Nu.

James K. Shimizu (S'51-A'52-M'57) was born in San Diego, Calif., on October 28, 1924. He received the B.S.E.E. degree in 1950 from Indiana Technical College, Fort Wayne, and the M.S.E.E. degree in 1952 from the University of Notre Dame, Notre Dame, Ind. While at Notre Dame, he was a teaching fellow in the electrical engineering department. During this time, he was also employed as



J. K. SHIMIZU

a Research Assistant for the Office of Air Research. In 1952, he joined the staff of Stanford Research Institute, Menlo Park, Calif., where he has been engaged in research and development of various microwave antennas and components, and of filters.

Mr. Shimizu is a member of the Scientific Research Society of America.



B. J. MAXUM



P. C. PATTON



Alan J. Simmons (A'47-SM'60) was born in 1924 in New York, N. Y. He received the B.S. degree from Harvard College, Cambridge, Mass., in 1945 in physics and chemistry.



A. J. SIMMONS

After a tour of duty as a radar engineering officer in the Navy, he was employed at the M.I.T. Research Laboratory for Electronics, while pursuing studies which led to the M.S. degree in electrical engineering in 1948.

He then joined the Microwave Antennas and Components Branch at Naval Research Laboratory in Washington, D. C. After receiving the Ph.D. degree in 1957 from the University of Maryland, College Park, Md., he joined Technical Research Group and helped start a microwave and antenna department of that company in the Boston area.

He is a member of Sigma Xi and Phi Kappa Phi.



S. A. Stone (A'54-M'59) was born in Winnipeg, Manitoba, Can., on April 10, 1932. He received the B.S.E.E. degree from the University of Manitoba, Can., in 1954, and the M. Eng. degree in electrical en-

gineering from McGill University, Montreal, Can., in 1958.

He joined the staff of the Radio and Electrical Engineering Division of the National Research Council of Canada, in Ottawa, in 1954 and since that time has been a member of the Microwave Section, working in the field of tropospheric propagation.



S. A. STONE

Mr. Stone is a member of Sigma Xi.



Richard K. Thomas (A'48-M'51-SM'54) was born in Kingston, N. Y., on December 8, 1914. He received the B.A. and B.S.E.E. degrees in 1935 and 1948, respectively,



R. K. THOMAS

from New York University, New York, and the M.S.E. degree in 1957 from The Johns Hopkins University, Baltimore, Md.

From 1946 to 1948, he worked in antenna design at Airborne Instruments Labora-

tory, Mineola, N. Y., followed by four years at Bendix Radio Company, Towson, Md., where he was in charge of the Research Department antenna section. During 1953 and 1954, he was engaged in countermeasures work at the Radiation Laboratory at Johns Hopkins, and carried on the same work at Stanford Research Institute, Menlo Park, Calif., during 1955. In 1956, he participated in the organization of the Research Division of Electronic Communications, Inc., Timonium, Md., as the Assistant to the Vice-President, and is currently engaged there in antenna design and development.



Andreas Tonning was born in Stryn, Norway, on July 23, 1922. He received the Electrical Engineering degree from the Norwegian Institute of Technology, Trondheim, in 1948, and the Doctor's degree in 1959.



A. TONNING

Since 1948 Dr. Tonning has been employed at the Norwegian Defence Research Establishment, Bergen, Norway, and has done experimental and theoretical work in the field of microwave communication and electromagnetic theory.







FOR INFORMATION CONCERNING ADVERTISING RATES

Contact

MR. DELMER C. PORTS  
Jansky and Bailey, Inc.  
1339 Wisconsin Avenue N.W.  
Washington 7, D.C.  
Telephone: Federal 3-4800



## INSTITUTIONAL LISTINGS

The IRE Professional Group on Antennas and Propagation is grateful for the assistance given by the firms listed below, and invites application for Institutional Listing from other firms interested in the field of Antennas and Propagation.

**AERO GEO ASTRO CORP.**, 1200 Duke St., Alexandria, Va.  
Research and Development; Antennas; Transponders; Command Receivers; Augmenters; Telemetry-Radar.

**ANDREW CORPORATION**, 363 E. 75th St., Chicago 19, Ill.  
Antennas, Antenna Systems, Transmission Lines, Development and Production.

**ANTLAB, INC.**, 6330 Proprietors Rd., Worthington, Ohio  
Antenna Pattern Range Systems—Recorders & Mounts.

**BLAINE ELECTRONETICS, INC.**, 14757 Keswick St., Van Nuys, Calif.  
Antennas, Paraboloids, Scale Models, Antenna Radiation Pattern Measurement Towers.

**DEVELOPMENTAL ENGINEERING CORP.**, 1001 Conn. Ave. N.W., Washington, D. C. and Leesburg, Va.  
Research, Development, Installation of Antennas and Antenna Equipment for Super Power Stations.

**GABRIEL ELECTRONICS**, Division of The Gabriel Company, Main & Pleasant Sts., Millis, Mass.  
Research, Engineering and Manufacture of Antenna Equipment for Government and Industry.

**I-T-E CIRCUIT BREAKER CO.**, Special Products Div., 601 E. Erie Ave., Philadelphia 34, Pa.  
Design, Development and Manufacture of Antennas, and Related Equipment.

**JANSKY & BAILEY, INC.**, An Affiliate of Atlantic Research Corp.,  
1339 Wisconsin Ave., N.W., Washington, D. C.  
Complete Engineering Services for Antennas and Propagation Programs.

**MARK PRODUCTS CO.**, 6412 W. Lincoln Ave., Morton Grove, Ill.  
Multi Element Grid Parabolas, Antennas for Two-Way Communications, R & D.

**THE W. L. MAXSON CORP.**, 475 Tenth Ave., New York 18, N.Y.  
Research, Development, & Manufacture of Airborne, Missile & Ordnance Systems & Equipment.

**TRANSCO PRODUCTS, INC.**, 12210 Nebraska Ave., Los Angeles 25, Calif.  
Res., Design, Dev., & Mfr. of Antenna Systems & Components for Missile, Aircraft & Ground Installations.

**WEINSCHEL ENGINEERING COMPANY, INC.**, Kensington, Md.  
Antenna Pattern Receivers; Bolometer Amplifiers; Modulated Microwave Sources;  
Insertion Loss Measuring Systems; Calibrated Attenuators.

**WHEELER LABORATORIES, INC.**, Great Neck, N. Y.; Antenna Lab., Smithtown, N. Y.  
Consulting Services, Research and Development, Microwave Antennas and Waveguide Components.

The charge for Institutional Listing is \$25 for one issue or \$100 for six consecutive issues (one year). Application may be made to the Technical Secretary, The Institute of Radio Engineers, 1 East 79th Street, New York 21, N. Y.